Mechanics of Deformation at Plate Corners

DISSERTATION

der Mathematisch-Naturwissenschaftlichen Fakultät
der Eberhard Karls Universität Tübingen
zur Erlangung des Grades eines
Doktors der Naturwissenschaften
(Dr. rer. nat.)

vorgelegt von
MATTHIAS NETTESHEIM
aus Rosenheim

Tübingen
2021

Gedruckt mit Genehmigung der Mathematisch-Naturwissenschaftlichen Fakultät der Eberhard Karls Universität Tübingen.

Tag der mündlichen Qualifikation:	23.07.2021
Dekan:	Prof. Dr. Thilo Stehle
1. Berichterstatter:	Prof. Dr. Todd A. Ehlers
2. Berichterstatter:	Prof. Dr. Paul D. Bons

Abstract

Extreme features naturally draw attention and often provide unique opportunities to study the underlying processes at work. In recent years, the fast and localized exhumation observed at the Namche Barwa (Eastern Tibet, China), Nanga Parbat (Northern Pakistan), and St. Elias (South-East Alaska) orogen syntaxes have enticed scientific interest. While some attribute these exceptional features to the strong and focused erosion at these locations, others see the three-dimensional curved geometry of the subducting plate as the cause. For the most part, Earth's subduction plate boundaries consist of long, straight to slightly concave segments connected by short, convex bends, the plate corners. At these corners, the folding required to accommodate subduction of the spherical plates creates stiffened indenters that provide more resistance to subduction and thus may affect deformation in the overriding plate.

In this thesis, the mechanics of deformation at plate corners with such an indenter geometry are investigated through three-dimensional, fully coupled thermo-mechanical numerical models. For that, the modeling program DOUAR was enhanced and expanded with additional geometry options, efficient erosion algorithms and thermochronometric age prediction. Thus we created the opportunity to study the effects of various material properties and model configurations on upper plate deformation and directly compare results to observed cooling ages. The effect of erosion is investigated by contrasting flat and fluvial erosion modes. Flat erosion enforces a flat top surface, which allows the isolation of tectonic processes, while fluvial erosion represents a more realistic scenario. Overall, 43 model scenarios are evaluated and discussed.

Model results reveal how a rigid indenter may generate rapid and localized uplift: because of the changed subducting plate's geometry, the style and pattern of shear zones that accommodate crustal shortening in the overriding plate are changed. More specifically, models show a basal décollement above the indenter that creates an area of focused uplift and is separated from other shear zones and uplift fields forming along the straight-slab segments besides the indenter. The intensity of this isolated uplift depends on the amount of total shortening that is accommodated by the indenter shear zone, which in turn is influenced by several other model parameters. One important factor is the upper plate's motion relative to the trench: results suggest that some upper plate advance is required to bring the lower plate's indenter geometry into effect. In regards of material parameters, a low coupling between crust and upper mantle, i.e. a comparatively weak lower crust, strain weakening in the crust, as well as a weak interface layer between overriding and subducting plate increase shear along the basal décollement, which in turn, enhances localized uplift above the indenter apex. Additionally, models with fluvial erosion show an additional focusing of rock uplift where tectonic uplift fields coincide with a strong erosion potential from steeply incised valleys. Based on these findings, we are able to create numerical models with approximated plate geometries of the Cascadia Subduction Zone and the southern Alaska that correspond closely to the distribution of observed cooling ages of these locations.

In summary, the conducted fully coupled thermo-mechanical models contribute to understanding deformation at plate corners and identify several factors that facilitate the formation of rapid and localized uplift in the overriding plate. Results suggest the indenter-type plate geometry as primary driver for rapid and focused rock uplift, while erosion acts on top to focus uplift even further.

Zusammenfassung

Extreme Phänomene erwecken naturgemäß die Aufmerksamkeit des Betrachters und stellen oft eine besondere Möglichkeit dar, die zugrunde liegenden Prozesse zu erforschen. In den letzten Jahren haben Beobachtungen von schneller und lokal begrenzter Exhumation in den Syntaxen von (Osttibet, China), Nanga Parbat (nördliches Pakistan), and St. Elias (südöstliches Alaska) das Interesse der Forschungsgemeinschaft auf sich gezogen. Während manche die Ursache für diese außergewöhnlichen Phänomene in der starken, konzentrierten Erosion in diesen Gebieten sehen, schreiben andere diese der besonderen, dreidimensional gekrümmten Geometrie der subduzierenden Platten zu. Zum größten Teil bestehen die Subduktionsplattengrenzen der Erde aus langen, geraden bis leicht konkav gekrümmten Abschnitten, die über kürzere, konvex gebogene Plattenecken verbunden werden. An diesen Ecken faltet sich die subduzierende Platte auf, um das Abtauchen dieser sphärisch gekrümmten Platte zu ermöglichen. Dadurch tritt eine Längsversteifung ein, die der Subduktion einen größeren Widerstand darbietet und so die Deformation in der überfahrenden Platte beeinflussen kann.

In dieser Doktorarbeit werden die Deformationsmechanismen in der Oberplatte im Bereich von Plattenecken mit einer solchen Aufwölbungsgeometrie untersucht. Dies geschieht mit Hilfe von dreidimensionalen, thermo-mechanisch vollständig gekoppelten numerischen Modellen. Dafür wurden an dem Modellierungsprogramm DOUAR umfangreiche Erweiterungen und Verbesserungen vorgenommen, darunter neue Geometrievarianten, ein effizienterer Algorithmus zur Berechnung fluvialer Erosion und ein Modul zur Vorhersage thermochronometrischer Abkühlalter. Dies ermöglicht eine umfassende Untersuchung darüber, wie sich Materialeigenschaften und andere Modellparameter auf die Deformation der Oberplatte auswirken, wobei die Ergebnisse direkt mit gemessenen Abkühlaltern verglichen werden können. Der Einfluss von Erosion wird durch den Vergleich von zwei Arten der Erosion, plan und fluvial, untersucht. Bei planer Erosion wird die Oberfläche dabei stets auf ein Grundniveau zurückgesetzt, was einen unverfälschten Blick auf die tektonischen Prozesse ermöglicht. Im Gegensatz dazu stellt die fluviale Erosion ein realistischeres Modellszenario dar. Insgesamt wurden 43 verschiedene Modellszenarien ausgewertet und besprochen.

Die Modellergebnisse zeigen, wie eine versteifte Auswölbung zu schneller und lokal begrenzter Hebung führen kann: Aufgrund der veränderten Geometrie der abtauchenden Platte ändert sich die Art und Anordnung der Scherzonen, die die Krustenverkürzung aufnehmen. Insbesondere zeigen die Modelle ein décollement oberhalb der Auswölbung, die einen Bereich mit fokussierter Hebung erzeugt und von anderen Scher- und Hebungszonen getrennt ist, welche sich entlang der geraden Plattensegmente ausbilden. Bei der Bildung dieses décollements spielt die Bewegung der Oberplatte relativ zum Subduktionsgraben eine wichtige Rolle: Die Ergebnisse legen nahe, dass ein Vorrücken der Oberplatte benötigt wird, damit die Auswölbung der Unterplatte ihre Wirkung entfalten kann. Bezüglich der Materialeigenschaften wird der Anteil der Zusammenschubs, der von der Scherzone oberhalb der Auswölbung aufgenommen wird, durch eine geringe Bindung der Kruste, also eine verhältnismäßig schwache untere Kruste, eine Festigkeitsreduktion der oberen Kruste bei Verformung, sowie eine schwache Trennschicht zwischen der Ober- und der Unterplatte vergrößert. Darüber hinaus zeigen Modelle mit fluvialer Erosion eine weitere Fokussierung im Hebungsprozess, wo tektonische Hebung mit dem hohen Erosionspotential tief eingeschnittener Täler zusammentrifft.

Auf Grundlage dieser Erkenntnisse konnten Modelle mit angenäherten Plattengeometrien für die Cascadia Subduktionszone und von Südalaska erstellt werden, deren Verteilung von Abkühlaltern weitgehend mit den jeweiligen Beobachtungen übereinstimmen.

Zusammenfassend tragen diese vollständig gekoppelten thermomechanischen Modelle zum weiteren Verständnis der Deformation an Plattenecken bei und identifizieren mehrere Faktoren, die die Entstehung von schneller und lokal begrenzter Exhumation in der Oberplatte befördern. Die Ergebnisse legen dabei den Schluss nahe, dass die besondere Plattengeometrie mit ihrer versteiften Ausbuchtung die eigentliche Ursache darstellt, wobei durch starke Erosion eine darüber hinausgehende Fokussierung der Hebung stattfindet.

Acknowledgements

This thesis could not have been realized without the help and support I received from many people during my time at the University of Tübingen and afterwards. Such a list can never be complete, but I wish to acknowledge at least some of them.

First and foremost, I'd like to thank my supervisor, Todd Ehlers, for your continuous support in the various stages of this project. From beginning to the end, you always had an open ear, provided me with new and interesting input and helped me to clarify and focus my research project in numerous discussions. As a member of the EXTREME project and the Earth System Dynamics research group, I learned so many different things, from research and Geosciences in general to the specifics of Geodynamic modeling, that changed my view on the world. I deeply enjoyed working in such a stimulating, diverse environment.

Many thanks to my second supervisor David Whipp for introducing me to DOUAR and hosting me at the University of Helsinki. From this starting point, you were a reliable and invaluable support to discuss the details of programming and modeling that only made this thesis possible in the first place.

Willi Kappler and Lars Kaislaniemi also contributed to DOUAR and made improvements that I gladly used. Willi deserves special mentions as the silent hero who keeps the ESD IT infrastructure up and running smoothly and provides fast help in any kind of computer troubles with a constant cheerful attitude.

This thanks also extends to all colleagues that became friends and made Tübingen not only a place to work, but a home to live in. Sarah, Elena, Sebastian, and Solmaz – thank you for all the great time we had together.

Last but not least, I thank my family – my parents, for their continuous support, helpful conversation and deep trust, but most of all my wife Clara. This project did not always go as I envisioned it, but thanks to you at my side, I managed to find a way through and bring this to its conclusion.

Contents

1 Introduction

Earth's mountain ranges are the magnificent and serene witnesses of continuous forces and processes in the earth system that are imperceptible to normal humans senses. And yet those processes affect the face of the earth in myriad ways that shape life on this planet. Mountain ranges act as drivers for multiple systems. They are physical barriers that will re-route rivers, alter prevailing wind patterns and weather systems, or separate biologic populations into different ecosystems. By chemical weathering of exposed minerals, atmospheric and oceanic chemistry is affected. Mountain ranges host important mineral deposits that drive human prosperity, but also endanger millions by the high susceptibility to natural hazards.

In geosciences, the acceptance of continental drift (Pichon 1968) and discovery of plate tectonics (Wilson 1966) in the 1960s has revolutionized our understanding of continental deformation and mountain building. But even to date, despite continuous research, many aspects and processes in the formation and evolution of mountain ranges remain the subject of ongoing scientific debate. This holds especially true in regards to interactions with other systems, such as climate or the biosphere, where interactions are often indirect and may happen at different timescales.

This dissertation aims to add another piece to the puzzle by investigating deformation at convergent plate corners and possible interactions with erosion processes. Continent-continent- or ocean-continent-collision of tectonic plates are the origin of most of the Earth's mountain ranges including the European Alps, Asian Himalayas, and South American Andes (Grotzinger et al. 2009). However diverse these orogens and the environmental factors affecting erosion therein might be, scientist are limited to select from the given, finite set of the present day. Moreover, key parameters and the temporal evolution are not accessible directly, but must be estimated or inferred through proxies. Here, numerical modeling can be of great help. By distilling hypotheses into a set of numerical equations, boundary conditions and material parameters, it allows to test hypotheses in a controlled and quantitative way. However, model building is likewise restricted by the inherent, necessary simplifications. Only in combination with observations, through comparison and continuous refinement can both approaches work together to create a deeper understanding of the investigated systems.

1.1 Coupled Systems: Climate and Tectonics

One topic that has seen and continues to attract high interest is the interaction of climate and tectonics. Coupling between these systems occurs on every scale, from local to global (Champagnac et al. 2012; Whipple 2014). The topography of mountains naturally can create local orographic precipitation (e.g. Roe 2005), but entire mountain ranges have even larger capacity to affect global climate by altering wind and thus precipitation patterns (Ehlers and Poulsen 2009) or even a negative greenhouse effect through increased chemical weathering (Molnar and England 1990; Ruddiman and Kutzbach 1989). The impact and implications remain subject of ongoing discussions (e.g Herman et al. 2013; Willenbring and von Blanckenburg 2010).

On the other hand, climate governs surface processes such as fluvial or glacial erosion, and finally sedimentation. The resulting change of loads then affects the style and location of deformation (Avouac and Burov 1996; Willett 1999). Additionally, rock uplift and exhumation cause an upward advection of heat. The increased thermal gradient will weaken the upper crust and thus render it more susceptible to further deformation (Koons 1987). Several studies have found evidence that the pattern of erosion governs deformation on orogen-scale, for example in the Himalayas (Beaumont et al. 2001; Hodges et al. 2001) or the Southern Alps of New Zealand (Beaumont et al. 1992).

1.2 Localized Feedbacks at Orogen Syntaxes

In addition to global and regional feedback cycles, a mechanism for highly localized positive feedback between erosion and deformation has been proposed by Zeitler et al. (2001), dubbed the tectonic aneurysm. It is based on observations of the Himalayan syntaxes, Namche Barwa and Nanga Parbat. There, intense deformation and rapid exhumation can be inferred from the presence of extremely young plutonic bodies and high-grade metamorphic rocks exposed at the surface (Burg et al. 1998; Craw et al. 1994; Liu and Zhong 1997; Schneider et al. 1999). Both syntaxes are deeply incised by rivers draining the Himalayan plateau, the Indus and Tasangpo-Brahmaputra, respectively, which have created high local relief without equal elsewhere. This lead the authors to formulate the hypothesis that this rapid and focused erosion is not only a product of the tectonic setting, but rather "*owe their origin to rapid exhumation by great orogen-scale rivers*" (Zeitler et al. 2001). The deep incision is thought to initiate a feedback loop of thermal advection, crustal weakening, and further diversion of material flow towards the weakened region (the aneurysm). The cartoon in Figure 1.1 illustrates these proposed dynamics. In Koons et al. (2002), the necessary conditions for erosional thinning were narrowed down: models required a layered lithosphere in which the upper crust can sustain higher stresses than the lower. Furthermore, incision must occur with sufficient rate and extent in an area that is already close to failure.

This provocative hypothesis has incited intense discussion: Since then, quantitative measurements of sustained exhumation rates exceeding $5\,\mathrm{mm\,yr^{-1}}$ on million-year timescales for the Namche Barwa (Enkelmann et al. 2011; Stewart et al. 2008) and Nanga Parbat (J. L. Crowley et al. 2009) have corroborated the special properties of the Himalayan syntaxes. Studies of the St. Elias syntaxis in South-East Alaska have identified this area as another potential tectonic aneurysm. There, evidence for an extended episode fast and localized uplift ($5\,\mathrm{mm\,yr^{-1}}$ to $10\,\mathrm{mm\,yr^{-1}}$) from great depths has been found (Berger et al. 2008; Enkelmann et al. 2010; Falkowski et al. 2014). The center of uplift has shifted over time, probably due to changing tectonic and climatic conditions (Enkelmann et al. 2017; Falkowski et al. 2016). Furthermore, the Olympic mountains (North-West USA) are considered an intermediary system that shows elevated erosion rates around $1\,\mathrm{mm\,yr^{-1}}$, but does not exhibit the degree of erosion-tectonic coupling as observed at the other tectonic aneurysm candidates (Adams and Ehlers 2017; Batt et al. 2001; Michel et al. 2018; Stewart and Brandon 2004).

A prominent counter-argument to the tectonic aneurysm hypothesis was made by Bendick and Ehlers (2014), who stressed the governing role of the subducting plate geometry at plate corners for distribution of deformation in the upper plate. They were inspired by previous findings of Mahadevan et al. (2010), who explained the natural arrangement of plate boundaries into long, straight segments and sharply curved corners as result of competing gravitational body forces and applied loads. Under the lateral bending at plate corners, which is necessary to accommodate subduction on the Earth's spherical shell, the lower plates form stiffened indenters that will provide increased resistance to subduction compared to the straight, flat segments. Bendick and Ehlers (2014) conducted a numerical modeling study and argued that these rigid indenters are sufficient to induce rapid and localized uplift that is comparable to observations of tectonic aneurysms without initiation of feedbacks by localized erosion.

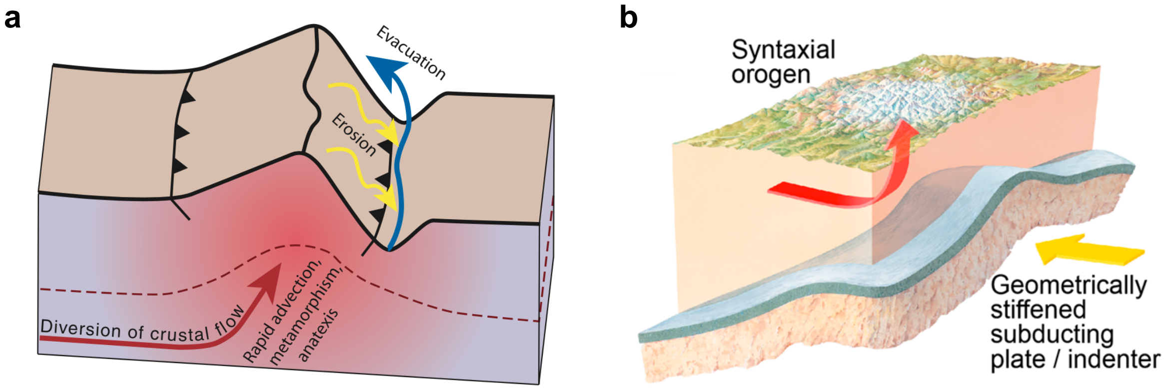

Figure 1.1: Top-Down or Bottom-Up? Competing interpretations of the formation of localized uplift.
a Illustration of a tectonic aneurysm at an evolved state (taken from Zeitler et al. 2001). Through incision by a large river, the crust is weakened and crustal flow is drawn towards this area. As topography builds up, a positive feedback loop of increasing erosion, crustal weakening through advection of heat, and accelerated crustal flow ensues.
b Schematic depiction of increased uplift due to a geometrically stiffened lower plate (taken from Bendick and Ehlers 2014). The forward-bulging indenter of the subducting slab provides an obstacle to the opposing crustal flow, which is diverted upward and builds the syntaxial orogen.

1.3 Aims of this Dissertation

The goal of this dissertation is to deepen our knowledge of upper plate deformation at syntaxes via numerical modeling. Starting from the work of Bendick and Ehlers (2014), an improved understanding especially of the formation of "bull's-eye" uplift, i.e. areas of rapid and focused rock uplift, is aspired. Their work clearly showed that an indenter geometry can create such uplift patterns resembling observations at plate corners. However, the choice of an purely viscous, homogeneous overriding plate does not allow to capture essential details of tectonic deformation. This leaves a wealth of parameters and potential connections to be explored and clarified.

1.3.1 Hypotheses addressed

Hypothesis 1 If lower plate geometry governs upper plate deformation, then modeling different plate geometries will create differences the style and pattern of deformation that correspond observations at the respective plate corners.

First and foremost, the role of the subducting plate's geometry is of interest. Bendick and Ehlers (2014) showed that an indenter-style lower plate has direct effect upon upper plate deformation and identified a possible relation to the observed extent of young thermochronometric ages at the Namche Barwa and St. Elias syntaxes. This relation should also be established under the more complex model setup used in this thesis.

Hypothesis 2 If lower plate geometry governs upper plate deformation, then a focusing effect will be observable independent of upper plate motion.

Furthermore, the velocity boundary conditions used in Bendick and Ehlers (2014) model the advance of the upper plate towards the trench with no motion of the down-going plate. At most plate boundaries, however, the greater part of shortening is accommodated by subduction of the lower plate. That is another aspect demands careful attention when transferring model results natural settings.

Hypothesis 3 Focused deformation at plate corners only occurs for favorable thermo-mechanical structure of the overriding plate.

An important aspect of numerical modeling is the adequate representation of mechanical properties and temperature distribution in the crust and lithospheric mantle. Upon trying to tune the model to represent a specific region, one cannot neglect the composition and strength of the various geologic units undergoing deformation. Bendick and Ehlers (2014) used a thin-sheet viscous approximation, which does not allow strain localization and formation of shear zones. In this thesis, the upper plate is modeled as three layers of visco-plastic material representing upper crust, lower crust and lithospheric mantle. Nevertheless, material property values and the thermal gradient can only be partially constrained by observations. Discussion over best representation of the thermo-rheological structiour of the lithosphere in numerical models is ongoing (e.g. Burov and Watts 2006; Burov 2011; Hirth and Kohlstedt 2003; J. Jackson 2002). Material differences and variations in the thermal field are surely a candidate to explain the variations among different plate corner settings.

Hypothesis 4 If erosion governs tectonic deformation, then rock uplift will adapt to the pattern of erosion.

In the ongoing discussion over the prevalence of tectonic or erosional forcing on the generation of rapid and focused uplift, erosion must not be left out. While Bendick and Ehlers used perfect erosion to retain a flat upper surface, the extended capabilities of DOUAR allow to study the interactions between tectonics and erosion. Previously, other numerical studies were able to model these (Koons et al. 2002; Willett 1999). However, none of these studies employed a full landscape evolution model coupled to the 3D geodynamic model as in this thesis. Here, we will study potential feedbacks under free conditions.

These four hypotheses constitute the thread that runs through the individual studies presented within this thesis, each of which focus on separate aspects of the mechanics of deformation on plate corners.

1.3.2 Overview of Chapters

This thesis is organized in seven chapters. Chapter 2 lays out the foundations of relevant methods and geodynamic modeling. Based on this, it describes the new features and necessary changes to DOUAR's program code in order to conduct the envisioned studies.

The main part consists of four science chapters. Since the effects of plate geometry, boundary conditions, material properties and erosion are interdependent and cannot be fully isolated from each other, the hypotheses formulated above are addressed in multiple chapters. Finally, the overarching hypotheses formulated in the previous section are revisited in chapter 7, and an overall conclusion is drawn.

Chapter 3 focuses on the effect of plate geometry (hypothesis 1), relative plate motion (hypothesis 2), and the erosional effect (hypothesis 4). The investigated plate geometries range from wide to narrow indenters to a direct comparison with straight lower plate geometries. The effect of upper plate advance is discussed using the full range of plate convergence scenarios, from subduction-only without movement of the upper plate to full upper-plate advance. Last but not least, the effect of erosion is investigated by contrasting flat and fluvial erosion models.

Chapter 4 investigates different configurations of lithospheric strength profiles for the overriding plate, an important aspect in overall model configuration (hypothesis 3). Additionally, the indenter width and relative upper plate motion are revisited (hypotheses 1 and 2).

Chapter 5 discusses the role of lower plate properties. This includes the mechanical strength of the subduction channel (hypothesis 3) as well as variations to the modeled rigidity of the subducting plate. This also allows to validate the chosen approximation of a completely rigid lower plate.

In the last study, chapter 6, an asymmetric indenter geometry of the lower plate is explored. This configuration might be more appropriate for tightly curved plate corner, such as St. Elias or the Himalayan syntaxes, where a transition from strike-slip to subduction occurs (hypothesis 1).

Finally, chapter 7 revisits the four working hypotheses of the previous section and an overall conclusion is drawn.

1.4 Work not included in this dissertation

Aside from the work presented in this thesis, the author has made contributions to an monitoring project that analyzes rockfalls in the Lauterbrunnen valley in Switzerland by repeated TLS (terrestrial laser scanning) measurements. Results of this work have been published in

> J. Strunden, T. A. Ehlers, D. Brehm, and M. Nettesheim (2015). “Spatial and temporal variations in rockfall determined from TLS measurements in a deglaciated valley, Switzerland”. *Journal of Geophysical Research: Earth Surface* 120.7, pp. 1251–1273. DOI: `10.1002/2014JF003274`

and

> S. Mohadjer, T. A. Ehlers, M. Nettesheim, M. B. Ott, C. Glotzbach, and R. Drews (2020). “Temporal variations in rockfall and rock-wall retreat rates in a deglaciated valley over the past 11 k.y.” *Geology* 48.6, pp. 594–598. DOI: `10.1130/G47092.1`

The author’s contribution lay in developing scripts for the statistical analysis of collected data in order to identify the underlying distribution. With this insight, one can estimate the long-term erosion rates and return times of large rockfall events, which is essential for hazard assessment. Furthermore, the robustness of these results with respect to measurement intervals and the applied method of statistical analysis was investigated. Although a significant contribution to the articles listed above was made, the focus of that work lies far from this thesis’ scope and therefore is not presented in greater detail.

2 Methods and Software Development

The fundamental challenge of geosciences lies in observing processes that happen on timescales that are beyond human lifetimes and are not directly accessible. While episodic events like earthquakes, rockfalls, or landslides can be observed and monitored, the rise and fall of mountains lies way beyond that. However, various techniques have been developed that allow to infer deformation on all timescales. These are referenced and drawn on for comparisons throughout this thesis and shall be shortly discussed. In contrast, the values of deformation rates, temperature, or pressure of numerical models are directly available for the entire model history. Thankfully, a current version of DOUAR was provided, which enabled state-of-the-art simulation of tectonic settings.

Section 2.1 presents a short introduction to the principles of geodynamic modeling at lithospheric scale and DOUAR in particular. Several alterations to the DOUAR's source code were necessary. These included new features, but also continuous improvements and bug-fixes throughout the conducted studies. The most important aspects are presented in this chapter. The adaptations required to model the particular geometry at plate corners are outlined in Section 2.2. Section 2.3 presents the different methods to quantify deformation in natural settings. In order to allow direct comparison of model results with measured thermochronometric ages, a module for forward modeling of cooling was added to DOUAR. The second major new feature implemented in DOUAR is the integration of the landscape evolution model FastScape, by which feedbacks between erosion and geodynamics can be investigated. The basic principles and necessary code developments are discussed in Section 2.4.3. Finally, Section 2.5 highlights additional improvements made to DOUAR during this research project.

All source code files discussed in this chapter are available on the USB drive included with this dissertation.

2.1 Geodynamic Modeling with DOUAR

DOUAR is a fully coupled thermo-mechanical finite element model developed to simulate geodynamic processes at lithospheric scale (Braun et al. 2008; Thieulot et al. 2008). It has been under continuous development and adjustment to tailor its features for application in a variety of scientific investigations. In the following, a short description of DOUAR, its structure and methods will be given. For full details, we refer the reader to Braun et al. (2008).

2.1.1 Physical Equations

At the heart of many geodynamic simulation programs lies the Navier-Stokes equation. Due to the high viscosities and slow motion tectonic deformation, the momentum can be neglected (creeping flow). This assumption simplifies the problem significantly and yields the Stokes equations. For incompressible fluids, conservation of momentum (Eq. 2.1) and conservation of mass (Eq. 2.2) thus read:

$$\nabla \cdot \mu \left(\nabla \vec{V} + \nabla \vec{V}^T \right) - \nabla P = \varrho g; \tag{2.1}$$

$$\nabla \vec{V} = 0, \tag{2.2}$$

where μ is the material shear viscosity, $\vec{V}$ is the velocity field, P the pressure, ϱ is the density and g gravity acceleration. Additional simplification is achieved by the penalty formulation (e.g. Bathe 1982), in which the incompressibility is dropped in favor of expressing pressure through:

$$P = -\lambda \nabla \cdot \vec{V}. \tag{2.3}$$

The penalty factor λ typically is several orders of magnitude larger than the viscosity μ, which ensures compression is negligible compared to the creeping flow velocities.

The solution to those partial differential equations (PDEs) is computed with the Finite Element method (Zienkiewicz and Cheung 1967), i.e. the resulting function is approximated by a number of piecewise linear interpolation functions over the smaller computation cells ($q1$-elements), all of which must fulfill above equations.

Furthermore, temperature diffusion is taken to be much slower than momentum diffusion (high Prandtl number). By this, the temperature can be solved independently after the velocity solution, for which a constant temperature is assumed. The full heat transport equation with terms for heat conduction, advection, and production to be solved is defined as:

$$\frac{\partial T}{\partial t} = \frac{k}{\rho c} \Delta T - \frac{\vec{V}}{\rho c} \nabla T + \frac{H}{\rho} \tag{2.4}$$

Here, T denotes the temperature, $\vec{V}$ the velocity, k the heat conductivity, ρ the material density, c the heat capacity, and H the heat production rate. The first term denotes temperature diffusion from warmer to cooler regions, the second term describes advection of heat due to material motion. The last term represents internal heat production by radioactive decay.

2.1.2 Material Properties

When assigning the free parameters (viscosity μ and density ρ) in each computation cell, DOUAR follows an Arbitrary Lagrangian Eulerian approach. While PDEs are significantly easier to solve on a regular, eulerian grid, Lagrangian grids that deform with the velocity field are better suited to track material properties. DOUAR uses a hybrid approach both tracer particles and triangulated surfaces to determine the composition of each cell for the Lagrangian part. The Eulerian grid is an *octree* structure, which consists of cubes nested within cubes at increasingly smaller levels. This approach offers the advantage of a non-uniform discretization while the grid remains regular. However, strain localization depends on cell size. Therefore, any simulation employing visco-plastic material, as do all models in this study, need to use a uniform grid.

Materials can be either purely viscous or frictional visco-plastic. Viscosity μ follows a thermally activated creep law:

$$\mu_{visc} = \mu_0 \dot{\varepsilon}^{1/n-1} e^{Q/nRT} \tag{2.5}$$

where μ_0 is the intrinsic viscosity, $\dot{\varepsilon}$ the second invariant of the deviatoric strain rate tensor, n the stress exponent, Q the activation energy, R the gas constant and T the temperature. If the stress exponent $n = 1$, the material is linear viscous and $n > 1$ denotes non-Newtonian viscosity, where viscosity increases under higher strain rates.

For visco-plastic materials, material deformation at lower temperatures is dictated by the Mohr-Coulomb failure criterion:

$$\tau = C_0 - \sigma_n \tan\phi \tag{2.6}$$

where τ is the deviatoric shear stress, C_0 the material cohesion, σ_n the normal stress and ϕ the material angle of friction. For each model element, the effective stress τ_{eff} is calculated from strain rate:

$$\tau_{eff} = 2\mu\dot{\varepsilon}. \tag{2.7}$$

If this effective stress exceeds the Mohr-Coulomb yield stress τ, elemental viscosity is reduced to an effective viscosity

$$\mu_{eff} = \frac{\tau}{2\dot{\varepsilon}}, \tag{2.8}$$

otherwise viscosity is kept at the initial viscous value ($\mu = \min(\mu_{eff}, \mu_{visc})$).

To calculate the properties of each cells in the octree grid, the material composition needs to be derived from the Lagrangian elements. For this, a *level set function* is calculated for each material interface and interpolated onto the octree nodes. These function's values range from -1 to +1 and are 0 at the interface, so that the position of each node with respect to the surface (i.e. "above" or "below") is easily identified. When a cell is cut by an interface, the respective material volumes are determined and material properties calculated as weighted average. Additionally, dynamic material properties, such as accumulated strain, are tracked by tracer particles. The values are averaged over all particles currently residing within the cell.

	Upper Crust Wet Granite	Lower Crust Dry Diabase	Lithospheric Mantle Olivine aggregates
Density ρ [$\mathrm{kg\,m^{-3}}$]	2750	2900	3300
Thermal Diffusivity $k/\rho c$ [$\mathrm{m^2\,a^{-1}}$]	$1.0 \cdot 10^{-6}$	$1.0 \cdot 10^{-6}$	$1.0 \cdot 10^{-6}$
Heat Production H [$\mathrm{\mu W\,ka^{-1}\,m^{-3}}$]	1.8	0.6	0.0
Viscosity Prefactor B [$\mathrm{Pa\,s^{1/n}}$]	$4.43 \cdot 10^{7}$	$1.24 \cdot 10^{6}$	$1.21 \cdot 10^{7}$
Activation Energy Q [$\mathrm{kJ\,mol^{-1}}$]	140.6	276.0	324.3
Stress Exponent n [1]	1.9	3.05	3.5
Cohesion C_0 [MPa]	10	10	2
Friction Angle ϕ [°]	15 → 5	15 → 5	10
Strain Weakening Interval [1]	0.05 → 0.55	0.05 → 0.55	–

Table 2.1: Baseline material parameters for the visco-plastic overriding plate. Values for upper and lower crust are taken from Carter and Tsenn (1987) and Hirth and Kohlstedt (2003), values for the lithospheric mantle follow Hirth and Kohlstedt (2003) and Jadamec and Billen (2012).
The **subducting plate** and **plate interface** are identical to the lithospheric mantle in respect to density, thermal diffusivity, and heat production, but use a constant, linear viscosity of $1 \cdot 10^{25}$ Pa s and $1 \cdot 10^{19}$ Pa s, respectively, without plasticity.

Table 2.1 lists the baseline material parameters used in the studies of this thesis. They represent a generic continental lithosphere with intermediate coupling between the crust and the lithospheric mantle. Heat production is decreasing exponentially with depth and the heat conductivity chosen such that the thermal diffusivity remains constant for all materials. The activation energy Q regulates how weak the material becomes as it heats up, while the stress exponents $n > 1$ effect a strengthening at higher strain rates (see equation 2.8). In contrast, the frictional parameters employ a strain weakening for the friction angle ϕ based on the total accumulated strain. This is important to facilitate localization of shear zones in numerical simulations.

2.1.3 Solution scheme

In each timestep, two nested iterative loops are executed: gradual grid refinement and the nonlinear solver.

First, the grid is initialized at a coarse level to calculate an initial, approximate solution. For this grid, the PDEs are translated into a set of linear equations with parameters taken from the material properties of each cell as described in the previous section. Although a direct matrix solver is employed (WSMP, Gupta 2000), the solution has to be obtained iteratively due to the nonlinearity of the underlying equations. Once nonlinear convergence is reached, the grid refinement is increased by one level. Starting from the approximate solution of the previous refinement level, a solution on the refined grid is calculated. These grid iterations are repeated until a converged solution on a grid with the desired level of refinement is obtained. The velocity field solution is then applied to surfaces and material tracer particles.

After grid iterations are completed, additional vertical displacements due to erosion, isostasy, or compaction are calculated if enabled by the user. This separate calculation step is required as those processes depend on the updated surface positions. Surfaces and tracer particles are moved a second time.

At the end, temperature diffusion and advection are calculated from the combined velocity field. This concludes one timestep and current state of the model is written to disk.

2.2 Modeling Plate Corners

2.2.1 Curved Plate Geometry

The geometries of plate corners around the world vary substantially in width and curvature. Some exhibit a prominent indenter, while others are smoothly curved. In order to provide a simple but flexible way of defining plate corner geometries, we decided to model the subducting plate geometry as a composite of two spheroids with the same, horizontal rotational axis. The rotational form allows to model the subduction of the lower plate as smooth motion without internal deformation or shear and thus ensures mass balance under all velocity boundary conditions.

Figure 2.1 shows the lower plate's geometry parameters. Each of the two spheroids 1 and 2 is described by four parameters: h denotes the height of the plate crest above the base level z_0, while rx is the distance where the crest intersects the base level, i.e. the maximum extent along dip. From these two values, the radius r_1 and vertical position zc of the rotational axis is calculated:

$$r_1 = \frac{h^2 + (rx_1)^2}{2h} \Rightarrow zc = z_0 + h_1 - r_1$$

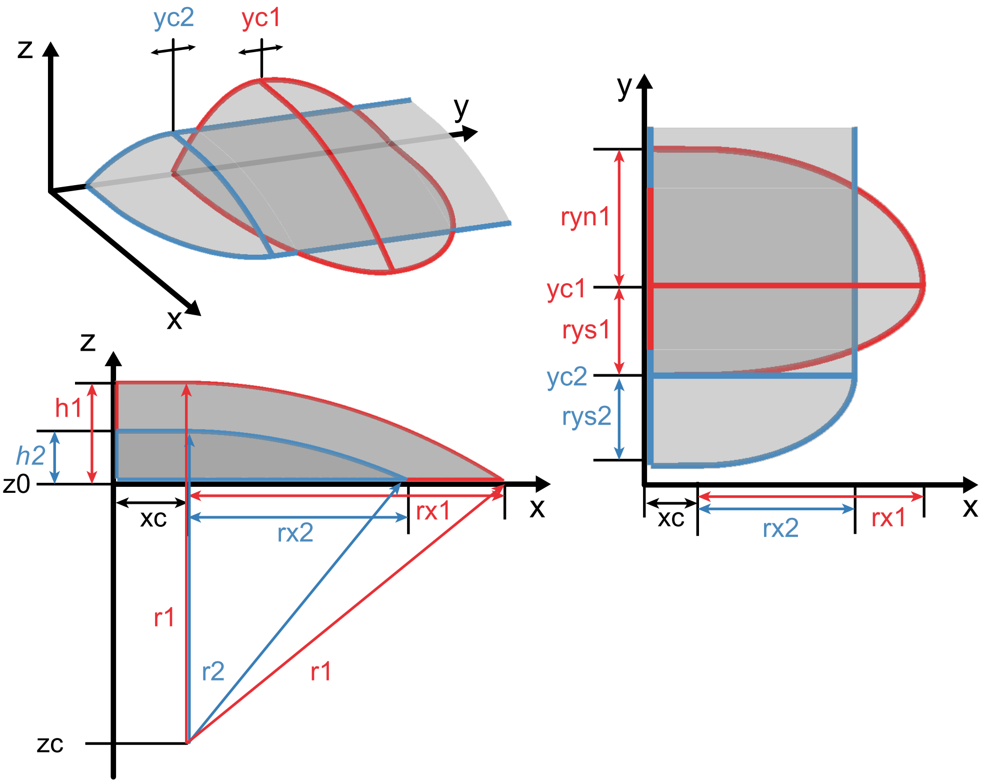

Figure 2.1: Parameters for the geometry of the lower plate.

Additionally, the axis' position can be shifted forward by xc, which allows an extended horizontal feed at the model's edge before the subduction initiates. The crests' position along y is defined by yc. The shape to either side is denoted independently ($r_{y,n}$ and $r_{y,s}$ – north and south), so that asymmetric shapes can be realized. Instead of spherical shape, the components can also be cylindrical, equivalent to an infinite radius along the y-axis (see the blue component for $y > yc_2$ in Fig. 2.1). The shape of the two components in y-direction can be independently set for each hemisphere. However, both must share the same rotational axis. This is achieved by letting the user only set the extent along dip rx_2 for the second indenter, the radius r_2 is derived from the values of the first indenter, so that both parts move as one unit.

$$r_2 = \sqrt{(rx_2)^2 + (z_0 - zc)^2} \Rightarrow h_2 = r_2 - zc.$$

Combining everything, the top surface can be expressed as

$$(x - xc)^2 + \left(\frac{rx_i}{ry_i}(y - yc_i)\right)^2 + (z - zc)^2 = r_i^2$$

for each hemishpere of the two components respectively. The implementation of this surface geometry was added to the existing options of surfaces in `create_surfaces.f90`.

2.2.2 Plate Corner Boundary Conditions

The description of material motion needs more parameters in addition to the geometry. The model domain is divided into three regions: (1) within the subducting plate, (2) model edges above the subducting plate, and (3) within the overriding plate. The motion within the subducting plate is cross-product with the rotational axis. The angular speed ω is defined by the influx velocity at the primary indenter crest v_{in}.

$$\vec{v}(x,z) = \vec{\omega} \times \vec{r} = \frac{v_{in}}{|r_1|} \begin{pmatrix} 0 \\ 1 \\ 0 \end{pmatrix} \times \begin{pmatrix} x - xc \\ 0 \\ z - zc \end{pmatrix} = \frac{v_{in}}{|r_1|} \begin{pmatrix} z - zc \\ 0 \\ xc - x \end{pmatrix}$$

Along the left model boundary ($x = 0$) above the subducting plate, material inflow is uniform in x-direction with the velocity v_{in}. Finally, material flow in the overriding plate is also defined as horizontally uniform along x, but in opposite direction. This velocity is prescribed at the model's bottom and right side ($x = 1$), as well as at the $x = 0$ boundary if the subducting plate does not cover the whole width. At the lateral boundaries ($y = 0$ and 1), free slip boundary condition is enforced. The implementation for these velocity boundary conditions is found in `define_bc_rot_subduction.f90`.

Additionally, temperature boundary conditions and initial values need to be defined as well. Along the bottom, these usually are set to a constant temperature, while the edges are defined as no-flux (insulating) boundaries. For temperature initialization, a new option to calculate the steady-state temperatures from the domain's material layers and their respective heat production was implemented (see `initialize_temperature.f90`). This allows to create temperature profiles of roughly parabolic shape, which conforms to typical geologic settings with increasing concentration of radiogenic material towards the surface.

2.3 Quantifying Deformation and Erosion

2.3.1 Terms and Definitions

When discussing temporal evolution and deformation of the Earth's surface, different terms are of relevance. In this study, we follow England and Molnar (1990) in their definitions. *Rock uplift* U is the upward displacement of material with respect to the Earth's center. It may lead to surface uplift, i.e. the upward displacement of the Earth's surface with respect to its center, but this depends on surfaces processes. *Erosion* E describes the removal of material at the surface. *Denudation* encompasses the entire process of weathering, erosion, and transportation, but is often used interchangeably with the term erosion. If the erosion rate were zero, then rock uplift would equal surface uplift. The overall change in surface elevation for a given location over time can thus be formulated as

$$\frac{\partial z}{\partial t} = U(t) - E(t). \tag{2.9}$$

While these are directly accessible in numerical models with an absolute coordinate system, natural observations and measurements can only infer *exhumation*, which describes the displacement of material with respect to the surface, which constitutes the moving frame of reference.

2.3.2 Timescales of Relevant Methods

The only methods that can be seen to operate with an absolute frame of reference are those based on satellites, most notably GPS (*global positioning system*). Measurement campaigns give direct measurements of surface uplift and horizontal displacement (e.g. Allmendinger et al. 2007; Elliott et al. 2013), yet they are only a snapshot of the present-day deformation field.

All measurements of deformation reaching back in time must rely on proxies, i.e. properties that closely depend on the property one wishes to obtain.

For intermediate timescales, dating of cosomogenic nuclides can be used. This method uses the accumulation of specific isotopes that do not occur naturally, but are created when cosmic rays hit the earth, for example ^{10}Be or ^{27}Al (von Blanckenburg 2005). The relevant particle radiation is absorbed almost completely within 2 m below the surface. The final concentration at the surface therefore depends on the time of residence in this thin layer below the surface, i.e. the denudation rate, and thus is insensitive to surface uplift. Over time, an equilibrium between generation and radioactive decay will be established, so that denudation rates over the last 10^3 to 10^5 years is can be determined.

The dating method of greatest relevance for this thesis is thermochronology. It relies on the accumulation of radioactive decay products in minerals as they cool on their exhumation path to the surface (Dodson 1973). However, it requires knowledge of the geothermal gradient in order to convert measurable cooling ages into exhumation rates (see e.g. Reiners and Ehlers 2005). Thermochronology can be applied to various systems of different sensitivity, which additionally depend on the actual cooling rate. By this method, one can obtain exhumation rates over the last 10^6 to 10^8 years. Since a module for the prediction of thermochronometric ages was added to the modeling program (see section 2.3.4) and its results are widely used for comparison of models with natural observations in this thesis, it will be discussed in greater detail in the following.

2.3.3 Thermochronology

Thermochronology is set apart from other radiometric dating methods by the fact that it measures the thermal history of samples, rather than their time of formation. Common host minerals include apatite, zircon, biotite, and muscovite, with measurable daughter products of helium, fission tracks or argon (Reiners et al. 2005). The temperature-dependence derives from the property that daughter products of radioactive decay will be lost from the mineral grain through diffusion and annealing at high temperatures. Only below a system-specific temperature, daughter products will start to accumulate. The duration of this accumulation phase can be derived from the ratio of parent isotopes and daughter products within one mineral grain.

2.3.3.1 (U-Th)/He Dating

The (U-Th-Sm)/He method measures the accumulated He produced by the radioactive decay of ^{238}U, ^{235}U, ^{232}Th, and ^{147}Sm:

$$C_{He}(t) = \sum N_i \cdot C_i \cdot (\exp(\lambda_i t) - 1) \tag{2.10}$$

with λ_i being the radioactive decay constant, C_i the parent isotope concentration and N_i the number of ejected α-particles along the decay chain for each respective system. Helium dating is commonly used in apatite, zircon, and titanite minerals. Oftentimes the contribution of Sm decay is negligible so that the method and its name are shortened to (U-Th)/He-dating.

In addition to the production of He, the calculation of (U-Th)/He cooling ages also has to factor in the loss via α-particle ejection and diffusion. While the first is a geometric factor that depends on the grain geometry and can be handled by a correction factor, diffusion is temperature dependent. The partial retention zone (PRZ) denotes the temperature range in which a given mineral will retain between 10 % and 90 % of all produced He atoms. Above and below these temperatures, the system is considered *open* or *closed*, respectively. The partial retention zone for helium in apatites lies between 45 °C and 80 °C (Farley 2000; Flowers et al. 2009; Zeitler et al. 1987), in zircon between 130 °C and 200 °C (Reiners et al. 2002, 2004; Wolfe and Stockli 2010).

The concentration of parent isotopes and accumulated helium is determined in a two-step process. First, the ^{4}He content is measured by heating manually selected mineral grains (*degassing*) and performing mass spectrometry on the released gases. In a second step, the concentration of parent isotopes within the same grain is determined by dissolution of the grain in acids, extraction of uranium and thorium, and ultimately measurement of isotope ratios in an inductively-coupled plasma mass spectrometer (IC-PMS) (Reiners and Brandon 2006). In recent years, technical advances enabled the measurements of Helium and parent isotopes in one combined process using laser ablation-IC-PMS. This allows to measure more samples in shorter times, and also helps to overcome limitations when dealing low-quality or zoned grains (Farley et al. 2011; Pickering et al. 2020).

2.3.3.2 Fission Track Dating

^{238}U does not only show α-decay, but a tiny fraction also undergoes spontaneous fission. The two generated atomic fragments shoot away in opposite direction, creating a trail of lattice defects in the surrounding crystal. These *fission tracks* can be made easily observable under an ordinary microscope by chemical etching, which preferentially attacks the damaged crystal lattice. Analogous to the (U-Th)/He method, the observed density of tracks in relation to the amount of ^{238}U in the crystal reveals the thermochronometric age (see e.g. Tagami and O'Sullivan (2005) for an in-depth review). At higher temperatures, the crystal structure can heal from the sustained damages (*annealing*), which can also be described as diffusion of lattice defects. Analogous to the PRZ, the partial annealing zone PAZ is defined as the temperature range in which between 10 % and 90 % of all induced lattice damage is annealed. However, since complete annealing of a fission track is an extended process with specific activation energies to different kind of defects, it makes for a more complex evaluation. On the positive side, this also allows to recover more detailed thermal histories through the analysis of fission track lengths (Ketcham et al. 2007), for example episodes of re-heating after initial cooling. Average values for partial retention zone lies between 80 °C and 130 °C for apatite (Barbarand et al. 2003; Carlson et al. 1999; Ketcham et al. 2007) and 260 °C and 290 °C for zircon (Brandon et al. 1998; Reiners and Brandon 2006).

Measurements of fission track density is done by manual counting under an optical microscope with at least 1000x magnification. Beforehand, sample crystals must be mounted, their surfaces polished, and etched with acid. The concentration of parent ^{238}U is measured indirectly via induced fission of ^{235}U in an external detector (*External Detector Method*). This is valid because the ratio of ^{235}U to ^{238}U is constant in nature. A low-uranium muscovite mica plate is attached to the polished grain surface and the sample irradiated with slow neutrons. This will induce fission of ^{235}U, with fission tracks also extending into the mica plate. The ratio of spontaneous fission tracks in the grain versus the induced tracks in the external detector reveals the thermochronometric cooling age of this sample (Reiners and Brandon 2006). Alternatively, uranium content can also be measured via ICP-MS, which is becoming increasingly more common. Apart from faster measurement times, it offers the advantage of measuring not only uranium, but also lead or additional trace element concentrations (S. E. Jackson et al. 2004; Johnston et al. 2009).

2.3.3.3 Effective Closure Temperature

Dodson (1973) introduced the concept of an effective closure temperature T_c, which represents the equivalent temperature of an abrupt switch from open to closed system instead. It can be applied to both the (U-Th)/He and the fission track dating method. Using one single temperature value instead of dealing with a range for the PAZ or PRZ, respectively, simplifies reporting and comparison with other systems. However, it should be noted that effective closure assumes monotonic cooling and therefore cannot be applied universally. It is defined by

$$\dot{T} = \Omega \frac{RT_c^2}{E_a} \exp\left(-\frac{E_a}{RT_c}\right). \tag{2.11}$$

Here, $\dot{T}$ denotes the cooling rate, Ω is a proportionality factor, E_a the diffusion activation energy and R the universal gas constant (Reiners and Brandon 2006). For (U-Th)/He measurements, $\Omega = \frac{55D_0}{a_s}$, where D_0 is the diffusion frequency factor and a_s the grain's effective spherical radius (including geometry corrections), which can be derived from controlled experiments. For fission track thermochronometers, Ω can be measured directly (e.g. Farley 2000; Ketcham et al. 1999; Reiners et al. 2004). However, actual measurements are further complicated by the fact that each grain's properties also depend on individual factors, such as grain composition (Green et al. 1986; Ketcham et al. 1999) or radiation damage (Flowers et al. 2009; Rahn et al. 2004) and careful analysis and assessment of obtained results is required.

2.3.4 Forward Modeling of Thermochronometric Ages

In order to convert measured thermochronometric ages into uplift rates, the thermal structure of the subsurface has to be known – or, more often, inferred and estimated. For comparison of natural settings with measured ages to numerical models, it is advantageous to predict expected thermochronometric ages from model results, where the entire temperature history is readily available. For each timestep, creation from parent nuclides and loss via diffusion can be directly calculated. Additional inputs for grain size, composition, age and other parameters allow to tailor the prediction to conditions encountered in nature. Various programs have already been developed to that purpose and re-used in this thesis. We used age-prediction algorithms from Braun (2003) and van der Beek (1995), with modeling parameters from K. D. Crowley et al. (1991), Tagami et al. (1998), Farley (2000), and Reiners et al. (2004).

2.3.4.1 Introduction of Tracer Particles in DOUAR

Tracking particles allow to extract the entire history of material exhumed at the surface. Logging the evolution of position, pressure and temperature over time in a transient simulation allows a direct comparison of model results with natural observations. For this thesis, a module to insert tracking particles and calculate thermochronometric cooling ages from the obtained pressure-temperature-history (p-T-t-paths) was added to DOUAR.

DOUAR already used two types of particles – one type to represent the surfaces, the other to store material properties (named cloud particles). The new tracking particles were implemented as a third type instead of expanding the already existing cloud particles. The material cloud uses a dynamic density adaption, i.e. particles are created and deleted based on particle densities, which contradicts the usage of continuous tracking. Furthermore, tracking particles are only required in those model regions which will potentially be exhumed. In stationary or subducting parts of the model domain, they would only pose a waste of memory and computational resources.

The file `update_tracking_cloud.f90` contains the central code parts. The tracking particles are initialized within a box defined by the user, either along a regular grid or randomly distributed. It has proven beneficial to delay the initialization until the initial mechanical spin-up phase is completed and the model has converged to a stable solution. During the model run, the tracking particles are moved with all other particles at the end of each timestep. New values of temperature and pressure at the updated particle positions are obtained. The level set function of the top surface is used to identify any particles that have been exhumed. In that case, the particle id and timestep information is saved in a log array, which identifies all surfaced particles to be evaluated in post-processing. After this information is saved, the surfaced particle is reset to its initial position and a new track started. This way, continuous recording of exhumation dynamics is ensured. Finally, the updated log array and the current values for all tracking particles are written to disk in a separate tracking output file.

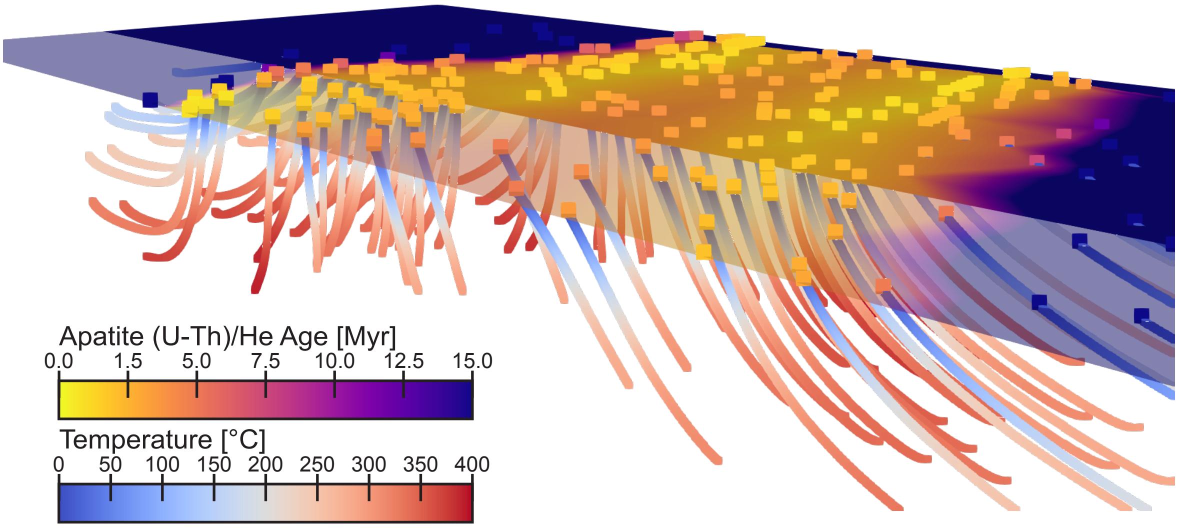

Figure 2.2: Example of recorded particle tracks and calculated thermochronometric age. As the tracking particles are moved through the model domain, they record the values of pressure and temperature (shown here in blue to red color scale). When a track reaches the top surface, it is registered in the log file and to be analyzed in post-processing. There, thermochronometric ages for various system can be calculated from each time-temperature-history (square points). These ages are interpolated onto the surface to produce a continuous pattern of exhumation dynamics.

2.3.4.2 Post-Processing of Tracking Data

The analysis of the recorded tracking paths is done in post-processing within `post_tracking.f90`. The information on which tracks reached the surface are collected from the log array. These are read from the output files and registered to their respective timesteps. For each track, a number of values can be directly obtained, for example maximum depth, temperature, or pressure. Thermochronometric cooling ages require additional calculation. For that, age-prediction algorithms taken from Braun (2003) and van der Beek (1995) are utilized. The user can select multiple thermochronometers and configurations. Since calculation of cooling ages is computationally expensive, tracks will be processed in parallel if resources are available. After results from all tracks have been obtained, they need to be interpolated onto the top surface. Here, an external interpolation routine written in Python (`interpolate_ages.py`) is used, which uses Python's powerful *SciPy* library to interpolate ages onto a regular grid. Additionally, smoothing can be applied. Figure 2.2 illustrates this processing of particle tracks to an interpolated age distribution at the surface.

2.4 Landscape Evolution Modeling

Modeling landscape dynamics at the surface is an integral part of geodynamic modeling. Several studies have shown that the pattern of erosion influences the pattern of uplift (e.g. Beaumont et al. 2001; Beaumont et al. 1992; Godard et al. 2004; Willett 1999). In order to clarify potential interaction between erosion and tectonics as intended in this thesis, a numerical representation of processes removing and redistributing mass at the surface has to be found.

In this thesis, we decided to integrate the recently developed landscape evolution model FastScape (Braun and Willett 2013). It offers a very efficient algorithm to construct the fluvial network that works on irregular networks and can be parallelized. Moreover, FastScape allows to use spatially variable precipitation and erodibility parameters. In the following, the basic concepts of landscape modeling are laid out.

2.4.1 Fluvial Erosion

The main erosional agent on earth is running water, which has consequently received most attention. Since the 1990s, numerous numerical fluvial erosion models of increasing complexity and sophistication were developed (Tucker and Hancock 2010). Yet at their core, all models rely on the same equation of fluvial shear stress τ_s exerted onto the channel bed:

$$\tau_s = k_s q^m S^n \tag{2.12}$$

where k_s is a constant, q the water discharge, and S the local slope. If erosion is assumed to be proportional to the shear stress and precipitation uniform across the modeled area, equation 2.12 can be simplified to the common "stream power law":

$$E_F = \frac{\partial z}{\partial t} = K_S A^m S^n \tag{2.13}$$

where A denotes the upstream area of catchment above the given point. K_s is a "fudge factor" to describe the channel's erodibility and incorporates all other dependencies. Several models have been developed that resolve some of these implicit dependencies, e.g. sediment cover (Davy and Lague 2009; Kooi and Beaumont 1994), the episodic nature of precipitation and discharge (Lague et al. 2005), or channel width (Turowski et al. 2009). However, on large spatial and temporal scales, the simple form has proven sufficient and thus was adopted in the newly developed landscape evolution model FastScape (Braun and Willett 2013).

The key to the highly efficient solution to the stream power law by *FastScape* lies in a novel approach to calculate the drainage network. First, the receiving node (i.e. the lowest neighbor) to each node is identified. This is transformed into an ordered stack of nodes which guarantees that all contributing nodes (i.e. nodes that lie upstream) have a higher index in the stack. With this obtained ordering, the calculation of erosion rates can be performed implicitly starting from the baseline nodes and working its way upstream. This results in a very fast and stable algorithm of computational complexity $O(n_p)$ (Braun and Willett 2013).

2.4.2 Hillslope Processes

In comparison to fluvial erosion, hillslope processes such as soil creep, rain splash or landsliding play a minor role in active orogens (Whipple 2004). For most erosion models, especially on millennial timescales, it suffices to subsume these processes within a diffusive erosion term (see e.g. Howard et al. 1994; Tucker et al. 2001; Willgoose 2005). This approach has also been chosen in *FastScape* (Braun and Willett 2013). With K_D denoting the overall diffusivity, this erosion term is then defined as:

$$E_D = \frac{\partial z}{\partial t} = K_D \left(\frac{\partial^2 z}{\partial x^2} + \frac{\partial^2 z}{\partial y^2} \right) = K_D \Delta z. \tag{2.14}$$

For this diffusion equation, well-established and stable solutions exist that are easily integrated (Press et al. 1992).

2.4.3 Integration of FastScape in DOUAR

FastScape provides an efficient and powerful option to calculate realistic fluvial erosion. DOUAR did include the option to use the landscape evolution model Cascade. However, its older algorithm is orders of magnitude slower. In order to fully couple landscape evolution with tectonic forcing, the erosion model must be run at each time step. To be precise, erosion is evaluated after the mechanical solution is obtained, before the isostasy calculation, so that isostatic adjustment follows the already re-distributed weight.

Implementation of FastScape itself required few alterations, as it could be added to the existing options in `erosion.f90`. However, the provided version of FastScape operates on a regular, rectangular grid only. This demanded a different formulation of the surface, with different ordering of the nodes and separate identification of the convex hull (see section 2.5.1). Furthermore, FastScape applies both the tectonic and erosional velocity components to the surface nodes, so care needs to be taken that other velocity updates are skipped for the top surface when FastScape is active.

Horizontal Resolution	780 m
Fluvial Erodibility K_S	$8.0 \cdot 10^{-5}\,\mathrm{m}^{-2}$
Area Exponent m	0.4
Slope Exponent n	1
Diffusive Erodibility K_D	$4.0\,\mathrm{m}^2\,\mathrm{yr}^{-1}$

Table 2.2: Baseline parameters for fluvial (eq. 2.13) and diffusive (eq. 2.14) erosion used in this thesis. Parameters were adjusted to yield realistic drainage density and elevation profiles under typical model settings.

2.5 Performance and Usability Improvements

2.5.1 Surface Routines

The term surface in DOUAR denotes not only the modeled earth surface, but all material interfaces. They are composed of numerous interconnected particles (or nodes) particles that span a triangulated mesh. The individual nodes are moved according to the model's velocity solution and the mesh is dynamically updated. For example, nodes that have been advected outside of the model domain are removed, whereas new nodes are created when two connected nodes have moved too far apart. The nodes that lie on the outer model boundaries form the surfaces' convex hull and require special handling. These can only move along the respective model edge, so that the surface always spans the entire domain.

The most important code updates to the handling of surfaces were made to the refinement mechanism. Continuous refinement ensures an appropriate node density and a correct Delaunay triangulation of the surface. In particular, the node removal routine needed to be re-written to deal with removal of several neighboring nodes at once. This may happen if material is advected out of the model domain. The fundamentals of the previous and improved process are illustrated in Figure 2.3. Upon removal, the nearest neighbor of the node to be removed will inherit all its connections to other nodes (Fig. 2.3a). If a number of neighboring nodes is removed consecutively, a badly triangulated surface can ensue (Fig. 2.3b). Since surfaces are essential to a correct modeling flow, this will then abort the model run. However, when the entire list of nodes to be removed is passed to the new routine `remove_multiple_points`, the list of suitable neighboring nodes can be restricted and a proper triangulation retained (Fig. 2.3c). If one node has no valid nearest neighbor because all neighboring nodes are marked for removal, the removal routine is called recursively to remove this deadlock. Furthermore, an additional routine to check for incorrect triangulations `remove_bad_triangles` was introduced, which will identify and remove nodes that are not part of the continuous surface interpolation.

In addition, the identification of convex hull nodes was improved. Previously, these were identified by their position in the node storage array, based on the initial resolution of the surface. However, this inhibits any refinement of these outer edges as the number and ordering of convex hull nodes must be kept constant. Moreover, this specific order conflicted with FastScape, which requires a regular $n \times m$ grid for the top surface (see also section 2.4.3). In order to resolve these restriction, a new surface node property `convexhull` was introduced, which stores the node's assignment to the respective model boundaries as bit array. This property must be respected when moving surfaces – convex hull nodes must only move within their boundary edge – as well as in the refinement process. It must be ensured at all times that the surface's convex hull is continuous and coincides with the lateral model boundaries. The corresponding implementations can be found in `create_surfaces.f90`, `move_surface.f90`, `refine_surface.f90`, and `remove_multiple_points.f90`.

2.5.2 Bugfixes

Continuous exploration of new model scenarios sometimes requires code changes in order to represent the different behavior in the model. At other times, it uncovers aspects that are not handled correctly because the new scenario was not considered during initial development. This was also the case in the calculation of isostatic compensation. Isostasy is calculated by subdividing the

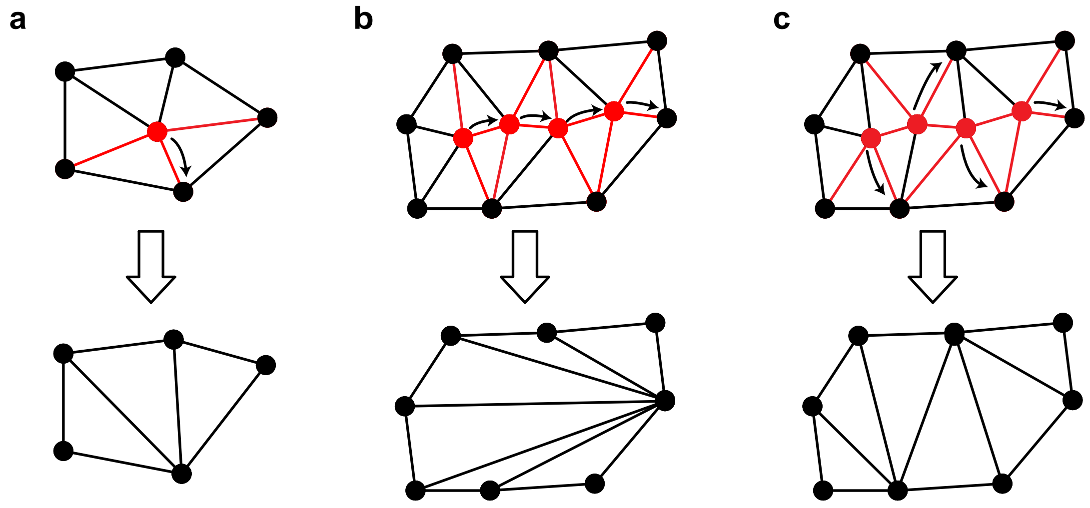

Figure 2.3: Illustration of node removal in a triangulated surface. **a** When a node is marked for removal, the nearest neighbor is identified (curved black arrow). The two triangles containing both the node to be removed and its nearest neighbor will be removed as well (red edges). The other edges are "inherited" by the nearest neighbor. **b** Consecutive removal of neighboring nodes may pass along connections. The result is a bad triangulation, which may ultimately abort the model. **c** Simultaneous removal of neighboring nodes will find nearest neighbors only from nodes that are not to be deleted. This way, a proper triangulation is maintained.

model domain into vertical columns arranged in a regular grid and comparing their current weight against a reference value. Originally, the highest column weight was taken as reference. However, this implies that parts of the model domain can initially be out of isostatic equilibrium, for example when different material layers are not horizontal. In order to avoid substantial compensating motion at model startup for the curved lower plate geometry, a new option was introduced. Instead of storing one global value, the reference weight can now also be saved individually for each column in the `weightref` array. These weights must be saved and restored at model startup. During implementation of these improvements in `isotasy.f90`, a bug was uncovered. The calculated isostatic displacement did not obey the vertical exaggeration `vex` (a parameter that allows to increase vertical resolution). Luckily, a fix was easily applied to the respective function calls in `move_surfaces.f90`.

2.5.3 Natural Unit Conversion

Beyond expanding DOUAR's modeling capabilities, ease of use was also improved by the addition of a natural unit parsing. Internally, DOUAR is scaled to dimensionless units and had do be entered in that format. With this new feature, the user is able to directly enter the reference values for length, velocity, density and temperature and use natural units throughout the input file. The conversion is handled while parsing the input file. This removes a potentially error-prone process and greatly improves readability of the input files. Even better, a back-conversion is also applied to the output files so that the resulting values are given in natural units. Thus, the user can immediately interpret and compare model results to observations from natural settings.

3 The Influence of Upper Plate Advance and Erosion on Overriding Plate Deformation in Orogen Syntaxes

3.1 Declaration on Contributions to Joint Work

The contents of this chapter are published and freely available. The full citation is:

> M. Nettesheim, T. A. Ehlers, D. M. Whipp, and A. Koptev (2018). "The influence of upper-plate advance and erosion on overriding plate deformation in orogen syntaxes". *Solid Earth* 9.6, pp. 1207–1224. DOI: `10.5194/se-9-1207-2018`

Four authors contributed to this joint work: Matthias Nettesheim (MN), Todd A. Ehlers (TE), David M. Whipp (DW), and Alexander Koptev (AK). The initial research questions were developed by TE, who then acquired funding for the project. Software development consisted of extending DOUAR functionality and continuous bug-fixing, which was done by MN with support from DW and TE. MN designed and carried out simulations and defined the scope of this study in close collaboration with TE and DW. Manuscript preparation was done by MN with regular feedback from TE. Finally, all co-authors contributed with comments, suggestions and proof-reading. The manuscript was further improved during the publication process in response to comments from Anne Replumaz and two anonymous reviewers.

Author	**Position**	**Scientific ideas**	**Data generation**	**Analysis and Interpretation**	**Paper writing**
MN	[1]	45%	70%	65%	65%
TE	[2]	45%	10%	20%	20%
DW	[3]	10%	15%	5%	5%
AK	[4]	0%	5%	10%	10%

Table 3.1: Author contributions to *The influence of upper-plate advance and erosion on overriding plate deformation in orogen syntaxes*, published in *Solid Earth*, vol. 9, 2018

The supporting information to this publication can be found in appendix B (page 103)

3.2 Published Manuscript

Solid Earth, 9, 1207–1224, 2018
https://doi.org/10.5194/se-9-1207-2018

Solid Earth
Open Access

The influence of upper-plate advance and erosion on overriding plate deformation in orogen syntaxes

Matthias Nettesheim[1], **Todd A. Ehlers**[1], **David M. Whipp**[2], **and Alexander Koptev**[1]

[1]Department of Geology, University of Tübingen, Tübingen, Germany
[2]Department of Geosciences and Geography, University of Helsinki, Helsinki, Finland

Correspondence: Todd A. Ehlers (todd.ehlers@uni-tuebingen.de)

Received: 26 February 2018 – Discussion started: 21 March 2018
Revised: 11 October 2018 – Accepted: 15 October 2018 – Published: 5 November 2018

Abstract. Focused, rapid exhumation of rocks is observed at some orogen syntaxes, but the driving mechanisms remain poorly understood and contested. In this study, we use a fully coupled thermomechanical numerical model to investigate the effect of upper-plate advance and different erosion scenarios on overriding plate deformation. The subducting slab in the model is curved in 3-D, analogous to the indenter geometry observed in seismic studies. We find that the amount of upper-plate advance toward the trench dramatically changes the orientation of major shear zones in the upper plate and the location of rock uplift. Shear along the subduction interface facilitates the formation of a basal detachment situated above the indenter, causing localized rock uplift there. We conclude that the change in orientation and dip angle set by the indenter geometry creates a region of localized uplift as long as subduction of the down-going plate is active. Switching from flat (total) erosion to more realistic fluvial erosion using a landscape evolution model leads to variations in rock uplift at the scale of large catchments. In this case, deepest exhumation again occurs above the indenter apex, but tectonic uplift is modulated on even smaller scales by lithostatic pressure from the overburden of the growing orogen. Highest rock uplift can occur when a strong tectonic uplift field spatially coincides with large erosion potential. This implies that both the geometry of the subducting plate and the geomorphic and climatic conditions are important for the creation of focused, rapid exhumation.

1 Introduction

The deformation around orogen syntaxes has been the subject of widespread attention over the last years due to the observed high, sustained, and spatially focused exhumation with rates in excess of 5 mm a^{-1} over million-year timescales. Examples of focused exhumation have been documented for the Olympic Mountains of the Cascadia subduction zone (e.g., Brandon et al., 1998; Michel et al., 2018; Adams and Ehlers, 2017, 2018); the Himalayan syntaxes, Namche Barwa (e.g., Burg et al., 1998; Enkelmann et al., 2011; Stewart et al., 2008) and Nanga Parbat (Craw et al., 1994; Crowley et al., 2009); and the Saint Elias syntaxis (Berger et al., 2008; Enkelmann et al., 2010; Falkowski et al., 2014) in Alaska. Despite nearly 2 decades of work, the tectonic- and climate-driven erosional mechanisms responsible for patterns and rates of upper-plate deformation in these areas remain debated (Bendick and Ehlers, 2014; Lang et al., 2016; Wang et al., 2014; Whipp et al., 2014; Zeitler et al., 2001).

The characteristic 3-D indenter geometry of the subducting plate at syntaxes can also be observed, to a lesser extent, at other locations. We use the term “plate corners” in this study to refer to all short, convex bends that separate the longer, straight to slightly concave plate boundary segments. This alternation between bends in the subducting plate and straight segments is a direct consequence of the slab bending that is required to accommodate subduction on a sphere (Frank, 1968; Mahadevan et al., 2010). Slab curvature and dip angles naturally vary widely across subduction settings observed around the world (Hayes et al., 2012), but common to all of them is their specific 3-D geometry. The change in orientation of neighboring subducting slab segments ef-

Published by Copernicus Publications on behalf of the European Geosciences Union.

fects flexural stiffening of the connecting region and thus creates a convex forward bend in the subducting slab (Mahadevan et al., 2010), referred to here as an indenter. Figure 1 shows the subducting slab geometry at the Cascadia subduction zone, which served as a template for the plate geometry used in this study, although we note that the results presented here can provide insight into exhumation patterns of other regions where similar plate geometries exist.

In previous studies, numerical modeling has played a central role towards understanding focused exhumation in orogen syntaxes. Work by Koons et al. (2002, 2013) simulated focused exhumation in syntaxes as a function of focused (climate-driven) denudation. In their approach, they approximate the subsurface to be of homogeneous composition and define a straight boundary between the subducting and the overriding plate, thus not accounting for the 3-D geometry of subducting plates observed in many syntaxes. Although the link between erosion and uplift through isostasy is well established (Molnar and England, 1990; Montgomery, 1994; Simpson, 2004), their hypothesis of additional positive feedback by thermal weakening of the crust, causing accelerated deformation beneath deeply incised valleys (see also Zeitler et al., 2001), is controversial. Following this, work by Bendick and Ehlers (2014) considered the effect of the 3-D subducting plate geometry, albeit with simplified upper-plate rheology and erosion. However, it has been identified that rheological stratification of the lithosphere (Ranalli and Murphy, 1987; Burov, 2011) is one of the key factors that determines deformation and rock exhumation in convergent orogens, by means of both numerical (e.g., Erdos et al., 2014; Vogt et al., 2017) and analog modeling (e.g., Willingshofer et al., 2013).

Depending on the direction of mantle flow, the amount of slab pull, and whether the subducting slab is anchored in the deep mantle, convergence of plates can be accommodated both by subduction of the down-going plate and by advance of the overriding plate towards the trench (e.g., Heuret and Lallemand, 2005; Faccenna et al., 2013). While subduction of the down-going plate commonly accounts for the larger part of shortening (e.g., Sumatra and Java (Chamot-Rooke and Le Pichon, 1999) or Aleutian (Gripp and Gordon, 2002) subduction zones), an additional component of shortening can be taken up by trench or upper-plate advance, i.e., migration of the overriding upper plate toward the down-going plate (Heuret and Lallemand, 2005). The Nazca–South America subduction zone (Russo and Silver, 1994; Schellart et al., 2007) and the early stages of the India–Eurasia collision (Capitanio et al., 2010) provide examples of shortening with large amounts of upper-plate advance. While Koons et al. (2002, 2013) used a stationary upper plate in their studies, Bendick and Ehlers (2014) considered solely the case of an advancing upper plate.

In this study, we complement previous work by Bendick and Ehlers (2014) and investigate how a rheologically realistic upper-plate and slab advance and erosion impact the pattern and rates of exhumation in a generalized plate corner setting. We do this for regions featuring a subducting plate that is bent in 3-D and flexurally stiffened at the plate corner. Our first aim is the characterization of upper-plate deformation in convergent settings with a subducting 3-D indenter geometry. Since Bendick and Ehlers (2014) employed an advancing upper plate, we additionally focus on possible effects caused by lower-plate subduction and the degree to which the upper plate is advancing towards the subduction zone. Our second aim is to understand the effect of erosional efficiency on upper-plate deformation and exhumation by contrasting total erosion (i.e., a constant flat surface) with more realistic fluvial erosion calculated with a surface processes model. It is important to note that we do not aim for exact representation of a specific region, which would require a more detailed and site-specific adjustment of material and thermal properties as well model geometry and boundary conditions, all of which may affect the style of deformation. Rather, we try to assess the impact of an indenter geometry in generic terms in order to understand the underlying mechanisms.

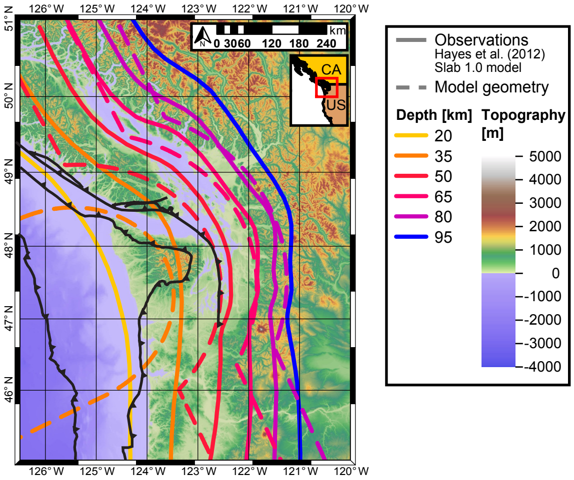

Figure 1. Observed subducting plate geometry and simplified model representation for the Cascadia subduction zone. Model geometry was chosen to best conform to the forward bulge of the down-going plate. The rotational shape and straight background slab of the model geometry allow consistent velocity boundary conditions and reduce edge effects. Slab contours from Hayes et al. (2012) Slab 1.0 global subduction zone geometry model; major structures in black from Brandon et al. (1998).

2 Methods

2.1 Numerical modeling approach

We conduct geodynamical simulations of plate corner subduction with the program DOUAR (Braun et al., 2008; Thieulot et al., 2008), a fully coupled three-dimensional thermomechanical numerical modeling program designed to solve visco-plastic creeping flow equations at the lithospheric scale. Models in DOUAR are defined by a set of velocity boundary conditions, material properties, and model geometry defining the material domains. Bulk velocities are the result of solving the quasi-steady-state force balance equations for nearly incompressible fluids with a finite-element approach on an octree mesh. Pressure values are derived indirectly from the velocity solution by the penalty method (e.g., Bathe, 1982), and local smoothing is applied to avoid small-scale pressure oscillations. Finally, temperature is computed, incorporating the effects of material velocities and thermal properties. Material interfaces and bulk volume properties are stored on a self-adapting cloud of particles advected within the model domain. Additional details of the model and governing equations are given in the Appendix.

For this study, we developed a new module that makes use of DOUAR's particle-in-cell approach and permits extraction of the pressure and temperature history (p–T–t paths) of particles exhumed at the free surface. Following the methods detailed in Braun (2003), Ehlers (2005), and Whipp et al. (2009), and using the parameters given therein, thermochronometric cooling ages are calculated from these paths to quantify upper-plate exhumation patterns and rates over time.

2.2 Model setup

2.2.1 Geometry

The model domain is 800×800 km in plan form and 81 km deep. The element size is $6.25 \times 6.25 \times 1.56$ km, corresponding to $128 \times 128 \times 52$ elements for the entire domain. The direction of subduction is parallel to the x axis, and the entire setup is symmetric with respect to the $y = 400$ km plane. We refer to the $x = 0$ and $x = 800$ km model boundaries as *left* and *right*, respectively, and to $y = 0$ and $y = 800$ km boundaries as model *front* and *back*. The model consists of a layered overriding plate, which is divided into upper and lower crust and lithospheric mantle. We use different geometries for the subducting plate in this study to investigate its effect on overriding plate deformation. The quasi-2-D reference geometry is a downward-curved slab with straight edges along strike. It is 30 km high and terminates at $x = 320$ km. The standard indenter is modeled after the Cascadia subduction zone (see Fig. 1) and is 50 km high and 350 km wide and terminates at $x = 400$ km. Additionally, we show a narrower and a wider indenter (200 and 570 km wide, respectively).

We simplify the model setup to approximate the effect of a flexurally stiffened indenter by prescribing the geometry of the indenter and subducting plate as fixed through time. Furthermore, we set the shape and motion of the down-going plate to be rotational; i.e., the curved indenter and along-strike continuation of the plate (referred to as the *background slab*) are spheroidal and cylindrical in cross section, respectively (Fig. 2). This approach minimizes internal deformation and ensures mass balance of the in- and outgoing lower plate.

Additionally, a thin, weak layer on top of the down-going plate is added to ensure partial decoupling, which also reduces indenter deformation (e.g., Willingshofer and Sokoutis, 2009). The thickness of this weak layer is 3.0 km above the indenter and 4.0 km above the lower slab in order to compensate for the changing depth to the slab, such that material inflow along the left domain edge is well-nigh horizontal.

2.2.2 Material parameters

Corresponding to the focus of this study, we use different material properties for the down-going and the overriding plate. In order to approximate the flexural stiffening of the buckled slab, we use a constant viscosity of 10^{25} Pa s and no plasticity for the rigid subducting plate. For the overriding plate, we adopt a layered, visco-plastic rheology. The ductile properties of the upper crust, lower crust, and lithospheric mantle are based on wet granite, dry diabase, and olivine viscous flow laws, respectively (Carter and Tsenn, 1987; Hirth and Kohlstedt, 2003; Jadamec and Billen, 2012). The lithospheric mantle viscosity was designed to conform to the known deformation of olivine aggregates (Hirth and Kohlstedt, 2003). Its pressure dependence was eliminated by using parameters from Jadamec and Billen (2012) and recalculation of the remaining parameters (i.e., stress exponent and activation energy) under lithostatic pressure conditions. Brittle parameters are uniform in the crust with 10 MPa cohesion and an initial friction angle of 15°. Linear strain softening reduces the friction angle to 5° at a strain value of 0.55. In the lithospheric mantle, the friction angle is constant 10°. An overview of all material parameters is given in Table S1 in the Supplement.

2.2.3 Temperature setup

Model temperatures are set by constant temperature boundary conditions of 0 °C at the surface and 930 °C at the bottom. Along all vertical sides, zero-flux Neumann boundary conditions are applied. Heat production in the upper and lower crust is chosen to reproduce the thermal structure of Bendick and Ehlers (2014) (see Table S1). At startup, temperatures are run to conductive steady state, resulting in a Moho temperature of 600 °C and heat flux of 25 and 70 mW m^{-2} at the model bottom and surface, respectively.

2.2.4 Velocity boundary conditions

We model the two end-member cases, where convergence is completely accommodated either by overriding plate advance (*full advance*) or by subduction and accretion (*no advance*), as well as the intermediate case (*half advance*). In order to keep these scenarios comparable, we choose a constant overall convergence rate of 30 mm a^{-1} in all cases (except for model 7 with doubled convergence rate for comparison; see Table 1).

Table 1. Controlling parameters overview.

Model number	Subducting plate geometry	v_{sub} [mm a^{-1}]	v_{adv} [mm a^{-1}]	Upper-plate advance	Erosion type	In Figs.
1	Straight slab	30	0	No	Flat	4, S1
2	Straight slab	15	15	Half	Flat	3, 4, S1
3	Straight slab	0	30	Full	Flat	4, S1
4	Indenter	30	0	No	Flat	4–6, S1
5	Indenter	15	15	Half	Flat	3–7, 9, S1–S3
6	Indenter	0	30	Full	Flat	4–6, S1
7	Indenter	30	30	Half	Flat	S2
8	Narrow indenter	15	15	Half	Flat	7
9	Wide indenter	15	15	Half	Flat	7
10	Indenter	30	0	No	Fluvial	S4
11	Indenter	15	15	Half	Fluvial	8, 9
12	Indenter	0	320	Full	Fluvial	S4

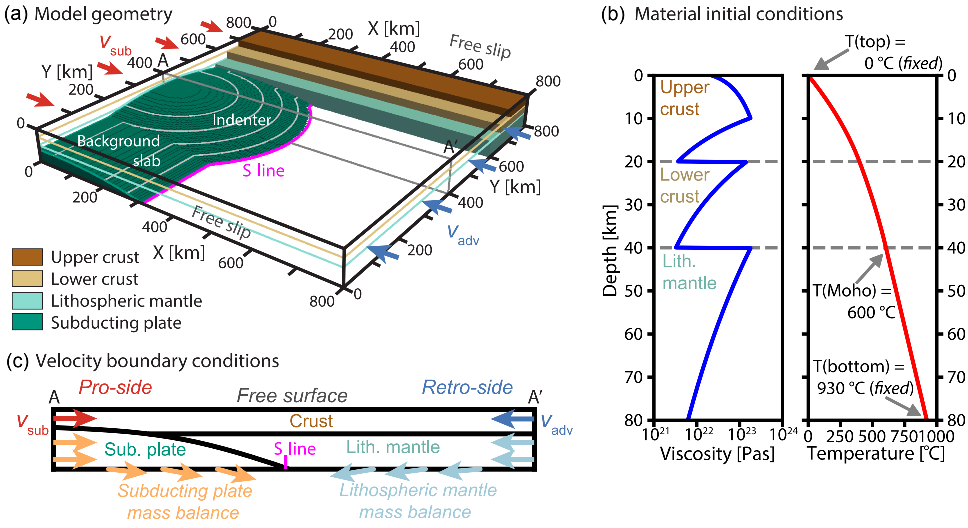

Figure 2. Model setup and properties. **(a)** Cut-out oblique view of the model domain illustrating the geometry and material layers: the overriding plate is divided into an upper and lower crust and lithospheric mantle. The down-going plate is of uniform rigid material. **(b)** Velocity boundary conditions. Horizontal material influx with v_{sub} from the left ($x = 0$ km) and v_{adv} from the right ($x = 800$ km), and continued transport towards the S line along the bottom boundary. Material influx of subducting plate and lithospheric mantle is compensated for by rotational motion of the subducting plate and outflux of the lithospheric mantle increasing towards the center; i.e., only crustal influx is added to the domain. Additionally, vertical velocities are modified by isostasy. Velocity boundary conditions along front and back ($y = 0$ and $y = 800$ km) are free slip; top is free surface. **(c)** Vertical profiles of the overriding plate effective viscosity and initial temperature conditions. Temperature boundary conditions are fixed temperatures at bottom and top, and zero flux is imposed at all horizontal sides. Detailed material parameters are given in Table S1.

These three scenarios translate into different sets of velocity boundary conditions in our models. Subduction and accretion correspond to horizontal influx on the left boundary ($x = 0$ km), while overriding plate advance translates to horizontal influx on the right boundary ($x = 800$ km), with velocity v_{sub} and v_{adv}, respectively. Boundary conditions at the front and back ($y = 0$ and 800 km) are free slip. The bottom boundary is set up to ensure the same mass added to the domain in all scenarios. It is separated into two regimes by the S line (the kinematic boundary between upper and lower plate at the model bottom): to the left, velocities match a downward rotation of the subducting plate, which translates to an increasingly downward direction of motion with velocity v_{sub} up to the S line; to the right, horizontal velocity is directed along the x axis with velocity v_{adv} and an additional linearly increasing material outflux that compensates for the influx of material from the right up to the height of the background slab. Finally, material flux through the bottom boundary is also governed by isostasy, which is calculated for an effective elastic thickness of 25 km.

2.2.5 Erosion

The top surface is free, with a surface stabilization algorithm based on Kaus et al. (2010) applied. In models 1 through 9, all topography created is immediately removed down to baselevel (*flat* or *total erosion*; see also Table 1), which lies 81.0 km above the model bottom. Under total erosion, rock uplift rate is equal to the exhumation rate (England and Molnar, 1990). The last part of this study contrasts flat erosion with more realistic fluvial and diffusive erosion (models 10–12, Table 1). For this, the landscape evolution model FastScape (Braun and Willett, 2013) was coupled to DOUAR.

Erosion in FastScape is computed on a regular grid of 0.78 km resolution with uniform precipitation of $1\,\mathrm{mm\,a^{-1}}$. Erosion constants were $8.0 \times 10^{-5}\,\mathrm{m^{-2}}$ for fluvial and $4.0\,\mathrm{m^2\,a^{-1}}$ for hillslope erosion with a stream power exponent of 0.4. The edges at $x = 0$ and $x = 800$ km are fixed to baselevel, and local minima are filled so that each catchment drains to one of those sides.

2.2.6 Thermochronometric cooling ages

Thermochronometry determines the time since a mineral has cooled below a characteristic temperature, referred to as the *closure temperature* (Dodson, 1973). This is achieved by the measurement of accumulated decay products in relation to the abundance of radioactive mother nuclides. The loss of decay products – He atoms for the (U−Th)/He method and crystal lattice damage for the fission track method – is thermally activated and specific to each system. At high enough temperatures, all products are lost by diffusion or annealing. The depth at which temperatures mandate the transition from an open to a closed system is called the partial retention or annealing zone. Above that zone, decay products are accumulated, so their total amount observed at the surface indicates the time since cooling. In order to convert cooling rates into exhumation rates, the geothermal gradient must be known (see, e.g., Reiners et al., 2005, for a more in-depth description).

In our numerical models, thermochronometric cooling ages are calculated using tracer particles within the domain and assuming no deformation for 30 Myr prior to the model start. Each predicted age represents an integration of deformation from its respective partial annealing or retention zone to the surface (Dodson, 1973; Reiners et al., 2005). Consequently, exhumation of material from the respective zone to the surface is required before the predicted cooling age can be interpreted in a meaningful way. As thermochronometric ages are sensitive to both changes in particle trajectory and thermal gradients, thermochronometric ages will continuously adjust to the evolving geodynamic conditions.

2.2.7 Modeling strategy

In this study, we investigate the effects of subduction and frontal accretion ($v_{\mathrm{sub}} > 0$) and upper-plate advance ($v_{\mathrm{adv}} > 0$) on upper-plate deformation. To study the effect of subduction zone geometry, we first compare straight-slab models with indenter-type models under different velocity boundary conditions. Furthermore, we model different indenter geometries. In the last step, we use a landscape evolution model to study the effect of erosion. We evaluate all models with respect to the resulting rock uplift and strain rates. Additionally, we discuss the models' temporal evolution and the predicted thermochronometric ages at the surface. An overview of all model scenarios is given in Table 1.

3 Results

3.1 Effect of indenter presence and upper-plate advance

3.1.1 Overview

Figure 3 illustrates the key features of the indenter geometry effect on upper-plate deformation. It shows a snapshot after 4 Myr simulation time of the indenter-type model under half-advance boundary conditions (model 5; $v_{\mathrm{sub}} = 50\,\%$ and $v_{\mathrm{adv}} = 50\,\%$).

At the model front and back ($y < 200$ and $y > 600$ km), which correspond to the geometry of the straight-slab models (see model 2 in Fig. 4b4), shortening is accommodated by a lithospheric scale pop-up structure formed by two broad shear zones, indicated by strain rates above $5.0 \times 10^{-15}\,\mathrm{s^{-1}}$. These are referred to hereafter as *pro-* and *retro-shear zone* to the left and right of the S line and labeled (p) and (r), respectively. The two shear zones root to the S line at an angle of ∼ 60° and comprise shallow dipping detachments and steeply dipping reverse faults. However, due to mostly viscous deformation in the lower crust and lithospheric mantle (see Fig. 2), the shear bands are not as strongly localized there. The particle trajectories on the slices at $y = 50$ and 225 km show that material is transported horizontally towards the S line, near which paths for crustal material turn upward. In contrast, the lithospheric mantle is gradually subducted. In the central part of the model domain, the active structures change due to the different subducting plate geometry. Above the indenter, deformation is mostly localized in a retro-dipping, upper-crustal detachment (referred to as *indenter detachment*, labeled i), while the pro- and retro-shear zones are attenuated. The indenter detachment is better localized (strain rates $> 25 \times 10^{-15}\,\mathrm{s^{-1}}$) and is separated from the two previously discussed shear zones; it originates above the subduction interface rather than rooting to the S line. The

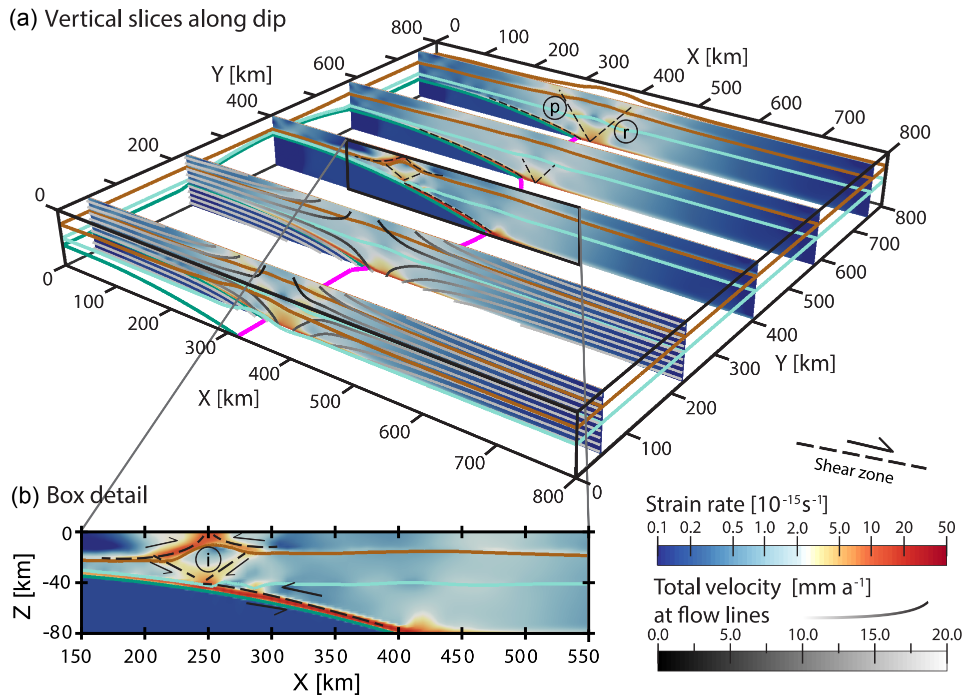

Figure 3. Vertical slices along dip after 4.0 Myr simulation time showing the second invariant of the strain rate tensor and particle trajectories for the indenter geometry under half-advance boundary conditions. Brown, light green, and dark green lines denote the material layer boundaries between upper crust, lower crust, and lithospheric mantle, respectively; magenta marks the S line. Pro- and retro-shear zone are labeled (p) and (r), respectively, while indenter detachment is labeled (i). Note that results are symmetrical about the $y = 400$ km plane. **(a)** Slices along dip in 3-D: deformation at the front and back is weakly localized in two symmetrical shear zones rooting to the S line, forming a lithospheric-scale pop-up structure. Above the indenter, shortening is accommodated by a newly formed basal detachment replacing the steeply dipping shear zones. **(b)** Detail inset shows the strain rates along the central slice.

material layer boundaries illustrate cumulative deformation by the deviation from the initial horizontal layout.

The differences between the straight trench and indenter models are shown in more detail for all boundary condition scenarios in Fig. 4. Since changes in deformation are confined to the indenter's vicinity, this figure depicts strain rates and rock uplift rates along a central slice along dip. Comparing the straight-slab models (left-hand panels) shows that deformation and thus rock uplift are always strongest toward the direction of main material inflow. The half-advance scenario exhibits a nearly symmetrical pattern of shear zones and rock uplift (Fig. 4b1 and b2), but in the case of no ($v_{\mathrm{sub}} = 100\,\%$, $v_{\mathrm{adv}} = 0\,\%$, panels Fig. 4a1 and a2) or full advance ($v_{\mathrm{sub}} = 0\,\%$, $v_{\mathrm{adv}} = 100\,\%$, panels Fig. 4c1 and c2), deformation shifts to the left or right of the S line, respectively.

In all models with an indenter geometry, a basal detachment, situated centrally above the indenter, forms the third major structure. It accommodates shortening in the central part of the model and concurrently reduces deformation in the pro- and retro-shear zone (Fig. 4a5–c5). Its position shifts trenchward with increasing upper-plate advance. It is strongest directly above the model center and decreases laterally as the height and dip of the subducting plate transition from indenter to the background slab. The straight-slab models show a more even and nearly symmetrical upper-crustal thinning, whereas material uplift in the indenter models is much stronger and focused at the location of the indenter detachment.

From these three structures, three corresponding zones of rock uplift can be identified. For both the pro- and retro-shear zones, uplift is localized in the hanging wall of the upper-crustal shallow detachments, forming two continuous bands of uplift in the straight-slab models to the left and right of the S line, respectively (Fig. 4a1–c1). The deformation located in the hanging wall of the indenter basal detachment gives rise to the third zone, an elliptical region of rock uplift (Fig. 4a3–c3).

In all models shown in Fig. 4, the mean uplift rate is about 1.3 mm a^{-1}, but the distribution of rock uplift strongly depends on velocity boundary conditions. For no slab advance, deformation is strongest on the pro-side, to the left

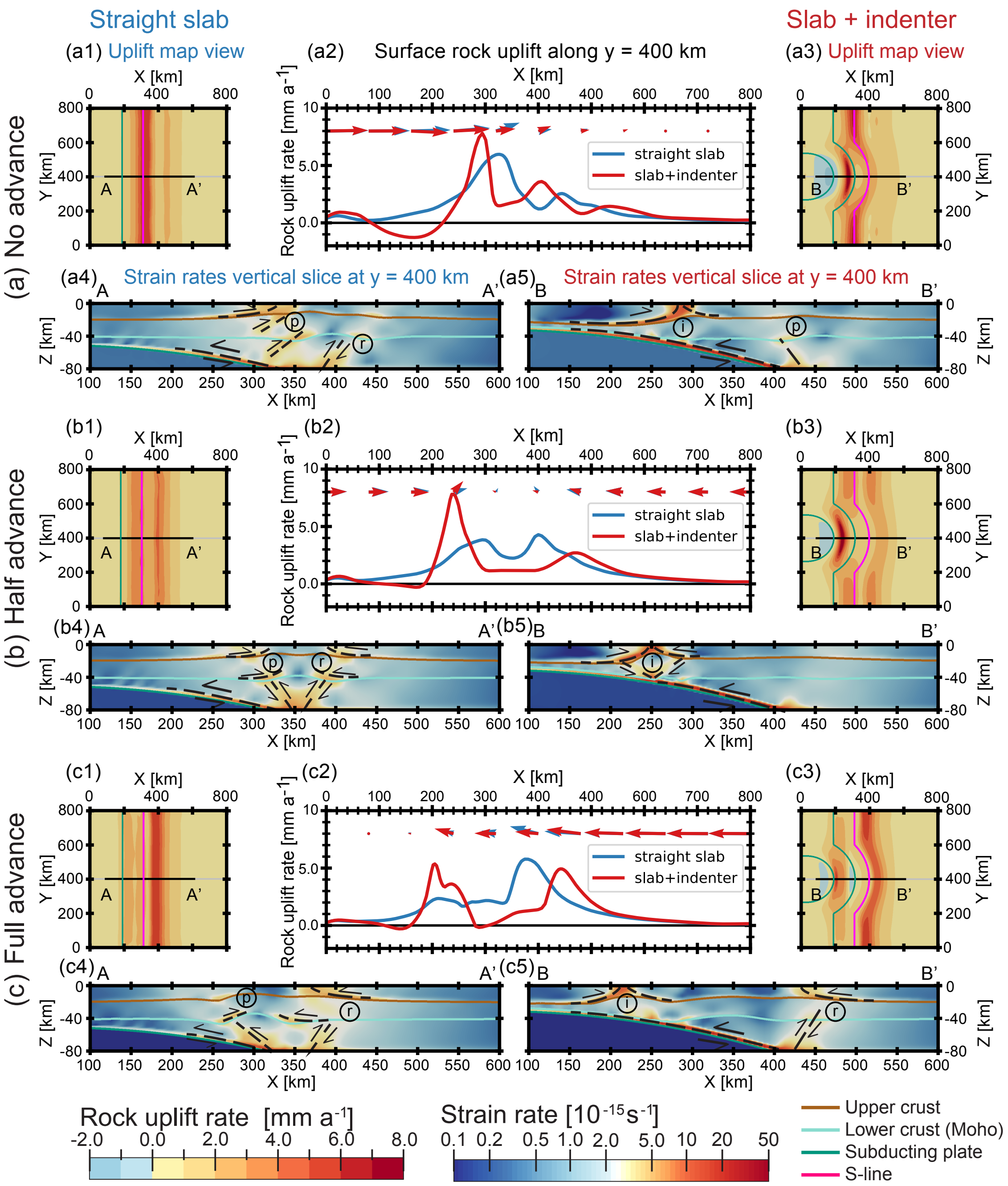

Figure 4. Effect of indenter geometry on rock uplift and strain rates for models 1–6 (Table 1). For each of the three upper-plate motion scenarios **a**–**c**, panels **(1)** and **(3)** show the plan view distribution of rock uplift rates (vertical component of velocity) for the straight-slab and indenter geometry, respectively. Magenta lines mark the position of the S line, and dark green lines are indenter contours at 40 and 60 km depth. **(2)** Rock uplift rates at the surface along dip at $y = 400$ km (gray line in **1** and **3**). Arrows indicate orientation of total velocity. **(4)** and **(5)** show strain rates for vertical slice along dip at $y = 400$ km (black line in **1** and **3**). Brown, light green, and dark green indicate the material boundaries between upper plate, lower plate, and lithospheric mantle, respectively. Pro- and retro-shear zone are labeled (p) and (r), respectively; indenter detachment is labeled (i). In all scenarios, the indenter gives rise to an ellipsoidal region of increased uplift above its apex, caused by the indenter detachment that accommodates shortening in the indenter's vicinity.

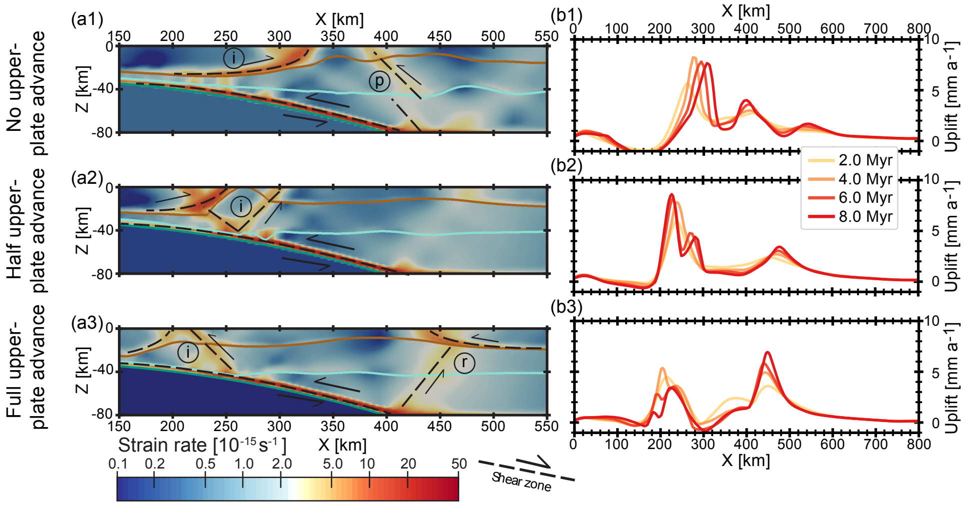

Figure 5. Temporal evolution of the no-, half-, and full-uadvance indenter geometry models (4–6). **(a)** Strain rates on the $y = 400$ km cross section at 8 Myr modeling time (cf. Fig. 4 showing same slices at 4 Myr). **(b)** Time slices of surface rock uplift rates along $y = 400$ km. No-upper-plate advance (model 3; **a1, b1**) scenario shows an indenter detachment in dynamic steady state, which slowly migrates to the right. In the half-advance scenario (model 4; **a2, b2**), uplift above the indenter likewise saturates, but its position is stable, and additional shear zones form in the last stage. Lastly, the full-advance case (model 6; **a3, b3**) exhibits most uplift at the right uplift band, which continuously increases, whereas the indenter uplift ceases again after reaching a peak at 4 Myr simulation time.

of the S line. Uplift rates above the indenter are 30 % higher than in the straight-slab reference model (8.3 mm a^{-1} vs. 6.4 mm a^{-1}). In the half-advance scenario, rock uplift in the straight-slab model is evenly distributed between the pro- and retro-side uplift band (3.8 and 4.3 mm a^{-1}), while the indenter detachment creates a prominent ellipsis-shaped zone reaching almost twice-as-fast uplift rates of 7.8 mm a^{-1}. Finally, the full-advance scenario exhibits lowest peak uplift rates above the indenter of all models (5.4 mm a^{-1}), yet twice as fast as the surrounding area. However, retro-side uplift also reaches equally high rates in both the straight-slab and indenter model (5.8 and 5.0 mm a^{-1}, respectively). To summarize, all models with indenter geometry exhibit a region of focused and increased rock uplift above the indenter. This effect is small in the full-advance model but much stronger for the no- and half-advance scenarios.

Finally, we tested the effect of the chosen convergence rate by running a model with twice the standard value, i.e., at 60 mm a^{-1}. It is shown in comparison to the standard half-advance model in Fig. S2 in the Supplement. There is little difference in the relative distribution of strain and rock uplift between the two models, except at the front and back, where uplift between the pro- and retro-shear zones is increased in the fast convergence model.

3.1.2 Temporal evolution under different plate motion scenarios

As simulation time progresses, the deformation patterns and rock uplift change differently for the three scenarios. Figure 5 shows strain rates at 8 Myr modeling time and the gradual evolution of surface rock uplift rates along the central slice ($y = 200$ km). In both the no- and half-advance scenario, the peak in uplift above the indenter increases and reaches a quasi-steady state. In the case of full upper-plate advance, its uplift decreases after reaching a maximum at ~ 4 Myr. In this scenario, the strong and lasting increase can be observed in the right uplift band instead. These changes in uplift are also reflected in the position and modes of shear zones (compare strain rates at 4 Myr simulation time in Figs. 3 and 4 with strain rates at 8 Myr in Fig. 5). Without slab advance, the indenter basal detachment slowly shifts to the right over time, while keeping its general shape. In contrast, additional shear zones develop alongside the basal detachment for the half-advance scenario. In the case of full advance, however, motion across the indenter detachment almost ceases in favor of a reverse fault dipping in the pro-direction.

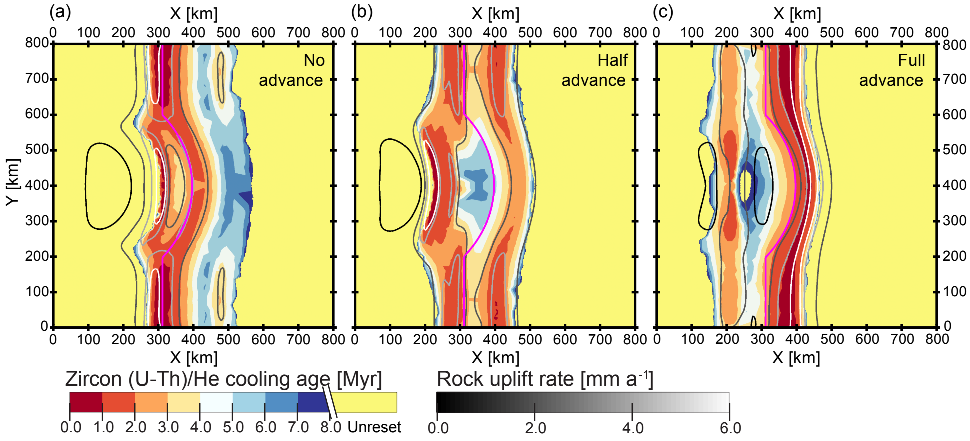

Figure 6. Comparison of zircon (U−Th)/He cooling age for the three standard indenter flat erosion scenarios (models 4–6). In all cases, cooling ages match well with the distribution of rock uplift (see Figs. 4 and 5). The shift in deformation focus toward the direction of main material influx is clearly visible by the concentration of young ages shifting from the left to the right of the S line with increasing upper-plate advance.

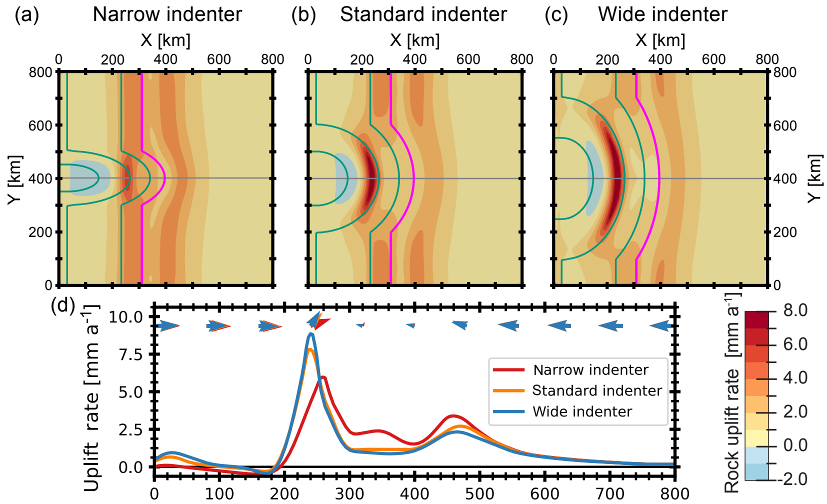

Figure 7. Comparison of different indenter geometries under half-advance boundary conditions. **(a–c)** Map of surface rock uplift rates for narrow, standard, and wide indenter geometry. **(d)** Rock uplift rates along a central cross section (gray line in **a–c**). Basic distribution of uplift is similar in all models with a region of increased uplift above the indenter apex at $x \approx 225$ km, $y \approx 400$ km. Maximum rock uplift rates increase with indenter width.

3.1.3 Prediction of thermochronometric ages

Figure 6 shows a comparison of resulting zircon (U−Th)/He cooling ages and rock uplift rates for models 4–6 (indenter geometry with flat erosion) after 8 Myr of simulation time. In all cases, the distribution of cooling ages matches that of rock uplift rates at the surface (see corresponding plots in Figs. 4 and 5). This can also be observed in other thermochronometric systems as well as physical exhumation parameters, which are shown in Fig. S3 for reference. In Fig. 6, the shift in deformation from pro- to retro-shear zone with increasing upper-plate advance is clearly visible. Additionally, the concentration of young ages above the indenter can be seen in all scenarios. Even in the case of full upper-plate advance (Fig. 6c), where most deformation is accommodated by the shallow detachment of the retro-shear zone, this decrease in ages towards the area above the indenter is visible in the zircon (U−Th)/He ages.

3.2 Effect of indenter geometry

In addition to comparing a straight slab to an indenter-type subducting slab, we investigate the indenter's effect on upper-plate deformation by modeling different geometries. Figure 7 shows the distribution of rock uplift rates for both a narrower and wider indenter geometry compared to the standard/reference geometry discussed previously. For all models, the basic effect of the indenter is the same in that an ellipsoidal region of increased rock uplift is generated above its apex around $x \approx 225$ km, $y \approx 400$ km. The maximum uplift rates, however, increase with indenter width. While the narrow indenter reaches only 6 mm a^{-1}, rock uplift rates increase to 8 mm a^{-1} and even 9 mm a^{-1} for the standard and wider indenter, respectively. Furthermore, in the narrow indenter model, the region of high uplift is not as clearly separated from the uplift caused by the pro-shear zone.

3.3 Effect of variable erosion

For the standard indenter geometry, three additional experiments coupled to a landscape evolution model (FastScape; Braun and Willett, 2013) were performed under no-, half-, and full-advance boundary conditions. The distribution of strain rates and large-scale particle trajectories, as described in Sect. 3.1.1, are only weakly affected by this switch to fluvial erosion. However, the creation of topography and the resulting variations in lithostatic pressure cause changes in upper-crustal deformation as illustrated by Fig. 8, which shows the half-advance fluvial erosion model (model 11).

Figure 8a shows the topography created after 6.0 Myr simulation time, with highest peaks towards the model edge and lower topography and a curved flank above the indenter. The distribution of rock uplift (Fig. 8b) forms two broad bands situated on the flanks of the forming orogen. The left band follows the shape of the slab contour at 50 km depth, with a slight increase in uplift rate above the indenter apex; the right one is only slightly curved and located at $x = 500$ km. In comparison with flat erosion (Fig. 8d), rock uplift zones are much wider, especially towards the model front and back, and uplift rates are reduced by roughly half. Additionally, there are strong local variations, with peaks in rock uplift situated in river valleys. These local maxima (up to 3 mm a^{-1} compared to an average 1.0 mm a^{-1}) correspondingly show deeper exhumation, as can be seen from Fig. 8c. The two uplift peaks in the marked catchments show the deepest exhumation (~ 8 km). They are situated above the indenter and within the region of deepest exhumation in the flat erosion scenario, shown in Fig. 8e for comparison. They also comprise locations where the youngest thermochronometric ages are predicted (Fig. 9). The fluvial erosion models for no and full upper-plate advance (shown in Fig. S4) exhibit a close correspondence to the flat erosion models, as well. However, only much smaller catchments cut across regions of increased tectonic uplift. Consequently, there is no local increase in rock uplift as substantial as observed in the half-advance scenario. In summary, fluvial erosion leads to variation of rock uplift and exhumation on the catchment scale and maxima in rock uplift roughly 60 km in diameter, while regions of high uplift in the flat erosion scenarios extend ~ 250 km along strike. These zones of deepest and fastest exhumation are situated above the indenter apex.

4 Discussion

4.1 Summary of model results

The simulations with a rigid subducting plate presented here indicate that shortening is accommodated by a lithospheric-scale pop-up structure formed by two broad shear zones rooting to the S line (pro- and retro-shear zone). Each shear zone comprises shallow detachments and steeply dipping faults. The shear zone oriented towards the direction of material influx is expressed more strongly. In experiments with an indenter bulging forward from the subducting plate (models 4–12), a more localized basal detachment forms above its apex (indenter detachment) and accommodates shortening there. Concurrently, shear across the pro-shear zone is strongly reduced. This effect is limited to the indenter's vicinity, as can be seen from models with a narrower and wider indenter (Fig. 7). These shear zones give rise to three regions of rock uplift in the flat erosion scenarios: the shallow crustal detachments of the pro- and retro-shear zones create two bands that follow along the trace of the S line, offset to the left and right, respectively. The third zone of high uplift, created by the indenter detachment, is shifted further trenchward (left) and forms an isolated, elliptical region of uplift that is stronger in the no- and half-advance scenarios (e.g., Figs. 4 and 5).

4.2 Model caveats and limitations

Our model setup is generalized to include the first-order features of plate corner settings but is not designed to reproduce a specific region, given limitations due to numeric resolution and large uncertainties in rheologic and thermal parameters of any particular region. Moreover, rock uplift rates in our model are overestimated for flat erosion simulations (models 1–9, shown in Figs. 3–7), which inhibits the creation of topography that would exert an isostatic counterforce to material uplift. With these caveats in mind, rock uplift rates in the flat erosion models should be seen as an upper bound in cases of extremely high erosion. Corresponding to the high rock uplift rates, our predicted cooling ages are very young but nevertheless consistent with the range of exhumation rates reported at syntaxes: ~ 1 mm a^{-1} in the Olympic Mountains (Brandon et al., 1998; Michel et al., 2018), 3–5 mm a^{-1} in the St. Elias range in SE Alaska (Enkelmann et al., 2016), and 5–9 mm a^{-1} in the eastern Himalayan syntaxis (Enkelmann et al., 2011; Lang et al., 2016). It is also worth noting that in the fluvial erosion simula-

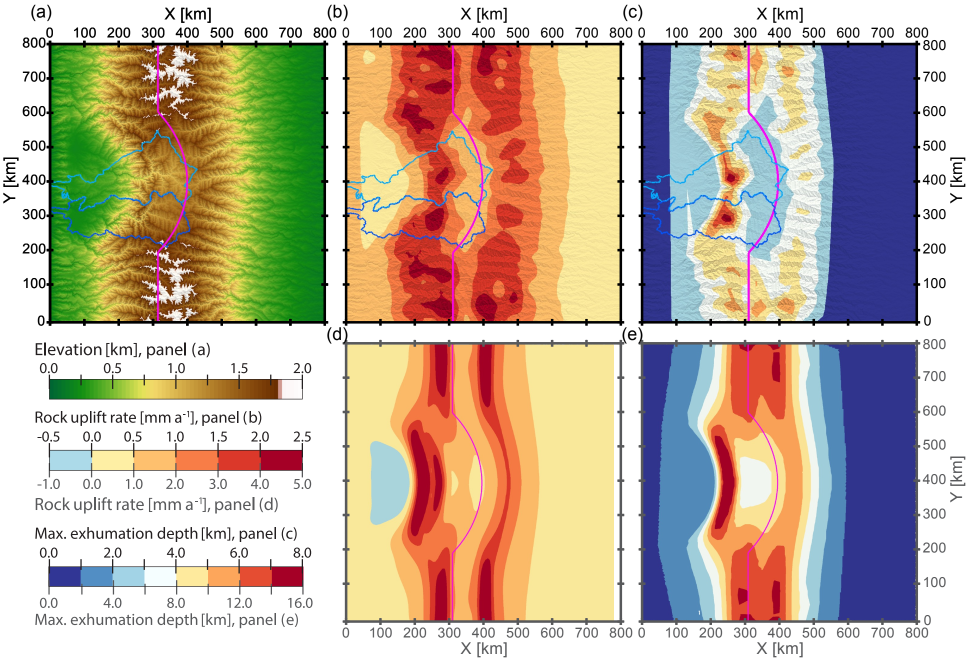

Figure 8. Comparison of rock uplift and exhumation depths with fluvial versus total erosion. **(a)** Surface elevations, **(b)** rock uplift rates, and **(c)** exhumation depth for model 11 (half-advance fluvial erosion) after 6.0 Myr simulation time. Uplift is focused along the flanks of the orogen, with the two maxima in exhumation situated in river valleys of high erosion potential. Deepest exhumation occurs in the two uplift foci situated above the indenter ($x = 265$ km, $y = 410$ km; $x = 250$ km, $y = 300$ km), situated within the catchments outlined in blue. Predicted thermochronometric ages are as follows: apatite (U−Th)/He: 1.3 and 1.1 Ma; apatite fission track: 1.9 and 1.65 Ma; and zircon (U−Th)/He 4.2 and 4.1 Ma for the upper (light blue catchment) and lower (dark blue) hotspot, respectively. **(d)** and **(e)** show the flat erosion results for rock uplift rates and exhumation depth for comparison. Note the range is increased by a factor of 2 for those two plots (gray labels).

tions uniform precipitation was used throughout the model run. While this is justifiable for our study of contrasting erosional efficiency, it has been shown that changes in precipitation by orographic effects strongly influence the distribution of rock uplift and consequently orogen dynamics (Willett, 1999). Despite these limitations, several general lessons emerge from our simulations that have bearing on understanding exhumation processes in plate corner settings. In the following, we will discuss key aspects and mechanisms of exhumation at plate corners.

4.3 Effect of indenter presence and geometry

The variation in subducting plate geometry from background slab to the indenter causes different structures to evolve to accommodate shortening (e.g., Figs. 3 and 4). Through this change in structures along strike, localized exhumation is created. Once deformation is localized, both strain and thermal weakening contribute to intensifying shear across those structures (see temperatures in Fig. S1) and focus deformation even further in that region, thereby increasing uplift rates. In our models, the indenter detachment is created by the shallower slab and lower dip angle of the indenter, which exerts a stronger traction on the overriding plate, both forward and downward (see Fig. 4 and velocities in Fig. S1). Additionally, the indenter detachment partially takes up strain that would otherwise be accommodated by the pro-shear zone. Strain transfer between these systems occurs along the weak subducting plate interface. Along the background slab, the interface's lower dip angle seemingly makes strain transfer less favorable (cf. Fig. 4). The extent of the indenter detachment is limited to the indenter width, but a minimum size is required to observe its effect. For the narrow indenter, material is displaced laterally rather than exhumed. This is also evident by the higher uplift rates for the wider indenter, where lateral displacement is most strongly impeded. Detachment-like shallow faults dipping towards the subducting plate have been reported for the Andean orogen (e.g., Horton, 2018b). It is important to note that the lateral variation in depth to the subducting slab in our models may contribute to the changing style of deformation. Still, the Cascadia subduction zone, template for our model geometry, is an example of such a change along strike. Above the indenter bulge, the Hurricane Ridge fault warps from off-

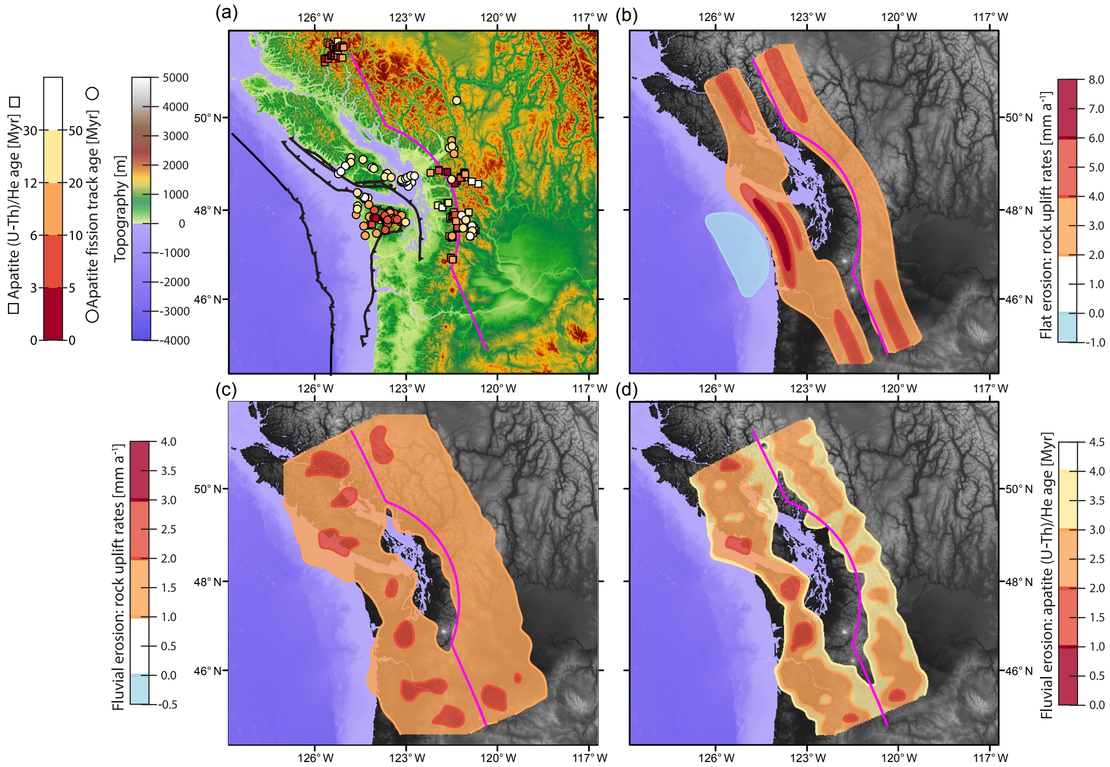

Figure 9. Comparison of Cascadia topography with model results: **(a)** apatite (U−Th)/He (squares; Batt et al., 2001; Ehlers et al., 2006; Reiners et al., 2002, 2003; Simon-Labric et al., 2014) and apatite fission track cooling ages (circles; Brandon et al., 1998; England et al., 1997; Currie and Grist, 1996; Reiners et al., 2002; Johnson et al., 1986). Major structures from Brandon et al. (1998). **(b)** Flat erosion (model 5) rock uplift rates. **(c)** Fluvial erosion (model 11) rock uplift rates and **(d)** fluvial erosion (model 11) predicted apatite (U−Th)/He cooling ages. Model S line in magenta for orientation. The region of increased uplift above the indenter for the flat erosion model coincides with the location of the Olympic Mountains. The fluvial erosion model shows smaller variations in rock uplift rates and cooling ages that are roughly the same size as the extent of young cooling ages in the Olympic Mountains.

shore to on land and exposes the accretionary wedge in the Olympic Mountains, directly above the indenter apex (Figs. 1 and 9, Brandon et al., 1998). This is supported by the work of Calvert et al. (2011), who deduce strongly increased underplating of sedimentary material above the indenter bulge from seismic tomography.

4.4 Effect of upper-plate advance

Many numerical models of subduction processes use a fixed overriding plate with respect to the trench position (see, e.g., Koons et al., 2010; Braun and Yamato, 2010; Willett, 1999). In contrast, Bendick and Ehlers (2014) used a stationary indenter and advancing upper plate. Our models explore how focused uplift created by an indenter geometry varies with respect to different velocity boundary conditions. The indenter detachment is more active in the no- and half-advance scenarios, corresponding to the behavior of the pro-shear zone. In the full-advance scenario, however, the indenter detachment is only of transient nature, and rock uplift rates above this feature reach barely half those seen in the other models (Fig. 5). Since localization of rock uplift by the indenter detachment corresponds to a different accommodation of shortening along strike caused by the indenter geometry, it seems evident that sufficient deformation in the indenters' vicinity is required to make those different structures observable. As much of the overall shortening in the full-advance case is taken up by the retro-shear band, even increasing over time through thermal and strain weakening, strain transfer along the weak subduction interface and thus uplift above the indenter are strongly reduced. The increased deformation in the retro-shear zone – associated rock uplift rates increase by ∼ 40 % from 4 to 8 Myr simulation time – leads to subsidence above the indenter (see Fig. 5a3), because the correspondingly reduced material flow along the subducting plate interface can no longer support the thinned crust, which then relaxes isostatically. This conforms to observations of the Chilean forearc, where compression has induced flexural subsidence by thrust or reverse faulting in the late Cenozoic (see Horton, 2018a, and references therein).

Additional effects of the different velocity boundary conditions can be observed between the no- and half-advance scenarios. Both flat erosion models reach a dynamic steady state at ~ 4 Myr with rock uplift rates of $\sim 8\,\mathrm{mm\,a^{-1}}$ above the indenter. Although maximum uplift rates are about the same, the region of focused uplift above the indenter appears more prominent in the half-advance case. This is due to the even distribution of shear between the pro- and retro-shear zones in the half-advance scenario, which creates uplift over a wider area at consequently lower rates. Their respective rock uplift rates at the front and back reach only 4 and $5\,\mathrm{mm\,a^{-1}}$ in the half-advance scenario, whereas uplift rates in the no-advance model reach up to $9\,\mathrm{mm\,a^{-1}}$. Finally, the indenter detachment in the no-advance scenario is slowly shifting to the right (away from the trench). In the half-advance model, this motion is prevented by opposing material inflow, focusing deformation and thus stabilizing deformation through increased thermal weakening. The exhumation of lower-crustal material at 8 Myr simulation time (Fig. 5b4) illustrates this focusing effect well.

Note that the overall rate of convergence has only limited effect on the distribution of deformation. Naturally rock uplift is twice as fast for the doubled convergence rate (see Fig. S2), but the relative distribution is mostly the same. Small deviations in strain rate fields stem from different isostatic adjustment and the strain-dependent material viscosity.

As expected, predicted cooling ages and exhumation parameters calculated conform with the modeled velocity fields and offer an additional option to illustrate the distribution of deformation in the overriding plate. They provide the best option to relate model results to natural observations. However, rock uplift in our models is exceptionally fast due to flat erosion, which prevents the creation of topography that would counteract rock uplift. Given this, it is important to take the resulting values as only a general representation of what could be observed in natural systems and to focus on the age pattern rather than the absolute values.

4.5 Sensitivity of exhumation to different erosion parameters

The distribution of rock uplift is quite similar for the flat and fluvial erosion model runs. Nevertheless, the growing topography means an increased lithostatic overburden, causing both a general reduction in rate and redistribution of rock uplift. In general, rock uplift is spread out over a wider area than in the flat erosion models. Additional spatial variations in rock uplift occur on the catchment scale. Strong erosion removes lithostatic overburden and engenders higher uplift rates, mostly so in steep and sufficiently large catchments along the orogen flanks. Under half-advance conditions, two rivers with large upstream catchment area cut across the region of localized uplift above the indenter apex (Fig. 8). It is there that strong tectonic forcing coincides with a high erosion potential such that the deepest and fastest exhumation is observed. Both other fluvial erosion models (no and full advance) show variation in uplift on the catchment scale as well (Fig. S4) but lack comparably large rivers transecting regions of high tectonic uplift. Thus, no equivalent localization effects can be observed in these models. From these results, we hypothesize that both focused deformation and focused erosion are necessary in order to form a region of localized and rapid uplift. The curved 3-D geometry of the subducting plate at plate corners sets the stage, as proposed by Bendick and Ehlers (2014), but only when this concurs with a sufficiently high erosion potential can a spatially limited area of intense uplift be formed (see Zeitler et al., 2001). Prime examples for this are the Himalayan syntaxes, where the Yarlung Zangbo Jiang and Ganges rivers cut across the Himalayan range and steepen rapidly (Finlayson et al., 2002). In combination with active crustal-scale structures (Burg et al., 1998; Schneider et al., 1999), this has given rise to spatially limited, rapid exhumation as indicated by very young thermochronometric cooling ages (Zeitler et al., 1993, 2014; Winslow et al., 1996; Burg et al., 1998; Malloy, 2004).

Figure 9 shows model results in comparison to cooling age observations of the Cascadia region, which served as a template for the subducting plate geometry used in this study (see Fig. 1). In general, the modeled distribution of rock uplift rates reflects topographic highs and lows. Moreover, the concentration of young cooling ages (apatite (U–Th)/He < 3 Myr) and inferred uplift rates of $\sim 1.0\,\mathrm{mm\,a^{-1}}$ observed in the Olympic Mountains (Brandon et al., 1998; Michel et al., 2018) correspond quite well to the peak in rock uplift rates and cooling ages predicted from the fluvial erosion model. The length scale of variations in rock uplift introduced by fluvial erosion is also in agreement with the observed cooling age data, which show young and old ages often in close proximity. Nevertheless, our model overestimates rock uplift rates with large areas above $1\,\mathrm{mm\,a^{-1}}$ that do not agree with apatite fission track ages > 20 Myr on Vancouver Island, for example. The strong gradient of observed cooling ages also indicates that our limited model resolution is insufficient to capture material heterogeneities and processes acting on smaller scales as evident in nature. A comprehensive representation of this setting certainly calls for more rigorous tuning of model parameters, but even with our generalized approach the results presented here capture important first-order properties.

4.6 Comparison to previous studies

This work combines and builds upon previous studies. Koons et al. (2002) showed that locally enhanced erosion rates and pre-weakened crust can lead to focused exhumation. However, they used a uniform visco-plastic material for the both overriding and down-going plate and a straight S line and material influx with basal drag only on one side. This approach corresponds to our straight-slab no-advance simulation. Flat erosion was applied in only a limited region, while surrounding areas were not eroded, resulting in highest rock uplift rates in this very region. In contrast, Bendick and Ehlers (2014) used an indenter-type geometry, but temperature-dependent viscous rheology for the overriding plate and uniform, flat erosion. Due to the viscous rheology, no strain localization was observed, and rock uplift rates increased gradually from the edges toward the center, forming an uplift region extending several hundreds of kilometers. While they explored effects of viscosity and indenter geometry, only full-advance velocity boundary conditions were used. In contrast, the addition of frictional plasticity in this study naturally allows for strain localization. In combination with fluvial erosion, this illustrates possible mechanisms that create localized regions of uplift without relying on a priori defined structures.

5 Conclusions

This study investigates the thermomechanical response of upper-plate deformation and erosion to subduction of a rigid indenter. We do this by exploring the effect of the presence and shape of a subducting indenter, velocity boundary conditions (i.e., amount of upper-plate advance), and erosion on the resulting deformation pattern in the overriding plate. Key results from this study include the following:

1. For a straight subducting slab (without an indenter), shortening is accommodated by a lithospheric-scale pop-up structure composed of two broad shear zones rooting to the S line and cutting across the entire lithospheric mantle and crust. The shear zone oriented toward the side of influx accommodates more shortening; at half advance, shear is distributed evenly.
2. Adding an indenter to the subducting plate creates another major shear system and a strongly localized basal detachment situated above the indenter apex. Concurrently, shear across the pro-shear zone is strongly reduced. The indenter detachment gives rise to a zone of localized rock uplift. Its extent along strike is governed by the indenter width. While Bendick and Ehlers (2014) showed this indenter effect solely for upper-plate advance, we find that this localization effect is stronger if shortening is accommodated at least partially by lower-plate subduction.
3. Under no- or half-advance boundary conditions, uplift above the indenter reaches a quasi-steady state with uplift rates of 7.5 $\mathrm{mm\,a^{-1}}$ at ~ 4 Myr. In the case of a fully advancing upper plate, however, maximum uplift rates above the indenter are 4 $\mathrm{mm\,a^{-1}}$ and decrease after a peak at 3.5 Myr, when larger amounts of shortening are accommodated by the retro-shear zone.
4. Applying a landscape evolution model for the erosional response to rock uplift modifies rock uplift through the consequent creation of topography. The increased lithostatic overburden reduces uplift rates by roughly half and distributes uplift over a wider area. Furthermore, fluvial erosion causes rock uplift to vary on a smaller (catchment) scale than previously set by tectonics alone.
5. The deepest and fastest exhumation occurs where tectonic forcing coincides with large erosion potential. From this we conclude that both the subducting plate geometry and possible erosion effects need to be taken into account in order to understand the exceptional exhumation rates observed in orogen syntaxes.

Code and data availability. Model output is available upon request from Todd Ehlers. The software DOUAR is currently not open source. Requests for use should be made to the main author, Jean Braun (GFZ Potsdam), and Todd Ehlers (University of Tübingen).

Appendix A: Numerical model details

Lithospheric deformation and temperatures in this study are calculated with the program DOUAR (Braun et al., 2008; Thieulot et al., 2008), a fully coupled three-dimensional thermomechanical model. Further details can also be found in Braun and Yamato (2010) and Whipp et al. (2014).

DOUAR solves the three-dimensional Stokes (creeping) flow equations for incompressible fluids, constituted by conservation of momentum (Eq. A1) and conservation of mass (Eq. A2):

$$\nabla \cdot \mu \left(\nabla \boldsymbol{V} + \nabla \boldsymbol{V}^T \right) - \nabla P = \varrho g, \tag{A1}$$

$$\nabla \boldsymbol{V} = 0, \tag{A2}$$

where μ is the material shear viscosity, $\boldsymbol{V}$ the velocity field, P the pressure, ϱ is the density, and g the gravity acceleration. The solution is computed with the finite-element method using Q1P0 elements; i.e., the pressure is calculated from the velocity field by the penalty formulation (e.g., Bathe, 1982):

$$P = -\lambda \nabla \cdot \boldsymbol{V}. \tag{A3}$$

For this, conservation of mass is amended to near incompressibility with a penalty factor λ, which is typically 8 orders of magnitude larger than the viscosity μ. The model domain is subdivided into elements by a regular grid, on which the finite-element solution is calculated.

The material properties of each element are defined by marker particles of two types, which (a) track material interfaces (*surfaces*) or (b) record strain and pressure (*cloud*). Particles will be created or deleted automatically to ensure both a roughly homogeneous particle density and adequate base for material property calculations (*self-adapting density*). Additionally, a third type of particles stores position, temperature, and pressure for each time step. If those particles are exhumed at the surface, the *p–T–t* path is compiled from storage and registered at the current time step. From these paths, thermochronometric cooling ages can be calculated.

Materials can be either purely viscous or frictional visco-plastic. The viscosity μ follows a thermally activated creep law:

$$\mu = B_0 \dot{\varepsilon}^{1/n-1} e^{Q/nRT}, \tag{A4}$$

where B_0 is the viscosity prefactor, $\dot{\varepsilon}$ the second invariant of the deviatoric strain rate tensor, n the stress exponent, Q the activation energy, R the gas constant, and T the temperature. If the stress exponent $n = 1$, the material is linearly viscous, whereas $n > 1$ denotes non-Newtonian viscosity, where viscosity increases under higher strain rates.

When plasticity is enabled, material deformation is dictated by the Mohr–Coulomb failure criterion:

$$\tau = C_0 - \sigma_\mathrm{n} \tan\phi, \tag{A5}$$

where τ is the deviatoric shear stress, C_0 the material cohesion, σ_n the normal stress, and ϕ the material angle of friction. For each model element, the effective stress τ_eff is calculated from the strain rate:

$$\tau_\mathrm{eff} = 2\mu\dot{\varepsilon}. \tag{A6}$$

If this effective stress exceeds the Mohr–Coulomb yield stress τ, elemental viscosity is reduced to an effective viscosity

$$\mu_\mathrm{eff} = \frac{\tau}{2\dot{\varepsilon}}; \tag{A7}$$

otherwise viscosity is kept at the initial value.

The Supplement related to this article is available online at: https://doi.org/10.5194/se-9-1207-2018-supplement

Author contributions. Project design and funding was done by TAE. Software development was done by MN with support from DMW and TAE. MN designed and carried out simulations in close collaboration with TAE and DMW. Manuscript preparation was done by MN and TAE with contributions from all co-authors.

Competing interests. The authors declare that they have no conflict of interest.

Acknowledgements. This work was supported by a European Research Council (ERC) Consolidator Grant (615703) to Todd A. Ehlers. We also acknowledge support by the Deutsche Forschungsgemeinschaft and the Open Access Publishing Fund of the University of Tübingen. We thank Jean Braun for providing the FastScape source code used for the coupled erosion–deformation simulations and Rebecca Bendick for helpful discussions over the years. This paper benefited from thoughtful reviews by Anne Replumaz and two anonymous reviewers.

Edited by: Mark Allen
Reviewed by: two anonymous referees

References

Adams, B. A. and Ehlers, T. A.: Deciphering topographic signals of glaciation and rock uplift in an active orogen: a case study from the Olympic Mountains, USA, Earth Surf. Proc. Land., 42, 1680–1692, https://doi.org/10.1002/esp.4120, 2017.

Adams, B. A. and Ehlers, T. A.: Tectonic controls of Holocene erosion in a glaciated orogen, Earth Surf. Dynam. Discuss., https://doi.org/10.5194/esurf-2018-9, in review, 2018.

Bathe, K.-J.: Finite element procedures in engineering analysis, Prentice-Hall, New Jersey, 1982.

Batt, G. E., Brandon, M. T., Farley, K. A., and Roden-Tice, M.: Tectonic synthesis of the Olympic Mountains segment of the Cascadia wedge, using two-dimensional thermal and kinematic modeling of thermochronological ages, J. Geophys. Res.-Solid, 106, 26731–26746, https://doi.org/10.1029/2001JB000288, 2001.

Bendick, R. and Ehlers, T. A.: Extreme localized exhumation at syntaxes initiated by subduction geometry, Geophys. Res. Lett., 41, 5861–5867, https://doi.org/10.1002/2014GL061026, 2014.

Berger, A. L., Spotila, J. A., Chapman, J. B., Pavlis, T. L., Enkelmann, E., Ruppert, N. A., and Buscher, J. T.: Architecture, kinematics, and exhumation of a convergent orogenic wedge: A thermochronological investigation of tectonic–climatic interactions within the central St. Elias orogen, Alaska, Earth Planet. Sc. Lett., 270, 13–24, https://doi.org/10.1016/j.epsl.2008.02.034, 2008.

Brandon, M. T., Roden-Tice, M. K., and Garver, J. I.: Late Cenozoic exhumation of the Cascadia accretionary wedge in the Olympic Mountains, northwest Washington State, Geol. Soc. Am. Bull., 110, 985–1009, https://doi.org/10.1130/0016-7606(1998)110<0985:LCEOTC>2.3.CO;2, 1998.

Braun, J.: Pecube: a new finite-element code to solve the 3D heat transport equation including the effects of a time-varying, finite amplitude surface topography, Comput. Geosci., 29, 787–794, https://doi.org/10.1016/S0098-3004(03)00052-9, 2003.

Braun, J. and Willett, S. D.: A very efficient $O(n)$, implicit and parallel method to solve the stream power equation governing fluvial incision and landscape evolution, Geomorphology, 180–181, 170–179, https://doi.org/10.1016/j.geomorph.2012.10.008, 2013.

Braun, J. and Yamato, P.: Structural evolution of a three-dimensional, finite-width crustal wedge, Tectonophysics, 484, 181–192, https://doi.org/10.1016/j.tecto.2009.08.032, 2010.

Braun, J., Thieulot, C., Fullsack, P., DeKool, M., Beaumont, C., and Huismans, R.: DOUAR: A new three-dimensional creeping flow numerical model for the solution of geological problems, Phys. Earth Planet. Inter., 171, 76–91, https://doi.org/10.1016/j.pepi.2008.05.003, 2008.

Burg, J.-P., Nievergelt, P., Oberli, F., Seward, D., Davy, P., Maurin, J.-C., Diao, Z., and Meier, M.: The Namche Barwa syntaxis: evidence for exhumation related to compressional crustal folding, J. Asian Earth Sci., 16, 239–252, https://doi.org/10.1016/S0743-9547(98)00002-6, 1998.

Burov, E. B.: Rheology and strength of the lithosphere, Mar. Petrol. Geol., 28, 1402–1443, https://doi.org/10.1016/j.marpetgeo.2011.05.008, 2011.

Calvert, A. J., Preston, L. A., and Farahbod, A. M.: Sedimentary underplating at the Cascadia mantle-wedge corner revealed by seismic imaging, Nat. Geosci., 4, 545–548, https://doi.org/10.1038/ngeo1195, 2011.

Capitanio, F. A., Morra, G., Goes, S., Weinberg, R. F., and Moresi, L.: India–Asia convergence driven by the subduction of the Greater Indian continent, Nat. Geosci., 3, 136–139, https://doi.org/10.1038/ngeo725, 2010.

Carter, N. L. and Tsenn, M. C.: Flow properties of continental lithosphere, Tectonophysics, 136, 27–63, https://doi.org/10.1016/0040-1951(87)90333-7, 1987.

Chamot-Rooke, N. and Le Pichon, X.: GPS determined eastward Sundaland motion with respect to Eurasia confirmed by earthquakes slip vectors at Sunda and Philippine trenches, Earth Planet. Sc. Lett., 173, 439–455, https://doi.org/10.1016/S0012-821X(99)00239-3, 1999.

Craw, D., Koons, P. O., Winslow, D. M., Chamberlain, C. P., and Zeitler, P. K.: Boiling fluids in a region of rapid uplift, Nanga Parbat Massif, Pakistan, Earth Planet. Sc. Lett., 128, 169–182, https://doi.org/10.1016/0012-821X(94)90143-0, 1994.

Crowley, J. L., Waters, D. J., Searle, M. P., and Bowring, S. A.: Pleistocene melting and rapid exhumation of the Nanga Parbat massif, Pakistan: Age and P–T conditions of accessory mineral growth in migmatite and leucogranite, Earth Planet. Sc. Lett., 288, 408–420, https://doi.org/10.1016/j.epsl.2009.09.044, 2009.

Currie, L. and Grist, A.: Diachronous low temperature Paleogene cooling of the Alberni Inlet area, southern Vancouver Island, British Columbia: Evidence from apatite fission track analyses, Geological Survey of Canada Current Research, Vancouver, 119–125, 1996.

Dodson, M. H.: Closure temperature in cooling geochronological and petrological systems, Contrib. Mineral. Petrol., 40, 259–274, https://doi.org/10.1007/BF00373790, 1973.

Ehlers, T. A.: Computational Tools for Low-Temperature Thermochronometer Interpretation, Rev. Mineral. Geochem., 58, 589–622, https://doi.org/10.2138/rmg.2005.58.22, 2005.

Ehlers, T. A., Farley, K. A., Rusmore, M. E., and Woodsworth, G. J.: Apatite (U–Th)/He signal of large-magnitude accelerated glacial erosion, southwest British Columbia, Geology, 34, 765–768, https://doi.org/10.1130/G22507.1, 2006.

England, P. and Molnar, P.: Surface uplift, uplift of rocks, and exhumation of rocks, Geology, 18, 1173–1177, https://doi.org/10.1130/0091-7613(1990)018<1173:SUUORA>2.3.CO;2, 1990.

England, T. D. J., Currie, L. D., Massey, N. W. D., Roden-Tice, M. K., and Miller, D. S.: Apatite fission-track dating of the Cowichan fold and thrust system, southern Vancouver Island, British Columbia, Can. J. Earth Sci., 34, 635–645, https://doi.org/10.1139/e17-050, 1997.

Enkelmann, E., Zeitler, P. K., Garver, J. I., Pavlis, T. L., and Hooks, B. P.: The thermochronological record of tectonic and surface process interaction at the Yakutat–North American collision zone in southeast Alaska, Am. J. Sci., 310, 231–260, https://doi.org/10.2475/04.2010.01, 2010.

Enkelmann, E., Ehlers, T. A., Zeitler, P. K., and Hallet, B.: Denudation of the Namche Barwa antiform, eastern Himalaya, Earth Planet. Sc. Lett., 307, 323–333, https://doi.org/10.1016/j.epsl.2011.05.004, 2011.

Enkelmann, E., Piestrzeniewicz, A., Falkowski, S., Stübner, K., and Ehlers, T. A.: Thermochronology in southeast Alaska and southwest Yukon: Implications for North American Plate response to terrane accretion, Earth Planet. Sc. Lett., 457, 348–358, https://doi.org/10.1016/j.epsl.2016.10.032, 2016.

Erdos, Z., Huismans, R. S., v. d. Beek, P., and Thieulot, C.: Extensional inheritance and surface processes as controlling factors of mountain belt structure, J. Geophys. Res.-Solid, 119, 9042–9061, https://doi.org/10.1002/2014JB011408, 2014.

Faccenna, C., Becker, T. W., Conrad, C. P., and Husson, L.: Mountain building and mantle dynamics, Tectonics, 32, 80–93, https://doi.org/10.1029/2012TC003176, 2013.

Falkowski, S., Enkelmann, E., and Ehlers, T. A.: Constraining the area of rapid and deep-seated exhumation at the St. Elias syntaxis, Southeast Alaska, with detrital zircon fission-track analysis, Tectonics, 33, 597–616, https://doi.org/10.1002/2013TC003408, 2014.

Finlayson, D. P., Montgomery, D. R., and Hallet, B.: Spatial coincidence of rapid inferred erosion with young metamorphic massifs in the Himalayas, Geology, 30, 219–222, https://doi.org/10.1130/0091-7613(2002)030<0219:SCORIE>2.0.CO;2, 2002.

Frank, F. C.: Curvature of Island Arcs, Nature, 220, 363, https://doi.org/10.1038/220363a0, 1968.

Gripp, A. E. and Gordon, R. G.: Young tracks of hotspots and current plate velocities, Geophys. J. Int., 150, 321–361, https://doi.org/10.1046/j.1365-246X.2002.01627.x, 2002.

Hayes, G. P., Wald, D. J., and Johnson, R. .: Slab1.0: A three-dimensional model of global subduction zone geometries, J. Geophys. Res.-Solid, 117, B01302, https://doi.org/10.1029/2011JB008524, 2012.

Heuret, A. and Lallemand, S.: Plate motions, slab dynamics and back-arc deformation, Phys. Earth Planet. Inter., 149, 31–51, https://doi.org/10.1016/j.pepi.2004.08.022, 2005.

Hirth, G. and Kohlstedt, D.: Rheology of the upper mantle and the mantle wedge: A view from the experimentalists, in: Inside the subduction Factory, vol. 138 of Geophysical Monograph Series,edited by: Eiler, J., American Geophysical Union, Washington, D.C., 83–105, https://doi.org/10.1029/138GM06, 2003.

Horton, B. K.: Sedimentary record of Andean mountain building, Earth-Sci. Rev., 178, 279–309, https://doi.org/10.1016/j.earscirev.2017.11.025, 2018a.

Horton, B. K.: Tectonic Regimes of the Central and Southern Andes: Responses to Variations in Plate Coupling During Subduction, Tectonics, 37, 402–429, https://doi.org/10.1002/2017TC004624, 2018b.

Jadamec, M. A. and Billen, M. I.: The role of rheology and slab shape on rapid mantle flow: Three-dimensional numerical models of the Alaska slab edge, J. Geophys. Res.-Solid, 117, B02304, https://doi.org/10.1029/2011JB008563, 2012.

Johnson, S. Y., Zimmermann, R. A., Naeser, C. W., and Whetten, J. T.: Fission-track dating of the tectonic development of the San Juan Islands, Washington, Can. J. Earth Sci., 23, 1318–1330, https://doi.org/10.1139/e86-127, 1986.

Kaus, B. J. P., Mühlhaus, H., and May, D. A.: A stabilization algorithm for geodynamic numerical simulations with a free surface, Phys. Earth Planet. Inter., 181, 12–20, https://doi.org/10.1016/j.pepi.2010.04.007, 2010.

Koons, P. O., Zeitler, P. K., Chamberlain, C. P., Craw, D., and Meltzer, A. S.: Mechanical links between erosion and metamorphism in Nanga Parbat, Pakistan Himalaya, Am. J. Sci., 302, 749–773, https://doi.org/10.2475/ajs.302.9.749, 2002.

Koons, P. O., Hooks, B. P., Pavlis, T. L., Upton, P., and Barker, A. D.: Three-dimensional mechanics of Yakutat convergence in the southern Alaskan plate corner, Tectonics, 29, TC4008, https://doi.org/10.1029/2009TC002463, 2010.

Koons, P. O., Zeitler, P. K., and Hallet, B.: Tectonic Aneurysms and Mountain Building, in: Treatise on Geomorphology, vol. 5 of Reference Module in Earth Systems and Environmental Sciences, edited by: Owen, L. A. and Shroder, J. F., Academic Press, San Diego, 318–349, https://doi.org/10.1016/B978-0-12-374739-6.00094-4, 2013.

Lang, K. A., Huntington, K. W., Burmester, R., and Housen, B.: Rapid exhumation of the eastern Himalayan syntaxis since the late Miocene, Geol. Soc. Am. Bull., 128, 1403–1422, https://doi.org/10.1130/B31419.1, 2016.

Mahadevan, L., Bendick, R., and Liang, H.: Why subduction zones are curved, Tectonics, 29, TC6002, https://doi.org/10.1029/2010TC002720, 2010.

Malloy, M. A.: Rapid Erosion at the Tsangpo Knickpoint and Exhumation of Southeastern Tibet, MS thesis, Lehigh Universiy, Bethlehem, Pennsylvania, 2004.

Michel, L., Ehlers, T. A., Glotzbach, C., Adams, B. A., and Stübner, K.: Tectonic and glacial contributions to focused exhumation in the Olympic Mountains, Washington, USA, Geology, 46, 491–494, https://doi.org/10.1130/G39881.1, 2018.

Molnar, P. and England, P.: Late Cenozoic uplift of mountain ranges and global climate change: chicken or egg?, Nature, 346, 29–34, https://doi.org/10.1038/346029a0, 1990.

Montgomery, D. R.: Valley incision and the uplift of mountain peaks, J. Geophys. Res.-Solid, 99, 13913–13921, https://doi.org/10.1029/94JB00122, 1994.

Ranalli, G. and Murphy, D. C.: Rheological stratification of the lithosphere, Tectonophysics, 132, 281–295, https://doi.org/10.1016/0040-1951(87)90348-9, 1987.

Reiners, P. W., Ehlers, T. A., Garver, J. I., Mitchell, S. G., Montgomery, D. R., Vance, J. A., and Nicolescu, S.: Late Miocene exhumation and uplift of the Washington Cascade Range, Geology, 30, 767–770, https://doi.org/10.1130/0091-7613(2002)030<0767:LMEAUO>2.0.CO;2, 2002.

Reiners, P. W., Ehlers, T. A., Mitchell, S. G., and Montgomery, D. R.: Coupled spatial variations in precipitation and long-term erosion rates across the Washington Cascades, Nature, 426, 645–647, https://doi.org/10.1038/nature02111, 2003.

Reiners, P. W., Ehlers, T. A., and Zeitler, P. K.: Past, Present, and Future of Thermochronology, Rev. Mineral. Geochem., 58, 1–18, https://doi.org/10.2138/rmg.2005.58.1, 2005.

Russo, R. and Silver, P.: Trench-parallel flow beneath the Nazca plate from seismic anisotropy, Science, 263, 1105–1111, https://doi.org/10.1126/science.263.5150.1105, 1994.

Schellart, W. P., Freeman, J., Stegman, D. R., Moresi, L., and May, D. A.: Evolution and diversity of subduction zones controlled by slab width, Nature, 446, 308–311, https://doi.org/10.1038/nature05615, 2007.

Schneider, D. A., Edwards, M. A., Kidd, W. S. F., Zeitler, P. K., and Coath, C. D.: Early Miocene anatexis identified in the western syntaxis, Pakistan Himalaya, Earth Planet. Sc. Lett., 167, 121–129, https://doi.org/10.1016/S0012-821X(99)00022-9, 1999.

Simon-Labric, T., Brocard, G. Y., Teyssier, C., van der Beek, P. A., Reiners, P. W., Shuster, D. L., Murray, K. E., and Whitney, D. L.: Low-temperature thermochronologic signature of range-divide migration and breaching in the North Cascades, Lithosphere, 6, 473–482, https://doi.org/10.1130/L382.1, 2014.

Simpson, G.: Role of river incision in enhancing deformation, Geology, 32, 341–344, https://doi.org/10.1130/G20190.2, 2004.

Stewart, R. J., Hallet, B., Zeitler, P. K., Malloy, M. A., Allen, C. M., A., and Trippett, D.: Brahmaputra sediment flux dominated by highly localized rapid erosion from the easternmost Himalaya, Geology, 36, 711–714, https://doi.org/10.1130/G24890A.1, 2008.

Thieulot, C., Fullsack, P., and Braun, J.: Adaptive octree-based finite element analysis of two- and three-dimensional indentation problems, J. Geophys. Res.-Solid, 113, B12207, https://doi.org/10.1029/2008JB005591, 2008.

Vogt, K., Willingshofer, E., Matenco, L., Sokoutis, D., Gerya, T., and Cloetingh, S.: The role of lateral strength contrasts in orogenesis: A 2D numerical study, Tectonophysics, https://doi.org/10.1016/j.tecto.2017.08.010, in press, 2017.

Wang, P., Scherler, D., Liu-Zeng, J., Mey, J., Avouac, J.-P., Zhang, Y., and Shi, D.: Tectonic control of Yarlung Tsangpo Gorge revealed by a buried canyon in Southern Tibet, Science, 346, 978–981, https://doi.org/10.1126/science.1259041, 2014.

Whipp, D. M., Ehlers, T. A. E., Braun, J., and Spath, C. D.: Effects of exhumation kinematics and topographic evolution on detrital thermochronometer data, J. Geophys. Res., 114, F04021, https://doi.org/10.1029/2008JF001195, 2009.

Whipp, D. M., Beaumont, C., and Braun, J.: Feeding the "aneurysm": Orogen-parallel mass transport into Nanga Parbat and the western Himalayan syntaxis, J. Geophys. Res.-Solid, 119, 5077–5096, https://doi.org/10.1002/2013JB010929, 2014.

Willett, S. D.: Orogeny and orography: The effects of erosion on the structure of mountain belts, J. Geophys. Res.-Solid, 104, 28957–28981, https://doi.org/10.1029/1999JB900248, 1999.

Willingshofer, E. and Sokoutis, D.: Decoupling along plate boundaries: Key variable controlling the mode of deformation and the geometry of collisional mountain belts, Geology, 37, 39–42, https://doi.org/10.1130/G25321A.1, 2009.

Willingshofer, E., Sokoutis, D., Luth, S. W., Beekman, F., and Cloetingh, S.: Subduction and deformation of the continental lithosphere in response to plate and crust-mantle coupling, Geology, 41, 1239–1242, https://doi.org/10.1130/G34815.1, 2013.

Winslow, D. M., Zeitler, P. K., Chamberlain, C. P., and Williams, I. S.: Geochronologic constraints on syntaxial development in the Nanga Parbat region, Pakistan, Tectonics, 15, 1292–1308, https://doi.org/10.1029/96TC00032, 1996.

Zeitler, P. K., Chamberlain, C. P., and Smith, H. A.: Synchronous anatexis, metamorphism, and rapid denudation at Nanga Parbat (Pakistan Himalaya), Geology, 21, 347–350, https://doi.org/10.1130/0091-7613(1993)021<0347:SAMARD>2.3.CO;2, 1993.

Zeitler, P. K., Meltzer, A. S., Koons, P. O., Craw, D., Hallet, B., Chamberlain, C. P., Kidd, W. S. F., Park, S. K., Seeber, L., and Bishop, M.: Erosion, Himalayan geodynamics, and the geomorphology of metamorphism, GSA Today, 11, 4–9, 2001.

Zeitler, P. K., Meltzer, A. S., Brown, L., Kidd, W. S., Lim, C., and Enkelmann, E.: Tectonics and topographic evolution of Namche Barwa and the easternmost Lhasa block, Tibet, in: Toward an Improved Understanding of Uplift Mechanisms and the Elevation History of the Tibetan Plateau, vol. 507 of GSA Special Papers, edited by: Nie, J., Horton, B. K., and Hoke, G. D., Geological Society of America, Boulder, CO, https://doi.org/10.1130/2014.2507(02), 2014.

4 Response of a Rheologically Stratified Lithosphere to Subduction of an Indenter-Shaped Plate: Insights Into Localized Exhumation at Orogen Syntaxes

4.1 Declaration on Contributions to Joint Work

The contents of this chapter are published and freely available. The full citation is:

> A. Koptev, T. A. Ehlers, M. Nettesheim, and D. M. Whipp (2019). "Response of a Rheologically Stratified Lithosphere to Subduction of an Indenter-Shaped Plate: Insights Into Localized Exhumation at Orogen Syntaxes". *Tectonics* 38.6, pp. 1908–1930. DOI: `10.1029/2018TC005455`

Four authors contributed to this joint work: Alexander Koptev (AK), Todd A. Ehlers (TE), Matthias Nettesheim (MN), and David M. Whipp (DW). The initial research questions were developed by TE, who then acquired funding for the project. Initial hypotheses were developed by AK with contributions form TE and MN. Modeling was performed by AK with support from MN and derived from previous work by MN. Analysis, interpretation and manuscript preparation were done mainly by AK, with regular discussions with TE and MN. In the final stage, all co-authors contributed comments and suggestion to the manuscript. During the publication process, the manuscript was further improved in response to comments by three anonymous reviewers, Anne Replumaz, and Associate Editor Ernst Willingshofer.

Author	**Position**	**Scientific ideas**	**Data generation**	**Analysis and Interpretation**	**Paper writing**
AK	[1]	50%	70%	50%	60%
TE	[2]	30%	0%	30%	20%
MN	[3]	15%	30%	20%	15%
DW	[4]	5%	0%	0%	5%

Table 4.1: Author contributions to *Response of a Rheologically Stratified Lithosphere to Subduction of an Indenter-Shaped Plate: Insights Into Localized Exhumation at Orogen Syntaxes*, published in *Tectonics*, 38, 2019

The supporting information to this publication can be found in appendix C (page 109)

4.2 Published Manuscript

AGU100 ADVANCING EARTH AND SPACE SCIENCE

Tectonics

RESEARCH ARTICLE
10.1029/2018TC005455

Key Points:
- Rheological structure of the overriding plate controls resulting deformation pattern
- Isolated indenter-centered rock uplift develops in a weakly coupled plate only
- Narrow indenter excites localized rock exhumation as observed in orogen syntaxes

Supporting Information:
- Supporting Information S1

Correspondence to:
A. Koptev,
alexander.koptev@ifg.uni-tuebingen.de

Citation:
Koptev, A., Ehlers, T. A., Nettesheim, M., & Whipp, D. M. (2019). Response of a rheologically stratified lithosphere to subduction of an indenter-shaped plate: Insights into localized exhumation at orogen syntaxes. *Tectonics*, *38*, 1908–1930. https://doi.org/10.1029/2018TC005455

Received 14 DEC 2018
Accepted 15 MAY 2019
Accepted article online 21 MAY 2019
Published online 18 JUN 2019

Response of a Rheologically Stratified Lithosphere to Subduction of an Indenter-Shaped Plate: Insights Into Localized Exhumation at Orogen Syntaxes

Alexander Koptev[1], **Todd A. Ehlers**[1], **Matthias Nettesheim**[1], **and David M. Whipp**[2]

[1]Department of Geosciences, University of Tübingen, Tübingen, Germany, [2]Department of Geosciences and Geography, University of Helsinki, Helsinki, Finland

Abstract This study investigates the influence of the 3-D geometry of a down-going plate, the rheological structure of the upper plate, and the migration of the overriding plate toward the trench in relation to the overall subduction velocity on the exhumation pattern in orogen syntaxes. Using a thermomechanical numerical code (DOUAR), we analyze the strain localization, rock uplift, and exhumation response of a rheologically stratified continental lithosphere to subduction of a convex-upward-shaped indenter. The models consider three thermorheological lithospheric profiles that determine the degree of mechanical coupling between the upper crust and lithospheric mantle. These models include a strong, cratonic lithosphere; a weaker, younger (and hotter) continental plate; and an intermediate case. The strongly coupled case predicts a localization of high rock uplift rates along narrow linear bands crossing the entire model domain parallel to the trench. In contrast, in a weakly coupled lithosphere, rock uplift is concentrated within a curved ellipse region of anomalously high exhumation rates located above the indenter apex. The aspect ratio of the localized area of rapid rock uplift is controlled by the initial width of the rigid indenter and the relationship between boundary velocities. In particular, the combination of little or no upper plate migration with a narrow indenter causes a nearly circular region (~100-km diameter) of rapid exhumation that resembles the pattern of thermochronometer ages observed in orogen syntaxes such as the Southeast Alaska and the Olympic Mountains of the Cascadia subduction zone (western USA).

1. Introduction

The transition between adjacent subduction segments at plate corners represents an important type of tectonic setting (Figure 1). Recent observational (Hayes et al., 2012) and modeling studies (Mahadevan et al., 2010) show that 3-D bending at plate corner locations (Figures 1b–1d) required by subduction on a spherical Earth leads to geometric stiffening at the ends of subduction arcs producing a convex-upward-shaped bump of the subducting plate referred to hereafter as a “flexural bulge” or “indenter” (Figure 1a). The relatively narrow regions above these convex bends—termed “orogen syntaxes” or “syntaxial orogens” (cf. Bendick & Ehlers, 2014)—separate the longer straight plate boundaries.

Orogen syntaxes have attracted attention over recent years because they contain some of the most rapid rock exhumation rates (>5 mm/year) observed. This extreme exhumation is characterized by a circular (~100+-km diameter) zone of rock uplift (also dubbed a “bull's-eye” pattern, Bendick & Ehlers, 2014). Classical examples of strong bull's-eye spatial localization of rock uplift include regions such as the Southeast Alaska (Enkelmann et al., 2010; Falkowski et al., 2014; Koons et al., 2010), the Olympic Mountains in Washington State, USA (Brandon et al., 1998; Michel et al., 2018; Pazzaglia & Brandon, 2001), and Nanga Parbat and Namche Barwa in the Himalayan syntaxes (Crowley et al., 2009; Enkelmann et al., 2011; Lang et al., 2016; Zeitler et al., 2001, 2014).

Koons et al. (2002, 2013) showed that locally enhanced erosion rates can lead to focused exhumation through significantly reduced crustal strength caused by thermal weakening (the model dubbed a “tectonic aneurysm”—see also Zeitler et al., 2001, 2014). Their approach, however, does not account for the internal 3-D geometry of subducting plates while approximating the subsurface to be of homogeneous composition with straight-lined boundaries. Such geometric simplification is permissible for many parts of subduction zones but at the transition between adjacent plate boundary segments the impact of the 3-D configuration of the subducting lithosphere may be important. To investigate these 3-D geometric complexities Bendick and Ehlers (2014) applied a numerical model focused on the variations in shape of the 3-D down-going

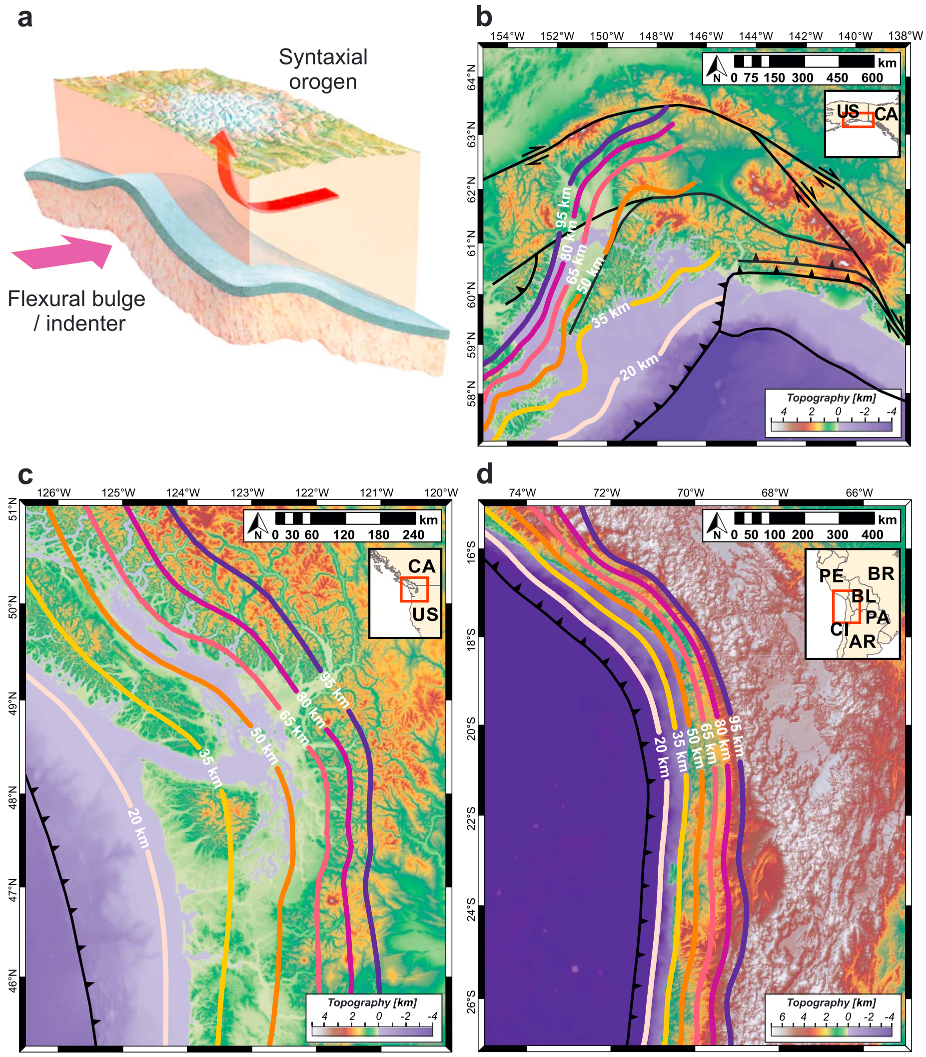

Figure 1. (a) Schematic representation for the flexural bulge of the subducting slab at the plate corner and syntaxial orogen above (modified from Bendick & Ehlers, 2014). (b–d) Observed subducting plate geometry in the plate corner locations (slab contours from the global 3-D model of subduction zones geometry by Hayes et al., 2012): (b) the Southeast Alaska (the major faults after Koons et al., 2010), (c) the Olympic Mountains of the Cascadia subduction zone, and (d) the South American subduction zone. The South American subduction zone is characterized by a moderate slab curvature comparing to the Southeast Alaska and the Cascadia subduction zone.

plate and its role in overriding plate deformation and rock exhumation. They found that rapid vertical uplift and exhumation can be localized into a bull's-eye region in response to a flexural bulge on the down-going plate. However, the rheological structure adopted in their work was simplified and allowed only for purely viscous deformation. Their approach also excluded the effects of brittle strain localization in the overriding plate that might be critical for the resulting strain and topographic evolution of the region (see, e.g., Vogt et al., 2017, 2018).

In recent decades, advances have been made to better understand the role of rheological stratification of the lithosphere (Burov, 2011; Ranalli & Murphy, 1987) on deformation and rock exhumation in convergent orogens. This has been done by means of analogue (e.g., Willingshofer et al., 2013) and numerical modeling (e.g., Burov et al., 2001; Erdos et al., 2014; Jammes & Huismans, 2012; Vogt et al., 2017, 2018). In view of these advances, the subduction of a down-going plate with a convex-upward-shaped indenter (as investigated by Bendick & Ehlers, 2014) has been further explored (Nettesheim et al., 2018) with a series of numerical thermomechanical experiments assuming a viscoplastic rheology and stratification of the overriding continental lithosphere. In these models, the highest rock uplift rates are localized within elongated areas above both the indenter bulge and straight segments of the subducting plate and thus not reproducing the observed concentric bull's-eye pattern of vertical uplift as described in Bendick and Ehlers (2014) and observed in some syntaxial orogens. Here we build upon the work of Nettesheim et al. (2018) with particular focus on variations in the style of deformation and associated rock uplift in syntaxial orogens as a function of the degree of rheological (de)coupling of the upper plate (see, e.g., Brun, 2002; Koptev et al., 2018; Tetreault & Buiter, 2018). In contrast to the work of Nettesheim et al. (2018) who focused on the effect of variable velocity boundary conditions and erosion mechanisms, we investigate the effect of different thermorheological lithospheric profiles ranging from mechanically decoupled to completely coupled by varying the lithology of the lower crust and the initial crustal geotherm in order to identify the role of rheological structure on the spatial localization of rock uplift. Similar to Nettesheim et al. (2018), we have also tested different contributions in the total shortening by subduction of the down-going plate and migration of the overriding plate toward the trench (Capitanio et al., 2010; Heuret & Lallemand, 2005; Schellart et al., 2007) through the introduction of variable rates of upper plate advance (V_{Adv}) that refers to the relation between boundary velocities applied at the opposite sides of the model. Finally, given the large uncertainty in seismic images of subducting plate geometries, various configurations of the flexural bulge geometry are also investigated here.

In this study, we compare our modeling results to natural settings; however, it is beyond the scope of this study to reproduce the detailed structure of observed deformation and rock uplift in any particular orogen syntax. At the current stage, this is not feasible due to the lack of available information on the lateral heterogeneity of the overriding lithosphere as well as indenter geometry and properties. In contrast, our main objective here is to quantify the general consequences of subduction of a flexural bulge underneath rheologically stratified continental lithosphere. For this purpose, we first investigate the influence of overriding lithosphere rheological profiles (strength envelopes) on the resulting pattern of strain localization and associated rock uplift. We follow this by a comparison of our model inferences with observed exhumation rates in the Southeast Alaska, the Olympic Mountains of the Cascadia subduction zone (western USA), and the South American subduction zone.

2. Methods

2.1. Model Design

The numerical simulations presented here were conducted using DOUAR (Braun et al., 2008; Thieulot et al., 2008), a three-dimensional finite element code designed to solve the Stokes and heat transfer equations. See the numerical methods section in supporting information for governing equations and material properties used in the model, and additional details. We also refer readers to Braun and Yamato (2010), Whipp et al. (2014) and Nettesheim et al. (2018) for further information.

The model setup encompasses an area of horizontal dimensions 800 km × 800 km with a thickness of 80 km (Figure 2a) using a 3-D box with 128 × 128 × 52 elements, resulting in a grid spacing of 6.25 and 1.54 km in horizontal and vertical directions, respectively.

Our model setup closely resembles that of Nettesheim et al. (2018): The internal model structure corresponds to a simplified two-block system that can be applied to both continental and oceanic collisional settings: a rigid wedge-shaped subducting plate with a central convex-upward-shaped bulge and a rheologically layered overriding lithosphere (Figure 2a). The background sections of the subducting plate have a minimum depth of 50 km at $y = 0$ km that gradually increases up to the slab termination at $y = 320$ km. In contrast, the indenter geometry is characterized by a 30-km minimum depth, termination at $y = 400$ km and lateral (along-strike) width varying from 450 to 150 km. The indenter width in the x direction is one of the variables explored in our study (see Figure 2b3 and Table 1). The overriding plate corresponds to a laterally homogeneous three-layered continental lithosphere composed of a 40-km-thick mantle overlain by the continental crust equally divided into upper (20 km) and lower crust (20 km).

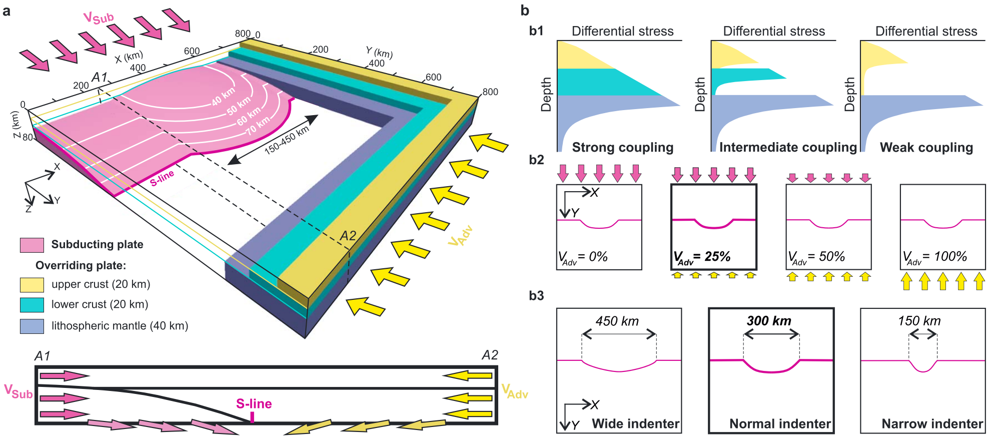

Figure 2. (a) Three- dimensionalview of modeling domain: a rheologically layered overriding lithosphere and a rigid subducting plate containing a central convex-upward-shaped bulge (indenter) and a background (i.e., nonindenter) portion. S line refers to intersection of the down-going plate with the model bottom plane; violet and yellow arrows show subduction (V_{Sub}) and upper plate advance (V_{Adv}) components of the shortening, respectively. Schematic vertical cross section: Horizontal velocities are directed along y axis with V_{Sub} and V_{Adv} to the left and right of the S line, respectively; vertical material outflux through the lower boundary is linearly increased from the model sides to the S line. (b) Key variable parameters: (b1) rheological structure of the overriding plate (from left to right): strong, intermediate, and weak coupling between the upper crust and lithospheric mantle; (b2) velocity boundary conditions (from left to right): 0%, 25%, 50%, and 100% of the upper plate advance in the total shortening rate; and (b3) width of the indenter (from left to right): 450, 300, and 150 km. The reference values of upper plate advance and indenter width (25% and 300 km, respectively) are highlighted by thick-line slots on b2 and b3.

Table 1
Experiments: Key Variable Parameters and Results

N	Lower crust composition[a]	Initial geotherm[b]	Rheological coupling[c]	Upper plate advance (V_{Adv})[d]	Indenter width (km)	Resulting aspect ratio of the isolated zone of rapid exhumation (if applicable[e])	Figures
	Model parameters						
	Properties of the overriding lithosphere						
1	mafic	“cold”	strong	25%	300	—	3, 6a, and S1
2	mafic	“normal”	intermediate	25%	300	—	4, 6b, andS2
3	felsic	“normal”	weak	25%	300	~1:4	5, 6c, S3, and 8b
4	felsic	“normal”	weak	0%	300	~1:3	7a, S4a, and S5
5	felsic	“normal”	weak	50%	300	—	7b, S4b, and S6
6	felsic	“normal”	weak	100%	300	—	7c, S4c, and S7
7	mafic	“cold”	strong	25%	150	—	S8a
8	mafic	“normal”	intermediate	25%	150	—	S8b
9	felsic	“normal”	weak	25%	150	~1:2	8c and S8c
10	felsic	“normal”	weak	25%	450	~1:6	8a
11	felsic	“normal”	weak	0%	150	~1:1.5	9a, 10a, S9 and S10, and S11c
12	felsic	“normal”	weak	50%	150	—	9b
13	felsic	“normal”	weak	100%	150	—	9c
14	mafic	“cold”	strong	0%	150	—	S11a
15	mafic	“normal”	intermediate	0%	150	—	S11b

[a] Mafic and felsic lower crust compositions refer to wet granite and dry diabase flow laws, respectively. [b] “Normal” initial geotherm is defined with taking into account crustal heat generation (see Table S1) whereas “cold” one corresponds to the models without radiogenic heat production. [c] Rheological coupling of the overriding plate is controlled by the lower crust composition and initial geotherm (see explanation in the section 2.2). [d] Upper plate advance (V_{Adv}) represents the contribution of the boundary velocity applied at the right side of the model box in the total shortening rate (see Figure 2a and explanation in the section 2.1). [e] Aspect ratio is indicated only for the cases when high exhumation rates are concentrated within the single curved ellipse region above the indenter bulge.

To identify the effect of a subducting indenter on the deformation pattern in the rheologically stratified upper plate, we follow the established approach of numerical (e.g., Cailleau & Oncken, 2008; Iwamori et al., 2007; Ruh et al., 2016; Wada et al., 2008) and analog (e.g., Buttles & Olson, 1998; Kincaid & Griffiths, 2003) modeling. We intentionally simplify our model by prescribing that the down-going plate (including indenter bulge) remains a rigid and undeformed mass and keeps its initial configuration through the entire model history. This approach precludes mass transfer between the subducting and overriding plates to ensure mass balance at every time step. While the rheology of the down-going plate is purely viscous at 10^{25} Pa·s, we additionally include a thin (3–4 km thick) and weak (a constant viscosity of 10^{19} Pa·s) layer on top in order to reduce its internal deformation as well (e.g., Willingshofer & Sokoutis, 2009). Despite this simplification, we expect general insights into the dominant controls on the tectonics of the upper plate to remain valid for the uppermost segment of the lithosphere-mantle system (0–80 km), given that most of internal slab deformation usually occurs at much greater depths (see, e.g., Gerya et al., 2004).

The upper plate (see Table S1) is modeled as a rheologically stratified continental lithosphere with an alternation of brittle and ductile layers. The viscous rheology of the felsic upper crust is described by a wet granite flow law (Carter & Tsenn, 1987) in all experiments. For the lower crust, we consider two different ductile flow laws—wet granite flow law (felsic lower crust) or dry diabase flow law (mafic lower crust)—in different experiments (see Table S1) in order to explore different levels of mechanical (de)coupling between the upper crust and the mantle lithosphere (e.g., Brun, 2002; Brun et al., 2018; Gueydan et al., 2008; Koptev et al., 2015, 2016; Koptev et al., 2018). The viscous rheology of the mantle is controlled by the flow law that conforms to the known deformation of olivine aggregates (Hirth & Kohlstedt, 2003; Jadamec & Billen, 2012). Brittle behavior is modeled by a Mohr-Coulomb failure criterion. In the upper and lower crust, this includes a linear reduction in the friction angle with increasing accumulated strain (linear strain softening; see, e.g., Huismans & Beaumont, 2002). For the lithospheric mantle, however, the coefficient of internal friction of the Mohr-Coulomb failure criterion remains strain independent (Table S1).

At the left (y = 0 km) and right (y = 800 km) sides of the model box, we apply kinematic boundary conditions of uniform and time-independent boundary velocities parallel to the y axis that define the material influx resulting in lateral shortening accommodated by subduction (V_{Sub}) or/and migration of the overriding plate toward the subducting plate referred below as "upper plate advance" (V_{Adv}), respectively (Figure 2a). The velocity boundary condition at the front (x = 0) and back (x = 800 km) sides are free slip. Conservation of mass is ensured by material outflux through the lower (z = 80 km) boundary. The upper surface remains flat from erosion that instantly removes all material uplifted above the initial surface elevation so that modeled near-surface vertical (rock uplift) velocities are equal to rock exhumation rates (England & Molnar, 1990). The relation between boundary velocities applied at the left (V_{Sub}) and right (V_{Adv}) model sides represents a variable parameter of this study (see section 2.2 and Table 1). Total shortening rate ($V_{\mathrm{Tot}} = V_{\mathrm{Sub}} + V_{\mathrm{Adv}}$), however, remains the same (V_{Tot} = 30 mm/year) in all experiments.

Initial "normal" nonlinear steady state geotherm is defined by boundary temperatures of 0 °C and 930 °C at the top (z = 0 km) and the bottom (z = 80 km) while taking into account heat production in the upper and lower crust (see Table S1 for parameters). This setup results in a geothermal gradient at the model surface of 27 °C/km, which decreases to 13 °C/km at the boundary between upper and lower crust and finally to 8 °C/km from the Moho downward. In contrast, models with no radiogenic heat generation in the crust result in linear temperature distribution with the constant geothermal gradient of 11.6 °C/km referred here as a "cold" initial geotherm (see Table S1). We apply insulating boundary conditions (zero conductive heat flux) for all vertical sides.

Predicted cooling ages are calculated using the time-temperature history of tracer particles within the model domain (see Braun, 2003; Ehlers, 2005; Whipp et al., 2009, for underlying principles and Nettesheim et al., 2018, for this specific implementation). We calculate apatite fission track (AFT) ages (referred below as "AFT-predicted ages") that indicate the time since an apatite grain has cooled below ~90–120 °C. We focus on this thermochronometer system because AFT measurements have been applied widely to quantify exhumation rates in the orogens we compare our model results to.

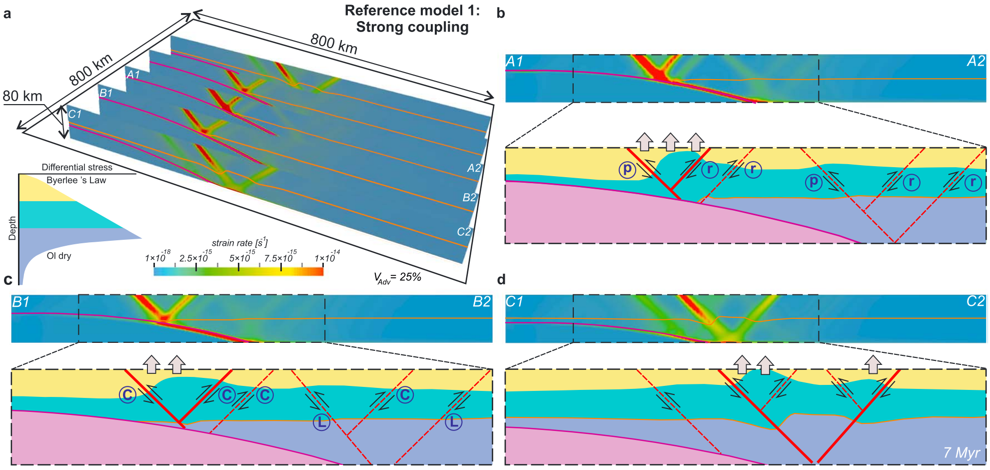

Figure 3. Reference experiment for strong rheological coupling of the overriding lithosphere (model **1**) after 7-Myr modeling time. (a) Three-dimensional view of the second invariant of strain rate tensor. (b–d) Vertical cross sections parallel to *y* axis with schematic interpretations for their central segments. The layer colors are as in Figure 2. The violet and orange lines refers to subducting plate and Moho interfaces, respectively. The red lines on the interpretation profiles represent the shear zones—the planes of stronger (solid lines) or weaker (dashed lines) localized high strain rate intensity ($>8 \times 10^{-15}$ 1/s and $>3\text{–}6 \times 10^{-15}$ 1/s, respectively). Gray arrows indicate high exhumation rates (>8 mm/year, see Figure 6). Proshear and retroshear zones are labeled by "**p**" and "**r**," and crustal- and lithospheric-scale shear zones by "**C**" and "**L**." The results of the presented experiments are symmetrical with respect to the central vertical cross section A1-A2.

2.2. Modeling Procedure and Free Parameters

In total, we performed 15 different experiments by varying three controlling parameters (Table 1): (1) rheological structure of the overriding continental lithosphere, (2) contribution of upper plate advance (V_{Adv}) in the total shortening rate (V_{Tot}), and (3) width of the indenter in the *x* direction.

We compare our simulations with three reference experiments (models **1–3**; Figures 3–6 and S1–S3 and Table 1) characterized by different rheological profiles (Figure 2b1) ranging from strongly coupled (model **1**) to weakly coupled (model **3**) and including an intermediate case (model **2**). The degree of mechanical coupling of the overriding plate is controlled by the lithology of the lower crust and by the initial crustal

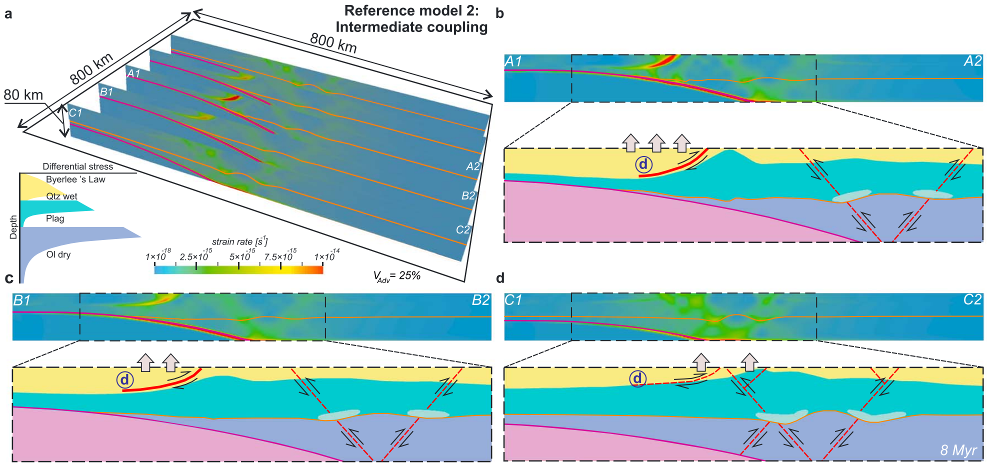

Figure 4. Reference experiment for intermediate rheological coupling of the overriding lithosphere (model **2**) after 8-Myr modeling time. Light aqua areas refer to distributed (nonlocalized) ductile strain in the lowermost crust. Deformation localizes along both the shallowly dipping (≤30°) retrodecollement (labeled by "**d**") and steeply dipping (~60°) shear zones.

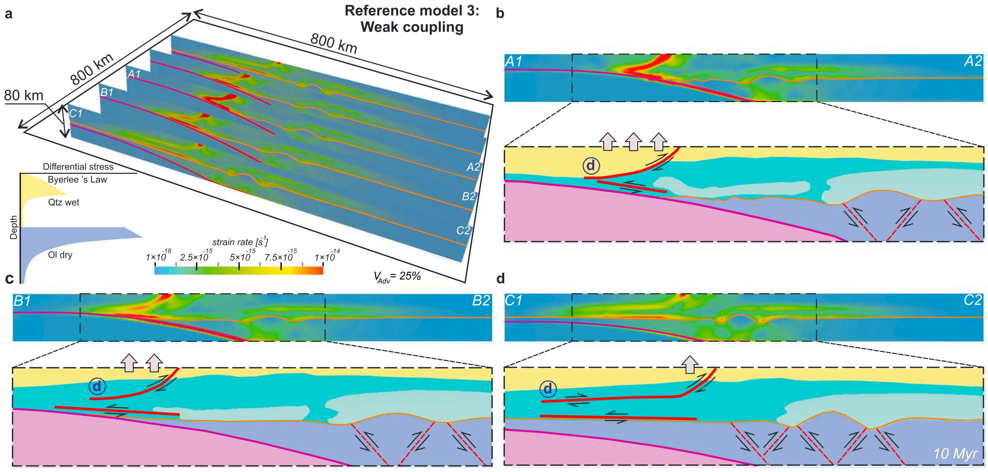

Figure 5. Reference experiment for weak rheological coupling of the overriding lithosphere (model **3**) after 10-Myr modeling time. Most of deformation concentrates in the shallow retrodipping decollement (labeled by "**d**") rooting into an underlying ductile lower crust.

geotherm. The mafic lower crustal composition (corresponding to the dry diabase flow law) combined with a relatively "cold" geotherm (465 °C at the Moho, resulting from no crustal heat production) leads to a very thick brittle part of the lower crust that almost completely couples the strain of the upper crust and lithospheric mantle (strong rheological coupling; model **1**). In contrast, a felsic lower crust (wet granite flow law) and "normal" crustal geotherm (610 °C at the Moho due to radiogenic heat generation in the crust) results in a completely ductile lower crust playing the role of a weak layer that decouples the brittle uppermost mantle and upper crust (weak rheological coupling; model **3**). The combination of a mafic lower crust and "normal" geotherm corresponds to the intermediate case (intermediate rheological coupling; model **2**) where the lower crust contains a brittle layer (in contrast to weakly coupled model **3**), which is thinner compared to model **1**. In all reference experiments (models **1**–**3**), we use following values for two remaining controlling parameters: 25% of upper plate advance (i.e., $V_{\mathrm{Sub}} = 22.5$ mm/year and $V_{\mathrm{Adv}} = 7.5$ mm/year) and a 300-km indenter width (see Figure 2b).

In the case of a weakly coupled upper plate (see Table 1), we tested the impact of the partitioning of velocity boundary conditions (models **4**–**6**; Figures 7 and S4–S7): V_{Adv} varied from 0% ($V_{\mathrm{Sub}} = 30.0$ mm/year and $V_{\mathrm{Adv}} = 0.0$ mm/year) to 50% ($V_{\mathrm{Sub}} = 15.0$ mm/year and $V_{\mathrm{Adv}} = 15.0$ mm/year) and also to 100% ($V_{\mathrm{Sub}} = 0.0$ mm/year and $V_{\mathrm{Adv}} = 30.0$ mm/year). Furthermore, we used different widths of the flexural bulge (Figures 8 and S8) for all coupling cases, including narrower (150 km wide, models **7**–**9**) and a wider indenter (450 km wide, model **10**). Finally, we investigate the effect of a narrow indenter width (150 km) combined with different values for upper plate advance (0%, 50%, and 100%) in models **11**–**13** (Figure 9), as well as different degrees of coupling under no upper plate advance ($V_{\mathrm{Adv}} = 0\%$) in models **14**–**15** (Figure S11).

3. Results

3.1. Effect of Rheological Structure of the Overriding Continental Lithosphere: Reference Experiments (Models 1–3)

3.1.1. Strong Rheological Coupling (Model 1)

The first reference experiment (model **1**; Figures 3, 6a, and S1) is characterized by strong rheological coupling of the overriding plate and by the reference boundary velocities (25% of upper plate advance) and indenter configuration (300 km wide in x direction).

A vertical cross section in the y direction through the segment corresponding to a background subducting plate (i.e., nonindenter portion outside of the central bulge; section C1-C2 shown on Figure 3d) indicates two oppositely dipping thrust-sense shear zones (localized strain rate $>8 \times 10^{-15}$ 1/s) rooting at an angle of ~60° next to the intersection of the subducting plate at the bottom of the model domain, referred to

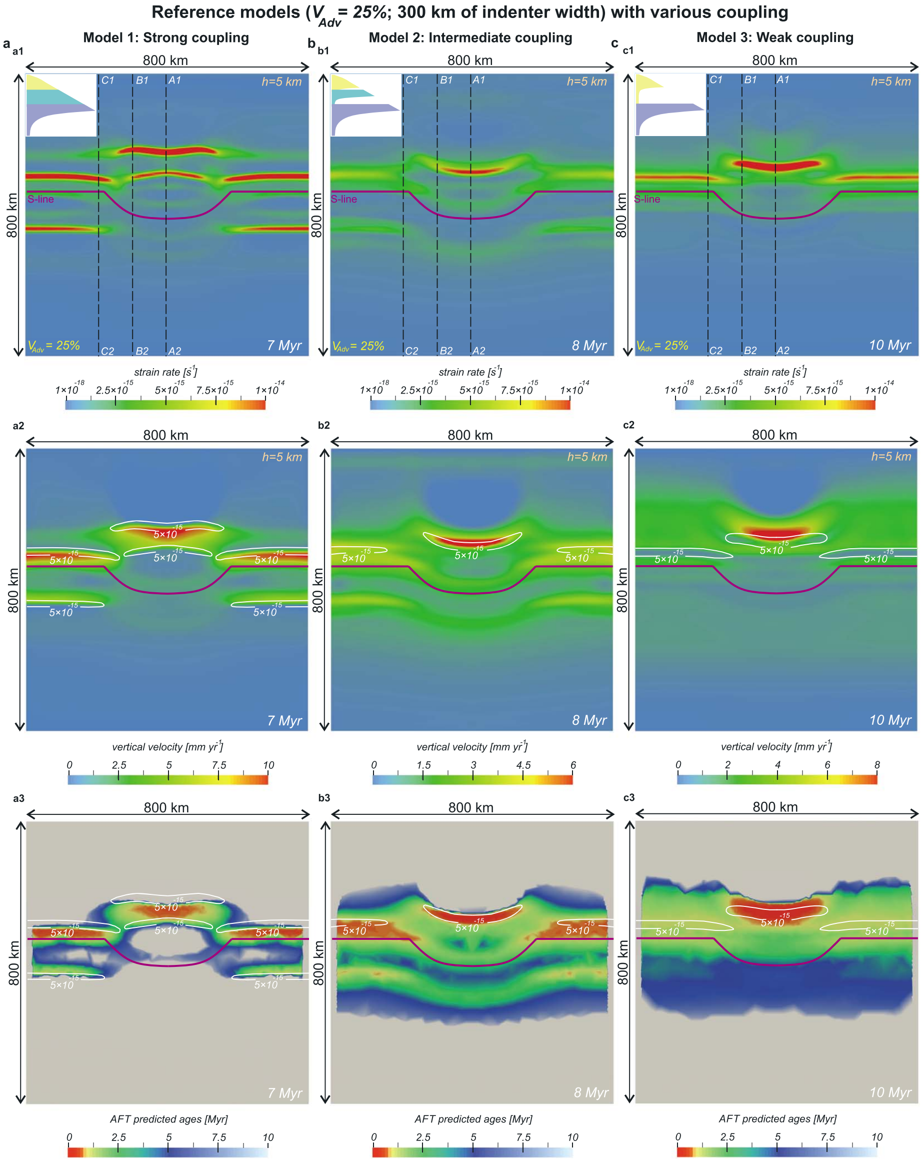

Figure 6. Plan views showing second invariant of computed strain rate and modeled vertical velocity (both at the 5-km depth; top and middle row, respectively) as well as predicted apatite fission track (AFT) ages (at the surface; bottom row) for the reference experiments characterized by different degrees of upper plate mechanical coupling: (a) strong coupling (model **1**), (b) intermediate coupling (model **2**), and (c) weak coupling (model **3**). White isolines in the middle and bottom rows outline the areas of the highest strain rate ($>5 \times 10^{-15}$ 1/s, see top row). Dashed lines indicate locations of the vertical cross sections shown on Figures 3–5. The weak rheological coupling (c) favors an isolated high (>8 mm/year) rock uplift developed over the central convex-upward indenter without any particular localization above background down-going plate.

here as the S line (see Figure 2). Two additional V-shaped wedges originate at these proshear and retroshear bands at the vertical level close to the Moho (Figures 3d and S1c, profile B1-B2). These shear bands create pop-up structures that are characterized by strong upward deflection of the upper-lower crust boundary (see interpretation profile on Figure 3d) and corresponding localized surface uplift (gray arrows on Figure 3d) in two narrow bands parallel to the plate interface (see plan view of rock uplift rate on Figure 6, slice

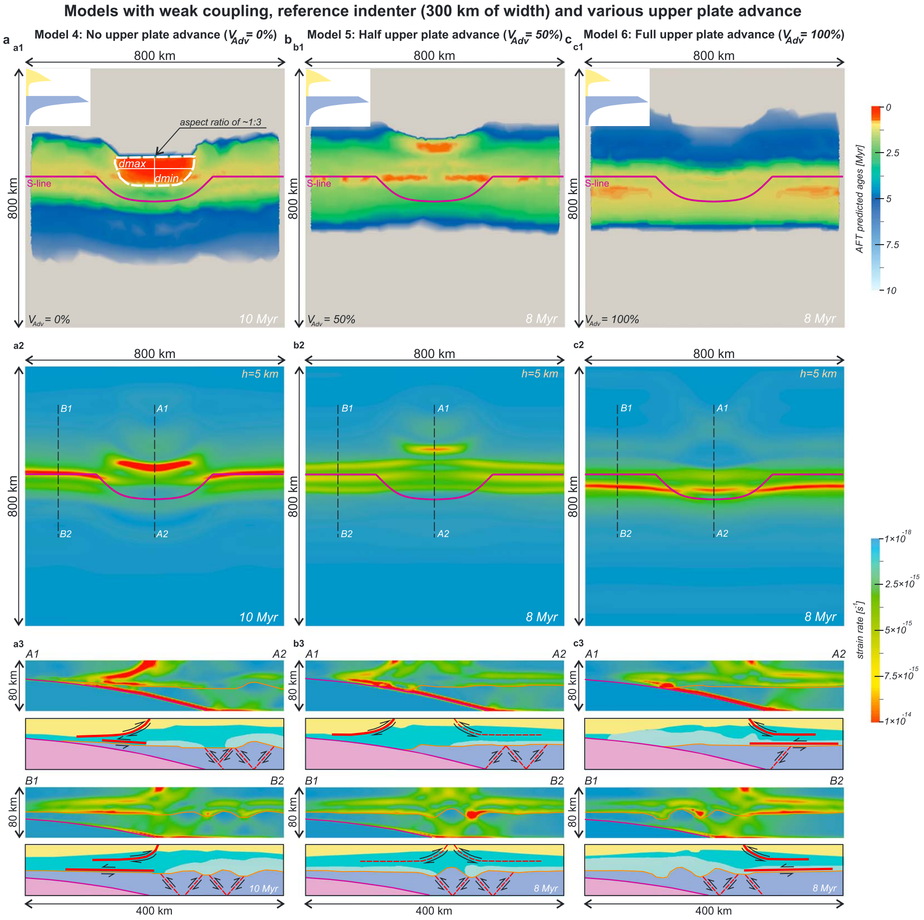

Figure 7. Plan views showing predicted apatite fission track (AFT) ages (top row) and strain rate (middle row), and corresponding vertical cross sections (bottom third) for the experiments characterized by weak rheological coupling of the overriding plate, reference indenter width (300 km) and different velocity boundary conditions: (a) no upper plate advance model **4** (V_{Adv} = 0%), (b) half upper plate advance model **5** (V_{Adv} = 50%), and (c) full upper plate advance model **6** (V_{Adv} = 100%). White dashed line on a1 indicates ellipsoidal zone above the indenter apex characterized by the youngest predicted (<1 Myr) AFT ages corresponding to localized rapid rock exhumation. Maximum and minimum diameter of this area are labeled by “dmax” and “dmin”; their relation defines the aspect ratio (1:3 in this case) for the corresponding curved ellipse region (see also Figures 8 and 9).

a2, and predicted AFT ages on Figure 6, slice a3). Along the entire length of the background slab segments (i.e., outside of the central part of the model), both deformation and associated rock uplift are better localized on the proside, while the retroside expression is weaker but still clearly visible in both the second invariant of strain rate tensor and vertical velocity fields (see Figures 3d and 6a).

These lithospheric-scale shear bands (i.e., shear bands cutting the entire model domain from the crust to the lithospheric mantle), however, attenuate toward the indenter in the model center, where deformation is accommodated along two different shear zones that nucleate where the subducting plate interface intersects the overriding plate's Moho (Figures 3b and 3c). As shown in plan view (Figure 6, slice a1), these crustal-scale shear zones (i.e., shear zones limited to the upper and lower crust) are shifted toward the down-going plate where they form an undeformed yet uplifted V-shape wedge directly above the indenter apex. Note that attenuated prolongation of proside shear zone of this wedge into adjacent areas of background slab (Figure 6, slice a1) can also be distinguished on corresponding vertical profiles (Figures 3d and S1c, profile B1-B2) as an additional proshear zone outboard of the principal wedge developed between the lithospheric-scale shear bands.

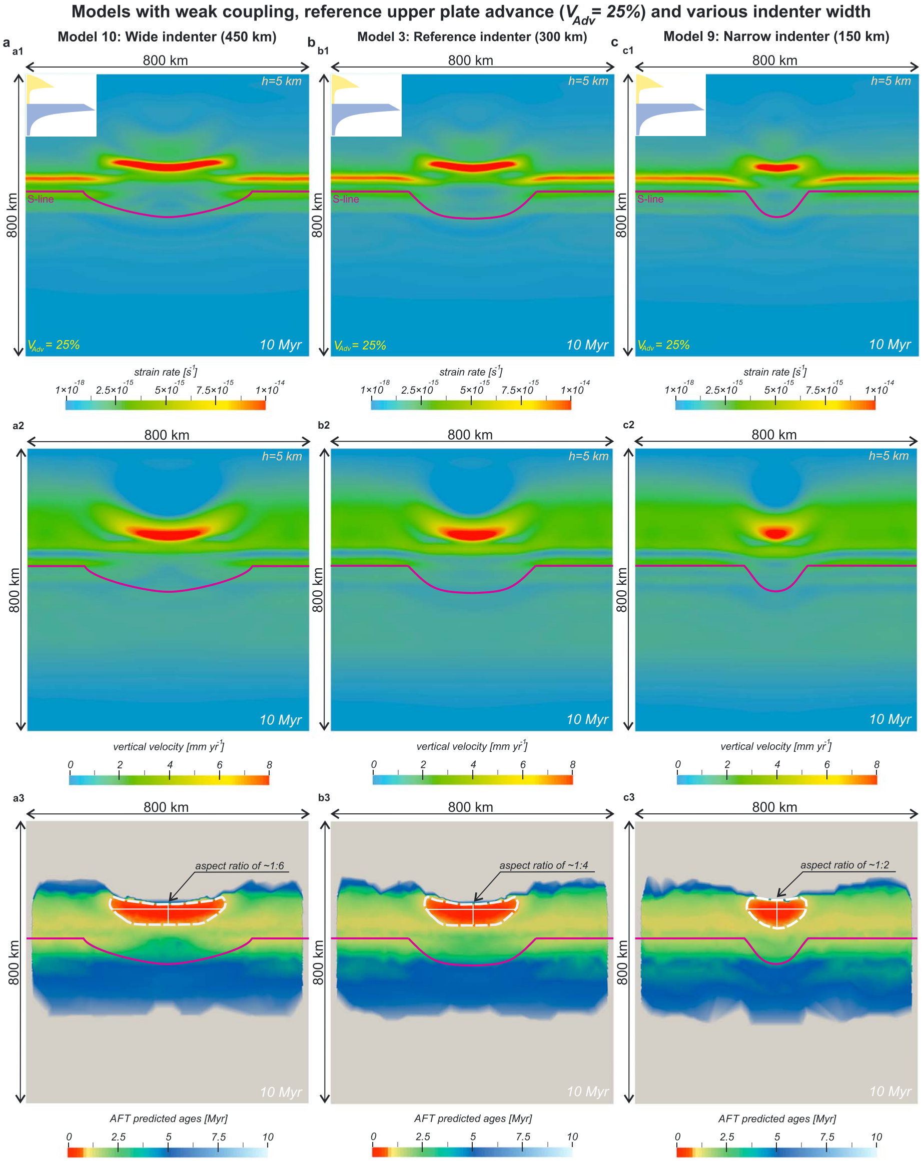

Figure 8. Experiments characterized by weak rheological coupling of overriding plate, reference upper plate advance (V_{Adv} = 25%) and different indenter width: (a) wide indenter model **10** (width of 450 km), (b) reference indenter model **3** (width of 300 km), and (c) narrow indenter model **9** (width of 150 km). Indenter configuration controls a final shape of curved ellipse that bounds area of the youngest (<1 Myr) apatite fission track (AFT) ages.

To summarize, the essential feature of this strongly coupled reference experiment (model **1**) is that uplift is localized within small wedges confined between oppositely dipping shear zones (Figures 3b–3d). This is also reflected at the surface in the narrow (~50–75 km wide) bands of the highest vertical velocities (>8 mm/year) and associated youngest predicted (<1 Myr) AFT ages elongated in the trench-parallel direction (Figure 6, slices a2 and a3). Conforming to the different shear zones, this band is shifted by ~100 km toward the subducting plate above the indenter with respect to adjacent model segments.

AGU 100 ADVANCING EARTH AND SPACE SCIENCE
Tectonics
10.1029/2018TC005455

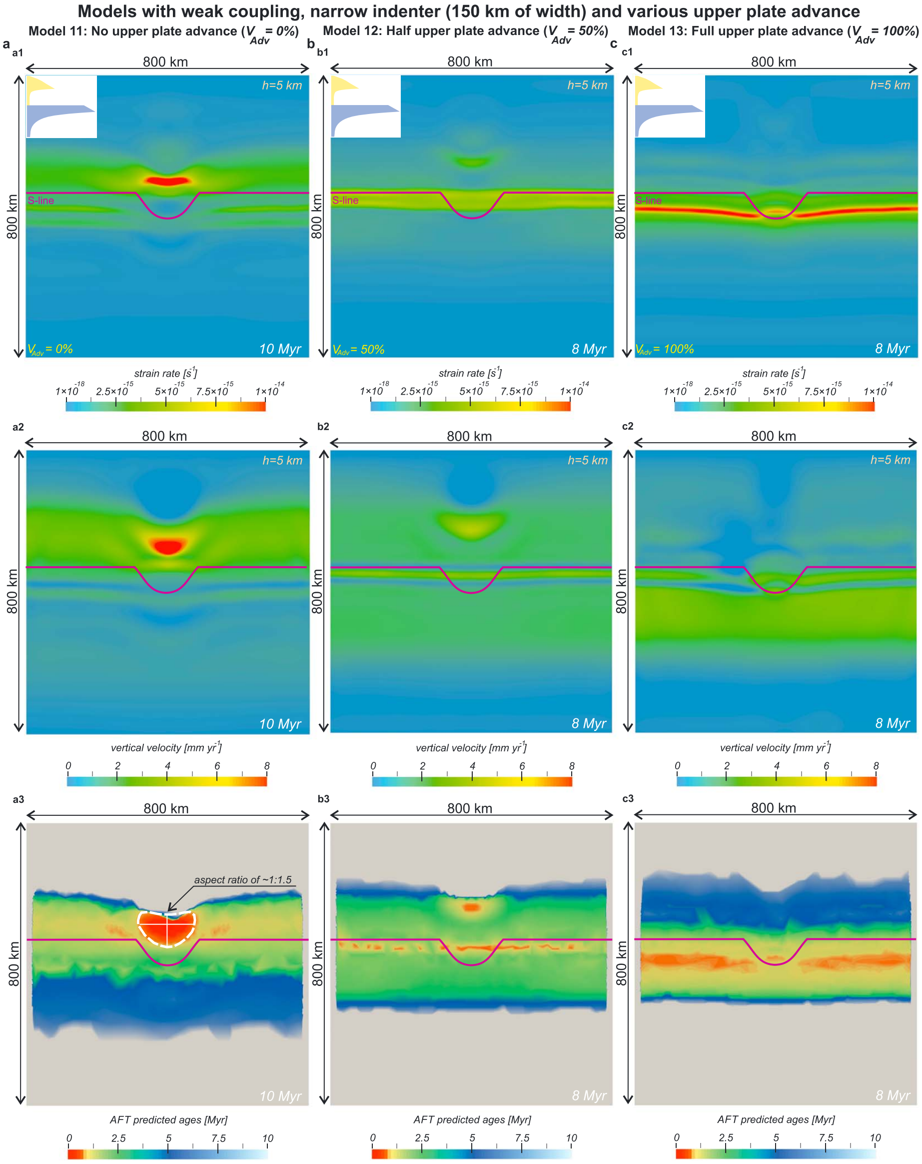

Figure 9. Experiments characterized by weak coupling of upper plate, narrow (150-km-wide) indenter and different velocity boundary conditions: (a) no upper plate advance model **11** ($V_{\mathrm{Adv}} = 0\%$), (b) half upper plate advance model **12** ($V_{\mathrm{Adv}} = 50\%$), and (c) full upper plate advance model **13** ($V_{\mathrm{Adv}} = 100\%$). No upper plate advance contribution ($V_{\mathrm{Adv}} = 0\%$) in the total shortening leads to an quasi-isometric (aspect ratio of 1:1.5) zone of localized exhumation above the indenter apex. AFT = apatite fission track.

3.1.2. Intermediate Rheological Coupling (Model 2)

The second reference experiment with intermediate mechanical coupling in the upper plate (model **2**; Figures 4, 6b, and S2) also includes steeply dipping shear zones crossing almost through the entire model domain and rooting into the S line at an angle of ~60°. However, compared to the previous strongly coupled model **1**, zones of elevated strain rate (3–6 × 10^{-15} 1/s) corresponding to these proshear and retroshear are much broader (tens of kilometers instead of some kilometers). In particular, due to the dominance of the ductile mode of deformation in the lowermost crust, relatively high strain rate intensity in this part of the section could be interpreted as distributed ductile strain rather than as a fragment of continuous steep shear zone crossing through the Moho (see interpretation sections on Figures 4b–4d).

In contrast to the previous experiment (model **1**), most of the deformation here in model **2** is accommodated by a thin low-angle decollement dipping ≤30°. Localized strain rates reach their highest values ($>8 \times 10^{-15}$ 1/s) in the decollement above the indenter (Figure 4b). Toward the background subduction zones, this shallowly dipping structure attenuates (to ~$5–7 \times 10^{-15}$ 1/s) but remains discernible both in plan view and corresponding vertical cross sections (see Figure 6, slice b1, and Figure 4d, and Figure S2c, profile B1-B2, respectively).

In the hanging wall above the background slab, elevated values (>4.5 mm/year) of the rock uplift rate and associated young (<1 Myr) AFT ages are distributed along relatively wide (~150 km) bands parallel to the S line. However, the highest rock uplift rates (>5 mm/year) are concentrated within a narrow zone in the center of the model directly above the indenter (Figure 6, slice b2). Thus, even a small amount of rheological decoupling in the overriding plate (as adopted in model **2**) leads to a large change in the mode of localized uplift such that vertical movements occur in the hanging wall of the shallowly dipping decollements (Figures 4b–4d). This is in contrast to V-shaped wedges localizing vertical motion between steep fault zones that occur in the previous case of a strongly coupled lithosphere (model **1**; Figures 3b–3d).

3.1.3. Weak Rheological Coupling (Model 3)

The response of a weakly coupled overriding continent (model **3**; Figures 5, 6c, and S3) to subduction of the down-going rigid plate is the formation of a basal decollement dipping in retrodirection and rooting into an underlying ductile lower crust. In contrast to the previous models **1** and **2**, steeply dipping shear zones are confined to the deepest part of the model box (40- to 80-km depth) corresponding to the mantle part of the lithosphere and do not penetrate into the crust (see vertical sections on Figures 5b–5d). The lower crust is subjected to distributed ductile deformation with strain rates typical for broad shear bands in the previous models **1** and **2** ($3–6 \times 10^{-15}$ 1/s). Nevertheless, the rate of deformation can exceed 8×10^{-15} 1/s in several strongly localized Moho-parallel shear zones located in the lowermost part of the crust (Figures 5b–5d). Similar to the previous experiments (models **1** and **2**), the area of high localized strain rate ($>8 \times 10^{-15}$ 1/s) in the model center (above the indenter) is laterally shifted toward the subducting slab (see plan view in Figure 6c1).

The key feature of this weakly coupled reference experiment (model **3**) is that the highest near-surface rock uplift rates (>8 mm/year; Figure 6, slice c2) and corresponding youngest AFT ages (<1 Myr; Figure 6, slice c3) are concentrated in a single elliptical area above the indenter apex. This result is in contrast to the previous models with strong (model **1**) and intermediate (model **2**) upper plate coupling where high vertical velocities and associated young thermochronometric ages localize not only above indenter but also above the background slab (Figures 6a and 6b).

3.1.4. Temporal Evolution of Reference Models 1–3

The rheological structure of the overriding lithosphere appears to be important not only in terms of the resulting deformation/rock uplift patterns of the reference models **1**–**3** (Figures 3–6) but also for their temporal evolution (Figures S1–S3). In the case of the intermediately coupled experiment **2**, strongly localized deformation and high rock uplift rates arise soon after the start of model (4 Myr) in the area above the central indenter (Figure S2a). Further system development (6–8 Myr) results in the appearance of secondary, more broadly distributed zones of high strain rate and uplift localization located over background segments of the subducting slab (Figures S2b and S2c). In contrast, for the end-member cases of the lithospheric rheological structure (models **1** and **3**), initial strain localization along linear structures parallel to the plate margin and associated surface uplift first occur in the lateral ends of the orogen (at 3–5 Myr; see Figures S1a and S3a), whereas the indenter-centered zone of rapid deformation and large vertical velocities develops later, at the mature stage only (5–10 Myr; Figures S1b and S1c and Figures S3b and S3c). However, only the strongly coupled end-member (model **1**) results in the final coexistence of both central and peripheral localized rock exhumation (Figure 6, slices a2 and a3, and Figure S1, slice c1). In contrast, in the case of the weakly coupled experiment (model **3**), the rock uplift pattern evolves from linear trench-parallel bands over the areas distant from the indenter (Figure S3, slice a1) to an isolated curved ellipse in the hanging wall above shallow decollement in the center of the model (Figure 6, slices c2 and c3, and Figure S3, slice c1).

3.2. Effect of the Partitioning of Velocity Boundary Conditions (Models 4–6)

Models **4**–**6** explore the relationship between boundary velocities applied at the left ($y = 0$ km; subduction and accretion) and right ($y = 800$ km; upper plate advance) sides of the model domain (see Figure 2) for the case of a weakly coupled overriding lithosphere (Table 1). Models **4** (Figure 7a), **5** (Figure 7b), and **6** (Figure 7c) correspond to 0%, 50%, and 100% of upper plate advance (velocity at the right side; V_{Adv}) in the total shortening ($V_{\mathrm{Tot}} = 30$ mm/year), respectively.

The no upper plate advance experiment **4** ($V_{\mathrm{Adv}} = 0\%$; Figures 7a and S4a) produces a deformation and rock uplift pattern that is similar to that of the corresponding reference model **3** ($V_{\mathrm{Adv}} = 25\%$; Figure 6c). The main difference is the aspect ratio of the elliptical zone (ratio between its shortest and longest axes) of rapid uplift (>8 mm/year) and youngest (<1 Myr) AFT ages above the indenter increasing from ~1:4 to ~1:3 as upper plate advance decreases from 25% (model **3**; Figure 6, slice c3) to 0% (model **4**; Figure 7, slice a1). Another important aspect of this no upper plate advance case is that the shallowly dipping decollement developing at the initial stage of orogen evolution (5 Myr) is not confined to the background slab section (as in reference model **3**—see Figure S3a) but crosses the entire width of the model domain forming a continuous initial linear band slightly bent by the subducting plate (Figure S5a).

Increasing the rate of upper plate advance to 50% (half upper plate advance case of model **5**; Figures 7b and S4b) leads to a significantly different system behavior: The localized uplift centered above the indenter becomes several times smaller in area, whereas another well-defined yet very narrow (<50 km) zone of young (<1 Myr) AFT ages spans the width of the model in the trench-parallel direction (Figure 7, slice b1). The central decollement dipping in the retrodirection (see vertical profile A1-A2 on Figure 7b) is less pronounced (localized strain rates of ~7–8 $\times$ 10^{-15} 1/s) compared to the no upper plate advance case (model **4**; Figure 7a, profile A1-A2). Here compressional deformation is additionally accumulated along a complementary broad shear zone located toward the continent and dipping in the opposite, prodirection. This second shallowly dipping zone of poorly localized strain (~4–7 $\times$ 10^{-15} 1/s) can be clearly identified on both central and peripheral cross sections (compare Figure 7b, profiles A1-A2 and B1-B2, respectively). The vertical section B1-B2 across the background subduction segment shows an almost symmetric deformation pattern with an identical degree of development in both the retrodecollement and prodecollement shear zones (Figure 7b, profile B1-B2) with positions remaining stable over the time scale considered (see Figure S6).

The shallow decollement zone dipping in the prodirection becomes the principal structure localizing crustal strain in the case of full upper plate advance model **6** ($V_{\mathrm{Adv}} = 100\%$; Figures 7c and S4c). In contrast to all previous experiments, no particular zone of indenter-related localized surface uplift can be observed in this model (Figure S4, slice c2). As a result, exhumation is poorly localized and AFT ages form a broad, straight band with only small variations between the indenter and background slab sections (Figure 7, slice c1). The temporal evolution of this experiment (see Figure S7) is characterized by a transition from slightly concave (Figure S7a) to quasi-linear (Figure S7c) shape of the localized near-surface deformation (in plan view) due to a slow lateral shift of the shallowly dipping shear zone accumulating most of the crustal deformation toward the right side of the model in the subduction peripheral segments (see vertical profile B1-B2 on Figure S7).

As shown by Nettesheim et al. (2018), increasing total convergence rate (V_{Tot}) up to 60 mm/year (instead of 30 mm/year) leads to higher maximum values of the vertical uplift (16 mm/year instead of 8 mm/year) without a change in the relative distribution of deformation and surface uplift. Therefore, the magnitude of total shortening plays a minor role in the resulting deformation and rock exhumation pattern in comparison to the relationship between boundary velocities applied at the opposite sides of the model.

3.3. Effect of Indenter Configuration (Models 7–15)

We evaluate the effect of a narrower flexural bulge (150 km of the width in x direction instead of 300 km as adopted in previous experiments) and different degrees of upper plate rheological (de)coupling in models **7**–**9** (see Figure S8). In these, the upper plate advance contribution (V_{Adv}) in the total shortening (V_{Tot}) corresponds to a reference value of 25%.

Strongly and intermediately coupled experiments (models **7** and **8**, respectively) result in narrow (~100–150 km across) trench-parallel bands of anomalously young (<1 Myr) AFT ages, which are thinner

(~75 km across, model **8**; Figure S8, slice b3) or interrupted (model **7**; Figure S8, slice a3) in the central part directly above the narrow indenter. In contrast to corresponding models with reference indenter widths of 300 km (models **1** and **2**), these narrow indenter experiments (models **7** and **8**) show no isolated areas of increased uplift but are rather characterized by a continuous straight line of rock exhumation, as indicated by thermochronological ages (compare Figures 6a and 6b and Figures S8a and S8b). This strongly reduced effect of a narrower indenter on upper plate deformation is in agreement with findings reported by Nettesheim et al. (2018) for half upper plate advance ($V_{\mathrm{Adv}} = 50\%$) experiments.

In contrast, the weakly coupled narrow indenter experiment (model **9**; Figure 8c) reproduces all the key features typical for the corresponding reference model **3** with indenter width of 300 km (Figure 6c). The area of high vertical velocities (>8 mm/year) and young AFT ages (<1 Myr) in the center of the model remains in the same spatial location, and its elliptical shape becomes more isometric: The ellipse aspect ratio decreases from ~1:4 to ~1:2 with the indenter narrowing from 300 to 150 km (compare Figure 6, slice c3, and Figure 8, slice c3). Correspondingly, deformation and rock uplift patterns for a wider indenter (model **10**; 450 km, see Figure 8a) are elongated with an aspect ratio of ~1:6 for the central area of fast uplift. Figure 8 shows a comparison of all three investigated indenter widths.

The combined impact of a narrower indenter width (150 km) and different magnitudes of subduction (V_{Sub}) and upper plate advance (V_{Adv}) components is presented in models **11**–**13** (Figure 9). These simulations are characterized by weakly coupled rheological structure of the overriding plate. As in the experiments with a reference indenter width (models **5** and **6** presented in section 3.2, see Figures 7b and 7c and Figures S4b and S4c), high upper plate advance ($V_{\mathrm{Adv}} = 50\%$ and 100%; models **12** and **13**, respectively) does not lend to localized uplift above the indenter (Figures 9b and 9c). Accordingly, a decrease in the upper plate advance from values of the reference case ($V_{\mathrm{Adv}} = 25\%$) to 0 ($V_{\mathrm{Adv}} = 0\%$) contributes to a more isometric configuration of the uplift area (compare models **3** and **4** with $V_{\mathrm{Adv}} = 25\%$ and $V_{\mathrm{Adv}} = 0\%$ shown in Figures 6c and 7a, respectively). In model **11** (Figure 9a), we combine the narrowing effects of both the reduced upper plate advance component ($V_{\mathrm{Adv}} = 0\%$) and narrower indenter shape (150-km width) that result in an almost circular rock exhumation pattern (ellipse aspect ratio ~1:1.5) that is in agreement with the localized bull's-eye surface deformation reported in syntaxial orogens (see Bendick & Ehlers, 2014, and references herein). This isolated indenter-centered area of anomalously high rock uplift rates (>8 mm/year) persists up to the depth of 15–20 km (Figure S9), whereas the corresponding thermal anomaly is shallower and completely disappears by 10-km depth (Figure S10).

Models **14** and **15** (Figures S11a and S11b) complete the comparison of the narrow indenter geometry by investigating upper plate rheology effects under no upper plate advance ($V_{\mathrm{Adv}} = 0\%$) conditions. This series of models **14**, **15**, and **11** is analogous to the comparison of models **7**–**9** (with reference upper plate advance of $V_{\mathrm{Adv}} = 25\%$) shown in Figure S8 with strong, intermediate, and weak coupling, respectively, and results in a similar trend (Figure S11). For intermediate or strong coupling (models **14** and **15**) rock exhumation evolves into continuous, linear zones elongated parallel to the trench. No localized exhumation over the indenter apex can be seen, this remains a feature solely found in case of a weakly coupled lithosphere (model **11**; Figures 9a and S11c).

4. Discussion

4.1. Summary of Numerical Results

Variations in the rheological coupling of the overriding continental plate lead to different structural styles of deformation. These styles range from steeply dipping shear zones cutting the entire model domain from the upper crust down to the lithospheric upper mantle (strongly coupled model **1**; Figure 3) to thin shallow decollements dipping in the retrodirection (weakly coupled model **3**; Figure 5). The intermediate case combines both of these two major types of localized deformation (intermediately coupled model **2**; Figure 4).

The common point of all reference experiments (models **1**–**3**) refers to the elongated areas of strong strain localization and associated focused rock uplift situated directly above the indenter apex (Figure 6). However, only the strongly coupled (model **1**) and weakly coupled (model **3**) end-member cases include well-developed faulting (localized strain rate of $>8 \times 10^{-15}$ 1/s) above the background subducting plate, whereas the intermediate model **2** shows an attenuated rate of deformation ($\sim 5–7 \times 10^{-15}$ 1/s) outboard of the indenter (compare Figure 6, slice a1; Figure 6, slice c1; and Figure 6, slice b1). The relatively weak and broad strain rate localization at the peripheral segments of the intermediately coupled lithosphere (model **2**) stem from the distribution of strain between both shallowly dipping decollements and steep shear zones (see corresponding vertical cross sections on Figures 4d and S2c, profile B1-B2). Nevertheless, localized fast rock uplift associated with these two structures (see gray arrows on Figure 4d) occurs in well-defined yet relatively wide (~150 km) trench-parallel bands in both the near-surface vertical velocities (>4.5 mm/year; Figure 6, slice b2) and predicted AFT ages (<1 Myr; Figure 6, slice b3). In contrast, the model with a weakly coupled rheological structure (model **3**; Figure 6, slice c1) develops a well-established decollement (localized strain rate of $>8 \times 10^{-15}$ 1/s) above the background slab sections, but no associated localized rock uplift (Figure 6, slice c2) or concentrated young AFT ages (Figure 6, slice c3) can be observed there. This feature distinguishes the weak rheological coupling in the overlying continent (model **3**; Figure 6c), which is the only of the three tested configurations that favors an isolated region of high vertical rock uplift rates (>8 mm/year) over the central convex-upward-shaped bulge without any particular localization above the background down-going plate.

For this weakly coupled lithosphere, additional parameters were investigated. Increasing the component of upper plate advance from reference value of $V_{\mathrm{Adv}} = 25\%$ (model **3**; Figure 6c) to $V_{\mathrm{Adv}} = 50\%$ (model **5**; Figure 7b) and $V_{\mathrm{Adv}} = 100\%$ (model **6**; Figure 7c) disfavors localized surface uplift over the flexural bulge. On the contrary, no upper plate advance ($V_{\mathrm{Adv}} = 0\%$, model **4** in Figure 7a) leads to a more symmetric shape of the indenter-centered ellipsoidal zone of high exhumation rates (ellipse aspect ratio increases from 1:4 to 1:3 with decreasing upper plate advance V_{Adv} from 25% to 0%; see Table 1). Additionally, the final configuration of the region of rapid exhumation is directly controlled by the shape of the indenter. Figure 8 compares results for deformation and rock uplift patterns for wide (450 km; model **10**), reference (300 km; model **3**), and narrow (150 km; model **9**) indenter widths. A wide indenter (450 km; Figure 8a) results in an elongated center of uplift with an aspect ratio of ~1:6, while narrowing of the indenter to 300 km width (Figure 8b) and to 150-km width (Figure 8c) leads to narrower ellipses with aspect ratios of ~1:4 and ~1:2, respectively. The combined effect of a narrow indenter (150-km width), shortening accommodated by subduction and accretion only (no upper plate advance; $V_{\mathrm{Adv}} = 0\%$), and a weakly coupled lithosphere (model **11**, see Figure 9a) gives rise to a quasi-isometric (ellipse aspect ratio ~1:1.5) indenter-centered area of rock exhumation similar to the bull's-eye pattern observed in some syntaxial orogens (Bendick & Ehlers, 2014).

It is also worth noting that regardless of indenter width and the contribution of upper plate advance to total shortening, all experiments with a strongly (models **1**, **7**, and **14**) and intermediately (models **2**, **8**, and **15**) coupled overriding plate do not show a spatially localized bull's-eye-like rock uplift above the flexural bulge (see Figures 6, S8, and S11).

4.2. Conditions for Producing a Symmetric Zone of Rapid Exhumation

Based on the results presented, we find that a bull's-eye-like exhumation pattern characterized by a quasi-symmetric (aspect ratio close to ~1:1.5) shape of localized uplift can be reproduced by subduction of an indenter-shaped plate only with an appropriate combination of all three controlling parameters: boundary velocities (amount of upper plate advance), width of the flexural bulge, and rheological structure of the overriding continent (see “best fit” model **11** shown on Figures 9a and 10a).

In more detail, the relationship between subduction and upper plate advance components of the total shortening may control the resulting shape of the ellipse outlining the boundary of rapid uplift: Increasing the upper plate advance fraction from 0% to 25% leads to a small elongation of the ellipse and a decrease in the ellipse aspect ratio (from ~1:1.5 to ~1:2 in the case of the models with a relatively narrow indenter width of 150 km—see Figures 9a and 8c, respectively). On the other hand, an increase in upper plate advance to 50–100% leads to the development of decollements dipping in the opposite direction that prevent localization of indenter-centered rock uplift (Figures 7b and 7c). These tendencies persist for the models with various indenter configurations (from 300 to 150 km wide; see Figures 7 and 9, respectively, and Table 1).

Second, the initial shape of the indenter plays an important role as well since even under the appropriate boundary conditions (upper plate advance of 25%) a wider indenter (450 km width) provides a considerably elongated zone of localized uplift (aspect ratio of ~1:6) that is too asymmetric to be classified as a bull's-eye structure (Figure 8a).

Tectonics 10.1029/2018TC005455

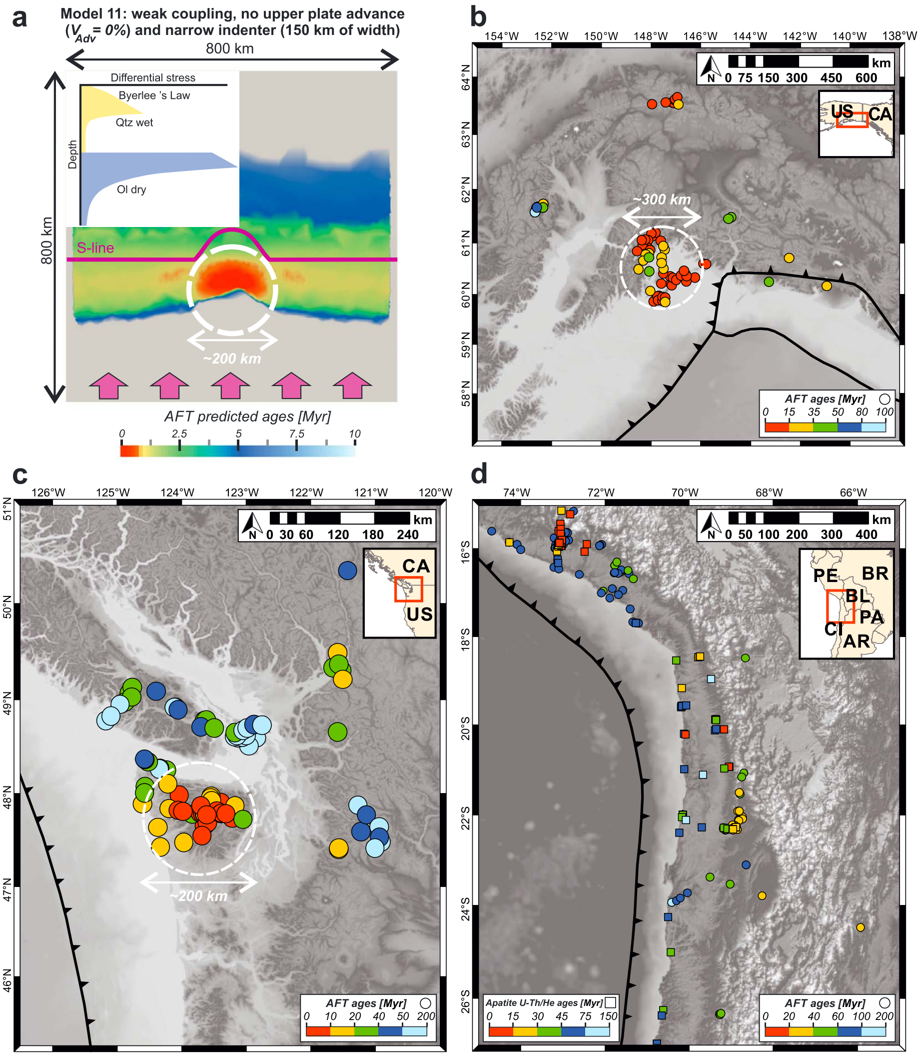

Figure 10. Comparison between modeled and observed spatial distributions of thermochronological cooling ages. (a) Predicted apatite fission track (AFT) ages for model **11** characterized by weakly coupled rheological structure and no upper plate advance contribution ($V_{\mathrm{Adv}} = 0\%$) in the total shortening and relatively narrow indenter width (150 km). (b–d) measured thermochronological cooling ages: (b) the Southeast Alaska (Arkle et al., 2013; Benowitz et al., 2011, 2012; Ferguson et al., 2015; Haeussler et al., 2008; O'Sullivan et al., 1997; Plafker et al., 1989; Spotila et al., 2004); (c) the Olympic Mountains of the Cascadia subduction zone (Brandon et al., 1998; Currie & Grist, 1996; England et al., 1997; Johnson et al., 1986; Reiners et al., 2002); and (d) the South American subduction zone (Andriessen & Reutter, 1994; Avdievitch et al., 2018; Barnes et al., 2008; Gunnell et al., 2010; Juez-Larré et al., 2010; Maksaev & Zentilli, 1999; McInnes et al., 1999; Noury et al., 2016; Schildgen et al., 2007, 2009; Wipf, 2006; Wipf et al., 2008). White circles indicate the concentric zones of vertical advection (bull's-eye pattern) in the modeled (a) and observed (b, c) AFT ages fields. No localized bull's-eye pattern characteristics associated with focused exhumation are detected in the overriding plate of the South American subduction zone (d).

Finally, we find that the rheological structure of the overlying lithosphere appears to be the most important controlling parameter for the localization of deformation. Strong-to-intermediate mechanical coupling between the upper crust and lithospheric mantle is incompatible with an axisymmetric bull's-eye exhumation pattern (Figures 3, 4 and 6a and 6b), even in the case of a considerably narrower indenter (Figures S8a and S8b) and no upper plate advance (Figures S11a and S11b). In contrast, a weakly coupled rheological profile isolates and concentrates rock uplift within a single indenter-centered zone (Figure 6c). Its geometry is further modified by the contribution of upper plate advance in the total shortening (Figure 7a), the indenter shape (Figure 8c), or both of them (Figure 9a). This is in agreement with a worldwide estimate of the lithospheric strength envelope showing that the upper continental crust is, in general, mechanically decoupled from the mantle within active subduction and collision zones (see Figure 4a in Tesauro et al., 2012).

To summarize, the subduction of a flexural bulge is a necessary but insufficient condition for spatial localization of anomalous exhumation rates within isometric (~1:1.5 aspect ratio) and small (~100-km diameter) bull's-eye regions. We suggest that other appropriate initial and boundary conditions including mechanical decoupling in the overriding lithosphere, relatively narrow indenter, and the dominance of subduction shortening are also required.

4.3. Rheology and Structure of the Continental Lithosphere in Orogen Syntaxes

As shown above, rheological properties of the overriding continental lithosphere may be a crucial parameter for the resulting deformation pattern in orogen syntaxes since even relatively small variations in mechanical coupling of the upper crust and lithospheric mantle cause large changes in the way upper plates strain is localized. The transition from strongly to intermediately/weakly coupled lithosphere switches the deformation mode from steep dipping shear zones that penetrate the entire model domain to shallowly dipping decollements rooting into the ductile lower part of the crust. The latter appears to be favorable for localized uplift above an indenter with concentrated vertical movements in the hanging wall. This uplift could be expressed at the surface through a characteristic bull's-eye structure under conditions of not only an appropriate degree of decoupling but also from a relatively narrow indenter configuration and small fractions (<25%) of upper plate advance. Despite the importance of the indenter geometry and velocity boundary conditions, our models identify a rheologically decoupled overlying lithosphere to be the key causal factor for spatially focused, rapid exhumation as it is observed in many transition zones of syntaxial orogens.

The long-term strength of lithosphere described by the Brace-Goetze yield-stress envelopes (Brace & Kohlstedt, 1980; Goetze & Evans, 1979) varies as a function of depth according to the plastic (e.g., Mohr-Coulomb failure criterion) and viscous (e.g., power law dislocation creep) deformation laws (see the numerical methods section in supporting information). The continental crust can provide a very large variety of possible rheological profiles due to variations in its structure and composition (Figure 2b) compared to oceanic crust. Considerable contrasts in rheological strength profiles between different segments of the continental part of the lithosphere have been reported by both geological observation and theoretical studies (see Burov, 2011, and references therein). The principal reason for this high diversity resides in the ductile parts of the crust, which are strongly influenced by the crustal thermal structure. That, in turn, is usually not well constrained because of the high uncertainty in (1) a region's thermal history (continents may have undergone several major thermal events), (2) current thermal thickness of the continents (defined by the depth of the 1330 °C isotherm), and (3) the distribution of radiogenic heat production in the crust that can contribute up to 50% of the continental surface heat flux. Moreover, unlike largely rock-independent brittle strength (Brace & Kohlstedt, 1980; Byerlee, 1978; Kohlstedt et al., 1995; Yamato & Brun, 2017), viscous parameters are also conditioned by rock type that may refer to either “strong” (wet granite flow law) or “weak” (dry diabase flow law) lower crust (Carter & Tsenn, 1987; Ranalli, 1995)—see supporting information Table 1. As shown in a review by Burov (2011), rheological decoupling should always occur in felsic-dominated crust (except for extremely thin, <20 km, rifted crust). In contrast, other crustal compositions (including a mafic lower crust) might result in strongly coupled lithosphere but only if the thermotectonic age is very old (>750 Myr). This means that a certain degree of the mechanical decoupling between the crust and lithosphere is the typical case of the rheological structure of continents except for old cratonic regions and thus can be applied for a broad range of possible geodynamical settings around the world. According to the global map of lithospheric strength (Tesauro et al., 2012), the lowest values of the integrated strength of the continental lithosphere ($<2.0 \times 10^{13}$ Pa·m) and associated decoupled rheological structure are mostly found in collisional belts and subduction zones. This ties into the principal findings of our study showing that bull's-eye rock exhumation at orogen syntaxes can be developed only in a weak, decoupled overriding plate.

Nevertheless, despite the progress in understanding the long-term strength of lithosphere (Burov, 2011; Tesauro et al., 2012, 2013), rheological parameters remain highly uncertain, and many additional sources of independent data are needed for further specification on the rheological profiles in different continental settings. They include seismic, petrologic, and gravitational data, as well as seismicity and surface heat flow distributions. Effective elastic thickness estimates provide a direct proxy for integrated strength of the lithosphere (Burov & Diament, 1995). Results of numerical and analog modeling also represent an independent class of constraints on the choice of the crustal rheology, since they allow identification of the surface and subsurface deformation patterns formed in response to different rheological models. In particular, the numerical experiments presented in this study assess the effects of the rheological structure of the overriding plate on the deformation and surface uplift patterns in the context of the subduction of a flexural bulge.

4.4. Link to Previous Studies

In most previous numerical modeling studies, contractional stresses and deformation at convergent plate boundaries have been investigated through 2-D vertical sections (e.g., Billen, 2008; Burov & Yamato, 2008; Ficini et al., 2017; Gerya et al., 2004, 2008; Grove et al., 2009; Yang et al., 2018) or by global (e.g., Bird, 1998; Bird et al., 2008; Coblentz et al., 1994; Koptev & Ershov, 2010; Lithgow-Bertelloni & Guynn, 2004; Naliboff et al., 2012; Wu et al., 2008; Yang & Gurnis, 2016) and regional (e.g., Coblentz & Richardson, 1996; Liu & Bird, 2002a, 2002b; Rajabi et al., 2017; Richardson & Reding, 1991) spherical shell models. Less common in previous work are 3-D modeling studies, and their focus is on subduction initiation (Gerya et al., 2015; Stern & Gerya, 2018), subduction obliquity (Plunder et al., 2018), lateral transition from oceanic subduction to continental collision (Li et al., 2013; Menant et al., 2016; Moresi et al., 2014; Pusok et al., 2018; Pusok & Kaus, 2015; Sternai et al., 2014) and the related impact of slab detachment in orogenic belts (Capitanio & Replumaz, 2013; Replumaz et al., 2014; Duretz et al., 2014; see also analogue laboratory experiments by Faccenna et al., 2006), opposing continental subduction zones (Liao et al., 2017), or subduction of cylindrical plates (e.g., Koons et al., 2010; Schellart et al., 2007) without particular focus on the effects of the subducting plate's internal 3-D geometry.

In contrast, Bendick and Ehlers (2014) investigated the impact of subducting plate geometry on upper-plate deformation. They attributed rapid localized exhumation (a bull's-eye pattern of surface deformation) reported in many transition zones between adjacent plate boundary segments around the world (e.g., the Southeast Alaska and the Cascadia subduction zone—see, e.g., Enkelmann et al., 2017; Brandon et al., 1998) to convex-upward-shaped flexural bulges of the subducting plate. However, the models in Bendick and Ehlers (2014) employed a simplified purely viscous rheology, which excludes brittle strain localization that has been shown to be important for the deformation and topographic evolution of the orogens (see, e.g., Vogt et al., 2017, 2018).

In view of the recent conceptual and methodical advances in our understanding of the rheological stratification of the lithosphere (Burov, 2011, and references therein), Nettesheim et al. (2018) investigated the subduction of an indenter-shaped plate with a layered viscoplastic upper plate. These models provided the basis on which this study was designed. However, their study focused on the effects of velocity conditions and variations in erosional efficiency. It did not consider the degree rheological coupling between the upper and lower crust, the parameter we found to be of high importance but restricts itself to the configuration of our intermediately coupled models **2**, **8**, and **15**. Moreover, Nettesheim et al. (2018) did not reproduce the concentric bull's-eye-like (with a characteristic diameter of ~100+ km) rock uplift as observed in extreme syntaxial orogens (Bendick & Ehlers, 2014).

4.5. Model Limitations and Perspectives

The extremely high erosional efficiency adopted in this study has a twofold effect: On one hand, it leads to unloading the topographic stresses that amplifies strain localization (Roy et al., 2016) in shear zones and decollements. On the other hand, it promotes an overestimation of the rock uplift that becomes close to the rock exhumation under nearly total erosion (England & Molnar, 1990). As a result, the absolute values of predicted AFT ages (<1 Myr within bull's-eye structures) are younger compared to observed ones (Figure 10). Nevertheless, a modeled bull's-eye-like age pattern (Figure 10a) resembles the known isometric structures with a characteristic size of ~200 km as observed in the Southeast Alaska (Figure 10b) and the Olympic Mountains (Figure 10c). In contrast, despite thick and mechanically weak crust in the central Andes (Capitanio et al., 2011; Kley & Monaldi, 1998; Sobolev & Babeyko, 2005), no concentric uplift is reported in the South American subduction zone (Figure 10d), possibly because of a relatively small concavity of the subducting plate (see Figure 1d) and considerable upper plate advance component due to accelerated westward drift of the South American plate during the past 30 Myr (Russo & Silver, 1996; Silver et al., 1998) and finally perhaps due to the limited exhumation magnitudes in the region due to the arid to hyper arid climate in the region. However, despite the lack of localized exhumation observed in the Arica bend of the central Andes due the arid climate, the long-wavelength topography of the region is highest at the Arica bend, before decreasing slightly to the south, away from the bend (Starke et al., 2017). This regional trend of decreasing elevations away from the Arica bend that is consistent with the high rock uplift rates predicted here above the bend causes higher elevations (in the absence of erosion).

Our generalized model setup does not aim to reproduce a specific region due to the restricted size of the model domain, the simplified erosional model, and the rigid slab rheology. However, this modeling approach can be used as an additional constraint for forthcoming geophysical studies because a comparison of the modeling results with observed structural features may help to discriminate the range of possible rheological (and thus compositional and thermal) characteristics that are permissible for a given geodynamic and geotectonic environment.

5. Summary and Conclusions

We presented results from numerical experiments that explore the three-dimensional response of a rheologically stratified overriding continental lithosphere to subduction of a rigid plate having a curved forward bulge. In this study, we have tested three controlling parameters (see Table 1): (1) rheological structure of the upper plate, (2) partitioning of velocity boundary conditions, and (3) indenter width. From this, we draw the following conclusions:

1. The rheological structure of the overriding plate plays a key role in the resulting deformation pattern: Strong rheological coupling favors steep dipping thrust-sense shear zones cutting the entire crust and the upper mantle; weakly coupled lithosphere, in contrast, localizes most of the deformation along shallowly dipping decollements rooting into ductile lower crust.
2. In the strongly coupled experiments, localized uplift within small V-shaped wedges squeezed between steep oppositely dipping shear zones is represented in plan view as narrow bands of rapid rock exhumation elongated perpendicular to the subduction direction and crossing through the entire model domain. In contrast, a rheologically decoupled lithosphere shows an isolated elliptical area of the highest rock uplift rates related to vertical movement in the hanging wall of the shallow retrodipping decollement developed in the continental crust over a central convex-upward-shaped indenter.
3. Increasing the component of upper plate advance in the shortening (i.e., the boundary velocity defining material influx in the direction opposite to that of the subduction of the down-going slab) disfavors localized surface uplift above an indenter. In contrast, shortening accommodated by subduction and accretion only (no upper plate advance case; $V_{\mathrm{Adv}} = 0\%$) results in a more isometric geometry of the indenter-centered zone of high exhumation rates.
4. In the case of a weakly coupled continental lithosphere, the resulting aspect ratio of the elliptical zone of high uplift rate is conditioned by the indenter geometry. In particular, an extremely narrow indenter (150-km width) results in a considerably more isometric shape of the final ellipse compared to that of a reference (300-km width) and wide indenter (450-km width) experiments.
5. Experiments with an appropriate combination of the upper plate rheological structure (weakly coupled upper crust and lithospheric mantle), velocity boundary conditions (limited upper plate advance), and indenter shape (narrow width) excites a bull's-eye-like exhumation pattern that resembles the concentric structures of vertical advection observed at orogen syntaxes in such regions as the Southeast Alaska and the Cascadia subduction zone (western USA).

Acknowledgments
We thank three anonymous reviewers, Anne Replumaz, and Associate Editor Ernst Willingshofer for their constructive comments that contributed to improving the manuscript. A. K., M. N., and T. A. E. acknowledge support from the ERC Consolidator Grant 615703 EXTREME to T. A. E. The numerical simulations were performed on the University of Tübingen cluster. We thank Jean Braun for providing an earlier version of the DOUAR source code that was modified and used in this study. Open source software ParaView (http://www.paraview.org) was used for 3-D visualization. Modeling results in ParaView format are available at https://drive.google.com/open?id=1xYP_6V_Ohja5CHh556NCH_Yrgd_xoqX4.

References

Andriessen, P. A., & Reutter, K. J. (1994). K-Ar and fission track mineral age determination of igneous rocks related to multiple magmatic arc systems along the 23 S latitude of Chile and NW Argentina. In *Tectonics of the southern central Andes*, (pp. 141–153). Berlin Heidelberg: Springer.

Arkle, J. C., Armstrong, P. A., Haeussler, P. J., Prior, M. G., Hartman, S., Sendziak, K. L., & Brush, J. A. (2013). Focused exhumation in the syntaxis of the western Chugach Mountains and Prince William Sound, Alaska. *Geological Society of America Bulletin*, *125*, 776–793.

Avdievitch, N. N., Ehlers, T. A., & Glotzbach, C. (2018). Slow long-term exhumation of the West Central Andean plate boundary, Chile. *Tectonics*, *37*, 2243–2267. https://doi.org/10.1029/2017TC004944

Barnes, J. B., Ehlers, T. A., McQuarrie, N., O'sullivan, P. B., & Tawackoli, S. (2008). Thermochronometer record of central Andean Plateau growth, Bolivia (19.5 S). *Tectonics*, *27*, TC3003. https://doi.org/10.1029/2007TC002174

Bendick, R., & Ehlers, T. A. (2014). Extreme localized exhumation at syntaxes initiated by subduction geometry. *Geophysical Research Letters*, *41*, 5861–5867. https://doi.org/10.1002/2014GL061026

Benowitz, J. A., Haeussler, P. J., Layer, P. W., O'Sullivan, P. B., Wallace, W. K., & Gillis, R. J. (2012). Cenozoic tectono-thermal history of the Tordrillo Mountains, Alaska: Paleocene-Eocene ridge subduction, decreasing relief, and late Neogene faulting. *Geochemistry, Geophysics, Geosystems*, *13*, Q04009. https://doi.org/10.1029/2011GC003951

Benowitz, J. A., Layer, P. W., Armstrong, P., Perry, S. E., Haeussler, P. J., Fitzgerald, P. G., & VanLaningham, S. (2011). Spatial variations in focused exhumation along a continental-scale strike-slip fault: The Denali fault of the eastern Alaska Range. *Geosphere*, *7*, 455–467.

Billen, M. I. (2008). Modeling the dynamics of subducting slabs. *Annual Review of Earth and Planetary Sciences*, *36*, 325–356.

Bird, P. (1998). Testing hypotheses on plate-driving mechanisms with global lithosphere models including topography, thermal structure, and faults. *Journal of Geophysical Research*, *103*, 10,115–10,129.

Bird, P., Liu, Z., & Rucker, W. K. (2008). Stresses that drive the plates from below: Definitions, computational path, model optimization, and error analysis. *Journal of Geophysical Research*, *113*, B11406. https://doi.org/10.1029/2007JB005460

Brace, W. F., & Kohlstedt, D. L. (1980). Limits on lithospheric stress imposed by laboratory experiments. *Journal of Geophysical Research*, *85*, 6248–6252.

Brandon, M. T., Roden-Tice, M. K., & Garver, J. I. (1998). Late Cenozoic exhumation of the Cascadia accretionary wedge in the Olympic Mountains, northwest Washington State. *Geological Society of America Bulletin*, *110*, 985–1009.

Braun, J. (2003). Pecube: A new finite-element code to solve the 3D heat transport equation including the effects of a time-varying, finite amplitude surface topography. *Computers & Geosciences*, *29*, 787–794.

Braun, J., Thieulot, C., Fullsack, P., DeKool, M., Beaumont, C., & Huismans, R. (2008). DOUAR: A new three-dimensional creeping flow numerical model for the solution of geological problems. *Physics of the Earth and Planetary Interiors*, *171*, 76–91.

Braun, J., & Yamato, P. (2010). Structural evolution of a three-dimensional, finite-width crustal wedge. *Tectonophysics*, *484*(1-4), 181–192. https://doi.org/10.1016/j.tecto.2009.08.032

Brun, J. P. (2002). Deformation of the continental lithosphere: Insights from brittle-ductile models. *Geological Society, London, Special Publications*, *200*, 355–370.

Brun, J. P., Sokoutis, D., Tirel, C., Gueydan, F., Van den Driessche, J., & Beslier, M. O. (2018). Crustal versus mantle core complexes. *Tectonophysics*, *746*, 22–45. https://doi.org/10.1016/j.tecto.2017.09.017

Burov, E., Jolivet, L., Le Pourhiet, L., & Poliakov, A. (2001). A thermomechanical model of exhumation of high pressure (HP) and ultra-high pressure (UHP) metamorphic rocks in Alpine-type collision belts. *Tectonophysics*, *342*, 113–136.

Burov, E., & Yamato, P. (2008). Continental plate collision, P-T-t-z conditions and unstable vs. stable plate dynamics: Insights from thermo-mechanical modelling. *Lithos*, *103*, 178–204.

Burov, E. B. (2011). Rheology and strength of the lithosphere. *Marine and Petroleum Geology*, *28*, 1402–1443.

Burov, E. B., & Diament, M. (1995). The effective elastic thickness (Te) of continental lithosphere: What does it really mean? *Journal of Geophysical Research*, *100*(B3), 3905–3927. https://doi.org/10.1029/94JB02770

Buttles, J., & Olson, P. (1998). A laboratory model of subduction zone anisotropy. *Earth and Planetary Science Letters*, *164*, 245–262.

Byerlee, J. (1978). Friction of rocks. *Pure and Applied Geophysics*, *116*, 615–626.

Cailleau, B., & Oncken, O. (2008). Past forearc deformation in Nicaragua and coupling at the megathrust interface: Evidence for subduction retreat? *Geochemistry, Geophysics, Geosystems*, *9*, Q03016. https://doi.org/10.1029/2007GC001754

Capitanio, F. A., Faccenna, C., Zlotnik, S., & Stegman, D. R. (2011). Subduction dynamics and the origin of Andean orogeny and the Bolivian orocline. *Nature*, *480*, 83.

Capitanio, F. A., Morra, G., Goes, S., Weinberg, R. F., & Moresi, L. (2010). India-Asia convergence driven by the subduction of the Greater Indian continent. *Nature Geoscience*, *3*, 136–139.

Capitanio, F. A., & Replumaz, A. (2013). Subduction and slab breakoff controls on Asian indentation tectonics and Himalayan western syntaxis formation. *Geochemistry, Geophysics, Geosystems*, *14*, 3515–3531. https://doi.org/10.1002/ggge.20171

Carter, N. L., & Tsenn, M. C. (1987). Flow properties of continental lithosphere. *Tectonophysics*, *136*(1-2), 27–63. https://doi.org/10.1016/0040-1951(87)90333-7

Coblentz, D. D., & Richardson, R. M. (1996). Analysis of the South American intraplate stress field. *Journal of Geophysical Research*, *101*, 8643–8657.

Coblentz, D. D., Richardson, R. M., & Sandiford, M. (1994). On the gravitational potential of the Earth's lithosphere. *Tectonics*, *13*(4), 929–945. https://doi.org/10.1029/94TC01033

Crowley, J. L., Waters, D. J., Searle, M. P., & Bowring, S. A. (2009). Pleistocene melting and rapid exhumation of the Nanga Parbat massif, Pakistan: Age and P-T conditions of accessory mineral growth in migmatite and leucogranite. *Earth and Planetary Science Letters*, *288*, 408–420.

Currie, L., & Grist, A. M. (1996). Diachronous low temperature Paleogene cooling of the Alberni Inlet area, southern Vancouver Island, British Columbia: Evidence from apatite fission track analyses. Geological Survey of Canada Current Research, 119-125.

Duretz, T., Gerya, T. V., & Spakman, W. (2014). Slab detachment in laterally varying subduction zones: 3-D numerical modeling. *Geophysical Research Letters*, *41*, 1951–1956. https://doi.org/10.1002/2014GL059472

Ehlers, T. A. (2005). Computational tools for low-temperature thermochronometer interpretation. *Reviews in Mineralogy and Geochemistry*, *58*(1), 589–622. https://doi.org/10.2138/rmg.2005.58.22

England, P., & Molnar, P. (1990). Surface uplift, uplift of rocks, and exhumation of rocks. *Geology*, *18*(12), 1173–1177. https://doi.org/10.1130/0091-7613(1990)018<1173:SUUORA>2.3.CO;2

England, T. D. J., Currie, L. D., Massey, N. W. D., Roden-Tice, M. K., & Miller, D. S. (1997). Apatite fission-track dating of the Cowichan fold and thrust system, southern Vancouver Island, British Columbia. *Canadian Journal of Earth Sciences*, *34*(5), 635–645. https://doi.org/10.1139/e17-050

Enkelmann, E., Ehlers, T. A., Zeitler, P. K., & Hallet, B. (2011). Denudation of the Namche Barwa antiform, eastern Himalaya. *Earth and Planetary Science Letters*, *307*(3-4), 323–333. https://doi.org/10.1016/j.epsl.2011.05.004

Enkelmann, E., Piestrzeniewicz, A., Falkowski, S., Stübner, K., & Ehlers, T. A. (2017). Thermochronology in southeast Alaska and southwest Yukon: Implications for North American Plate response to terrane accretion. *Earth and Planetary Science Letters*, *457*, 348–358. https://doi.org/10.1016/j.epsl.2016.10.032

Enkelmann, E., Zeitler, P. K., Garver, J. I., Pavlis, T. L., & Hooks, B. P. (2010). The thermochronological record of tectonic and surface process interaction at the Yakutat-North American collision zone in southeast Alaska. *American Journal of Science*, *310*(4), 231–260. https://doi.org/10.2475/04.2010.01

Erdos, Z., Huismans, R. S., van der Beek, P., & Thieulot, C. (2014). Extensional inheritance and surface processes as controlling factors of mountain belt structure. *Journal of Geophysical Research: Solid Earth*, *119*, 9042–9061. https://doi.org/10.1002/2014JB011408

Faccenna, C., Bellier, O., Martinod, J., Piromallo, C., & Regard, V. (2006). Slab detachment beneath eastern Anatolia: A possible cause for the formation of the North Anatolian fault. *Earth and Planetary Science Letters*, *242*, 85–97.

Falkowski, S., Enkelmann, E., & Ehlers, T. A. (2014). Constraining the area of rapid and deep-seated exhumation at the St. Elias syntaxis, Southeast Alaska, with detrital zircon fission-track analysis. *Tectonics*, *33*, 597–616. https://doi.org/10.1002/2013TC003408

Ferguson, K. M., Armstrong, P. A., Arkle, J. C., & Haeussler, P. J. (2015). Focused rock uplift above the subduction décollement at Montague and Hinchinbrook Islands, Prince William Sound, Alaska. *Geosphere*, *11*, 144–159.

Ficini, E., Dal Zilio, L., Doglioni, C., & Gerya, T. V. (2017). Horizontal mantle flow controls subduction dynamics. *Scientific Reports*, *7*, 7550.

Gerya, T. V., Connolly, J. A., & Yuen, D. A. (2008). Why is terrestrial subduction one-sided? *Geology*, *36*, 43–46.

Gerya, T. V., Stern, R. J., Baes, M., Sobolev, S. V., & Whattam, S. A. (2015). Plate tectonics on the Earth triggered by plume-induced subduction initiation. *Nature*, *527*, 221–225.

Gerya, T. V., Yuen, D. A., & Maresch, W. V. (2004). Thermomechanical modelling of slab detachment. *Earth and Planetary Science Letters*, *226*, 101–116.

Goetze, C., & Evans, B. (1979). Stress and temperature in the bending lithosphere as constrained by experimental rock mechanics. *Geophysical Journal International*, *59*, 463–478.

Grove, T. L., Till, C. B., Lev, E., Chatterjee, N., & Médard, E. (2009). Kinematic variables and water transport control the formation and location of arc volcanoes. *Nature*, *459*, 694–697.

Gueydan, F., Morency, C., & Brun, J. P. (2008). Continental rifting as a function of lithosphere mantle strength. *Tectonophysics*, *460*, 83–93.

Gunnell, Y., Thouret, J. C., Brichau, S., Carter, A., & Gallagher, K. (2010). Low-temperature thermochronology in the Peruvian Central Andes: Implications for long-term continental denudation, timing of plateau uplift, canyon incision and lithosphere dynamics. *Journal of the Geological Society*, *167*, 803–815.

Haeussler, P. J., O'Sullivan, P., Berger, A. L., & Spotila, J. A. (2008). Neogene exhumation of the Tordrillo Mountains, Alaska, and correlations with Denali (Mount McKinley). In *Active tectonics and seismic potential of Alaska*, (Vol. 179, pp. 269–285).

Hayes, G. P., Wald, D. J., & Johnson, R. L. (2012). Slab1. 0: A three-dimensional model of global subduction zone geometries. *Journal of Geophysical Research*, *117*, B01302. https://doi.org/10.1029/2011JB008524

Heuret, A., & Lallemand, S. (2005). Plate motions, slab dynamics and back-arc deformation. *Physics of the Earth and Planetary Interiors*, *149*, 31–51.

Hirth, G., & Kohlstedt, D. (2003). Rheology of the upper mantle and the mantle wedge: A view from the experimentalists. In *Inside the subduction Factory*, (pp. 83–105).

Huismans, R. S., & Beaumont, C. (2002). Asymmetric lithospheric extension: The role of frictional plastic strain softening inferred from numerical experiments. *Geology*, *30*, 211–214.

Iwamori, H., Richardson, C., & Maruyama, S. (2007). Numerical modeling of thermal structure, circulation of H2O, and magmatism-metamorphism in subduction zones: Implications for evolution of arcs. *Gondwana Research*, *11*, 109–119.

Jadamec, M. A., & Billen, M. I. (2012). The role of rheology and slab shape on rapid mantle flow: Three-dimensional numerical models of the Alaska slab edge. *Journal of Geophysical Research*, *117*, B02304. https://doi.org/10.1029/2011JB008563

Jammes, S., & Huismans, R. S. (2012). Structural styles of mountain building: Controls of lithospheric rheologic stratification and extensional inheritance. *Journal of Geophysical Research*, *117*, B10403. https://doi.org/10.1029/2012JB009376

Johnson, S. Y., Zimmermann, R. A., Naeser, C. W., & Whetten, J. T. (1986). Fission-track dating of the tectonic development of the San Juan Islands, Washington. *Canadian Journal of Earth Sciences*, *23*, 1318–1330.

Juez-Larré, J., Kukowski, N., Dunai, T. J., Hartley, A. J., & Andriessen, P. A. (2010). Thermal and exhumation history of the Coastal Cordillera arc of northern Chile revealed by thermochronological dating. *Tectonophysics*, *495*, 48–66.

Kincaid, C., & Griffiths, R. W. (2003). Laboratory models of the thermal evolution of the mantle during rollback subduction. *Nature*, *425*, 58.

Kley, J., & Monaldi, C. R. (1998). Tectonic shortening and crustal thickness in the Central Andes: How good is the correlation? *Geology*, *26*, 723–726.

Kohlstedt, D. L., Evans, B., & Mackwell, S. J. (1995). Strength of the lithosphere: Constraints imposed by laboratory experiments. *Journal of Geophysical Research*, *100*, 17,587–17,602.

Koons, P. O., Hooks, B. P., Pavlis, T., Upton, P., & Barker, A. D. (2010). Three-dimensional mechanics of Yakutat convergence in the southern Alaskan plate corner. *Tectonics*, *29*, TC4008. https://doi.org/10.1029/2009TC002463

Koons, P. O., Zeitler, P. K., Chamberlain, C. P., Craw, D., & Meltzer, A. S. (2002). Mechanical links between erosion and metamorphism in Nanga Parbat, Pakistan Himalaya. *American Journal of Science*, *302*, 749–773.

Koons, P. O., Zeitler, P. K., & Hallet, B. (2013). Tectonic aneurysms and mountain building. In *Treatise on Geomorphology*, (Vol. 5, pp. 318–349).

Koptev, A., Burov, E., Calais, E., Leroy, S., Gerya, T., Guillou-Frottier, L., & Cloetingh, S. (2016). Contrasted continental rifting via plume-craton interaction: Applications to Central East African Rift. *Geoscience Frontiers*, *7*, 221–236.

Koptev, A., Burov, E., Gerya, T., Le Pourhiet, L., Leroy, S., Calais, E., & Jolivet, L. (2018). Plume-induced continental rifting and break-up in ultra-slow extension context: Insights from 3D numerical modeling. *Tectonophysics*, *746*, 121–137.

Koptev, A., Calais, E., Burov, E., Leroy, S., & Gerya, T. (2015). Dual continental rift systems generated by plume–lithosphere interaction. *Nature Geoscience*, *8*, 388.

Koptev, A., Calais, E., Burov, E., Leroy, S., & Gerya, T. (2018). Along-axis variations of rift width in a coupled lithosphere-mantle system, Application to East Africa. *Geophysical Research Letters*, *45*, 5362–5370. https://doi.org/10.1029/2018GL077276

Koptev, A. I., & Ershov, A. V. (2010). The role of the gravitational potential of the lithosphere in the formation of a global stress field. *Izvestiya Physics of the Solid Earth*, *46*, 1080–1094.

Lang, K. A., Huntington, K. W., Burmester, R., & Housen, B. (2016). Rapid exhumation of the eastern Himalayan syntaxis since the late Miocene. *Geological Society of America Bulletin*, *128*, 1403–1422.

Li, Z. H., Xu, Z., Gerya, T., & Burg, J. P. (2013). Collision of continental corner from 3-D numerical modeling. *Earth and Planetary Science Letters*, *380*, 98–111.

Liao, J., Gerya, T., Thielmann, M., Webb, A. A. G., Kufner, S. K., & Yin, A. (2017). 3D geodynamic models for the development of opposing continental subduction zones: The Hindu Kush-Pamir example. *Earth and Planetary Science Letters*, *480*, 133–146.

Lithgow-Bertelloni, C., & Guynn, J. H. (2004). Origin of the lithospheric stress field. *Journal of Geophysical Research*, *109*, B01408. https://doi.org/10.1029/2003JB002467

Liu, Z., & Bird, P. (2002a). Finite element modeling of neotectonics in New Zealand. *Journal of Geophysical Research*, *107*(B12), 2328. https://doi.org/10.1029/2001JB001075

Liu, Z., & Bird, P. (2002b). North America plate is driven westward by lower mantle flow. *Geophysical Research Letters*, *29*(24), 2164. https://doi.org/10.1029/2002GL016002

Mahadevan, L., Bendick, R., & Liang, H. (2010). Why subduction zones are curved. *Tectonics*, *29*, TC6002. https://doi.org/10.1029/2010TC002720

Maksaev, V., & Zentilli, M. (1999). Fission track thermochronology of the Domeyko Cordillera, northern Chile: Implications for Andean tectonics and porphyry copper metallogenesis. *Exploration and Mining Geology*, *8*, 65–90.

McInnes, B. I., Farley, K. A., Sillitoe, R. H., & Kohn, B. P. (1999). Application of apatite (U-Th)/He thermochronometry to the determination of the sense and amount of vertical fault displacement at the Chuquicamata porphyry copper deposit, Chile. *Economic Geology*, *94*, 937–947.

Menant, A., Sternai, P., Jolivet, L., Guillou-Frottier, L., & Gerya, T. (2016). 3D numerical modeling of mantle flow, crustal dynamics and magma genesis associated with slab roll-back and tearing: The eastern Mediterranean case. *Earth and Planetary Science Letters*, *442*, 93–107.

Michel, L., Ehlers, T. A., Glotzbach, C., Adams, B. A., & Stübner, K. (2018). Tectonic and glacial contributions to focused exhumation in the Olympic Mountains, Washington, USA. *Geology*, *46*, 491–494.

Moresi, L., Betts, P. G., Miller, M. S., & Cayley, R. A. (2014). Dynamics of continental accretion. *Nature*, *508*, 245–248.

Naliboff, J. B., Lithgow-Bertelloni, C., Ruff, L. J., & de Koker, N. (2012). The effects of lithospheric thickness and density structure on Earth's stress field. *Geophysical Journal International*, *188*, 1–17.

Nettesheim, M., Ehlers, T. A., Whipp, D., & Koptev, A. (2018). The influence of upper-plate advance and erosion on overriding plate deformation in orogen syntaxes. *Solid Earth*, *9*, 1207–1224.

Noury, M., Bernet, M., Schildgen, T. F., Simon-Labric, T., Philippon, M., & Sempere, T. (2016). Crustal-scale block tilting during Andean trench-parallel extension: Structural and geo-thermochronological insights. *Tectonics*, *35*, 2052–2069. https://doi.org/10.1002/2016TC004231

O'Sullivan, P. B., Murphy, J. M., & Blythe, A. E. (1997). Late Mesozoic and Cenozoic thermotectonic evolution of the central Brooks Range and adjacent North Slope foreland basin, Alaska: Including fission track results from the Trans-Alaska Crustal Transect (TACT). *Journal of Geophysical Research*, *102*, 20821–20845.

Pazzaglia, F. J., & Brandon, M. T. (2001). A fluvial record of long-term steady-state uplift and erosion across the Cascadia forearc high, western Washington State. *American Journal of Science*, *301*, 385–431.

Plafker, G., Nokleberg, W. J., & Lull, J. S. (1989). Bedrock geology and tectonic evolution of the Wrangellia, Peninsular, and Chugach terranes along the Trans-Alaska Crustal Transect in the Chugach Mountains and southern Copper River Basin, Alaska. *Journal of Geophysical Research*, *94*, 4255–4295.

Plunder, A., Thieulot, C., & Van Hinsbergen, D. J. (2018). The effect of obliquity on temperature in subduction zones: Insights from 3-D numerical modeling. *Solid Earth*, *9*, 759–776.

Pusok, A. E., Kaus, B. J., & Popov, A. A. (2018). The effect of rheological approximations in 3-D numerical simulations of subduction and collision. *Tectonophysics*, *746*, 296–311.

Pusok, A. E., & Kaus, B. J. P. (2015). Development of topography in 3-D continental-collision models. *Geochemistry, Geophysics, Geosystems*, *16*, 1378–1400. https://doi.org/10.1002/2015GC005732

Rajabi, M., Tingay, M., Heidbach, O., Hillis, R., & Reynolds, S. (2017). The present-day stress field of Australia. *Earth-Science Reviews*, *168*, 165–189.

Ranalli, G. (1995). *Rheology of the Earth*, (second ed.p. 413). London: Chapman and Hall.

Ranalli, G., & Murphy, D. C. (1987). Rheological stratification of the lithosphere. *Tectonophysics*, *132*, 281–295.

Reiners, P. W., Ehlers, T. A., Garver, J. I., Mitchell, S. G., Montgomery, D. R., Vance, J. A., & Nicolescu, S. (2002). Late Miocene exhumation and uplift of the Washington Cascade Range. *Geology*, *30*, 767–770.

Replumaz, A., Capitanio, F. A., Guillot, S., Negredo, A. M., & Villaseñor, A. (2014). The coupling of Indian subduction and Asian continental tectonics. *Gondwana Research*, *26*, 608–626.

Richardson, R. M., & Reding, L. M. (1991). North American plate dynamics. *Journal of Geophysical Research*, *96*, 12,201–12,223.

Roy, S. G., Koons, P. O., Upton, P., & Tucker, G. E. (2016). Dynamic links among rock damage, erosion, and strain during orogenesis. *Geology*, *44*, 583–586.

Ruh, J. B., Sallarès, V., Ranero, C. R., & Gerya, T. (2016). Crustal deformation dynamics and stress evolution during seamount subduction: High-resolution 3-D numerical modeling. *Journal of Geophysical Research: Solid Earth*, *121*, 6880–6902. https://doi.org/10.1002/2016JB013250

Russo, R. M., & Silver, P. G. (1996). Cordillera formation, mantle dynamics, and the Wilson cycle. *Geology*, *24*, 511–514.

Schellart, W. P., Freeman, J., Stegman, D. R., Moresi, L., & May, D. (2007). Evolution and diversity of subduction zones controlled by slab width. *Nature*, *446*, 308–311.

Schildgen, T. F., Ehlers, T. A., Whipp, D. M., Van Soest, M. C., Whipple, K. X., & Hodges, K. V. (2009). Quantifying canyon incision and Andean Plateau surface uplift, southwest Peru: A thermochronometer and numerical modeling approach. *Journal of Geophysical Research*, *114*, F04014. https://doi.org/10.1029/2009JF001305

Schildgen, T. F., Hodges, K. V., Whipple, K. X., Reiners, P. W., & Pringle, M. S. (2007). Uplift of the western margin of the Andean plateau revealed from canyon incision history, southern Peru. *Geology*, *35*, 523–526.

Silver, P. G., Russo, R. M., & Lithgow-Bertelloni, C. (1998). Coupling of South American and African plate motion and plate deformation. *Science*, *279*, 60–63.

Sobolev, S. V., & Babeyko, A. Y. (2005). What drives orogeny in the Andes? *Geology*, *33*, 617–620.

Spotila, J. A., Buscher, J. T., Meigs, A. J., & Reiners, P. W. (2004). Long-term glacial erosion of active mountain belts: Example of the Chugach-St. Elias Range, Alaska. *Geology*, *32*, 501–504.

Starke, J., Ehlers, T. A., & Schaller, M. (2017). Tectonic and climatic controls on the spatial distribution of denudation rates in Northern Chile (18° S to 23° S) determined from cosmogenic nuclides. *Journal of Geophysical Research: Earth Surface*, *122*, 1949–1971. https://doi.org/10.1002/2016JF004153

Stern, R. J., & Gerya, T. (2018). Subduction initiation in nature and models: A review. *Tectonophysics*, *746*, 173–198.

Sternai, P., Jolivet, L., Menant, A., & Gerya, T. (2014). Driving the upper plate surface deformation by slab rollback and mantle flow. *Earth and Planetary Science Letters*, *405*, 110–118.

Tesauro, M., Kaban, M. K., & Cloetingh, S. A. (2012). Global strength and elastic thickness of the lithosphere. *Global and Planetary Change*, *90*, 51–57.

Tesauro, M., Kaban, M. K., & Cloetingh, S. A. (2013). Global model for the lithospheric strength and effective elastic thickness. *Tectonophysics*, *602*, 78–86.

Tetreault, J. L., & Buiter, S. J. H. (2018). The influence of extension rate and crustal rheology on the evolution of passive margins from rifting to break-up. *Tectonophysics*, *746*, 155–172.

Thieulot, C., Fullsack, P., & Braun, J. (2008). Adaptive octree-based finite element analysis of two- and three-dimensional indentation problems. *Journal of Geophysical Research*, *113*, B12207. https://doi.org/10.1029/2008JB005591

Vogt, K., Matenco, L., & Cloetingh, S. (2017). Crustal mechanics control the geometry of mountain belts. Insights from numerical modelling. *Earth and Planetary Science Letters*, *460*, 12–21.

Vogt, K., Willingshofer, E., Matenco, L., Sokoutis, D., Gerya, T., & Cloetingh, S. (2018). The role of lateral strength contrasts in orogenesis: A 2D numerical study. *Tectonophysics*, *746*, 549–561.

Wada, I., Wang, K., He, J., & Hyndman, R. D. (2008). Weakening of the subduction interface and its effects on surface heat flow, slab dehydration, and mantle wedge serpentinization. *Journal of Geophysical Research*, *113*, B04402. https://doi.org/10.1029/2007JB005190

Whipp, D. M. Jr., Beaumont, C., & Braun, J. (2014). Feeding the “aneurysm”: Orogen-parallel mass transport into Nanga Parbat and the western Himalayan syntaxis. *Journal of Geophysical Research: Solid Earth*, *119*, 5077–5096. https://doi.org/10.1002/2013JB010929

Whipp, D. M., Ehlers, T. A., Braun, J., & Spath, C. D. (2009). Effects of exhumation kinematics and topographic evolution on detrital thermochronometer data. *Journal of Geophysical Research*, *114*, F04021. https://doi.org/10.1029/2008JF001195

Willingshofer, E., & Sokoutis, D. (2009). Decoupling along plate boundaries: Key variable controlling the mode of deformation and the geometry of collisional mountain belts. *Geology*, *37*, 39–42.

Willingshofer, E., Sokoutis, D., Luth, S., Beekman, F., & Cloetingh, S. (2013). Subduction and deformation of the continental lithosphere in response to plate and crust-mantle coupling. *Geology*, *41*, 1239–1242.

Wipf, M., Zeilinger, G., Seward, D., & Schlunegger, F. (2008). Focused subaerial erosion during ridge subduction: Impact on the geomorphology in south-central Peru. *Terra Nova*, *20*, 1–10.

Wipf, M. A. (2006). Evolution of the Western Cordillera and Coastal Margin of Peru: Evidence from low-temperature thermochronology and geomorphology. PhD thesis, Swiss Federal Institute of Technology.

Wu, B., Conrad, C. P., Heuret, A., Lithgow-Bertelloni, C., & Lallemand, S. (2008). Reconciling strong slab pull and weak plate bending: The plate motion constraint on the strength of mantle slabs. *Earth and Planetary Science Letters*, *272*, 412–421.

Yamato, P., & Brun, J. P. (2017). Metamorphic record of catastrophic pressure drops in subduction zones. *Nature Geoscience*, *10*, 46–50.

Yang, T., & Gurnis, M. (2016). Dynamic topography, gravity and the role of lateral viscosity variations from inversion of global mantle flow. *Geophysical Journal International*, *207*, 1186–1202.

Yang, T., Gurnis, M., & Zahirovic, S. (2018). Slab avalanche-induced tectonics in self-consistent dynamic models. *Tectonophysics*, *746*, 251–265.

Zeitler, P. K., Meltzer, A. S., Brown, L., Kidd, W. S., Lim, C., & Enkelmann, E. (2014). *Tectonics and topographic evolution of Namche Barwa and the easternmost Lhasa block*, (Vol. 507, pp. 23–58). Tibet: Geological Society of America Special Papers.

Zeitler, P. K., et al. (2001). Erosion, Himalayan geodynamics, and the geomorphology of metamorphism. *GSA Today*, *11*, 4–9.

5 Effect of Lower Plate Properties on Upper Plate Deformation

5.1 Introduction

In numerical models that investigate convergent settings on crustal scale, the dynamic of the subducting slab is often abstracted away and treated as “conveyor belt”. Instead of modeling the full dynamic, the interface between overriding and subducting plate is taken as edge of the model boundary and the velocity along the model’s bottom prescribed (see e.g. Braun et al. 2014; Koons et al. 2002; Willett et al. 1993). If it is part of the model domain, both the geometry and internal velocities are prescribed and kept constant during the model run (Bendick and Ehlers 2014; Koons et al. 2010). This approach has also been used in Nettesheim et al. (2018) and Koptev et al. (2019) (see Chapters 3 and 4, respectively). However, lithospheric- and mantle-scale numerical studies (Bonnardot et al. 2008; Schellart et al. 2007) as well as observational studies of subduction zones (see e.g. Ramos and Folguera 2009, on the South American subduction zone) highlight the importance of lower-plate dynamics on the resulting deformation in the upper plate.

Another aspect previously not investigated in this dissertation is the effect of the subduction interface. Several analogue (e.g. Bajolet et al. 2013; Willingshofer and Sokoutis 2009) and numerical (e.g. Angiboust et al. 2012; Sandiford and Moresi 2019; Tan et al. 2012) studies stress the interface’s relevance in subduction dynamics and upper plate deformation. In this study, 12 additional models are presented in order to investigate the effect of lower plate rheology and shape in the already established model setup. The focus lies on the effect on upper plate deformation and how these new results relate to previous work.

5.2 Methods and Model Parameters

The numerical modeling approach and model setup in this setup closely resemble those of the previous chapters. Modeling was conducted with DOUAR, a program for fully-coupled thermomechanical simulations of crustal to lithospheric scale (Braun et al. 2008; Thieulot et al. 2008). A model is defined by velocity and temperature boundary conditions, material parameters. Additional processes, such as surface erosion and isostatic compensation, can be configured as well. We refer the reader to Chapter 2 for a more detailed description.

Figure 5.1 gives a graphical overview of model setup and parameters. Model geometry is characterized by a layered overriding plate, comprised of upper crust, lower crust, and lithospheric mantle, and the forward-bulging subducting plate. Both plates are separated by the weak interface layer, which is of particular interest in this study. The S-line, analogous to the S-point definition of Willett et al. (1993) marks the boundary between the overriding and down-going plates and their respective velocity regimes. In case of no upper-plate advance, material is accreted to the model domain only at the left boundary ($x = 0\,\mathrm{km}$) at $30\,\mathrm{mm\,yr^{-1}}$. The motion of the upper plate towards the subducting plate and the trench can be represented in a moving frame of reference, so that part of the material influx is instead imposed on the right boundary ($x = 800\,\mathrm{km}$). Half-upper plate advance corresponds to material influx with $15\,\mathrm{mm\,yr^{-1}}$ from both boundaries. Thus, the overall shortening rate is kept the same at $30\,\mathrm{mm\,yr^{-1}}$ in all models.

The difference to the models presented in previous chapters of this thesis lies in the properties of the subducting plate. Its shape is not fixed, but free to deform over time. This allows an interaction of upper and lower plate deformation and extends the role of the lower plate beyond that of an idealized conveyor belt that drives upper plate deformation. In previous chapters, a completely rigid lower plate was used, in which the subducting plate and material boundary layer are not moved with the velocity field in the model's update step, but remain fixed in place. The weak layer between the overriding plate and the rigid, high viscosity lower plate is slightly thicker than previously. It represents the subduction channel with its inclusion of sediment and high fluid pore pressure. Note that all layers in the overriding plate use a temperature-dependent, visco-plastic rheology of Mohr-Coulomb type, whereas the down-going plate ($1 \cdot 10^{25}\,\mathrm{Pa\,s}$) and the interface layer ($3 \cdot 10^{21}\,\mathrm{Pa\,s}$ to $8 \cdot 10^{21}\,\mathrm{Pa\,s}$) are purely viscous. The rheology parameters of the upper plate are identical to the default values given in Table 2.1 on page 9.

Table 5.1 gives an overview of all 12 model runs conducted for this study. For clarity, model names follow a pattern that denotes the values of the four relevant model parameters. Upper plate advance (half or no advance) and erosion type (flat or fluvial, see Table 2.2 on page 18 for parameter values) were also discussed in previous chapters. They are combined and contrasted with two new parameters: The strength of the plate interface layer is varied between $3 \cdot 10^{21}\,\mathrm{Pa\,s}$, $5 \cdot 10^{21}\,\mathrm{Pa\,s}$ and $8 \cdot 10^{21}\,\mathrm{Pa\,s}$ (weak, baseline, and strong interface, respectively). In addition, the lower plate has fully dynamic behavior, except in three models with a completely rigid lower plate to allow a direct comparison.

5.3 Results

5.3.1 Baseline Model

The baseline model HXM (half upper plate advance, intermediate coupling, and flat erosion) closely matches the parameters used in previous chapters. Therefore, it will be presented in greater detail in order to provide a reference to the changes that are caused by modeling a deformable lower plate. We refer the reader to previous chapters for additional discussion and a three-dimensional display of model results. Figure 5.2 shows detail views of the baseline model after 6 Myr modeling time. The second invariant of the strain rate tensor in panels a, d, and e is overlain with motion stream lines to convey the full picture of motion. The pro- and retro-shear zones are strong and without discontinuity along strike. Above the indenter, a basal decollement has formed (panel d), but it is less distinct than the adjacent pro-shear zone and only of limited extent (see map view in panel a). This is also reflected in the material velocities. Motion stream lines reveal the material influx from both sides in a near-parallel manner, with only minor motion perpendicular to the direction of convergence (panel a). Strongest upward motion occurs within the pro- and retro shear zone, while the basal decollement creates less upward deflection. Furthermore, material influx from the trenchward (i.e. left) side is horizontal above the background slab, whereas the central vertical slice (panel d) exhibits gradual subsidence for $x < 250\,\mathrm{km}$. The Moho, the material boundary between

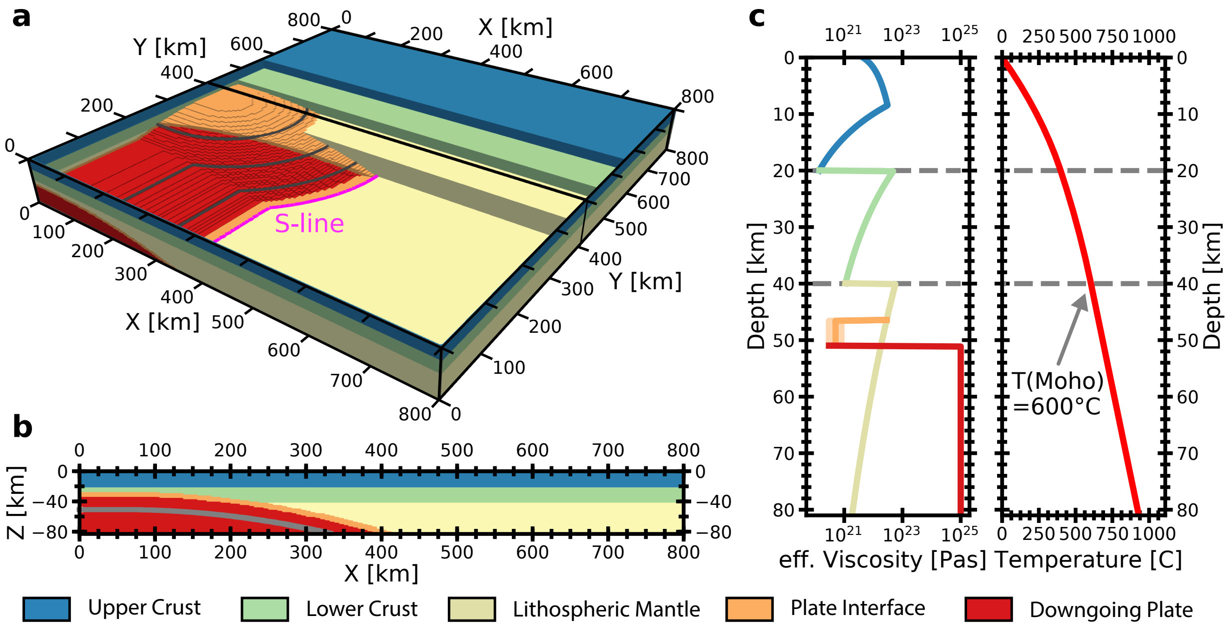

Figure 5.1: Model Setup: Geometry and initial values. **a** 3D-Geometry view: the upper plate comprises three layers (blue: upper crust, green: lower crust, yellow: lithospheric mantle). The lower plate (red) with the central indenter bulge (between $y \approx 200$ km and $y \approx 600$ km, shape indicated by gray contours) is overlain with a thin interface layer (orange). The magenta line indicates the S-line, which separates the velocity regime of the subducting, lower plate from that of the overriding, upper plate. **b** Geometry detail: vertical slice along $y = 400$ km. The gray contour indicates the background subducting slab beyond the indenter. **c** initial values of effective viscosity and temperature: colors denote the different layers, lighter hues of the interface layer viscosity indicate variations investigated in this study. Initial temperature profiles are identical across the model domain.

lower crust and lithospheric mantle, also represents the motion boundary between exhumation and subduction (panel d and e). Accordingly, surface rock uplift rates (panel b) show two continuous bands of uplift along the S-line with rates ranging between 5 and 6 $\mathrm{mm\,yr^{-1}}$. In contrast, uplift rates in the small peak above the indenter remain below 4 $\mathrm{mm\,yr^{-1}}$. This, in combination with the deeper source of material exhumed along the pro- and retro shear zones, leads to the pattern of apatite fission-track ages shown in panel c, in which the uplift region above the indenter is overshadowed by the two continuous bands of very young ages (< 1 Myr) along the S-line.

While the overall structure of deformation and uplift in these models remains the same over time, specific changes and trends can be observed. In general, a focusing and intensification of strain and uplift occurs as the model progresses. Panel b and c of Figure 5.3 depict surface rock uplift rates and strain rates at 4 Myr modeling time for the same views as in Figure 5.2b and d, respectively. These show that shear zones as well as surface rock uplift structures are wider and exhibit lower peak values at 4 Myr modeling time (Fig. 5.2) compared to those at 6 Myr (Fig. 5.3). In other words, rock uplift focuses and accelerates over time. However, the surface rock uplift rates along the central slice A-A' in Figure 5.3a reveal different behavior for the basal decollement and the orographic wedge. The two peaks in uplift rates created by the pro- and retro shear zone show a significant increase between 4 and 6 Myr modeling time, whereas uplift from the basal decollement is increasing evenly and more slowly.

Figure 5.4 gives insight into the sub-surface processes acting on the model and specifically the indenter. In panel 5.4a, the change of the indenter cross-section along dip is shown. A slight

Model Name	upper plate advance	erosion type	interface strength	lower plate	in Figures
HXW	half	flat	weak	deforming	5.5
HXM	half	flat	intermediate	deforming	5.2, 5.3, 5.4, 5.5
HXS	half	flat	strong	deforming	5.5
HXM-R	half	flat	intermediate	rigid	5.6
HFW	half	fluvial	weak	deforming	5.8
HFM	half	fluvial	intermediate	deforming	5.6
HFS	half	fluvial	strong	deforming	
HFM-R	half	fluvial	intermediate	rigid	5.6
NFW	no	fluvial	weak	deforming	5.7, 5.8, 5.9
NFM	no	fluvial	intermediate	deforming	5.7
NFS	no	fluvial	strong	deforming	5.7, 5.8
NFW-R	no	fluvial	weak	rigid	5.7, 5.8

Table 5.1: Overview of controlling parameters for model runs conducted in this study. The model names denote the values of the four controlling parameters:
upper plate advance: N (no advance) or H (half advance);
erosion type: X (flat) or F (fluvial);
coupling strength as per viscosity of the plate interface: W (weak, $3 \cdot 10^{21}$ Pa s), M (baseline, $5 \cdot 10^{21}$ Pa s), or S (strong, $8 \cdot 10^{21}$ Pa s);
lower plate dynamics: *none* (free deformation), -R (rigid)

forward motion of the entire down-going plate can be inferred. Panel b shows the vertical difference compared to the initial indenter shape. It depicts the forward push and rise of the indenter toe in a much clearer way. This motion is slow initially, but picks up speed as the model progresses. Panel c separates the contributions of the purely mechanical solution and the isostatic response to the indenter deformation. The mechanical solution represents a flattening and forward migration of the indenter, seemingly driven by the gradual subduction of material accreted at the trenchward model side. However, in combination with the retarding moment of isostasy, which always strives to push the model back into its original state of isostatic equilibrium, the observed forward and upward indenter motion results. Overall, the shape of the indenter adjusts towards that outlined by the stream lines in the vertical cross-sections of Figures 5.2 and 5.3.

5.3.2 Model Series 1: Half Upper-Plate Advance with Flat Erosion

The thin, weak plate interface layer takes a crucial function in mediating between the subducting and the overriding plate. Its strength does have a substantial impact on model dynamics, as can be seen from model results in Figure 5.5. There, a comparison of models HXW, HXS, and baseline model HXM is shown (all parameters identical except the viscosity of the plate interface). In panel a, surface rock uplift rates and relative deformation of the underlying indenter at 6 Myr modeling time are plotted. In combination with surface rock uplift rates in map view in panels f-h, one can see that the intensity and the separation of the localized indenter uplift field decreases with increasing coupling strength, while peak values and coherence of the uplift bands increase. Accordingly, strength of the basal decollement decreases at the expense of the pro-side shear zone as the coupling increases (panels b-d) and material motion is steeper in the model center ($X \approx 400$ km). Furthermore, upward deformation of the indenter is strongest in the strong coupling model HXS, whereas the weak coupling model HXW shows a flattening or pull-back motion. In the compiled

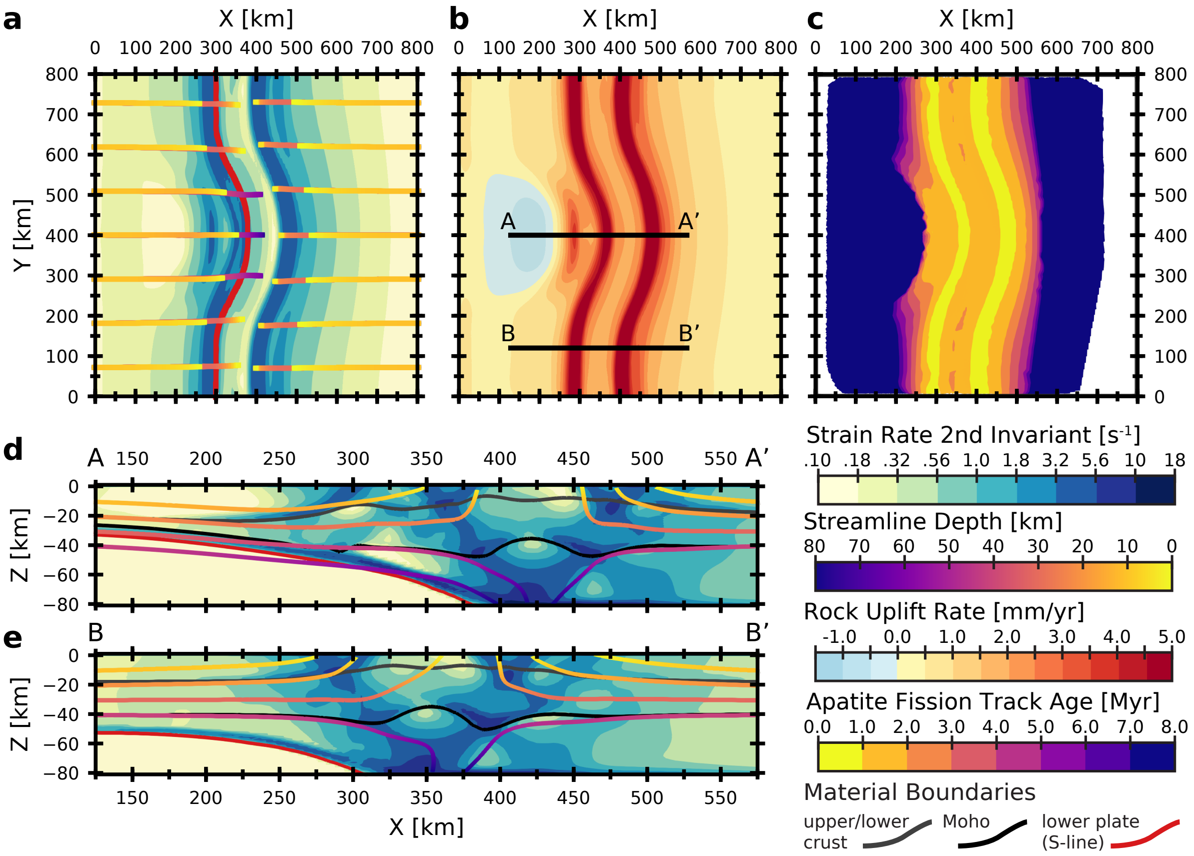

Figure 5.2: Motion results of baseline model HXM (half-advancing, flat erosion, baseline interface) after 6 Myr modeling time. Deformation is dominated by the orogenic wedge originating at the S-line. Above the indenter, a basal decollement has formed, but is weak in comparison to the pro- and retro-shear zones.
a Map view of Strain Rates at 5 km depth and streamlines originating at 10 and 30 km depth. **b** Surface Rock Uplift Rates **c** Predicted apatite fission-track ages **d** Strain Rates vertical slice at Y = 400 km **e** Strain Rates vertical slice at Y = 120 km.

central cross-sections shown in panel 5.5a, one clearly sees the transition of uplift created by the basal decollement, strongest in the weak plate interface model HXW, to the two uplift bands generated by the two shear zones originating at the S-line in the strong plate interface model HXS. Deformation of the subducting plate also depends on the interface strength. The weak interface model HXW shows a slight flattening, which gradually transitions to a steepening of the indenter toe with increasing interface layer viscosity.

Additionally, the rigid indenter model HXM-R (panels e and i) can be compared against the baseline model HXM which has a deformable lower plate. Overall, the geometry of active structures does not change, but shortening is accommodated differently. In the rigid indenter model HXM-R, the basal decollement above the indenter is more active, causing less subsidence and more upward deflection instead, leading to higher rock uplift rates above the indenter. Accordingly, the amount of strain along the pro- and retro shear zone is reduced. In model HXM with a deforming indenter, the pro- and retro shear zones accommodate most of the shortening. Thus, the indenter uplift field is shifted to the right and appears less significant compared to the uplift bands of the orogenic wedge. Indeed, model HXM-R rather shows a close resemblance to the weak interface model HXW both in the geometry of shear zones as well as in the pattern of resulting rock uplift.

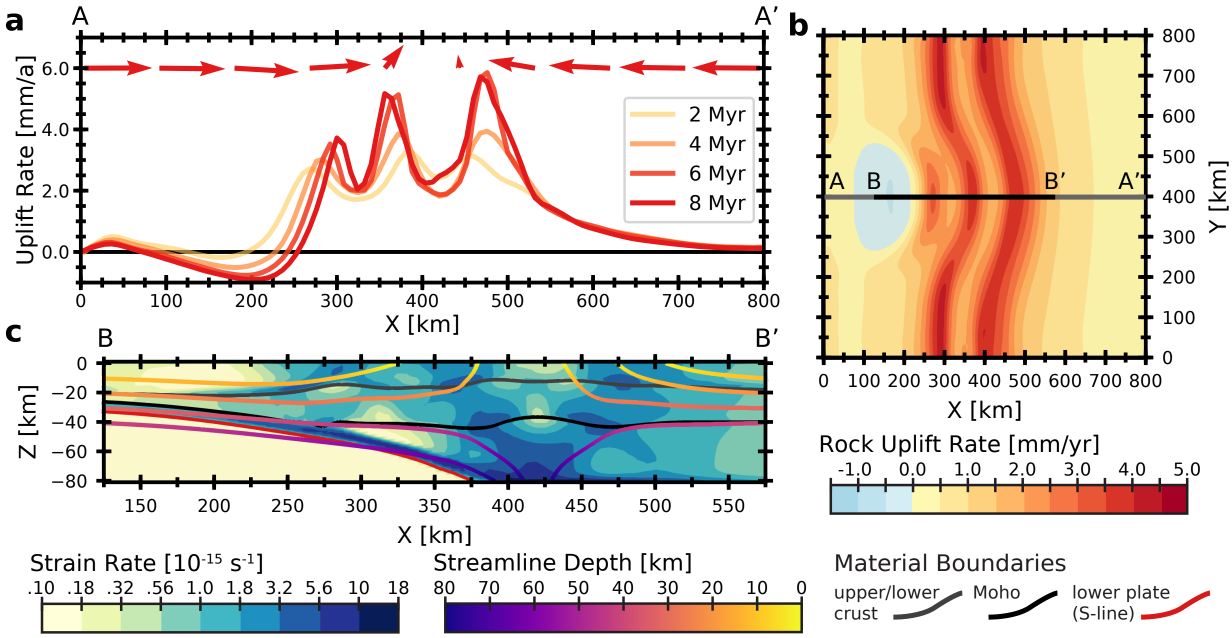

Figure 5.3: Temporal evolution of baseline model HMX (half-advancing, intermediate coupling, and flat erosion). **b** and **c** show model results after 4 Myr modeling time, compare with Figure 5.2.
a Evolution of Rock Uplift rates along central slice from 2 Myr to 8 Myr. Red arrows indicate the direction of motion along the slice (x- and z-component). **b** Map view of surface rock uplift rates **c** vertical slice at Y = 400 km showing strain rates.

5.3.3 Model Series 2: Half Upper-Plate Advance with Fluvial Erosion

The four models shown in Figure 5.6 repeat the configuration of model series 1, but with a more realistic fluvial erosion model. The contrasts between those two modes of erosion have been discussed in detail in previous chapters and are likewise observed here. First and foremost, rock uplift is distributed over a wider area, with significantly reduced peak values. The large-scale pattern, i.e. the position of regions high and low uplift rates, as well as their strength in relation to each other, mostly remains the same. However, the emerging topography induces modifications to the small-scale pattern, so that highest values of rock uplift can be found in valleys, where the erosion potential is highest.

In the half-advance, fluvial erosion models HFS, HFM and HFW, the strength of the plate interface layer has a comparable effect on model dynamics as observed previously. In case of a strong interface (model HFS, panel b and f), shortening is predominantly accommodated by the two major shear zones rooting to the S-line. With decreasing interface strength, strain localization in those reduces and shifts towards the indenter. However, strain rates and resulting uplift only reach much lower values in this area, both in comparison to their flat erosion counterparts as well as to the fixed-indenter model HFM-R (panels e and i). In all three free deformation models, uplift above the indenter does not exceed 3.0 mm yr^{-1}. Baseline and strong interface models HFM and HFS show a slight increase at the retro-side uplift band of 3.5 mm yr^{-1} and 4.1 mm yr^{-1}, respectively. Deformation of the lower plate has the same dependency on interface strength, but has been shifted overall to show an even stronger pull-back and flattening.

In contrast to the models with free deformation, the rigid indenter model HFM-R exhibits a clear focus of rock uplift towards the area above the indenter (peak rock uplift rates at 4.0 mm yr^{-1}),

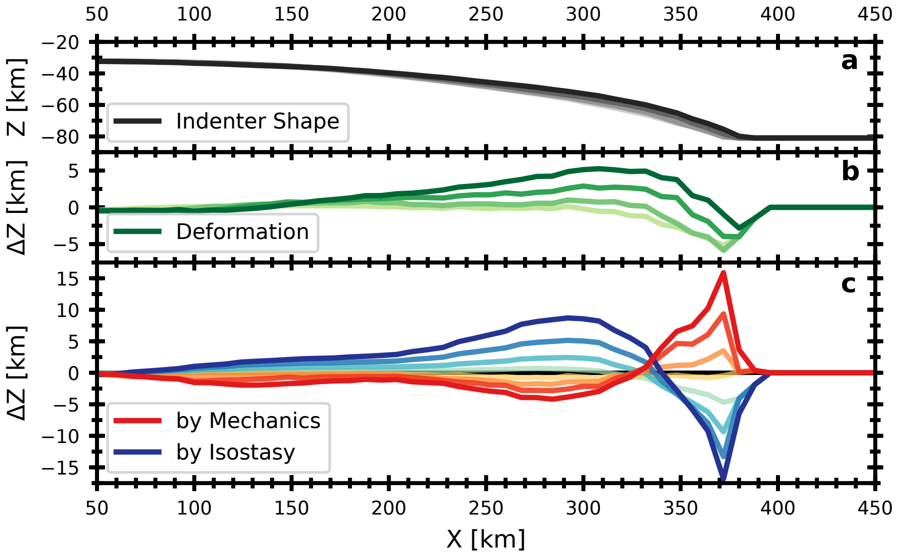

Figure 5.4: Indenter deformation details over time for central cross-section at Y = 400 km (along dip). Snapshots at 2 Myr to 8 Myr from light to dark shades.
a Evolution of lower-plate (indenter) cross-section. **b** Relative deformation of indenter compared to its initial shape. **c** Contributions of tectonic motion and isostatic response to total indenter deformation.

created by a wedge structure in the upper crust that extends down to the plate interface. This geometry of shear zones is loosely equivalent to the weak interface model HFW, although strain rates are significantly lower there.

5.3.4 Model Series 3: No Upper-Plate Advance with Fluvial Erosion

Previous chapters of this thesis show that relative plate motion has a first-order effect on how shortening is accommodated and the resulting pattern of rock uplift. Therefore, the effect of plate interface strength and indenter deformation style was also investigated under no-upper-plate-advance conditions with fluvial erosion. These four models (NFS, NFM, NFW, and NFW-R) are shown in Figure 5.7. The difference to the half-advance models in Figure 5.6 strikes the eye.

Shortening in all freely deforming models (NFS, NFM, and NFW) primarily above the indenter, while the pro- and retro shear zones rooting to the S-line are rather weak (strain rates $<1 \cdot 10^{-15}\,\mathrm{s}^{-1}$). Instead, strain is transferred along the indenter toe towards a secondary nucleation point, which is situated where the overriding plate's Moho intersects with the subduction interface. As coupling decreases, the nucleation point migrates further up the indenter. From this nucleation point, a strong shear zone connects up to the surface. In models NFS and NFM, this takes the form of a broad, retro-dipping shear zone. In the weak interface model NFW, a small pop-up structure forms in the upper crust. These structures generate an area of focused and accelerated uplift directly above the indenter apex, especially in the weak interface model NFW (panel h). For stronger coupling, structures gradually shift to the right and more uplift occurs along the S-line besides the indenter as well.

In this model series, the comparison with a rigid indenter configuration is done of the weak plate interface, since this exhibits the lowest indenter deformation. Model NFW-R shows lower rock uplift

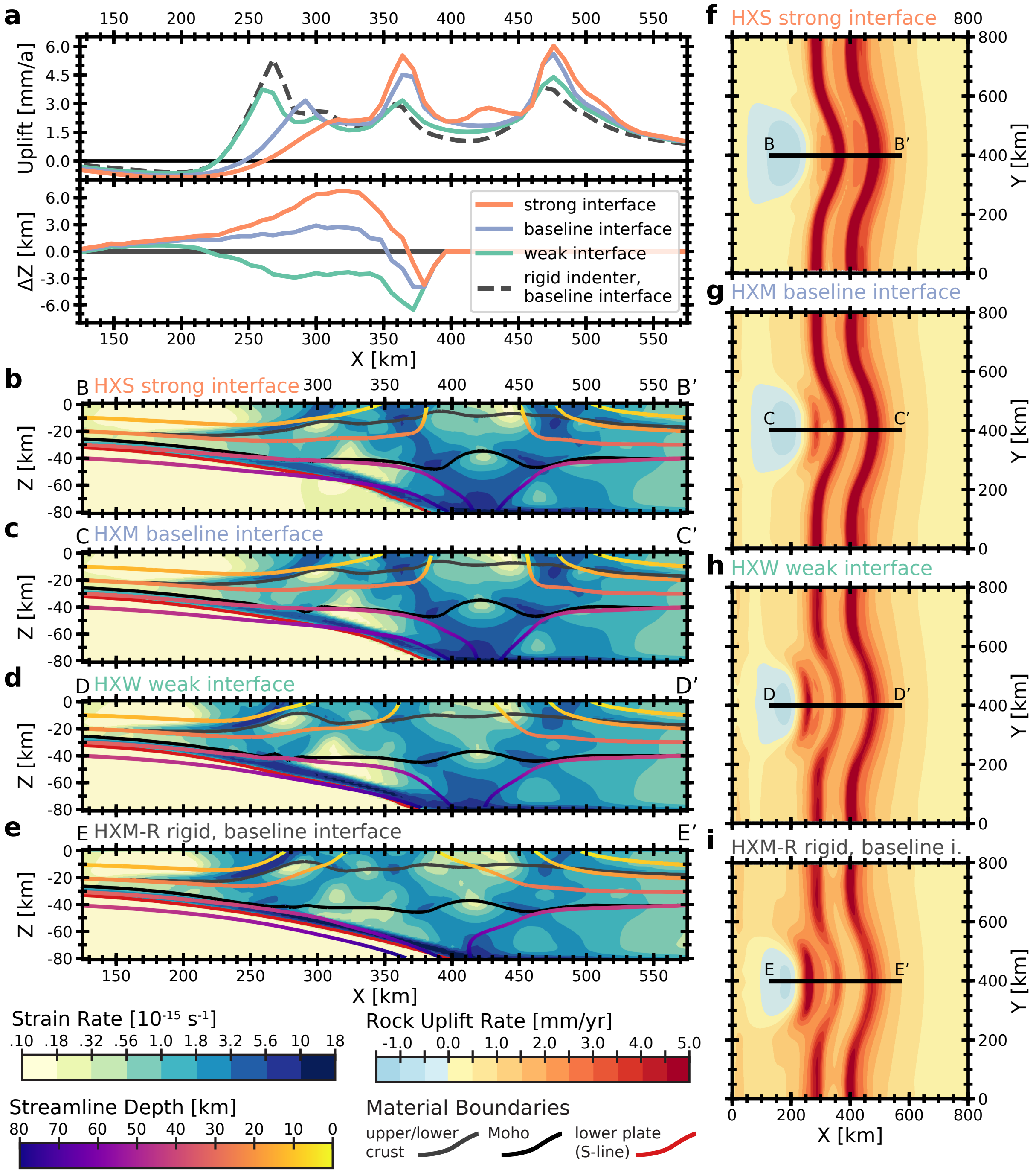

Figure 5.5: Comparison of upper plate deformation for half-advance and flat erosion: models HXS (strong interface), HXM (baseline interface), HXW (weak coupling), and HXM-R (intermediate coupling with rigid lower plate). Cross-sections of panels **a** to **e** are at Y = 400 km and modeling time is 6 Myr.
a Overview of rock uplift rates and relative indenter deformation. **b-e** Strain rates and motion streamlines for vertical slice at Y = 400 km. **f-i** Map view of surface rock uplift rates.
With decreasing interface strength, deformation shifts to the basal decollement above the indenter and forms a separated area of uplift in the model center. Models HXW and HXM-R show a close resemblance.

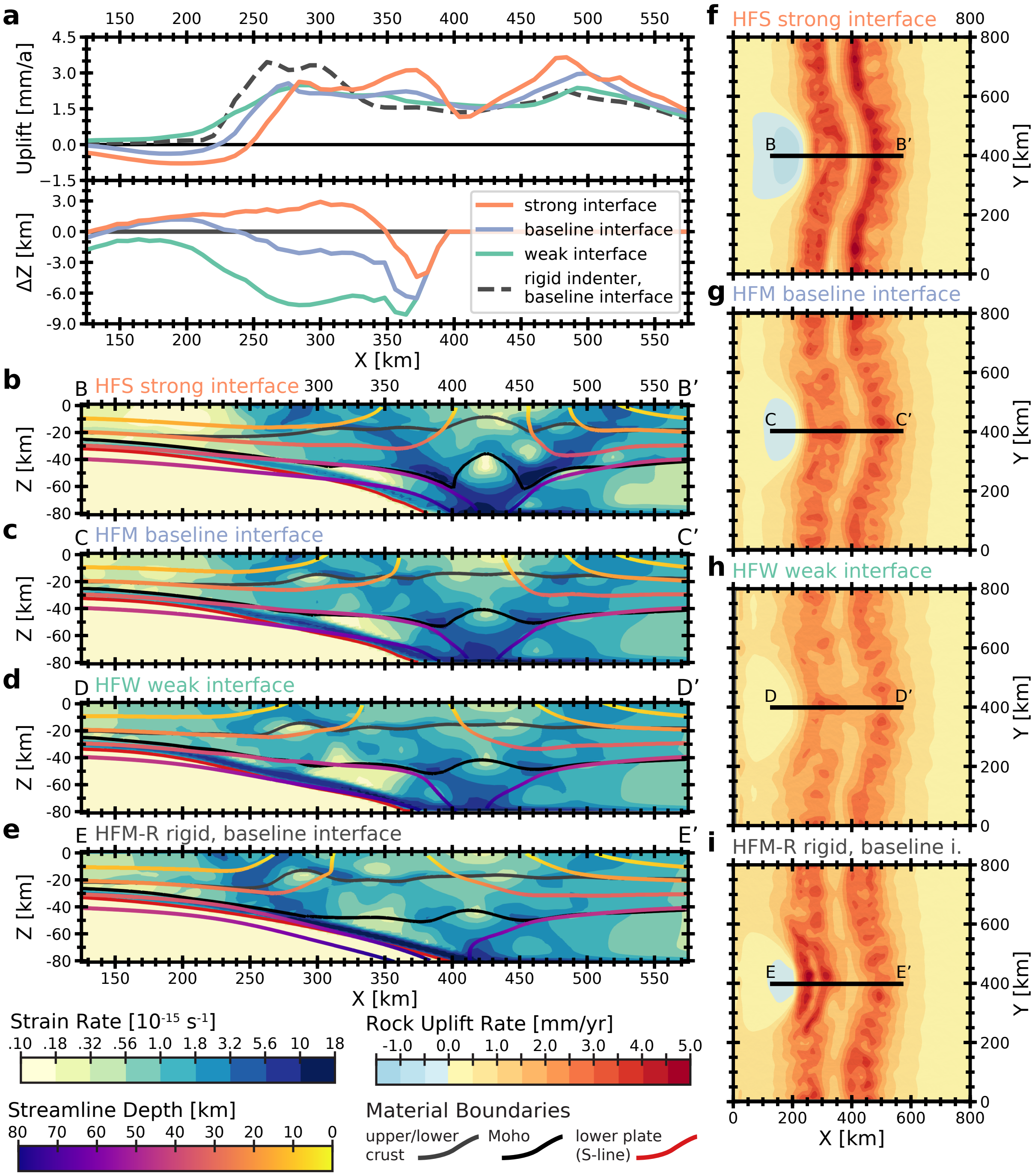

Figure 5.6: Comparison of upper plate deformation for half-advance and fluvial erosion: models HFS (strong interface), HFM (baseline interface), HFW (weak coupling), and HFM-R (baseline coupling with rigid lower plate). Cross-sections of panels **a** to **e** are at Y = 400 km and modeling time is 6 Myr. **a** Overview of rock uplift rates and relative indenter deformation. **b-e** Strain rates and motion streamlines for vertical slice at Y = 400 km. **f-i** Map view of surface rock uplift rates.
With decreasing interface strength, deformation shifts away from the retro-shear zone. However, slab rollback reduces rock uplift rates above the indenter. Only the rigid indenter model HMF-R shows focused uplift there.

rates throughout, especially to the left of the S-line. The area of focused uplift above the indenter also shows the highest values overall, but it is small and weak in comparison to the deforming indenter model NFW. This uplift is driven by a steeply dipping reverse fault in the upper crust. Strain transfer along the indenter, as observed in the deforming indenter models, does not occur.

5.4 Discussion

5.4.1 Results Summary

For this study, 12 model runs were conducted by varying parameters of plate interface layer viscosity, upper plate advance, and two different modes of erosion for both rigid and deforming subducting plates. All models share common traits in their dynamics of upper plate deformation, which is focused in three main structures: a lithospheric-scale orogenic wedge, comprising (1) pro- and (2) retro shear-zone rooting to the S-line, and (3) a structure (basal décollement or crustal wedge) situated above the indenter apex. The distribution of strain between these structures is interdependent, a stronger separate indenter structure goes hand in hand with a weaker pro-side shear zone. With respect to the investigated parameters, a number of trends can be identified. Firstly, higher viscosity of the plate interface, i.e. stronger mechanical link between subducting and overriding plate, favors accommodation of shortening in the orogenic wedge and reduces the impact of the indenter structure on the overall deformation. A weaker interface enhances the disparity between the indenter and the background subducting plate and gives rise to a focused region of uplift in the model center. Using a rigid or deforming subducting plate affects upper plate deformation, but the response depends on other factors. In half advance models, a rigid lower plate intensifies localized uplift above the indenter, while the opposite is observed for no-advance scenarios. Finally, models with no upper plate advance show a much stronger uplift peak above the indenter compared to the half-advance scenarios.

5.4.2 Role of Plate Interface Strength

The strength of the plate interface layer is partially constrained by the model setup. In case of too low viscosity, all accreted material is exhumed at the model's left side (X = 0 km). For too high values, however, the downward drag of the subducting plate will result in unrealistically fast subsidence. Moreover, the model's coarse resolution does not allow to infer estimated values for frictional and rheologic parameters from petrologic or geodynamic studies of actual subduction interfaces. The model's subduction shear zone spans two to three neighboring finite element cells, equivalent of 3–5 km, significantly larger than in nature. Nevertheless, within the model-inherent viscosity range, the effect of the subduction interface strength can be investigated.

Figure 5.5 offers this comparison under half-advance, flat erosion conditions and reveals a clear trend: a stronger interface results in reduced uplift above the indenter and increased uplift in the two bands along the S-line. For the strong interface model's uplift rates (Fig. 5.5f), the presence of the indenter created a bend in the two continuous uplift bands. Only in the weak coupling scenario, the indenter décollement is fully separated from the orogenic wedge. A closer inspection of the nucleation point reveals the mechanism behind this: for a weaker plate interface layer, a) the two shear zones radiating upward from the nucleation point grow stronger and b) the Moho gets warped locally there. In other words, the plate interface needs to be weak enough for an

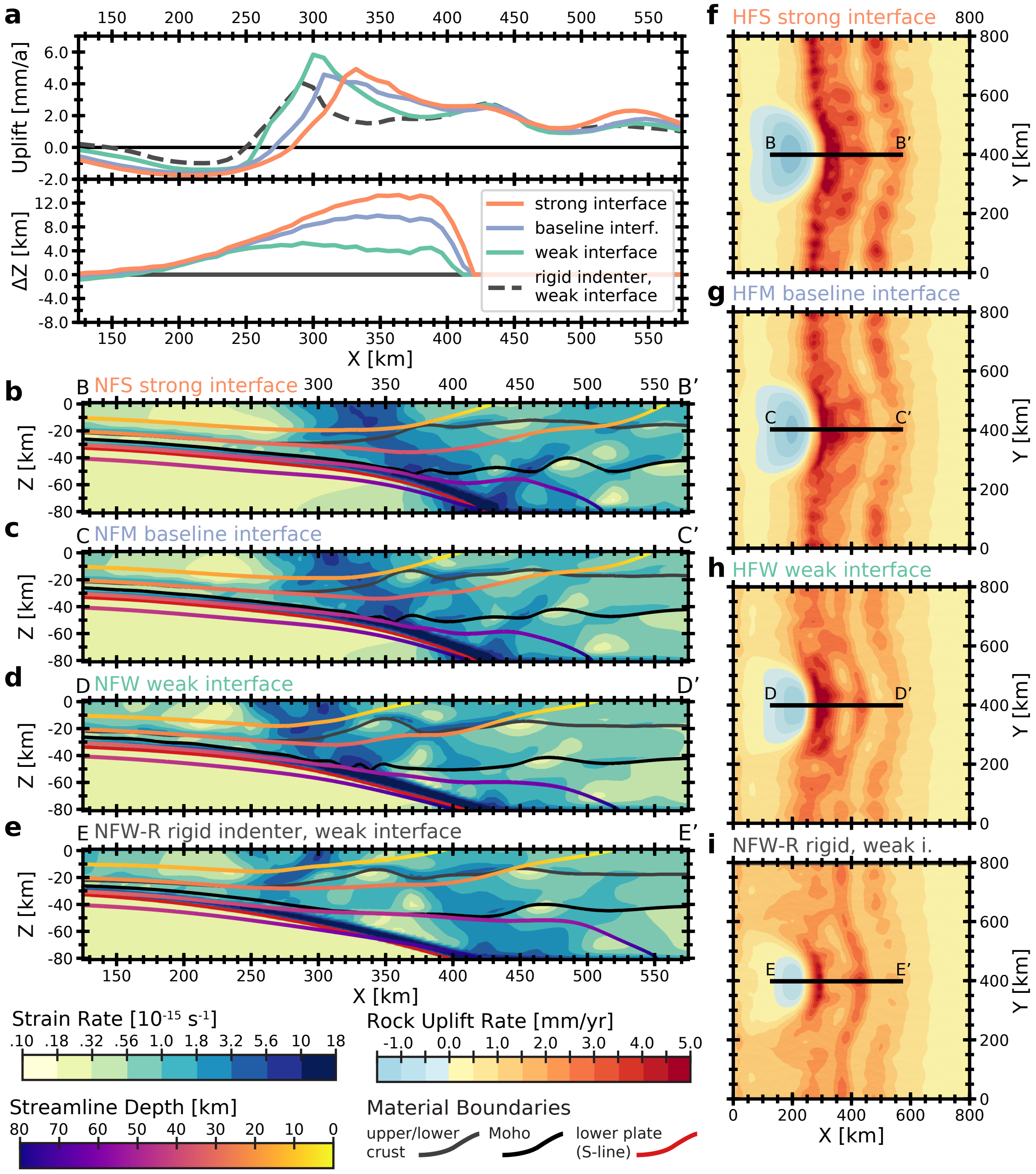

Figure 5.7: Comparison of upper plate deformation for no-advance, fluvial erosion: models NFS (strong interface), NFM (intermediate interface), NFW (weak interface), and NFW-R (weak interface and rigid lower plate). Cross-sections of panels **a** to **e** are at $Y = 400$ km and modeling time is 6 Myr.
a Overview of rock uplift rates and relative indenter deformation. **b-e** Strain rates and motion streamlines for vertical slice at $Y = 400$ km. **f-i** Map view of surface rock uplift rates.
With decreasing interface strength, rock uplift besides the indenter apex decreases, but increases directly above it. The rigid indenter model shows reduced rock uplift overall.

independent indenter structure to form, otherwise the induced upward motion of material is too weak to stand out against the uplift created by the pro-side shear zone. This becomes even clearer for the no-advance, fluvial-erosion scenarios shown in Figure 5.7. For the weak coupling case, a strong pop-up structure forms in the upper crust above the indenter while the pro-side shear zone is very weak, resulting in a clear bull's-eye pattern of uplift. On the contrary, strong coupling between overriding and down-going plate results in a single merged structure of indenter- and the pro-side shear zone and consequently only a small increase in uplift rates above the indenter.

For the half-advance fluvial erosion models in Figure 5.6, the transition away from deformation in the retro-side shear zone with decreasing interface strength can also be observed. However, this does not result in increased uplift on the pro-side, rather in a general reduction of rock uplift rates. Most likely, the stronger deformation of the subducting plate is the root cause here, which will be discussed in the following section.

5.4.3 Effect of Deformable Indenter

Across all models, deformation of the indenter and its effect on upper plate deformation is quite varied. The vertical indenter displacement in Figures 5.5–5.7 shows slab rollback with flattening (downward displacement everywhere: models HXW (Fig. 5.5), HFW, and HFM (both Fig. 5.6)), rollback with steepening (mostly upward displacement, but downward at the toe: models HXM, HXS (Fig. 5.5), and HFS (Fig. 5.6)), as well as slab advance with steepening (upward displacement everywhere: models NFW, NFM, and NFS (Fig. 5.7)). Additionally, each model series contains one model with rigid indenter for direct comparison. Here, too, different responses can be observed both in the organization of shear zones as well as in the pattern of rock uplift rates. In general, in models with a rigid lower plate, deformation shifts towards the structure above the indenter and reduces localization of strain in the retro-side shear zone. However, only in the flat-erosion model HXM-R does this reorganization result in increased uplift above the indenter. In the fluvial-erosion model HFM-R, the simultaneous rollback and flattening motion of the indenter takes up any additional uplift. In the no-advance scenarios, the opposite effect can be observed (Fig. 5.7). The forward push and steepening of the indenter create additional uplift, so that the deforming indenter models show increased rock uplift rates above the indenter.

Table 5.2 lists the vertical and horizontal deformation of the indenter at $\mathrm{Y} = 400\,\mathrm{km}$ for all models. All no-advance model scenarios show forward motion ($\Delta\mathrm{X} > 0$), whereas half-advance models exhibit slab retreat. Within each model set, the indenter advances and rises more with increasing interface strength. This appears plausible as the indenter shape is not modeled to actively change, but rather deforms within the overall velocity field and isostatic compensation. The horizontal motion is driven by the balance of subduction to upper plate advance fractions of the overall shortening, while an increased coupling to the overriding plate elicits stronger deformation. This changes the overall model behavior in contrast to a non-deforming, rigid subducting plate.

The main driver of the differences in upper plate deformation most likely lies in the changed slope of the lower plate, as well as the position of the detachment point and the mechanical coupling between subducting and overriding plate by the interface layer. These parameters govern whether it is energetically favorable to partition the strain into multiple structures or transfer it along the subduction interface in order to form a single structure. The combination of these parameters determines the final equilibrium state towards which the model trends.

Furthermore, it needs to be noted that the amount of deformation due to isostatic adjustments can

Model Abbreviation	max. ΔZ [km]	avg. ΔZ [km]	ΔX at toe [km]
NFW	5.32	2.32	14.61
NFM	9.90	3.82	27.52
NFS	13.35	4.58	34.85
HFW	0.00	−3.80	−26.92
HFM	1.18	−0.61	−20.91
HFS	2.91	1.41	−11.11
HXW	0.69	−0.89	−18.60
HXM	2.90	1.35	−10.06
HXS	6.78	2.71	−4.45

Table 5.2: Deformation of indenter after 6 Myr modeling time. Maximum and average vertical deformation for $X > 100\,\mathrm{km}$ and horizontal deformation of the indenter toe ($Z = -75\,\mathrm{km}$). Values refer to a 40 km wide swath around $Y = 400\,\mathrm{km}$.

locally exceed mechanical deformation (see Fig. 5.4). However, the isostasy module in DOUAR does not take rheology into account in its calculations, only the total column weight as defined by the material densities and a global effective elastic thickness. Therefore, one cannot model different degrees of rigidity on the subducting plate by using different material properties, because this would only affect the mechanical component of deformation.

5.4.4 Rapid, Localized Uplift

The no-upper-plate-advance, weakly coupled fluvial erosion model scenario (NFW, Fig. 5.7) stands out among the other scenarios conducted in this study. It shows the strongest focusing of uplift in the area above the indenter with uplift rates of up to $6.3\,\mathrm{mm\,yr^{-1}}$ and a bull's-eye pattern of rapid and localized uplift. Figure 5.8 illustrates that this bull's-eye focus is not driven by one single parameter, but rather through the combination of multiple factors. For half upper-plate advance, strong interface, or a rigid lower plate this unique focus is lost. The no-advance boundary conditions favor uplift on the orogen's trenchward side, compared to the almost symmetrical profile of rock uplift rates in model HFW (panel b). Model NFS (panel c) also shows highest rock uplift rates on the orogen's left side, but due to the stronger mechanical coupling, uplift is shifted slightly towards the right and forms one bigger, cohesive area of uplift.

In comparison with the rigid NFW-R (panel d), the indenter's upward deformation seems to make the distinction. Both models show an area of focused uplift, but the rate of exhumation is significantly higher with deforming indenter, exactly in that location where upward displacement of the lower plate occurs (see Figure 5.7). Thus, only model NFW shows this clear and isolated peak in both cooling age systems (apatite (U-Th)/He and apatite fission-track) as well as in model uplift rates. Note that AFT ages are more significant for these settings, because modeled uplift rates are too fast to create much variance in predicted AHe ages.

Fittingly, the pattern of rock uplift rates and cooling ages are reflected in elevation swath profiles (Figure 5.8). All no-advance models show an asymmetric elevation profile with steep slopes on the pro-side in contrast to the more symmetric half-advance model HFW. Moreover, minima in the predicted cooling ages coincide with high local relief. Here again, model NFW stands out, showing the highest local relief and a clear cut between pro- and retro-side orogen slopes.

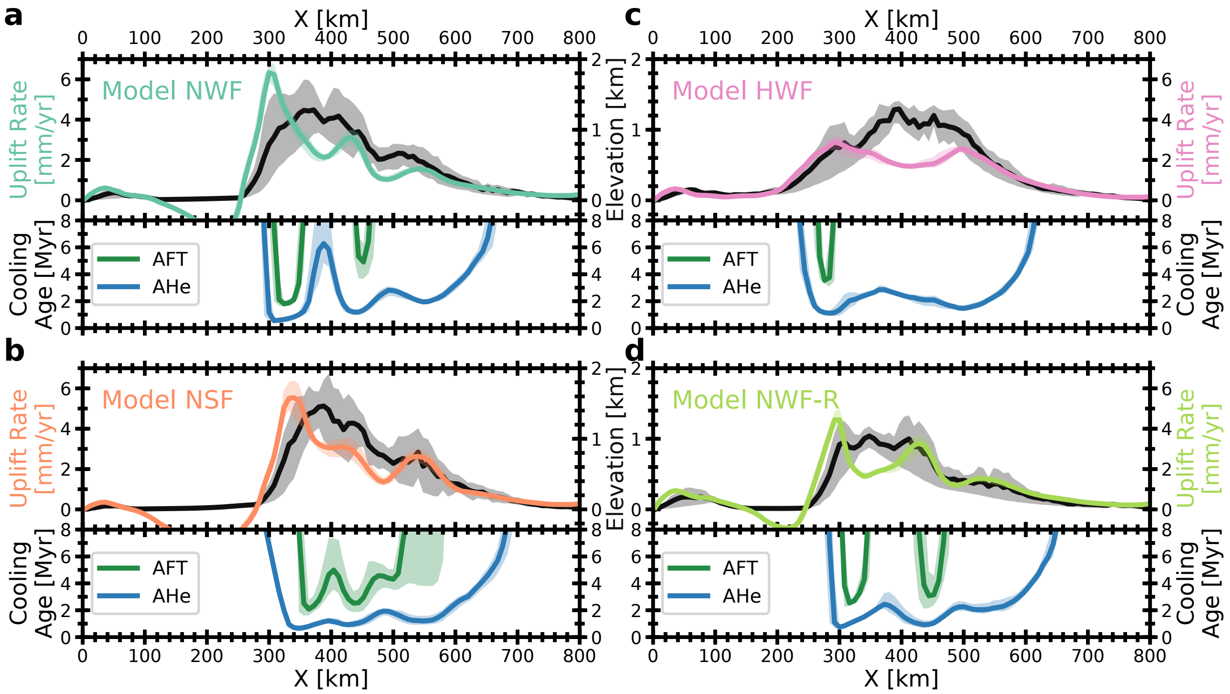

Figure 5.8: Swath profiles of Rock Uplift Rates, Model Elevation, and predicted Cooling Ages (apatite (U-Th)/He and apatite fission-track) for fluvial erosion scenarios. All panels show the central cross-sections along convergence (Y = 400 km) at 6 Myr modeling time.
Formation of rapid, focused uplift is most distinct for model NWF (**a** no advance, weak coupling, fluvial erosion), all other models differ in but one parameter, but show less focusing: **b** strong coupling, **c** half advance, **d** rigid lower plate.

The temporal evolution of model NFW (see Figure 5.9) also highlights the close link between tectonic rock uplift rates and focused erosion. In the early model stages, the rock uplift rates on the left peak are 1.8 times faster than at the right peak (2.3 vs. 1.3 $\mathrm{mm\,yr^{-1}}$ for X = 280 km and X = 420 km at 2 Myr modeling time, respectively), the ratio increases to 2.7 at 8 Myr modeling time (6.8 vs. 2.5 $\mathrm{mm\,yr^{-1}}$). The initial impulse must be attributed to tectonic conditions. However, the formation of a deeply incised valley with high local relief is surely an inherent part of the acceleration and focusing of rock uplift that can be observed. As reasoned in Chapter 3, it is tectonics that sets the stage and erosion that creates the focusing impulse.

5.4.5 Relation to Other Studies

The results of this study both complement and expand previous results. In Koptev et al. (2019) (Chapter 4), a clear link between a weak lower crust and the formation of a bull's-eye pattern was uncovered, analogous to the effect of the weak coupling layer of this study. With regards to the relative upper plate motion, however, this study finds the fastest localized uplift in a no-advance scenario in contrast to a half-advance scenario in Nettesheim et al. (2018) (Chapter 3). From this, the conclusion may be drawn that coupling strength is one of the governing factors in the emergence of localized uplift. Only if smaller, local structures can form, differences in depth and dip of the down-going plate can take effect. Otherwise, these differences will be overprinted by the large-scale regional settings. This sensitivity of upper plate deformation to the strength of the subduction interface has been identified as an important factor in mountain building (see e.g. Lamb and Davis

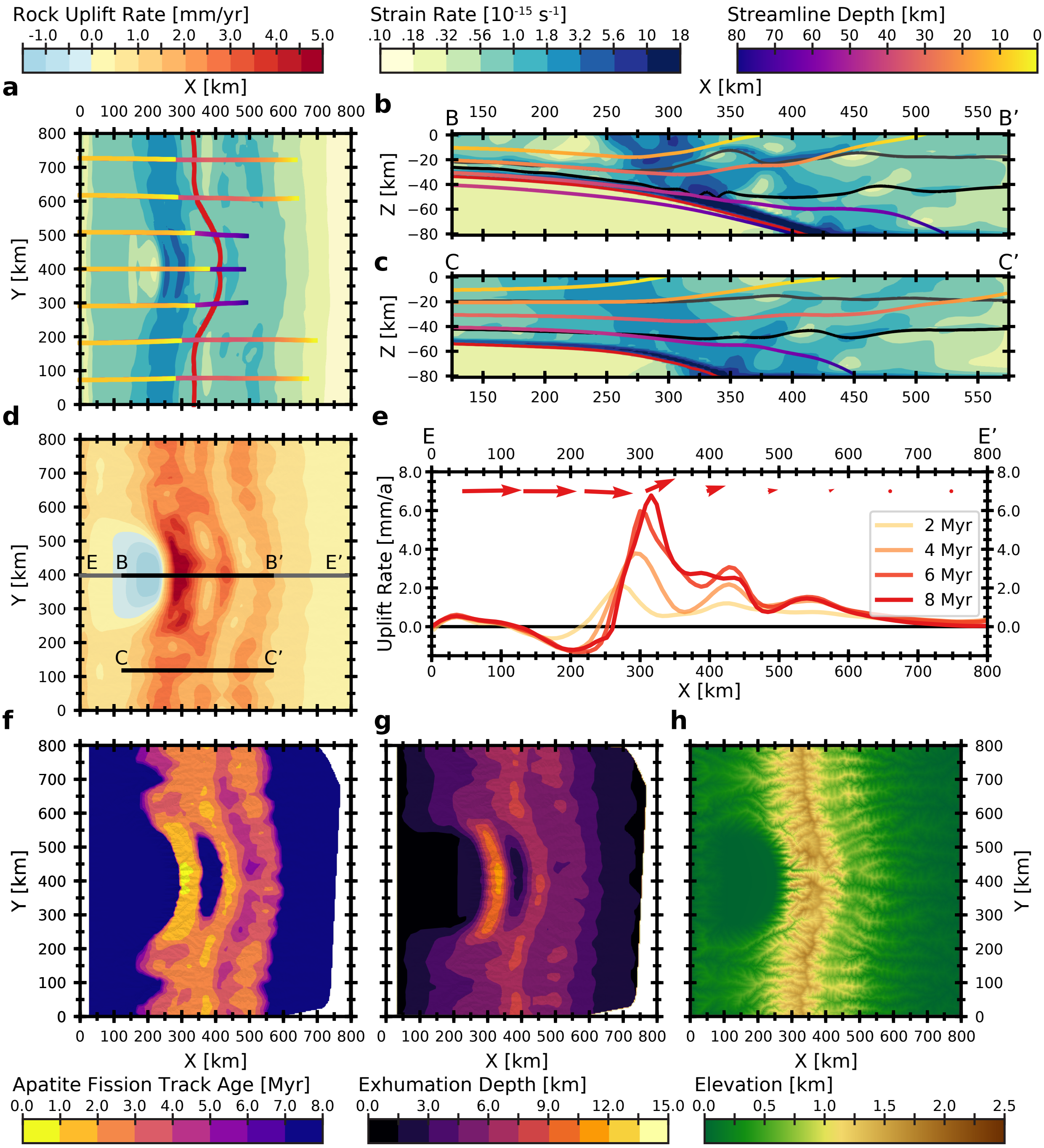

Figure 5.9: Comprehensive overview of model NWF (no advance, weak coupling, fluvial erosion) at 6 Myr modeling time. This scenario shows the strongest focusing of rock uplift in a bull's-eye pattern within this study.
a Map view of Strain Rates at 5 km depth and streamlines originating at 10 and 30 km depth. **b** and **c** Strain Rates vertical slice at Y = 400 km and Y = 120 km, respectively **d** Surface Rock Uplift Rates **e** Temporal evolution of Rock Uplift Rates along Y = 400 km **f** Predicted apatite fission-track ages **g** Exhumation Depth **h** Elevation.

2003). Even further, the retarding effect of higher mechanical coupling on formation of localized uplift patterns might explain the lack of a clear trend in erosion rates along strike at the Andean syntaxis (Starke et al. 2017).

In contrast, the subducting's plate mode of deformation (rigid vs. freely deforming) shows a varied influence on the formation of a bull's-eye uplift pattern. Under half upper-plate advance, the rigid indenter provides an insurmountable obstacle to the opposing flow and thus forces material upward. This creates the rapid and focused uplift postulated by Bendick and Ehlers (2014). Even more, the absence of increased uplift above the indenter in the half-advance fluvial-erosion models with deformable indenter must be attributed to the roll-back motion of the subducting plate. Without upper plate advance, however, it is the deforming indenter model that shows the strongest "bull's-eye" uplift pattern.

5.5 Conclusion

In this chapter, the effect of lower plate properties on upper plate deformation in numerical models of convergent plate corners with indenter geometry is investigated. The subducting plate has hitherto been treated in a simplified manner by explicitly keeping the geometry constant over time in previous studies. Nine models with freely deforming lower plate show that this simplification is not required. With the modification of a slightly thicker plate interface layer, it is possible to lift this artificial constraint and model the joint evolution of overriding and subducting plates. Furthermore, the viscosity of the plate interface layer, which determines the degree of mechanical coupling between overriding and subducting plate, was found to play a crucial role in model dynamics. Concerning the formation or absence of rapid and focused rock uplift in the upper plate, as observed at some plate corners, the following conclusions can be drawn:

1. Low viscosity of the plate interface layer leads to increased focusing of uplift above the indenter. A strong interface favors accommodation of shortening in the orogenic wedge, both above and besides the indenter, creating only small differences in how rock uplift is distributed along strike. In contrast, weak coupling will facilitate the formation of separate shear zones above the indenter, so that the induced upward material motion will form an isolated region of uplift.

2. Deformation of the lower plate depends on the tectonic boundary conditions and does not yield a clear effect on upper plate deformation by itself. Driven by three forces – (1) material accretion and downward drag on the trenchward model side, (2) the push of an advancing overriding plate, and (3) the isostatic compensation – models in this chapter show varying degrees of slab advance as well as rollback. Nevertheless, it can be asserted that the change in geometry affects how and where shear zones form in the upper plate. In particular, the dip angle at the intersection of the subducting plate with the Moho exerts a crucial control.

3. Lower plate retreat impedes focused uplift in the overriding plate. The upward or downward displacement of the subducting plate adds an additional component to overall motion, so that resulting rock uplift at the surface can be enhanced or reduced. This reduction in rock uplift rates observed with an advancing upper plate supports the hypothesis postulated by Bendick and Ehlers (2014) that it is the rigidity of the subducting indenter which generates rapid and focused uplift.

6 Upper Plate Deformation At Tightly Curved Plate Corners

6.1 Introduction

In previous chapters of this thesis, the subducting plate was modeled as spherical indenter bulge located on top of a cylindrical background plate. While this symmetrical setup applies well to areas such as the Olympic Mountains, other plate corners are curved more tightly. One area of particular interest is the southern Alaskan plate corner. Plate geometry reconstructions show an asymmetric shape, with flat-slab subduction to the west and a prominent, much steeper central indenter bulge (Hayes et al. 2012; Pavlis et al. 2019). This inferred geometry allows to develop a generic geodynamic model that may contribute to deepen our understanding of the mechanics of this region and other tightly curved plate corners.

Figure 6.1 shows the most important tectonic features of southern Alaska. At the plate corner, the Pacific-North American plate boundary transitions from transform faulting along the Candian west-coast (Fairweather fault) to subduction below the Alaska and the Aleutian island arch (Aleutian Megathrust). (e.g. Plafker and Berg 1994). The Alaskan orocline created from this subduction comprises several mountain ragnges with rugged, glaciated topography and peak elevations above 5000 m. The tectonic history of this region is characterized by the accretion of multiple allochthonous terranes since the Creatceous (Plafker and Berg 1994). The latest in the succession, the Yakutat Microplate, is subducting obliquely beneath North America at least since the Cenozoic (Haeussler et al. 2008; Plafker et al. 1989). It has been subducted and underplated about 500 km and created an stark contrast in the geometry of the subduction plane (Eberhart-Phillips et al. 2006; Fuis et al. 2008; Worthington et al. 2012). To the west, the pacific plate subducts steeply, while at the plate corner, a prominent indenter structure subducting at a shallow angle has formed (Hayes et al. 2012; Pavlis et al. 2019, see inferred plate contours in Figure 6.1). Numerous studies have contributed to unraveling the topographic response to this complex geodynamic setting. Among these, studies from the St. Elias Mountains have found evidence focused exhumation with rates exceeding 5 $\mathrm{mm\,yr^{-1}}$ (Berger et al. 2008; Enkelmann et al. 2015, 2010; Falkowski et al. 2014). This bull's-eye uplift was transient and has shifted over time due to changing tectonic and climatic conditions (Enkelmann et al. 2017; Falkowski et al. 2016), which identify this area as potential tectonic aneurysm. In addition, the central Chugach mountains are another location of focused exhumation, although exhumation rates are much slower at ~0.7 $\mathrm{mm\,yr^{-1}}$ (Arkle et al. 2013; Buscher et al. 2008).

Koons et al. (2010) applied numerical modeling to gain insights on regional crustal deformation. They observed a model evolution with two orogens that broadly corresponded to the St. Elias Mountains and the Central Alaskan Range. Results were both time- and material-dependent and allowed inferences about orogenesis. Despite that, a number of points reduce the general applicability of their model. First, the choice of a straight, flat ramp and uniform material properties is surely an oversimplification, and, just as the usage of a constant thermal state, falls short of today's improved modeling capabilities. Model results were reported for a time span of 350 kyr, i.e. did not adequately depict geologic timescales. In addition to these model caveats, new thermochronologic data of the wider region have been acquired in recent years, which allows for a better understanding and model validation. By using the improvements developed in this thesis – a fully-coupled themomechanical model with coupled erosion, a more realistic geometry, as well as thermochronometric age prediction, a better representation of this region can be achieved. However, it must be noted that this model still is a rather generic approach cannot fully represent the Alaskan plate corner with all its details.

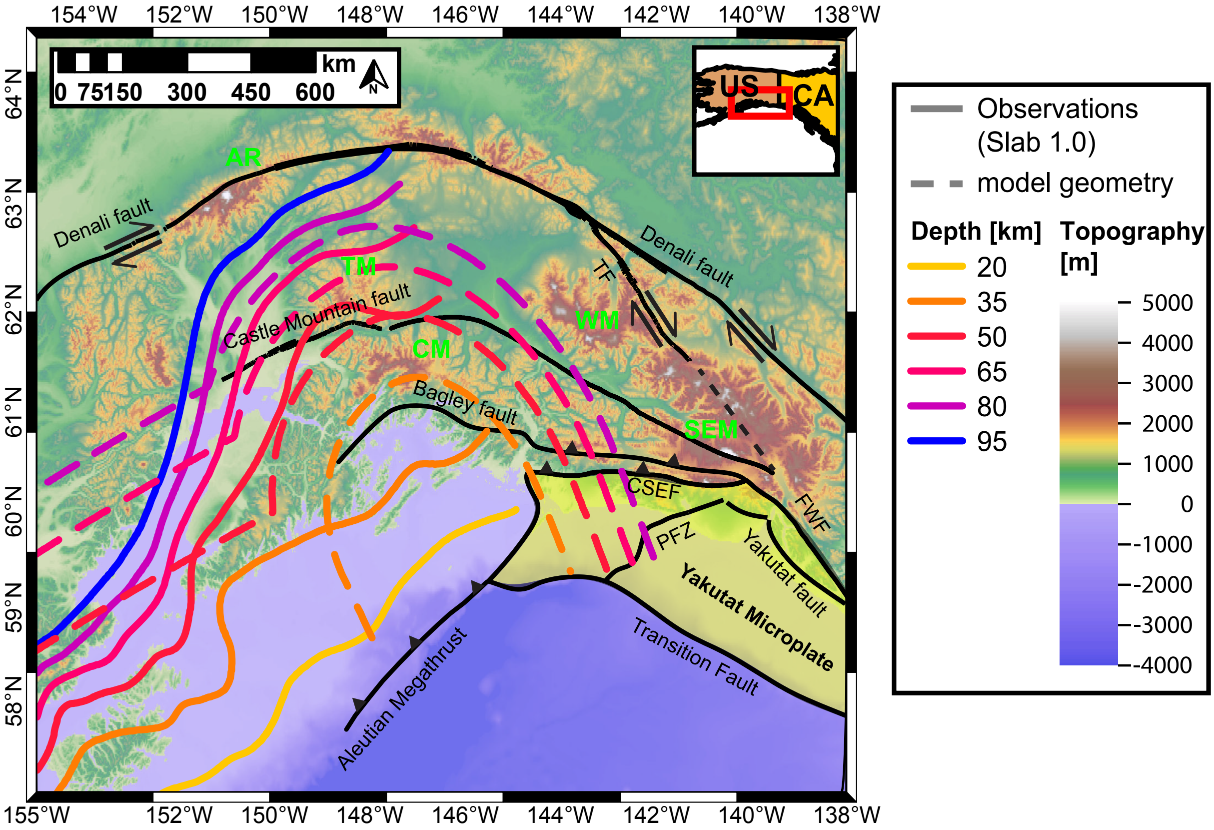

Figure 6.1: Topography and important features of southern Alaska.
Major faults are drawn black lines (Koehler 2013; Plafker and Berg 1994). CSEF - Chugach-St. Elias fault, FWF - Fairweather fault, PFZ - Pamplona fault zone, TF - Totschunda fault. Mountain ranges are denoted with green letters: AR - Alaska range, CM - Chugach Mountains, SEM - St. Elias Mountains, TM - Talkateena Mountains, WM - Wrangell Mountains.
The solid colored lines indicate depth contours after Slab 1.0 model (Hayes et al. 2012). Dashed lines show the corresponding, approximated model geometry used in this study.

6.2 Methods

6.2.1 Relation to Previous Chapters

This chapter is closely related to work presented in Nettesheim et al. (2018) (Chapter 3). The main difference lies in the asymmetric setup that improves the model's applicability to strongly curved plate corners. We refer the reader to Chapter 2 for an in-depth description of methodology and model setup, but will give a concise summary of the most important aspects here.

Modeling is conducted using DOUAR (Braun et al. 2008; Thieulot et al. 2008), a fully coupled three-dimensional thermomechanical numerical modeling program designed to solve visco-plastic creeping flows on crustal or lithospheric scales. It offers several options to consider additional geologic processes and parameters, including material strain weakening, isostasy, and different erosional models, which were applied in this study. A newly developed particle tracking module allows to extract the pressure-time-temperature-history (p-t-T) of material exhumed at the surface and to predict thermochronological cooling ages from these. Isostasy is calculated using the elastic plate model with an effective elastic thickness of 30 km. Two modes of erosion are used in this study: flat erosion, in which all material above the initial surface height is immediately removed, and fluvial erosion, in which a more realistic erosion is calculated in the coupled landscape evolution model FastScape. Model parameters for FastScape are given in Table 2.2 on page 18.

Material properties remain unchanged with respect to Nettesheim et al. (2018) (see Table 2.1 on page 9). The overriding plate consists of three layers: upper crust, lower crust, and lithospheric mantle (see Figure 6.2). The mode of deformation is visco-plastic, with viscous parameters reflecting wet granite, dry diabase, and olivine viscous flow laws, respectively (Carter and Tsenn 1987; Hirth and Kohlstedt 2003; Jadamec and Billen 2012). In the crust, the brittle strength can be reduced by strain weakening, which facilitates shear zones to localize in geodynamic modeling. The subducting plate's geometry is fixed, its material is purely viscous ($\mu = 1 \cdot 10^{25}\,\mathrm{Pa\,s}$). The coupling to the overriding plate is moderated by a 3-4 km thin, $10^{21}\,\mathrm{Pa\,s}$ weak layer on top, which ensures a balance between traction from the downwards moving subducting plate and the ability of upper plate material to shear away from the interface.

Model temperatures are defined by constant temperature boundary conditions of 0 °C and 930 °C at the model surface and bottom, respectively. Radiogenic heat production is chosen to resemble a typical crustal geotherm, which results in a Moho temperature of 930 °C and heat flux of $70\,\mathrm{mW\,m^{-2}}$ at the surface. A more detailed description of model and material properties can be found in Section 2.1.

6.2.2 Modifications to Geometry and Velocity Boundary Conditions

Modifications to the model setup stem from the goal to achieve a closer resemblance to the Alaskan plate Corner the wider region of South Alaska. Most importantly, the geometry in this study is asymmetric and includes a transform fault at the left (X = 0 km) boundary. The model geometry is shown in Figure 6.2a. The rear half ($400\,\mathrm{km} < \mathrm{Y} < 800\,\mathrm{km}$) is the same as in Nettesheim et al. (2018): the background plate is a cylindric section, 30 km high and terminating at X = 320 km. The indenter is a sphere sitting atop the background plate and shares its rotational axis in order to achieve a continuous motion of the down-going plate. The indenter height is 50 km and it reaches to X = 400 km accordingly. To the front, the indenter is more tightly curved (200 km radius) and lacks the background plate. The initial layering of the overriding plate is flat.

Velocity boundary conditions follow the model geometry and separate the domain in two corresponding regions, illustrated in Figure 6.2b. The down-going plate is characterized by a rotational motion, i.e. horizontal inflow of $v = v_{\mathrm{sub}}$ at the left side (X = 0 km, colored blue) and increasingly downward oriented outflow at the bottom. The other block of coherent motion is the overriding plate, which moves horizontally with $v = v_{\mathrm{adv}}$ in the opposite direction (colored red), its motion prescribed along the bottom and the left and right boundaries. At the model's front and back side (Y = 0 km and X = 800 km), a free slip boundary condition ($v_Y = 0$, colored gray) is imposed. This setup implies a transform fault along the lateral boundary of the subducting slab at Y = 200 km,

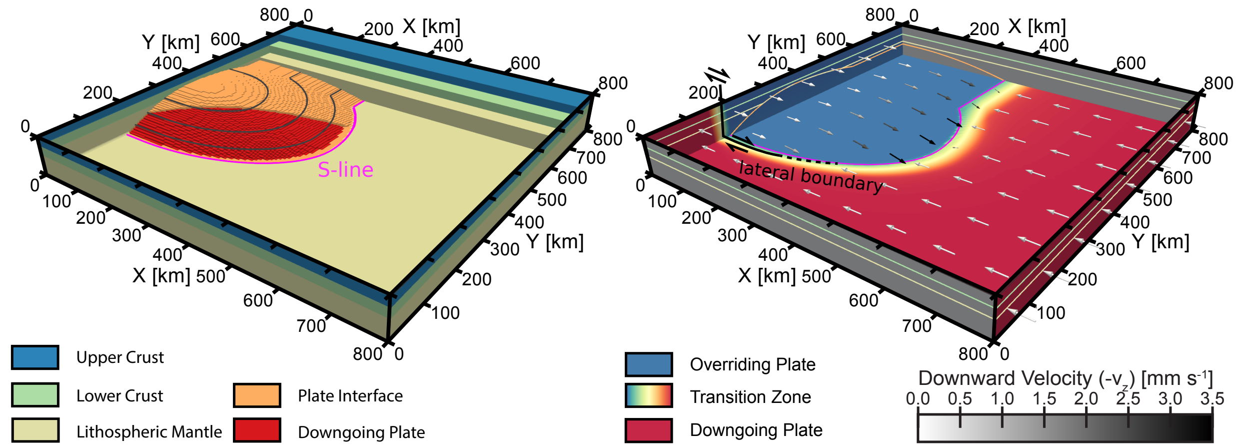

Figure 6.2: **a** Model geometry and material layout. The model domain is divided into an overriding plate comprising upper plate (blue), lower plate (green), and lithospheric mantle (sand), which are modeled with a visco-plastic rheology. The subducting plate (red) is separated from the overriding plate by a weak plate interface (orange), both of which are modeled with a purely viscous rheology. The subducting plate extends to one side and curves around strongly in order to emulate the geometry of a syntaxial subduction zone. **b** Velocity boundary conditions. Two velocity domains exist: the overriding plate moves horizontally in negative x-direction with velocity v_{sub}, while the down-going plate and the model section above it moves in the opposite direction. motion along the separating S-line changes from transform-faulting at the lateral boundary to subduction in the model center. The influx of lower-plate material, but not the accreted material above, is mass-balanced by a gradually increasing outflow at the indenter bottom, corresponding to a rotational motion. Velocity boundary conditions at the front and back (Y = 0 km and Y = 0 km) is free slip. Vertical material flows are additionally modified by flexural isostasy.

which wraps around the lower plate and transitions into a thrust fault. In this area, indicated by a color gradient, velocities are interpolated linearly between $v = v_{\text{adv}}$ and $v = v_{\text{sub}}$.

Through its definition as downward rotation, motion of the lower plate is mass balanced. The accreted material entering the domain above the subducting plate, however, is added to the domain. For the overriding plate, prescribing a bottom outflux in order to balance the in- and outflux of the lithospheric mantle bears the risk of over-constraining the problem. On the other side, the variable setting of upper plate motion and the possibility for the upper plate to thicken under compression, require a compensation mechanism. For this, we employ a dynamic calculation of isostatic compensation (elastic plate thickness of 30 km), which imposes a vertical velocity and thus achieves a comparable mass balance for the overriding as for the subducting plate.

6.3 Results

6.3.1 Strain Rates and Motion

6.3.1.1 Half Upper Plate Advance, Flat Erosion (Model A1)

Figure 6.3 illustrates resulting strain rates and motion of the half advance scenario with flat erosion. Panels 6.3a to 6.3e show the second invariant of the strain rate tensor in multiple perspectives and

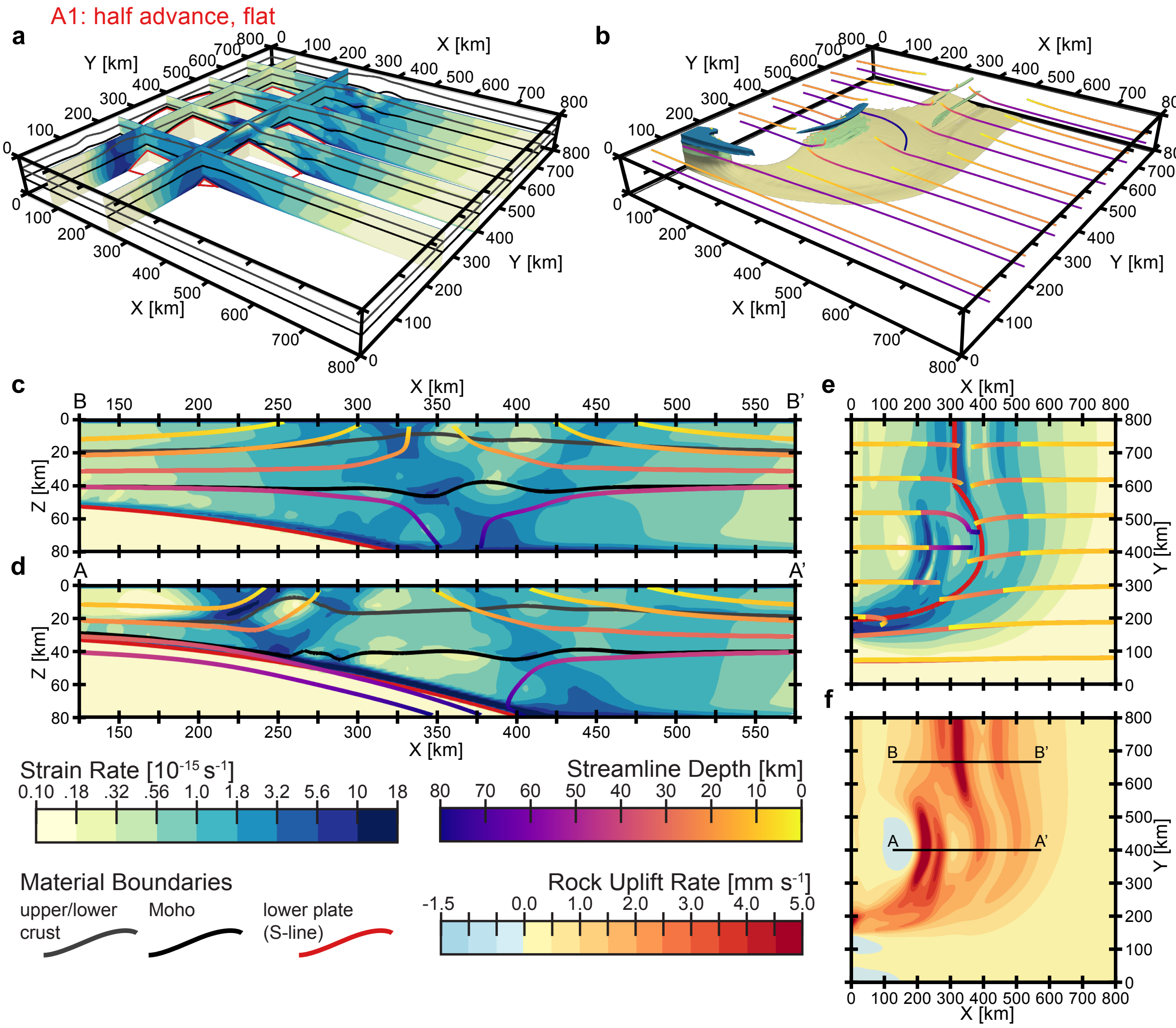

Figure 6.3: Strain Rates and Motion for half-advance, flat-erosion model A1. **a** to **e** show the second invariant of the strain rate tensor with streamlines to illustrate the material motion. **c** and **d** show vertical cross section at Y = 400 km and Y = 680 km, respectively, while **e** shows the map view at 5 km depth. **d** shows the isolated regions of high strain ($\dot{\varepsilon} > 6 \cdot 10^{-15}\,\mathrm{s}^{-1}$, colors denote material layer). From these views, three main structures can be identified: (1) a lithospheric-scale orographic wedge in the rear half of the model, (2) the décollement situated above the indenter, and (3) the transform fault at the strongly curved indenter edge. The motion streamlines indicate a gradual exhumation of upper and lower crust material that significantly steepens in the regions of the décollement and the orogenic wedge. Additionally, material flows are deflected in negative y-direction around the indenter. **e** shows the resulting rock uplift rates in map view. The regions of highest uplift coincide with the décollement and the pro-side shear zone of the orogenic wedge.

give insight into the different shear zones that govern motion in the different parts of the model domain. First and foremost, high values of strain can be found at the interface between subducting and overriding plate, especially in the lower model half. Where the lower plate curves backward, this transitions into a broad shear zone that cuts vertically through the entire model domain. Two further structures are noteworthy: the décollement above the indenter, and the lithospheric-scale orogenic wedge in the rear half (Y>500 km). The latter consists of two broad, steeply dipping shear zones oriented parallel to and rooting towards the S-line. The pro-side shear zone (towards the subducting plate) is expressed more strongly. In the model center, these shear zones attenuate, since part of the overall shortening there is accommodated by the décollement, which forms only above the indenter apex but not the background plate. Panel 6.3b offers an additional perspective on the model's behavior. The areas of high strain rates are isolated ($\dot{\varepsilon} > 5 \cdot 10^{-15}\,\mathrm{s}^{-1}$) and complemented with material flowlines. These show the material influx and gradual exhumation towards the center, which is accelerated dramatically at the main shear zones. Horizontally, flow lines are deflected to the model front by passing around the indenter, but there is no vertical gradient, i.e. motion at depth and at the surface is concurrent. The resulting rock uplift at the surface is shown in panel 6.3f. Rock uplift rates follow the distribution of strain rates. Fastest uplift occurs in the vicinity of the décollement and the pro-branch of the orogenic wedge in the upper half of the model and curve around to trace the geometry of the subducting plate and merge into the transform boundary. Since shearing is predominantly horizontal there, uplift is comparatively weaker despite the extensive region of high strain rates.

6.3.1.2 Half Upper Plate Advance, Fluvial Erosion (Model A3)

Figure 6.4 shows model results for half advance model with fluvial erosion (model A3), allowing a direct comparison of the two applied erosion modes. Results appear similar to first order, but a number of important differences strike the eye. First and foremost, stain in the upper crust is less localized for the fluvial erosion model, exhibiting a broader and more diffuse distribution, and lacking the clearly defined bands. The décollement above the indenter, clearly visible for the flat advance model A3, has vanished altogether. Instead, a weaker décollement dipping in the opposite direction exists above the indenter apex, inducing deep, almost vertical exhumation above the indenter (X = 250 km,Y = 400 km; see material streamlines in Figure 6.4, panels b and c). The high shear zone in the rear half of the model is more extensive and forms a symmetrical wedge in this model. Corresponding to the changes in strain distribution, uplift at the surface (Figure 6.4d) is also spread over a wider area and rates are slower. However, there are additional regions of rapid uplift at the outward slope of the orogen above the transform fault area (X = 0-250 km,Y = 200 km). Significant differences are also evident in the lower crust, where accreted material is now mostly subducted rather that exhumed in the model center and deflection of material flow around the subducting plate seems stronger.

6.3.1.3 No Upper Plate Advance (Models A2 and A4)

Analogous to models with half upper plate advance, two simulations were conducted with no advance boundary conditions. The strain and motion results for these are shown in Figures 6.5 and 6.6 (models A2 and A4 with flat and fluvial erosion, respectively). As a consequence of the changed direction of motion, deformation shifts away from the trench, while strain and uplift rates of the pro-side shear zone form a continuous band (see also results and discussion in Nettesheim et al. (2018)). In the flat erosion model, the continuous pro-shear zone follows the S-line and warps

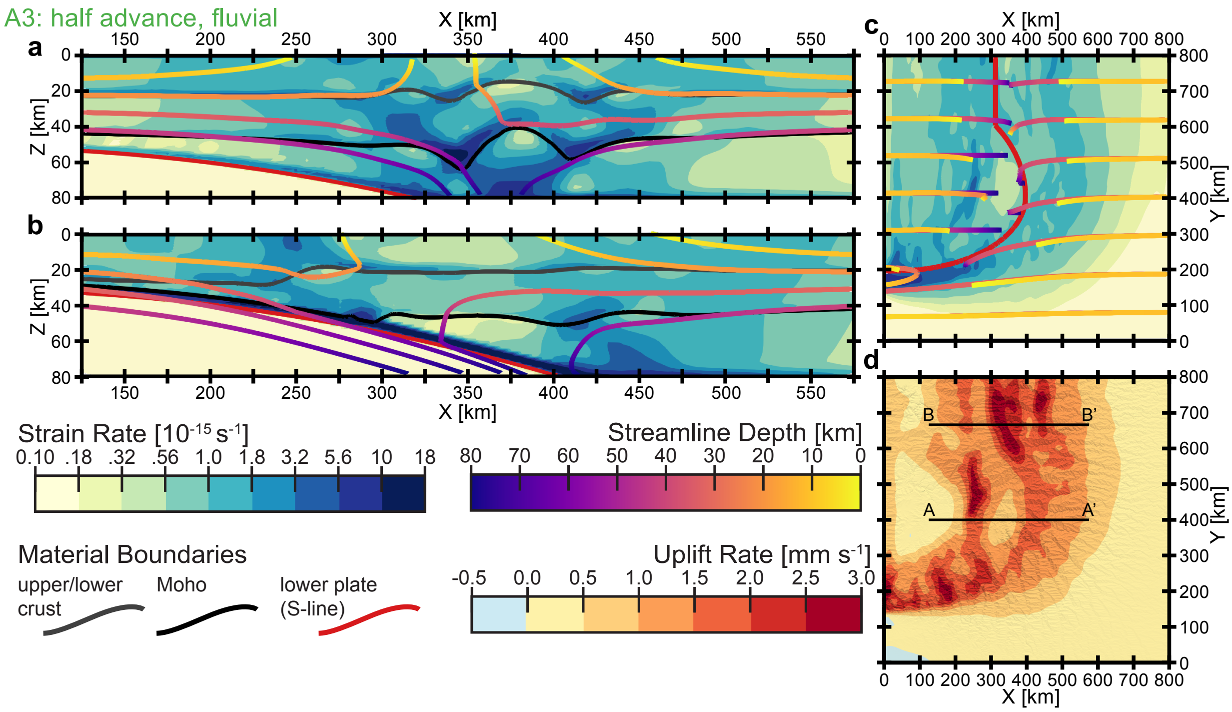

Figure 6.4: Strain Rates and Motion for half-advance, fluvial-erosion model A4 after 6 Myr modeling time. **a** and **b** show vertical slices of strain rates and material streamlines at Y = 400 km and Y = 680 km, and **c** in map view at 5 km depth. **d** shows surface rock uplift rates. Upper crust material is exhumed, while lower crust material is subducted and deflected around the indenter. Rock uplift rates show extensive high uplift rates above the orogenic wedge, as well as above the indenter apex and along the transform fault.

around the curved lower plate and thus is directly linked to the transform fault at the lateral plate boundary.

Due to the absence of an opposing flow, material accreted above the subducting plate is transported further into the model domain and exhumed at a lower angle. With this shift, the distance between uplift associated with the indenter décollement and the pro-side shear band is much smaller (uplift peaks at 310 km and 430 km, respectively, versus 230 km and 390 km for model A1), resulting in a narrower basin between these structures. With fluvial erosion, shear localization in the upper crust is strongly reduced except for the transform fault. The continuous band of uplift along the S-line, however, persists. In comparison to model A3, uplift above the indenter is slightly weaker and also less localized (see also Fig. 6.9).

6.3.2 Predicted Cooling Ages and Topography

The differences in model dynamics described in the previous section are also reflected in the distribution of cooling ages and, in the case of fluvial erosion, the resulting topography. Figure 6.7 shows a direct comparison of apatite fission-track ages (closing temperature $T_c \approx 120\,^{\circ}\mathrm{C}$) and exhumation depth for the flat erosion models A1 and A2. Figure 6.7 shows the analogue for the fluvial erosion models A3 and A4 with the resulting topography in addition. Due to the different dynamics and therefore lower uplift rates in the fluvial erosion scenarios, apatite (U-Th)/He ages ($T_c \approx 70\,^{\circ}\mathrm{C}$) are shown here. In general, the switch to fluvial erosion reduces the extent of very young ages at the

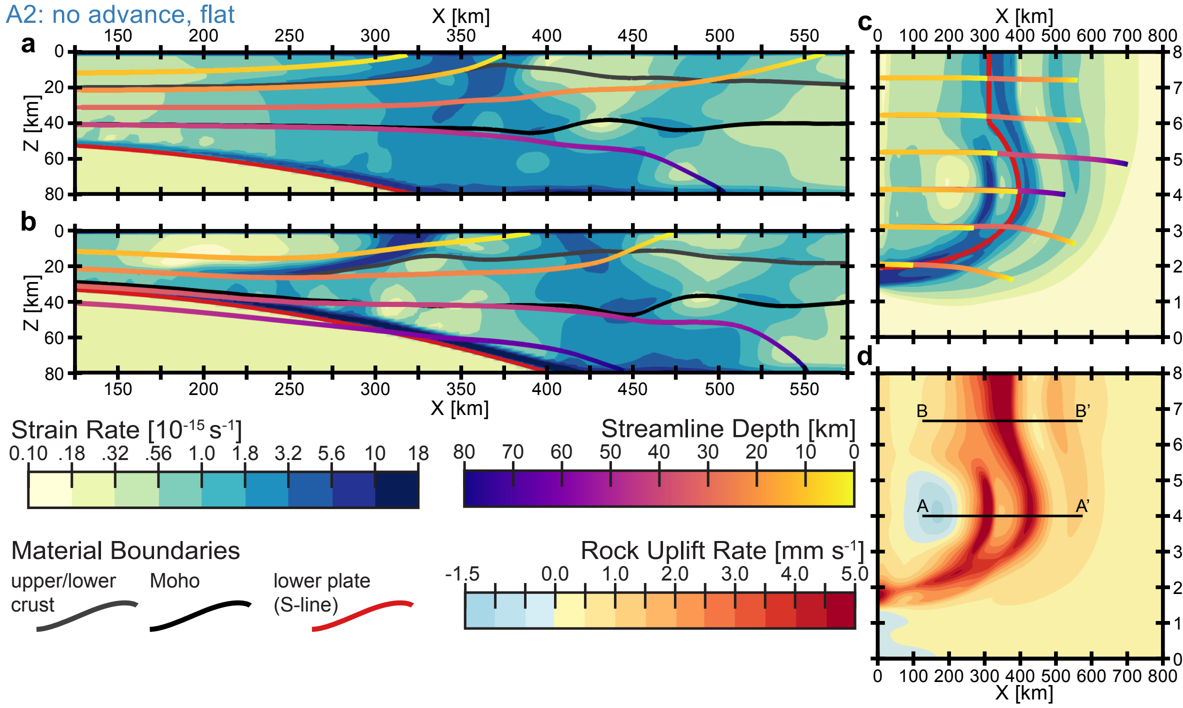

Figure 6.5: Strain Rates and Motion for no-advance, flat-erosion model A2 after 6 Myr modeling time. Views and color scales are identical to Figure 6.3. Highest Strain rates occur above the indenter in the shallowly dipping décollement. Above the background slab (panel **a**), basal deachment and pro-side shear zone combine and form a wider zone of lower strain rates but higher uplift rates. Streamlines in panel **a** and **b** indicate shallow exhumation extending far into the model domain. In the lower model half, material paths are steeper and curved. Panel **d** shows a continuous band of high uplift rates, mirroring the course of the S-line.

straight slab section and above the indenter apex, but leads to in younger ages along the transform fault. Furthermore, only the half-advance scenarios exhibit isolated regions of young cooling ages above the indenter, whereas a distinctive feature of the no-advance scenarios is a continuous band of young ages along the S-line. The youngest ages do not coincide with highest topography, but rather lie offset on the slopes of the orogen. The inspection of exhumation depth, which is not affected by thermal processes, reveals further details. It clearly shows that for the for fluvial erosion models (Fig. 6.8), exhumation is more focused along the S-line and above the indenter and that deepest exhumation in these cases shifts to the transform fault section.

6.4 Discussion

In the previous section, four models of convergent plates at a strongly curved plate corner with an indenter are presented. The velocity boundary conditions model half or no upper-plate-advance (i.e. convergence is accommodated by subduction of the lower plate and migration of the upper plate towards the trench, or by subduction only, respectively) and erosion is calculated in either flat or fluvial erosion mode. In general, deformation in all models occurs within a lithospheric-scale pop-up structure originating at the S-line, that followed the curvature of the indenter and merged into a transform fault along the lower plate boundary. Additionally, a low angle décollement above the indenter apex that accommodates strain in that model region and forms an area of localized uplift.

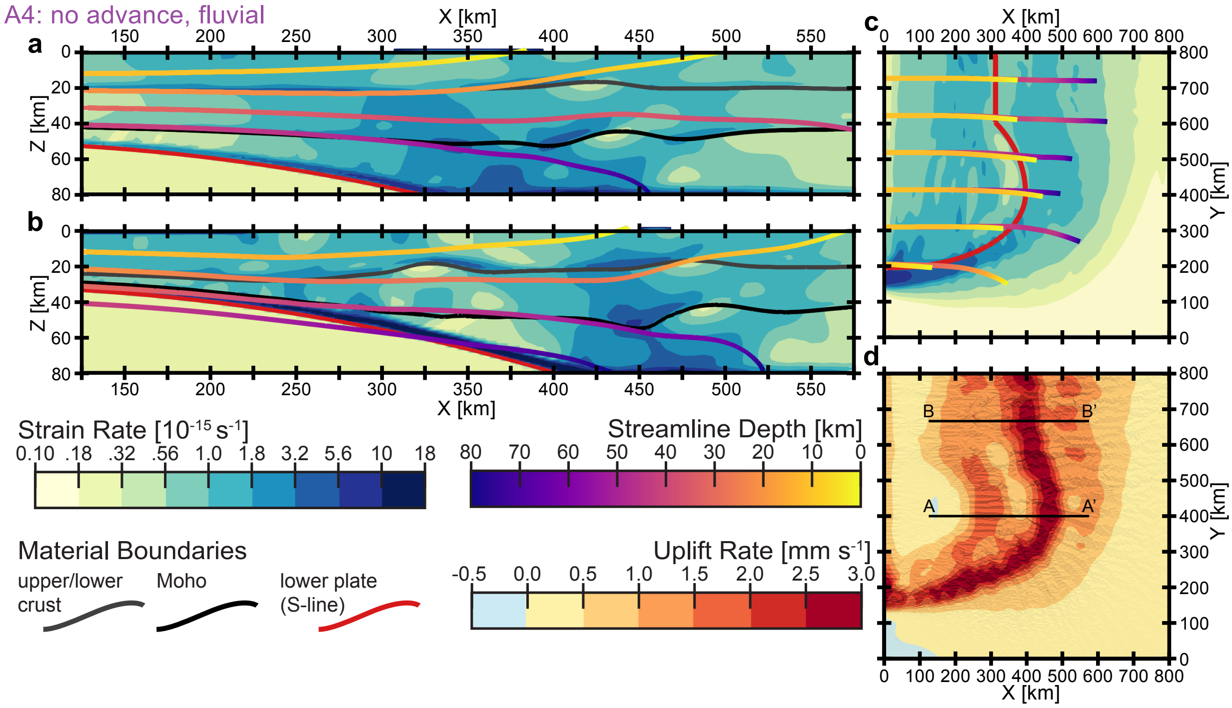

Figure 6.6: Strain Rates and Motion for no-advance, fluvial-erosion model A4 after 6 Myr modeling time. Views and color scales are identical to Figure 6.4. Highest Strain rates occur along the transform fault at X = 0-250 km, Y = 180 km, while strain in the upper model half (Y>400 km) is widely distributed and strain rates above $5 \cdot 10^{-15}\,\mathrm{s}^{-1}$ occur only in the lower crust and lithospheric mantle only. Streamlines in panel **a** and **b** indicate shallow exhumation extending far into the model domain. At the strongly curved indenter edge, material paths are steeper and curved. Panel **d** shows a continuous band of high uplift rates, mirroring the course of the S-line.

6.4.1 Influence of Relative Plate Motion

The effect of varying plate motion is also discussed in the previous chapters of this thesis. As expected, the same effect can be observed in this model setup: The distribution of deformation and corresponding uplift between the pro- and retro shear zone, which form the lithosphere-scale pop-up structure, shifts toward the direction of material influx into the model domain (see Figure 6.9a and b, for example). It is worth noting that the shape of the elevation profile across the orogen also reflects this relation. In model A4 (no advance, fluvial), uplift is dominated by the strong pro-side shear zone and the indenter décollement. This leads to a skewed topography, in which the slope on the retro (right) side is much steeper than the pro-side slope (Fig. 6.9a). The half-advance boundary conditions result in a more symmetrical orogen (Fig. 6.9b).

6.4.2 Influence of Fluvial Erosion

Comparison of flat and fluvial erosion scenarios reveals that the erosion process governs the details of rock uplift and exhumation, but has only small effect on the regional geodynamics (see Figs. 6.3-6.6). In the fluvial erosion models, uplift rates are much smaller due to the isostatic counterweight of the growing orogen, but large-scale distribution is mostly the same as in the flat erosion model. Fluvial erosion adds a more detailed pattern to the uplift rates, as erosion varies across valleys and ridges, as well as by the slope and upstream. The combination of these effects leads to a

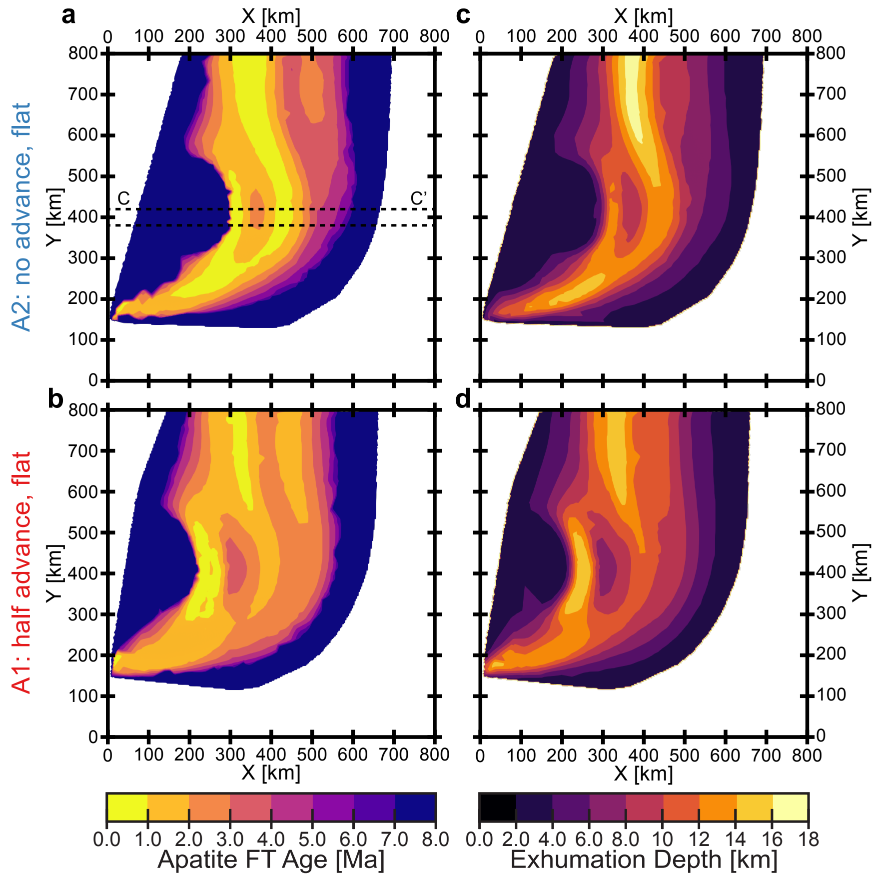

Figure 6.7: Predicted Apatite Fission Track cooling ages and Exhumation Depth after 6 Myr modeling time for flat-erosion models (no-advance model A2 in panels **a** and **c**) and half-advance model A1 in panels **b** and **d**), respectively) highlight the systematic variations for the applied model parameters. The cross-section C-C' is shown in Fig. 6.9.

spatially more variable distribution of rock uplift rates, where highest uplift occurs along the right and bottom slopes of the orogen. Localized uplift above the indenter apex is much weaker in the no-advance scenario (Fig. 6.6), but remains distinct and is even more focused in the half-advance scenario (Fig. 6.4).

6.4.3 Influence of Asymmetric Plate Geometry

The main feature of this study is the asymmetric plate geometry. All models clearly show a deflection of material paths toward the lower edge, i.e. around the indenter corner. Both deep and shallow material streamlines in Figures 6.3-6.6 are concurrent except for small deviations, which means there is no horizontal shear component. The material paths naturally are deflected most at the lower indenter edge, where the transition from subduction to transform faulting occurs. The swath profile perpendicular to subduction direction in Figure 6.9d reveals that the horizontal component increases from the orogen's center at $Y = 400$ km toward the left edge and is highest at the outer slopes ($Y = 200\text{-}300$ km). In combination with the increased erosion at the orogen slopes as discussed, this shows a preference of lateral orogen growth over vertical uplift.

Figure 6.10 shows model results of horizontal surface-velocities re-projected onto the topography of

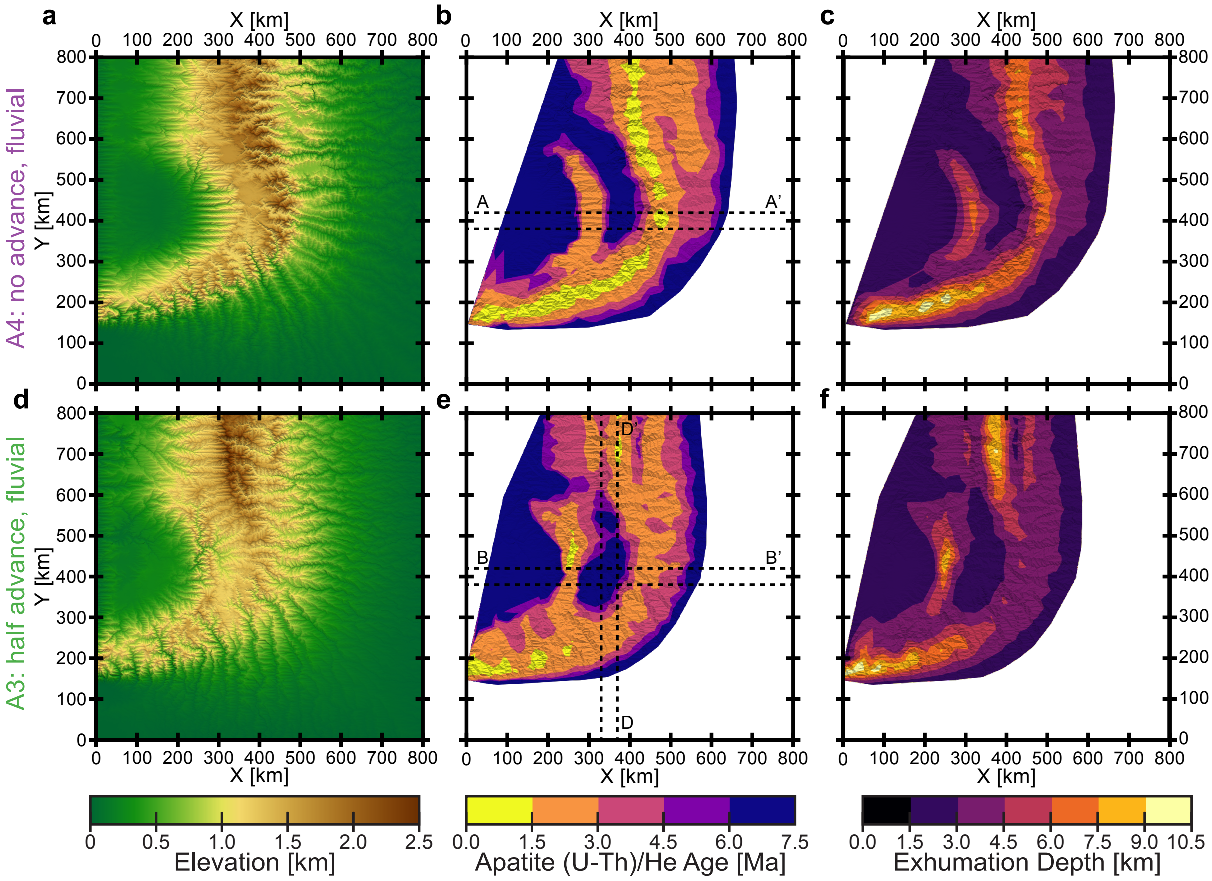

Figure 6.8: Resulting Topography, predicted Apatite (U/Th)-He ages and Exhumation Depth after 6 Myr modeling time for fluvial-erosion models (no-advance model A4 in panels **a-c** and half-advance model A3 in panels **d-f**, respectively) highlight the systematic variations for the applied model parameters. The cross-sections A-A', B-B', and D-D' are shown in Fig. 6.9.

southern Alaska in comparison with GPS-data observed in the same region as well as the Himalayan Plateau. The no-slab advance scenario shows the greatest horizontal deflection of material flows just at the outside corner of the indenter. In comparison with observed GPS-data, however, these deflections are minuscule, which is mostly an effect of the lateral free-slip boundary conditions. On top of that, deflection in all models is actually opposite to the observed counter-clockwise block rotation in southern Alaska (Elliott et al. 2013; Haeussler et al. 2008). It stands to reason that the orientation of geodynamic motion is governed by more than the regional plate geometry, but rather the position and relative strength of plates, so that motion will always follow the path of least resistance. More sophisticated boundary conditions and material parameters are needed in order to capture these outside constraints more accurately.

6.4.4 Predicted Thermochronometric Ages

In our fully coupled thermo-dynamical models, predicted thermochronologic ages can be easily calculated from tracking particles. Results are shown in Figures 6.7 and 6.8. Since models start with uniform temperature distribution and were run to 6 Myr modeling time, the patterns of rock uplift rates, exhumation depth and predicted cooling ages are quite similar. Note that for flat-erosion scenarios A1 and A3, apatite fission-track ages are shown, because due to the fast uplift,

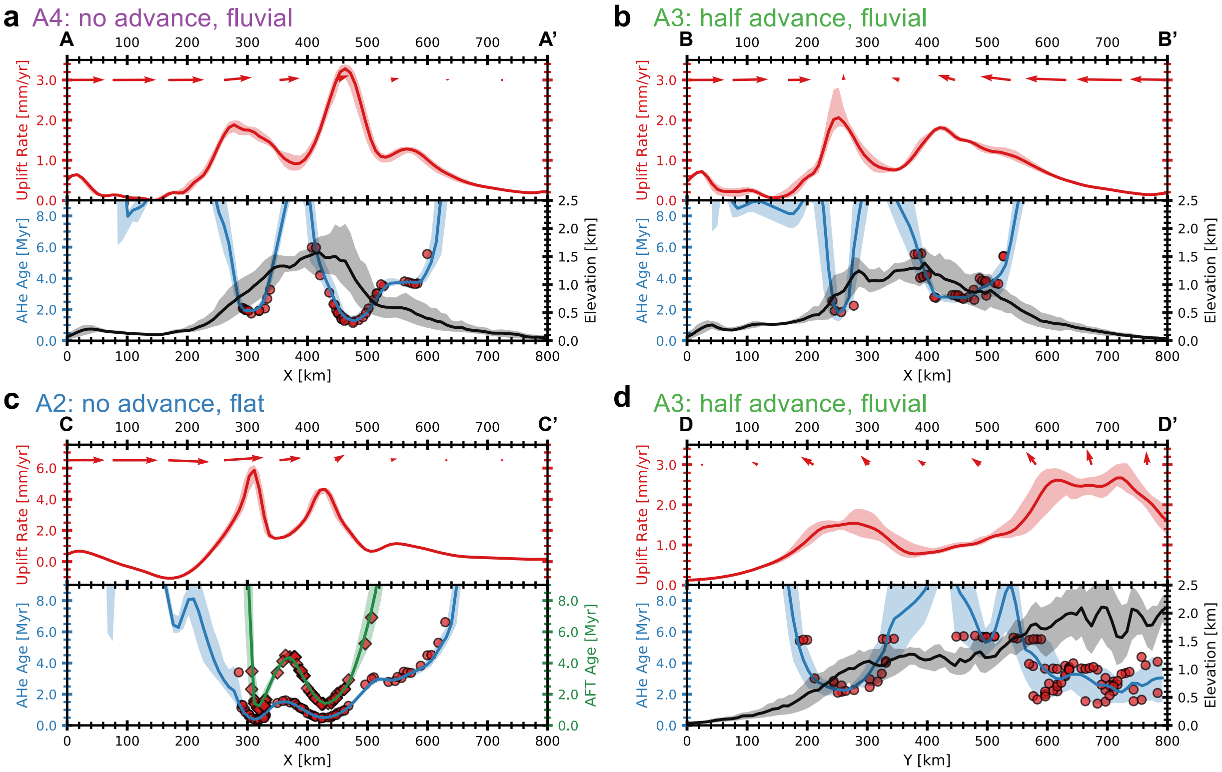

Figure 6.9: Relation between Rock Uplift Rates, Thermochronometric Ages and Elevation. Panels show 40 km wide swaths along direction of convergence for **a** no slab advance, fluvial erosion (model A4), **b** half slab advance, fluvial erosion (model A3), and **c** no slab advance, flat erosion (model A2). Panel **d** shows model A3 again, but across the direction of convergence. See Figs. 6.7 and 6.8 for the respective swath locations. The upper panel shows rock uplift rates (vertical velocity component), while arrows at the top indicate the total velocity and the orientation of motion in the plane. The lower panels show the elevation profile and the Apatite (U-Th)/He-Ages. Recorded tracking particles are shown as red circles, while the blue line denotes the interpolation that is shown in the other figures. For the flat erosion model in panel **c**, Apatite Fission-Track ages are shown instead of surface elevation.

apatite (U-Th)/He-Ages are very young and do not clearly resolve the peaks in rock uplift rates (see Fig. 6.9d).

The flat-erosion models provide an important reference as to how deformation would take shape in a world that is governed by tectonic forces alone. More interesting to comparison with observations, however, are the fluvial-erosion scenarios, which exhibit distinct differences. Most importantly, cooling ages are variable on shorter length scales and areas of very young ages much smaller. The general distribution still follows that set by tectonics, but is modified by topography so that youngest thermochronometric ages are found along the orogen slopes, preferentially within in steep valleys (see also discussion in Nettesheim et al. 2018). Figure 6.9 clearly shows this relation between slope and uplift, but also highlights another important aspect: as deformation is spatially variable, linear age-elevation-relations are only applicable to restricted areas. Even an inverse relation does not seem out of place when the generating rock uplift rates are known.

Figure 6.11 shows a comparison of predicted apatite (U-Th)/He cooling ages for the half-advance, fluvial-erosion model A4 with a complation of observed ages in southern Alaska (Ferguson et al. 2015). In general, the model-generated orogen and the distribution of predicted ages map well to actual topography. Although model results underestimate observed cooling ages for the greatest

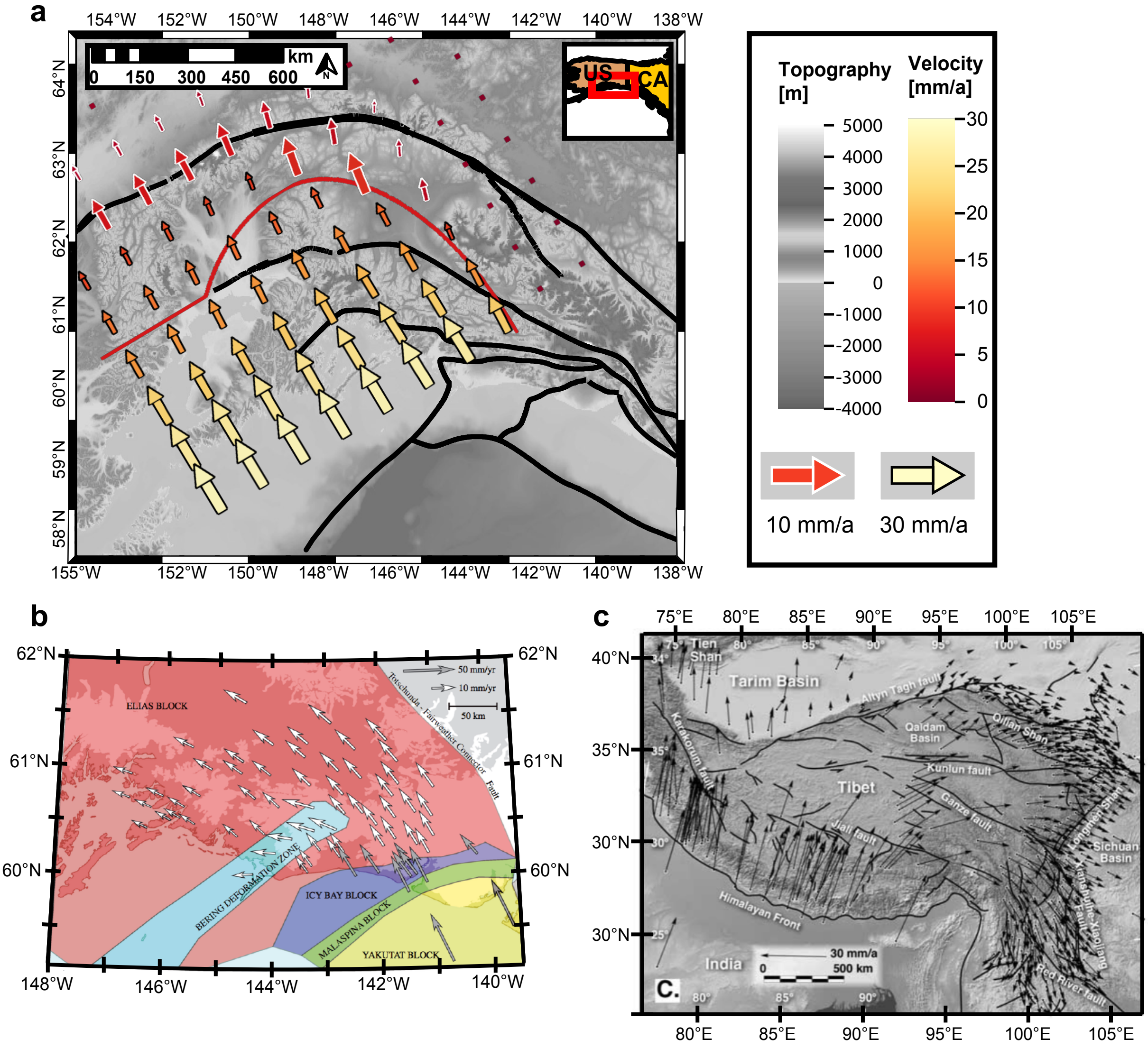

Figure 6.10: Modeled and observed horizontal velocity. **a** Results from model A2 (no advance, fluvial erosion) interpolated onto the topography of southern Alaska (same data and extent as Figure 6.1). Note that velocities below 10 mm yr^{-1} (white edges) are scaled 2.5 times more than higher velocities (black edges). **b** Observed GPS velocities for southern Alaska, colors indicate tectonic blocks. Taken from Elliott et al. (2013) (Figure 7). **c** Observed GPS velocities for the Himalayan Plateau, taken from Allmendinger et al. (2007).
Model results show the a counter-clockwise deviation from straight motion just north of the indenter apex, where the transition from compression to transform motion occurs. However, this divergence does not match the substantial change in direction of motion compared to the natural examples.

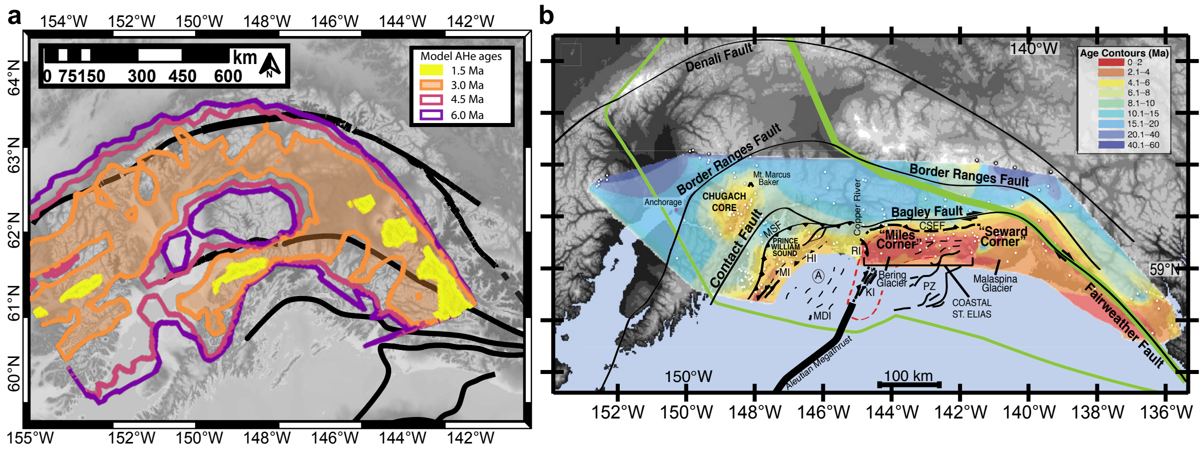

Figure 6.11: Model predicted and observed Apatite (U-Th)/He cooling ages. **a** Results from model A4 (half advance, fluvial erosion)interpolated onto the topography of South-East Alaska. **b** Contour map of compiled Apatite (U-Th)/He ages, taken from Ferguson et al. (2015) (Figure 8). The green outline denotes the extent of the partially subducted Yakutat microplate.
The extent of the resulting model orogen matches well with the delimiting Denali fault. The concentration of predicted young cooling ages above indenter apex and along the model's lateral transfer fault broadly corresponds to the focused uplift observed at the Chugach Core and Miles Corner south of the Chugach-St. Elias fault.

extent, both share important features considering the generic nature of our model's setup. Most importantly, the young ages at Miles Corner south of the Chugach-St. Elias fault are reproduced by the area above the model's lateral transfer fault (see also no-advance model A2 in Fig. 6.8). Moreover, the isolated uplift of the Chugach Core also finds its counterpart in the focused uplift above the indenter apex.

6.4.5 Model Caveats and Future Work

Despite equivalent features and analogous geodynamic behavior, model results fall still short of a close representation of the natural system. Among others, the role of the Yakutat microplate, which is considered paramount for a complete understanding of geodynamics in South-East Alaska, was neglected in this study. In order to adequately represent this, adjustments to the model geometry, material properties and boundary conditions will be necessary that could not be included in this generic approach. Further adjustment will also permit to apply the model to other strongly curved plate corners, for example the Himalayan plate corners, Nanga Parbat (Craw et al. 1994; J. L. Crowley et al. 2009) and Namche Barwa (Burg et al. 1998; Enkelmann et al. 2011; Stewart et al. 2008) orogen syntaxes. However, these are continent-continent rather than ocean-continent subduction zones, which might require adjustments to account for crustal strength, plate buoyancy, and other parameters.

Finally, this and previous studies (Beaumont et al. 2001; Willett 1999) showed that the mode of erosion can influence geodynamic deformation. However, the uniform precipitation rate presumed in this study is not accurate for the extent of the model domain. Using an orographic precipitation model that dynamically calculates precipitation will provide more natural distribution of precipitation and might offer additional insights in feedbacks between uplift and erosion. Neither can this study represent the implications of intense glaciation in this region or the effect vast amount of material that was eroded and deposited onto the Yakutat Microplate and altered subduction behavior (Enkelmann et al. 2015; Gulick et al. 2015)

6.5 Conclusions

In this study, we presented models of a converging plate corner with different amounts of upper plate advance in relation to the subducting plate. In order to best represent the observed plate geometry at the St. Elias Syntaxis, an asymmetric model geometry with prominent central indenter was chosen. Both flat-erosion and fluvial erosion modes were used to identify interactions between erosion and tectonics. In all models, we observed three majors shear zones with accompanying rock uplift that broadly correspond to Alaskan orogens: an extended band above the forward edge of the down-going plate (∼Alaska Range), a more localized décollement above the indenter apex (∼Chugach Mountains), both of which are connected to the third structure, a lateral bounding transfer fault that generates fast uplift (∼St. Elias Mountains). Relative plate motion as well as erosion parameters shift the relative strength of these uplift centers, but do not affect the underlying pattern. The main conclusions which can be drawn from these models are the following:

1. Intense erosion can modify deformation mechanics. In our models, highest values of rock uplift and erosion are found on the orogen slopes rather than in the center, preferentially in steep valleys with sufficient upstream drainage area.

2. This focusing effect of erosion is also reflected in predicted thermochronometric ages, which are variable on the meso-scale (10s of km) and are youngest on the orogen-flanks. Therefore, local age-elevation-relationships are not necessarily representative of the wider region.

3. To the first order, model results presented in this study match well with observations. Important features include the orientation of major faults and structures, a region of focused uplift above the indenter apex, and very young cooling ages located above the model's lateral transform fault. Nevertheless, a more detailed and fine-tuned approach is necessary to truly model the geologic history of this region.

7 Conclusions

This thesis was motivated by the conflicting hypotheses of Zeitler et al. (2001) and Bendick and Ehlers (2014), which attribute the observed rapid and focused uplift at plate corners to very different mechanisms. The tectonic aneurysm hypothesis, formulated by Zeitler et al. (2001), states that localized erosion accelerates uplift from the top down. This occurs by a feedback loop feedback between incision, exhumation, and thermal weakening. In contrast, Bendick and Ehlers (2014) argue that the folding of the subducting plate at plate corners crates a stiffened indenter geometry that exhibits increased resistance to subduction. Consequently, material is forced upward and drives localized uplift from the bottom up.

In the four science chapters, different aspects the mechanics of deformation at plate corners are investigated. The adaption and expansion of the modeling program DOUAR enabled an extensive numerical study on the effect of an indenter-type lower plate geometry under different tectonic, rheologic and erosional conditions. While the individual chapters focused on specific model parameters or settings, the overarching hypotheses formulated in Section 1.3.1 shall be revisited here.

7.1 Hypotheses Revisited

Hypothesis 1 If lower plate geometry governs upper plate deformation, then modeling different plate geometries will create differences the style and pattern of deformation that correspond observations at the respective plate corners.

Different aspects of this hypothesis are investigated in this thesis. In Chapter 3, models with straight subducting plate are contrasted against model with a prominent central indenter located atop a lower background plate. We find that the indenter strongly impacts the style and location deformation in the upper plate and generates an isolated area with increased rock uplift. Furthermore, both Nettesheim et al. (2018) and Koptev et al. (2019) (Chapters 3 and 4) show that the lateral extent of this area is determined by the width of the indenter bulge. Finally, the models with freely deforming lower plate (Chapter 5) stress the importance of the indenter's rigidity: if the indenter does not withstand the opposing flow but retracts backwards, the upward deflection of material flow is reduced.

The standard plate geometry with a gently curved indenter, which is used in the first three chapters of this thesis, was modeled after the Cascadia subduction zone. Model results share key features with deformation patterns observed there. By using a narrower indenter, more intense focusing of rock uplift into regions of only few hundred kilometers diameter, as observed at the St. Elias and both Himalayan syntaxes, can be modeled. Finally, the tightly curved and asymmetric geometry used in Chapter 6 well approximates the pattern of uplift in southern Alaska with intense exhumation both along the lateral plate boundary as well as above the indenter. Even the absence of focused uplift at the Andean syntaxis with its continuously curved subducting plate and no prominent indenter may be taken as further support to this hypothesis. However, one must note that despite similarities, the models presented in this thesis do not closely represent natural settings in all their details. Still, the plate geometry with its prominent indenter is an essential part of the whole and cannot be neglected. In summary, this hypothesis can be confirmed.

Hypothesis 2 If lower plate geometry governs upper plate deformation, then a focusing effect may be observed irrespective of relative upper plate motion.

Bendick and Ehlers (2014) used a simplified numerical model of an immobile indenter with opposing material flow to study the effect of lower plate geometry. These velocity boundary conditions represent a trenchward migration of the overriding plate without subduction of the lower plate. However, upper plate advance usually makes up only the smaller fraction of overall convergence in natural settings. Therefore, the studies of this thesis extend the investigation to model settings governed by lower plate subduction and accretion.

In all chapters of this thesis, we find that the partitioning of shortening into subduction and upper plate advance plays a major role in the localization of strain in the upper plate. In contrast to Bendick and Ehlers (2014), however, full upper plate advance poses the least favorable conditions for focused exhumation. In these scenarios, shortening is mainly accommodated by a lithospheric-scale orogenic wedge originating at the velocity discontinuity (S-line) along the model bottom and the lower plate geometry does not come into play. When velocity conditions include active subduction of the lower plate and accretion, the location of deformation shifts trenchward to the region above the lower plate. In this way, the different geometries of indenter and straight plate segments can have an effect. Across the different model setup studied in this thesis, no optimal partitioning to elicit focused uplift can be identified. In Chapter 4, the no-upper-plate advance scenario to created the strongest focusing effect for a weakly coupled lithosphere. Under other material parameter and model conditions, Chapters 3, 5, and 6 identify equal partitioning of subduction and upper plate advance as most favorable. In summary, this hypothesis in its original form must be rejected, as the upper plate motion has a significant impact on deformation in the upper plate. It may, however, be re-formulated in a weaker form: The focusing effect of an indenter-type lower plate geometry can be observed over a wide range of relative plate motions.

Hypothesis 3 Focused deformation at plate corners only occurs for favorable thermo-mechanical structure of the overriding plate.

The tectonic aneurysm hypothesis is based on the thermal weakening of the upper crust‘s mechanical strength following incision and material exhumation. This process demands that the upper crust has a higher mechanical strength than the lower (Koons et al. 2002). In contrast, the conceptual bottom-up model of Bendick and Ehlers (2014) used a viscous overriding plate. However, modeling the overriding plate with layers of visco-plastic material better represents the long-term mechanical behavior of the lithosphere (Burov 2011).

The influence of the upper plate's thermo-rheologic structure is studied in depth in Chapter 4, in which the intermediate lithospheric strength profile used in all other studies of this thesis was contrasted with two end-members – a strongly coupled case representing cratonic lithosphere, as well as a hotter, weakly coupled case for young continental plate. Two locations along the interface between down-going and overriding plate are most relevant for the accommodation of shortening: the S-line along the model bottom and the intersection with the overriding plate's Moho above the indenter. In the case of strong coupling, V-shaped steeply dipping shear zones originate from both location and create orogenic wedges. At the surface, these express as continuous, trench-parallel areas of uplift. Decreasing crustal coupling has a two-fold effect. Firstly, it reduces strain localization, especially for the shear zones originating from the S-line. Deformation is distributed over wider areas or multiple smaller structures, thus reducing the rate of uplift at the surface. Secondly, it changes the style of deformation above the indenter. Instead of forming a V-shaped wedge, strain localizes as basal décollement ramping up from the weaker crust, forming a single area of rock uplift at the surface. The combination of both effects creates a bull's-eye pattern of uplift.

The overall strength of the plate interface investigated in Chapter 5 causes a similar effect. For a strong interface, almost all shortening is accommodated by the two shear zones rooting down to the S-line and forming lithospheric-scale orogenic wedge, creating two continuous bands of uplift across the model domain. With decreasing interface strength, deformation is less localized and uplift distributed across a wider area. However, above the indenter localized deformation persists and thus forms an isolated area of focused uplift above the indenter.

In summary, the thermo-mechanical properties of the lithosphere as well as the strength of the plate interface are both important factors that govern the style and distribution of deformation and rock uplift. Zones of reduced material strength lead to wider distribution of deformation and enhance the differences between the background plate and the indenter. In this way, the numerical model can be tuned to generate rapid and focused uplift corresponding to observations at natural settings.

Hypothesis 4 If erosion governs tectonic deformation, then rock uplift will adapt to the pattern of erosion.

In previous lithospheric-scale modeling studies, erosion has either been neglected (e.g Bendick and Ehlers 2014; Koons et al. 2010) or explicitly constrained to achieve the erosion observed at specific locations (e.g Beaumont et al. 2001; Koons et al. 2002). In this dissertation, however, we have taken an alternative approach of contrasting two end-member scenarios: flat and fluvial erosion. With flat erosion, the surface is forced to an artificial steady state at zero elevation. In other words, model erosion rates always equal local rock uplift rates. This approach eliminates erosional influences and thus allows the isolation of tectonic deformation. Consequently, flat erosion was used in all studies of this dissertation to establish a baseline and investigate the effects of model parameters on upper plate deformation. In contrast, the fluvial erosion mode takes a step towards a more realistic modeling of erosion and denudation. By expanding DOUAR with FastScape algorithms, erosion is modeled as combination of stream power law and diffusive hillslope processes. With this fully coupled thermo-mechanical/landscape evolution model, emerging topography may induce feedbacks to tectonic deformation through the growing isostatic overburden as well as the spatial variations in erosion rate.

Throughout chapters 3, 5, and 6, some common patterns could be observed. First and foremost, fluvial erosion scenarios exhibit lower rock uplift rates distributed over a wider area than in flat erosion scenarios. This delocalizing effect is easily explained by the growing isostatic overburden of the emerging orogen, which facilitates lateral extension over straight vertical uplift. The orogen's crest line approximately followed the path of the S-line at the model bottom below, while erosion was strongest along the orogen slopes, corresponding to the position of the linear uplift bands observed in the flat-erosion models. Along the slopes, however, erosion rates varied on catchment-scale according to the erosion potential – steep, deeply incised with larger catchment areas showing highest rock uplift rates. These erosion patters were mirrored in rock uplift and thermochronometric cooling ages. In this regard, the hypothesis can be confirmed.

It must be noted that erosion cannot be considered independent of tectonic uplift. Steep slopes are created from fast uplift, so that the question of the actual driving mechanism cannot be easily resolved. However, most of the model scenarios that showed an isolated region of fast uplift with flat erosion automatically developed deeply incised valleys at those locations, which caused further focusing of rock uplift than by tectonics alone. Thus we conclude that the geodynamic properties of a system should be considered the main driver of rapid and focused uplift. If tectonic conditions are met, the feedback between strong erosion driven by steep slopes and thermal weakening from accelerating uplift, as formulated in the tectonic aneurysm hypothesis, will focus uplift even further on catchment-scale.

7.2 Outlook

Numerical modeling allows for endless variations of scenarios and parameters to be considered and evaluated. Furthermore, advances in computational algorithms and technological capabilities push the boundaries further and open up new possibilities and perspective. Fully-coupled thermo-mechanical geodynamic modeling in 3D is now becoming standard after years in which research questions had to be restricted to two dimensions. Nevertheless, modeling a specific region with all its intricate details may never be achieved due to our limited knowledge of these details and the staggering range of scales in time and space that need to be considered. In this regard, numerical modeling must always be restricted to approximations and comparisons in identifying the parameters of importance. Within these limitations, this thesis provides a better understanding of the mechanics of deformation at plate corners.

As with most research projects, not all imposing questions could be investigated and answered. Among these, the role of erosion might be of highest interest. Within this thesis, the modifying effect of erosion on tectonic uplift was investigated. However, all models used an constant, uniform precipitation rate. Investigating the effect of different precipitation levels spatial gradients might reveal thresholds required to initiate tectonic-erosional feedbacks and contribute to understanding between different plate corner settings. Taken on step further, dynamically calculated orographic precipitation would allow the model to simulate even more complex interactions between climate and tectonics.

A Source Code and Data Availability

All source code files discussed in Chapter 2 are stored on the USB drive included with this thesis.

The full source code of DOUAR is not openly available due to copyright restrictions. It is available upon request to David Whipp (david.whipp@helsinki.fi). The code is hosted in a GitLab repository, which allows to track contributions and versions reliably. Additionally, a local copy of the repository is also availablable on the ESD group server at `/esd/esd01/docs/mnettesheim/src/douar-wsmp`.

Model results are located on the ESD group server at `/esd/esd01/data/mnettesheim/`. Organized by publication or scientific chapter of this thesis, each folder contains the used version of the source code, input files, processed model output in *ParaView* (.vtk or .vtu) format as well as the *ParaView* state files that were used to create the figures. *ParaView* is freely available at `https://www.paraview.org/`.

B Supplementary information to Chapter 3

The following material was published as supporting information to Nettesheim et al. (2018), which is part of this thesis (Chapter 3).

	Upper Crust Wet Granite[a]	Lower Crust Dry Diabase[a]	Lithospheric Mantle Olivine aggregates[b]
Density ρ [$\mathrm{kg\,m^{-3}}$]	2750	2900	3300
Thermal Diffusivity $k/\rho c$ [$10^{-6}\,\mathrm{m^2\,a^{-1}}$]	1.0	1.0	1.0
Heat Production [$\mathrm{\mu W\,ka^{-1}\,m^{-3}}$]	1.8	0.6	0.0
Viscosity Prefactor B [$\mathrm{Pa\,s^{1/n}}$]	$4.43{\cdot}10^7$	$1.24{\cdot}10^6$	$1.21{\cdot}10^7$
Activation Energy Q [$\mathrm{kJ\,mol^{-1}}$]	140.6	276.0	324.3
Stress Exponent n [1]	1.9	3.05	3.5
Cohesion C_0 [MPa]	10	10	2
Friction Angle ϕ [$^\circ$]	15 → 5	15 → 5	10
Strain Weakening Interval [1]	0.05 → 0.55	0.05 → 0.55	-

[a] Carter and Tsenn (1987)

[b] Hirth and Kohlstedt (2003); Jadamec and Billen (2012)

Table S1. Overriding pate material parameters

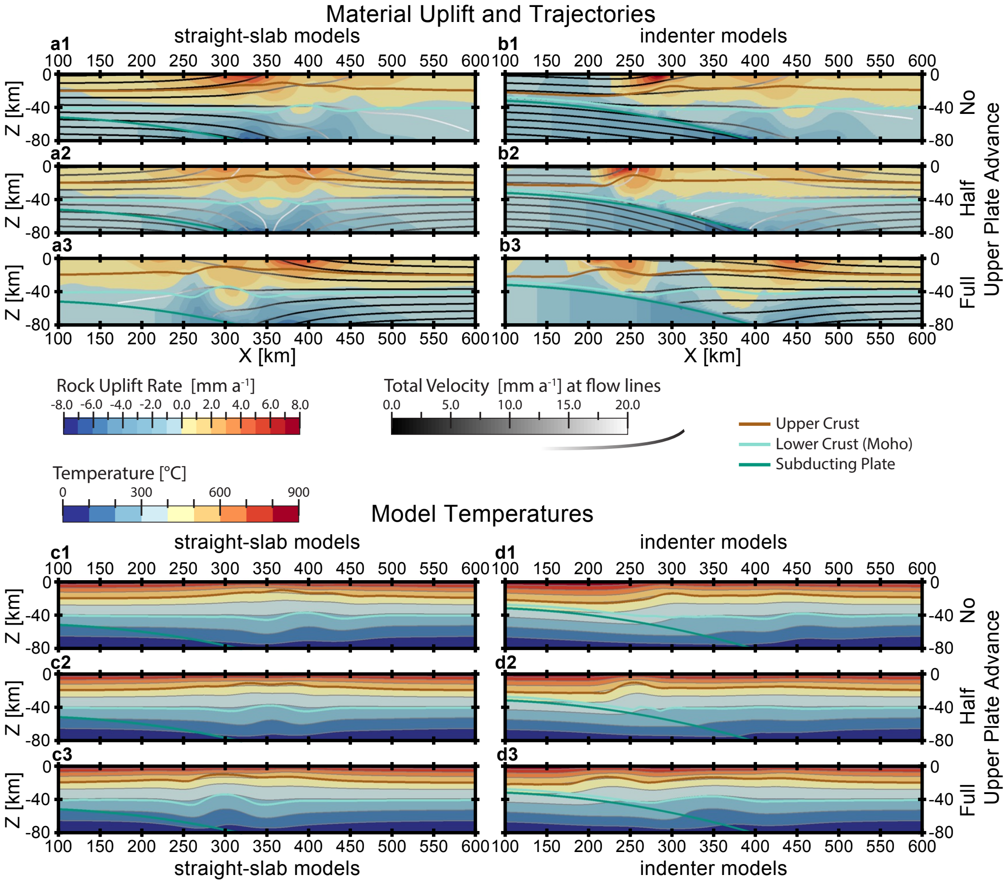

Figure S1. Comparison of velocities and temperatures between straight-slab (left column) and intenter-type (right column) flat erosion models (models 1–6). Colored lines denote material layer boundaries. Panels **a1**–**b3**: Background colors denote vertical velocity component, material flow lines are colored by total velocity. Panels **a1**–**b3**: Background color show temperatures. Colored lines denote material layer boundaries. Plots show the increased and focused uplift around $x = 250\,\mathrm{km}$ created by the indenter and the corresponding temperature anomalies, which mostly correspond to deformation.

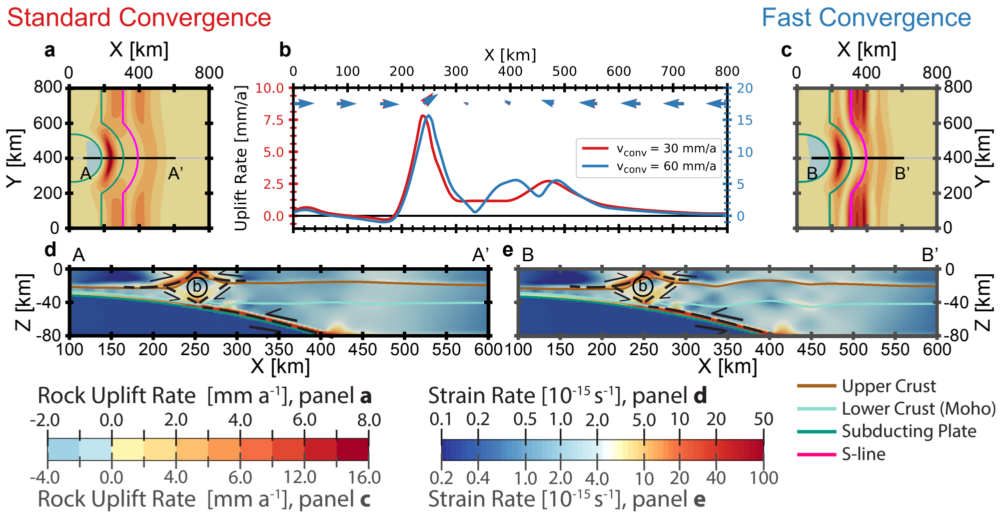

Figure S2. Comparison of standard and twice as fast convergence models (models 5 and 7) after 4 and 2 Myr modeling time, respectively (equal amount of material added to domain). Panels **a** and **c** show rock uplift rates, panels **d** and **e** strain rates at y =400 km and panel **b** shows surface rock uplift rates along y =400 km slice. Please note that all scales for fast convergence model are doubled (gray labels), but relative distribution of rock uplift and strain rates is almost the same.

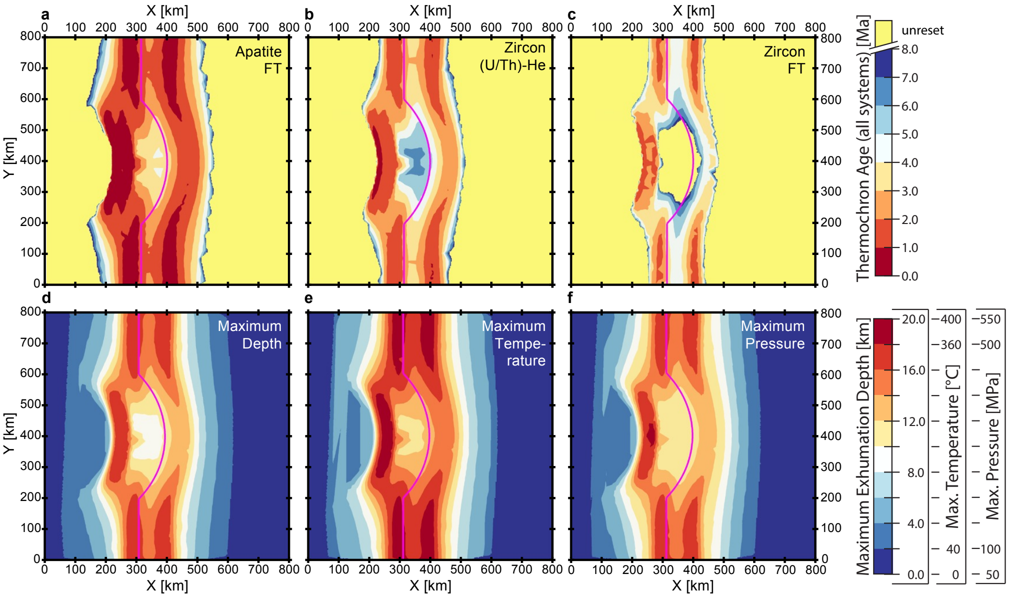

Figure S3. Thermochronometric cooling ages (Apatite fission track ($T_c \approx 120\,^\circ\mathrm{C}$), Zircon (U–Th)/He ($T_c \approx 180\,^\circ\mathrm{C}$), and Zircon fission track ($T_c \approx 240\,^\circ\mathrm{C}$)), as well as physical exhumation parameters (maximum depth, temperature, and pressure) of the half advance indenter model (model 5) after $8\,\mathrm{Myr}$ simulation time. All observables clearly follow the pattern set by rock uplift rates of two bands to the front and back, as well as a region of localized uplift above the indenter (see Figs. 4b3 and 5b). Thermochronometric age is increasingly older with a higher closing temperature of the respective system (from left to right). The cooling ages above the indenter are slightly but consistently younger than those related to the pro and retro shear zone at the model front and back ($y < 200\,\mathrm{km}$ and $y > 600\,\mathrm{km}$, respectively.

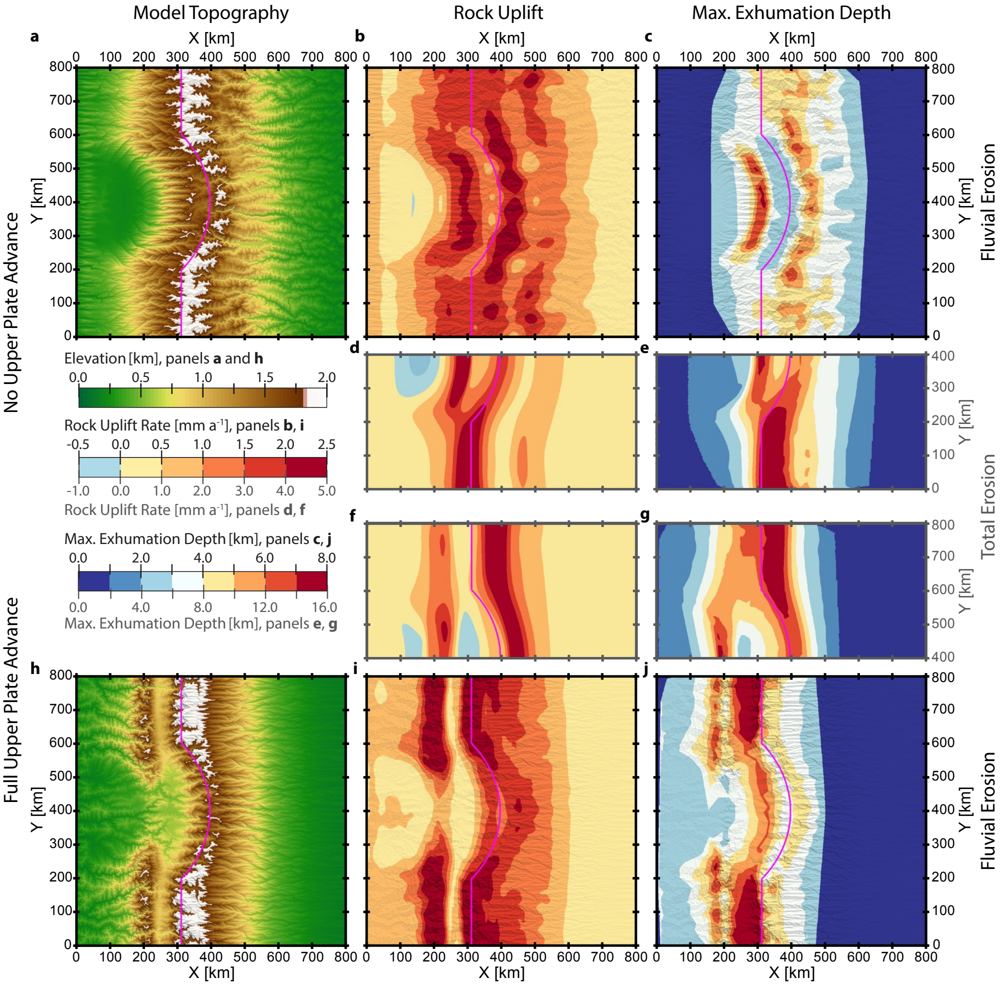

Figure S4. Comparison of rock uplift and exhumation depths with fluvial versus total erosion for no (model 10, upper half) and full (model 12, lower half) upper plate advance. **a** and **h** surface elevations, **b** and **i** rock uplift rates, and **c** and **j** exhumation depth after 6.0 Myr modeling time. Uplift is focused more toward the center for the no advance and more to the front and back for the full advance fluvial erosion model. **d**, **e**, **f**, and **g** show the respective flat erosion results (models 4 and 6) for rock uplift rates and exhumation depth for comparison. Note the range is increased by factor 2 for those four plots (gray labels).

C Supplementary information to Chapter 4

The following material was published as supporting information to Koptev et al. (2019), which is part of this thesis (Chapter 4).

Tectonics

Supporting Information for

Response of a rheologically stratified lithosphere to subduction of an indenter-shaped plate: Insights into localized exhumation at orogen syntaxes

Alexander Koptev[1], Todd Ehlers[1], Matthias Nettesheim[1], David Whipp[2]

[1]University of Tübingen, Department of Geosciences, Tübingen, Germany

[2]University of Helsinki, Department of Geosciences and Geography, Helsinki, Finland

Contents of this file

Introduction

This supplementary material includes the numerical methods section, the table with rheological and thermal parameters, and 11 figures providing additional background information about the modelling results.

Numerical methods

1. Governing equations

The 3D thermo-mechanical numerical code DOUAR (Braun et al., 2008; Thieulot et al., 2008) is designed to solve mass, momentum and energy conservation for an incompressible fluid. We refer readers to (Braun et al., 2008) for a more detailed description of the methods used.

DOUAR solves the Stokes flow equations, constituted by conservation of momentum (Eq. 1) and conservation of mass (Eq. 2):

$$\nabla \cdot \mu \left(\nabla v + \nabla v^T\right) - \nabla P = \rho g; \tag{1}$$

$$\nabla \cdot v = 0, \tag{2}$$

where μ is the material shear viscosity, v is the velocity field, P is the pressure, ρ is the density, and g is the gravity acceleration.

The pressure can be eliminated from these equations introducing a so-called penalty or compressibility factor, λ:

$$P = -\lambda \nabla \cdot v. \tag{3}$$

The compressibility factor is typically eight orders of magnitude larger than the shear viscosity to ensure a nearly incompressible behavior for the flow.

The mechanical equations are coupled to the heat conservation equation:

$$\rho c_p \left(\frac{\partial T}{\partial t} + v \cdot \nabla T\right) = \nabla \cdot k \nabla T + \rho H_r, \tag{4}$$

where T is the temperature, c_p is the heat capacity, k is the thermal conductivity, and H_r is the radiogenic heat production (Table S1).

2. Rheological model

The material deforms according to a thermally-activated creep law:

$$\mu = B\, \dot{\varepsilon}^{1/n-1} e^{Q/nRT}, \tag{5}$$

where μ is the viscosity, $\dot{\varepsilon} = \sqrt{1/2\, \dot{\varepsilon}_{ij} \dot{\varepsilon}_{ij}}$ is the second invariant of the strain rate tensor, and B is the pre-exponential factor, Q is the activation energy, n is the power-law exponent, and R is the gas constant (see Table S1).

When plasticity is enabled, material deformation is dictated by the Mohr-Coulomb failure criterion:

$$\tau = C - \sigma_n tan\varphi, \tag{6}$$

where τ is the shear stress, σ_n is the normal stress, C is the cohesion, and φ is the material friction angle (Table S1). The friction angle decreases with increasing values of total strain (linear strain softening).

The viscous-plastic rheology is assigned to the model by means of a Christmas tree-like criterion, where the rheological behavior is defined by the minimum differential stress (or viscosity) attained between ductile and brittle/plastic fields (Ranalli, 1995).

3. Thermochronometric cooling ages

In our numerical models, the marker particles store their position, pressure and temperature for each element at each time step. Once a particle has reached the surface, the corresponding p–T–t (pressure-temperature-time) path is compiled from storage and registered at the current time step. From these paths, thermochronometric cooling age is calculated with the assumption of no deformation for 30 Myr prior to the model start in post-processing. We refer the readers to Nettesheim et al. (2018) for the further details.

Table S1. Density and rheological and thermal parameters for the overriding continental plate

Material		*Density* ρ *[kg/m^3]*	*Rheological parameters*							*Thermal parameters*		
			Ductile				*Brittle/plastic*			*Thermal diffusivity* $\alpha = \frac{k}{\rho c_p}$ *[10^{-6} × m^2/s]*	*Heat production* H_r *[μW/(kg m^3)]*	
			Flow law	*Activation energy* Q *[kJ/mol]*	*Power-law exponent* n	*Pre-exponential factor* B *[Pa s$^{1/n}$]*	*Cohesion* C *[MPa]*	*Friction angle* φ *[°]*	*Strain weakening interval*		*"Normal" geotherm*	*"Cold" geotherm*
Upper crust		2750	Wet granite[a]	140.6	1.9	4.43×10^7	10	15 –> 5	0.05 –> 0.55	1.0	1.8	0
Lower crust	**felsic**	2900	Wet granite[a]	140.6	1.9	4.43×10^7	10	15 –> 5	0.05 –> 0.55	1.0	0.6	0
	mafic		Dry diabase[a]	276.0	3.05	1.24×10^6						
Lithospheric mantle		3300	Olivine aggregates[b]	324.3	3.5	1.21×10^7	2	10	–	1.0	0	

[a] Carter & Tsenn (1987)

[b] Hirth & Kohlstedt (2003); Jadamec & Billen (2012)

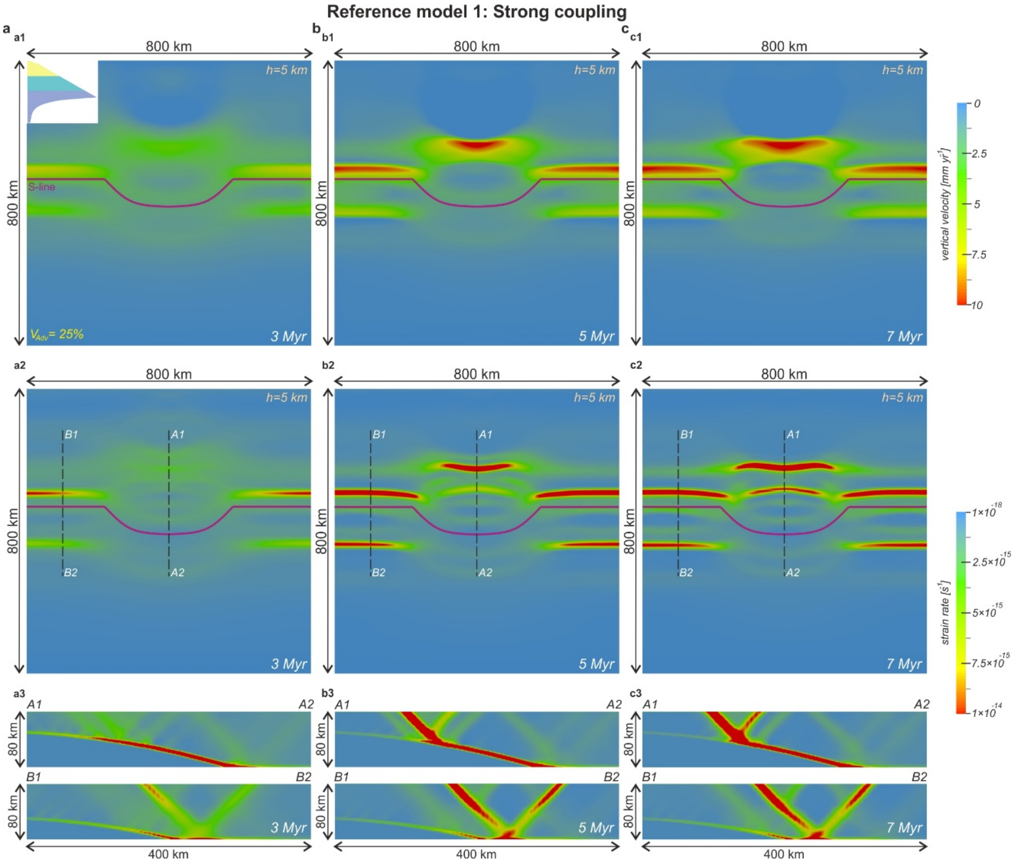

Figure S1. Temporal evolution of the reference experiment for strong rheological coupling (model **1**). Plan views show computed vertical velocity and second invariant of modelled strain rate (at 5 km depth; top and middle row, respectively). Vertical cross-sections (bottom third) illustrate strain rate distributions along dashed lines indicated above.

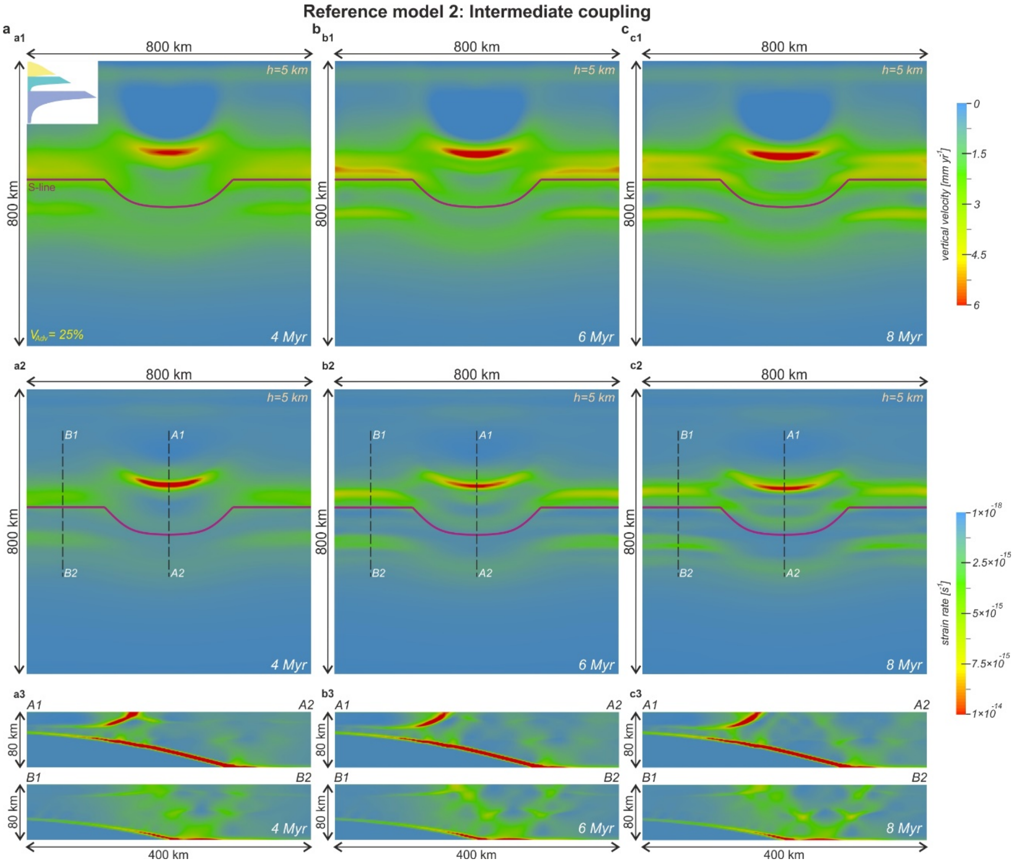

Figure S2. Temporal evolution of the reference experiment for intermediate rheological coupling (model **2**).

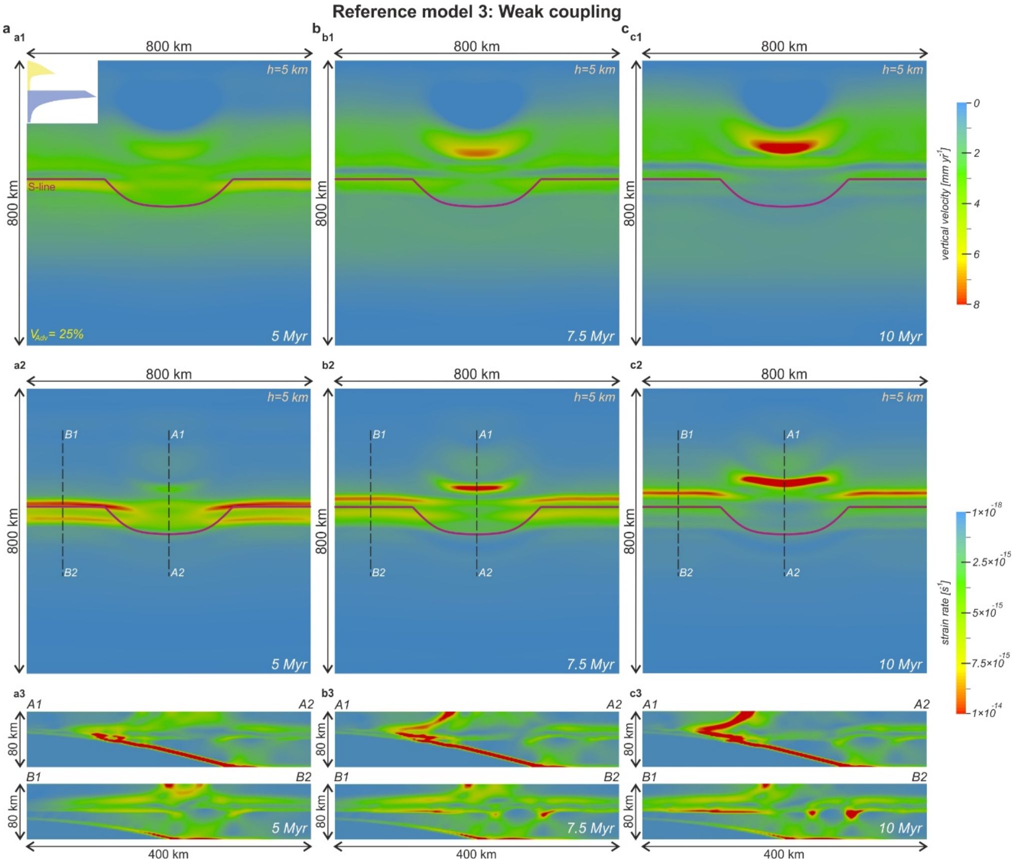

Figure S3. Temporal evolution of the reference experiment for weak rheological coupling (model **3**).

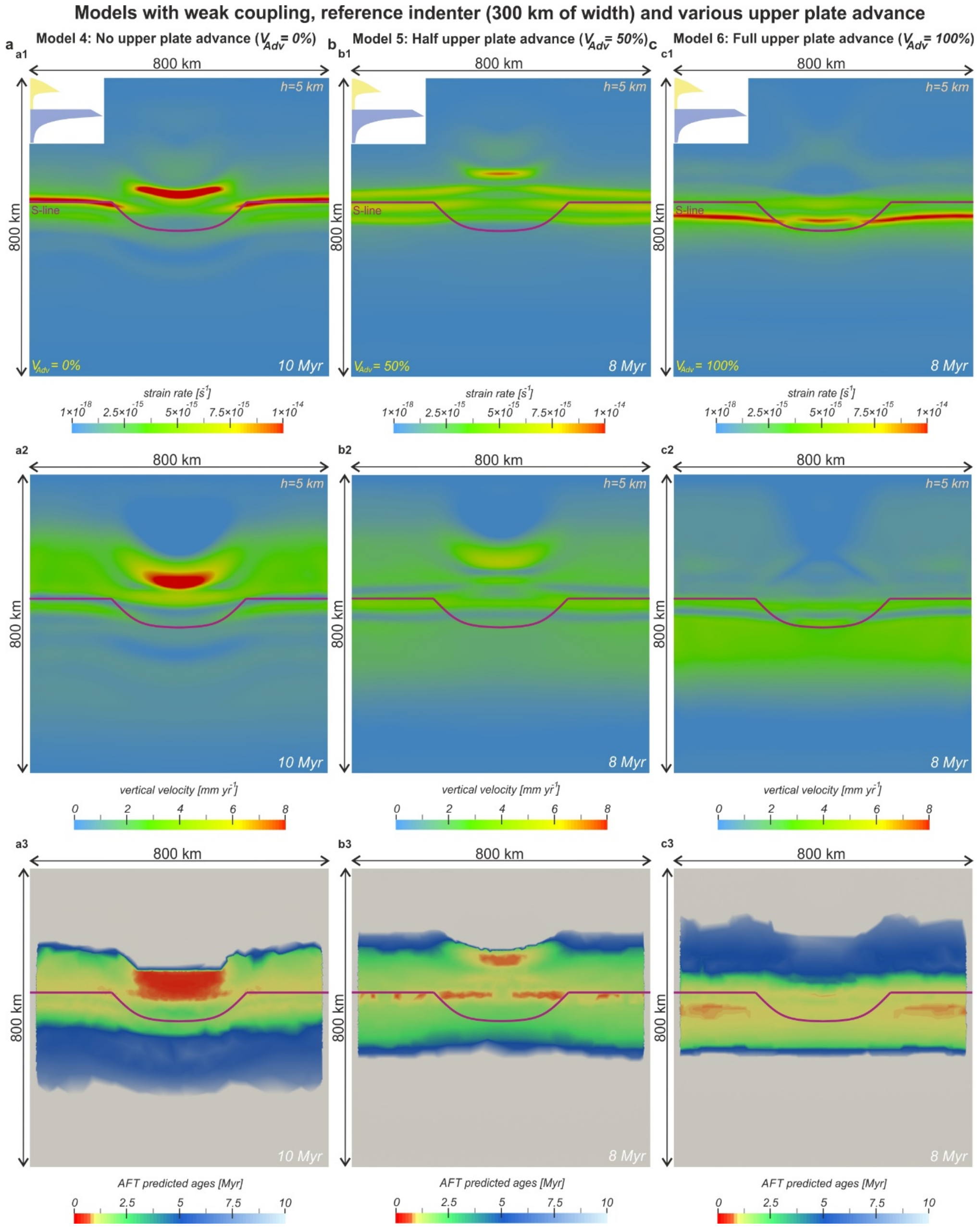

Figure S4. Experiments characterized by weak rheological coupling of overriding lithosphere, reference indenter width (300 km) and different velocity boundary conditions: a) no upper plate advance model **4** (V_{Adv} = 0%); b) half upper plate advance model **5** (V_{Adv} = 50%); c) full upper plate advance model **6** (V_{Adv} = 100%).

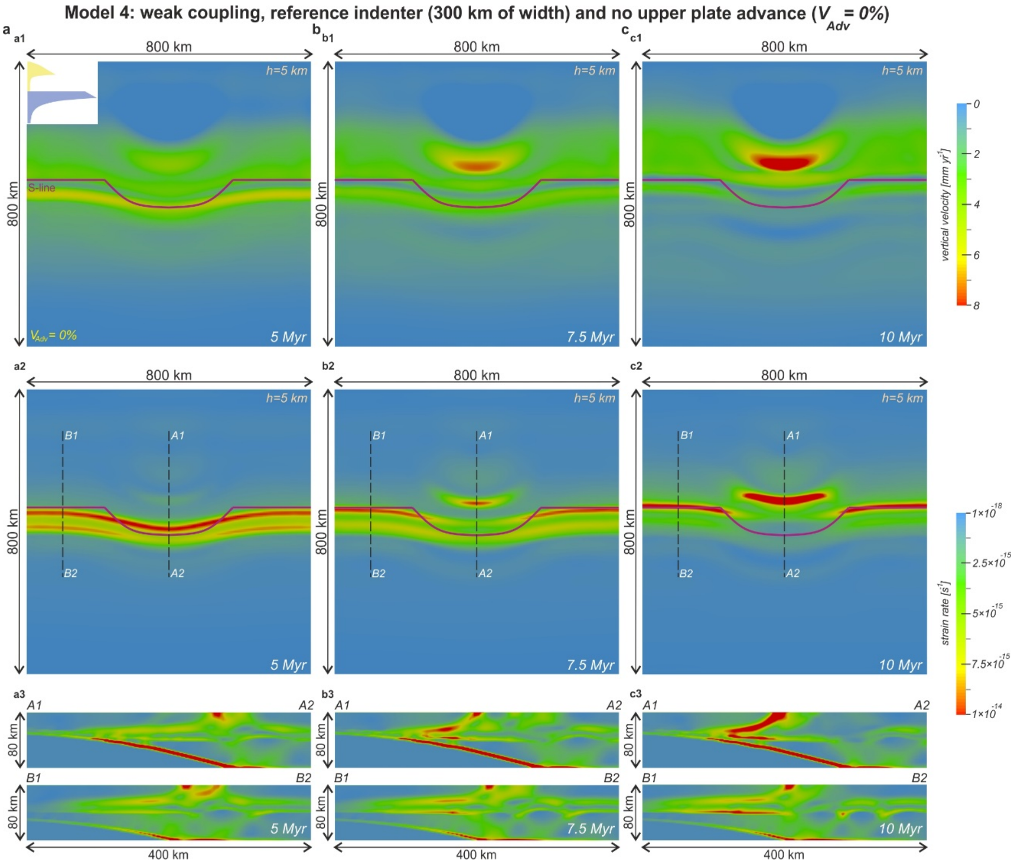

Figure S5. Temporal evolution of weakly coupled no upper plate advance model **4** (V_{Adv} = 0%).

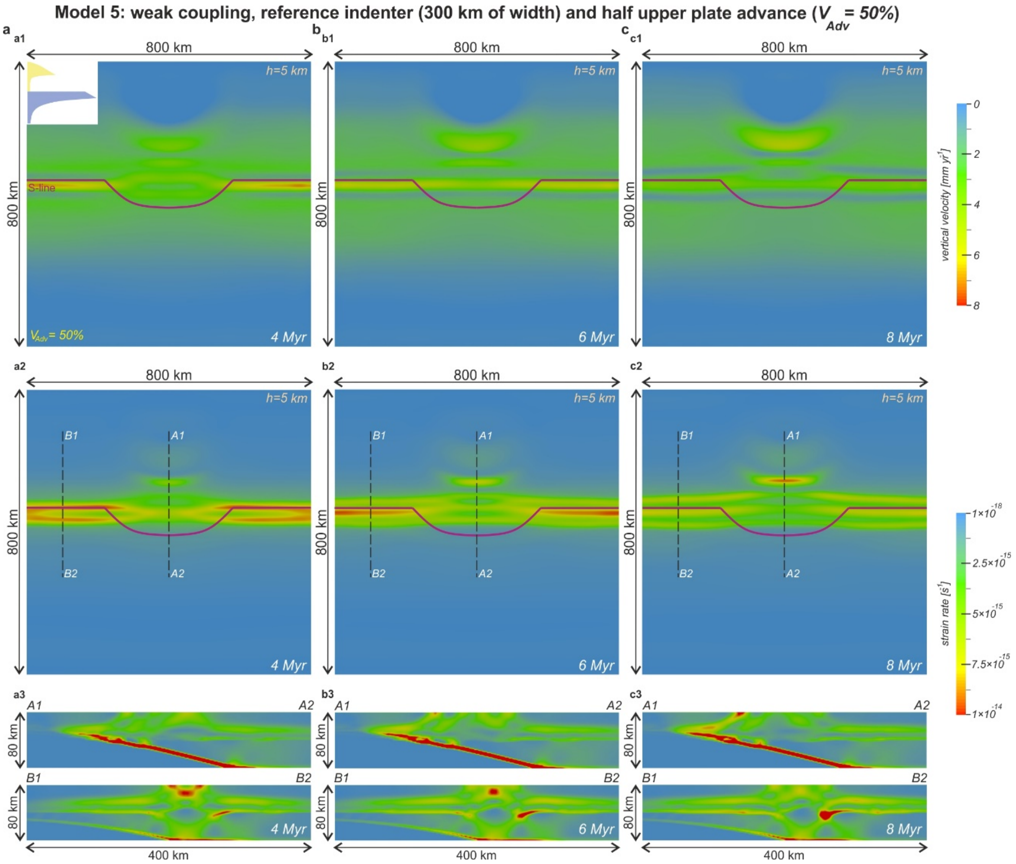

Figure S6. Temporal evolution of weakly coupled half upper plate advance model **5** (V_{Adv} = 50%).

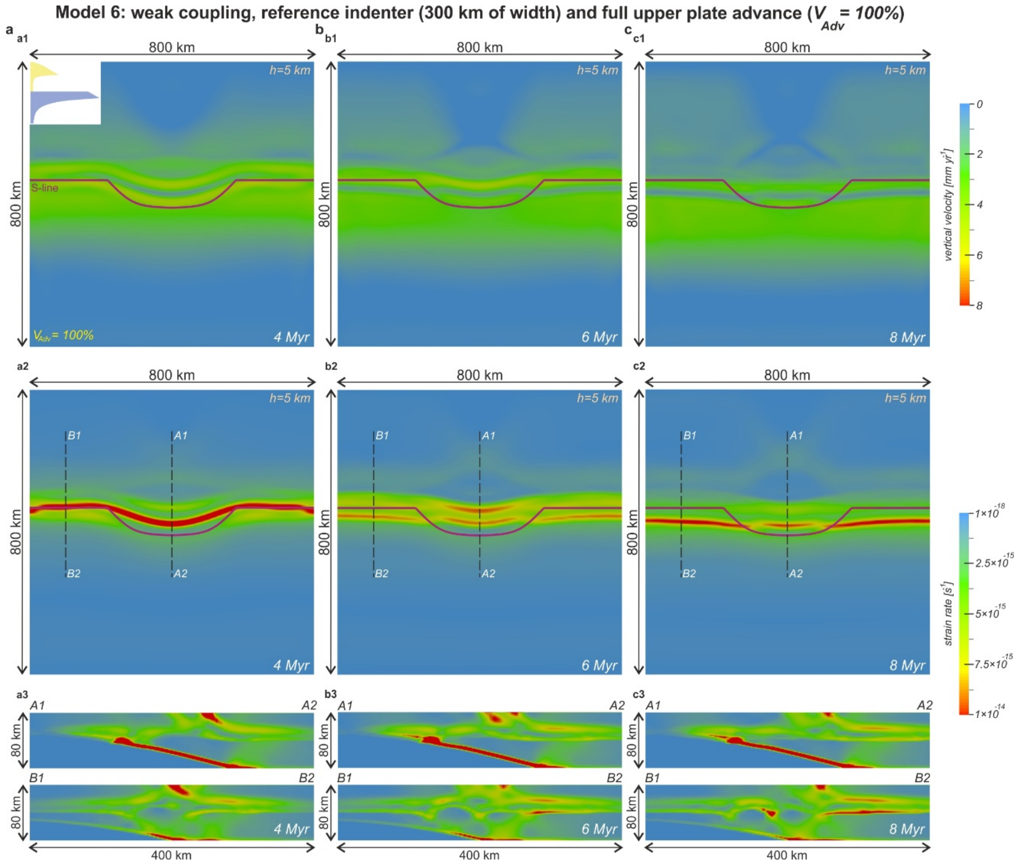

Figure S7. Temporal evolution of weakly coupled full upper plate advance model **6** (V_{Adv} = 100%).

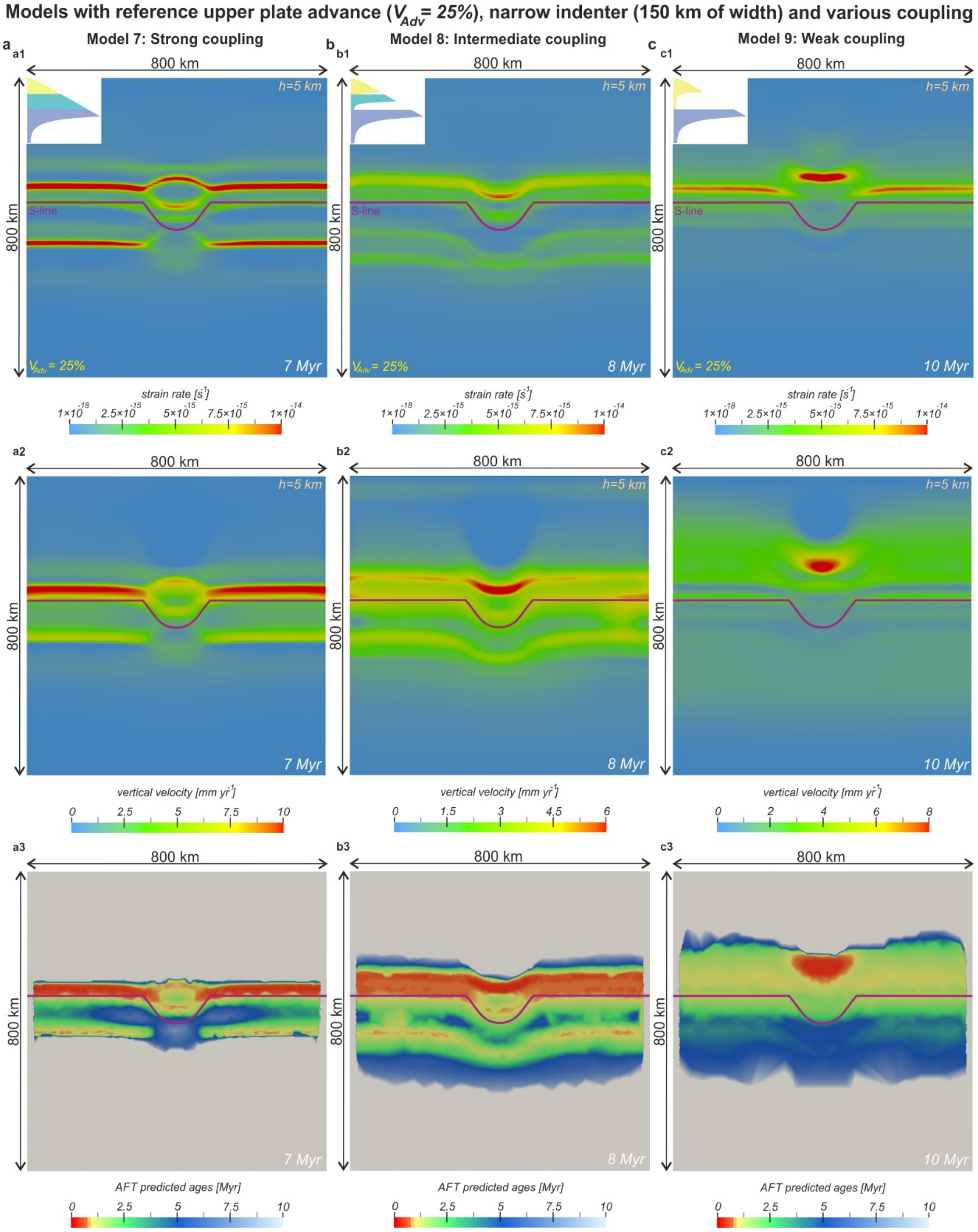

Figure S8. Experiments characterized by reference upper plate advance (V_{Adv} = 25%), narrow (150 km-wide) indenter and different rheological structure of the overriding continent: a) strongly coupled model **7**; b) intermediately coupled model **8**; c) weakly coupled model **9**.

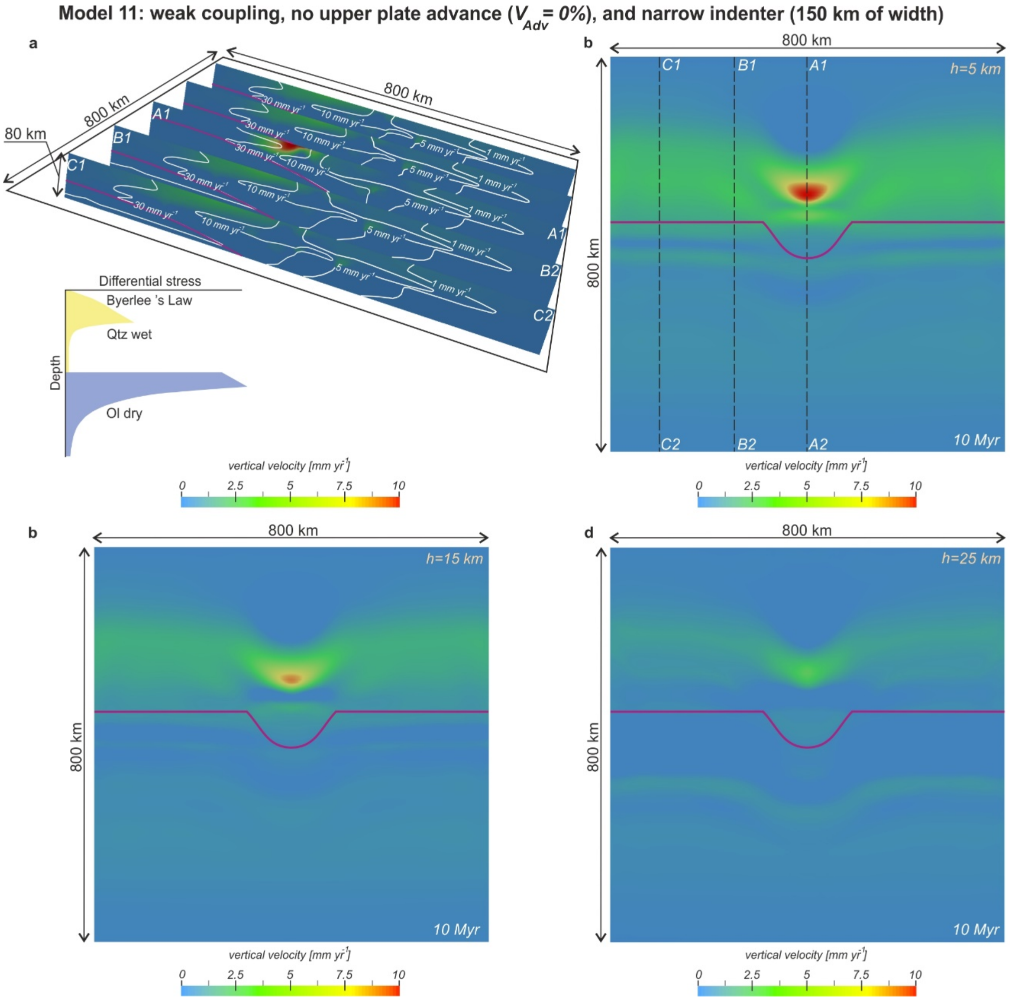

Figure S9. The distribution of vertical velocity for model **11** characterized by weakly coupled rheological structure, no upper plate advance contribution (V_{Adv} = 0%) in the total shortening and narrow indenter width (150 km): a) 3D view, white lines show the isolines for the horizontal component of the total velocity; b-d) Plan-views at the 5, 15 and 25 km depth.

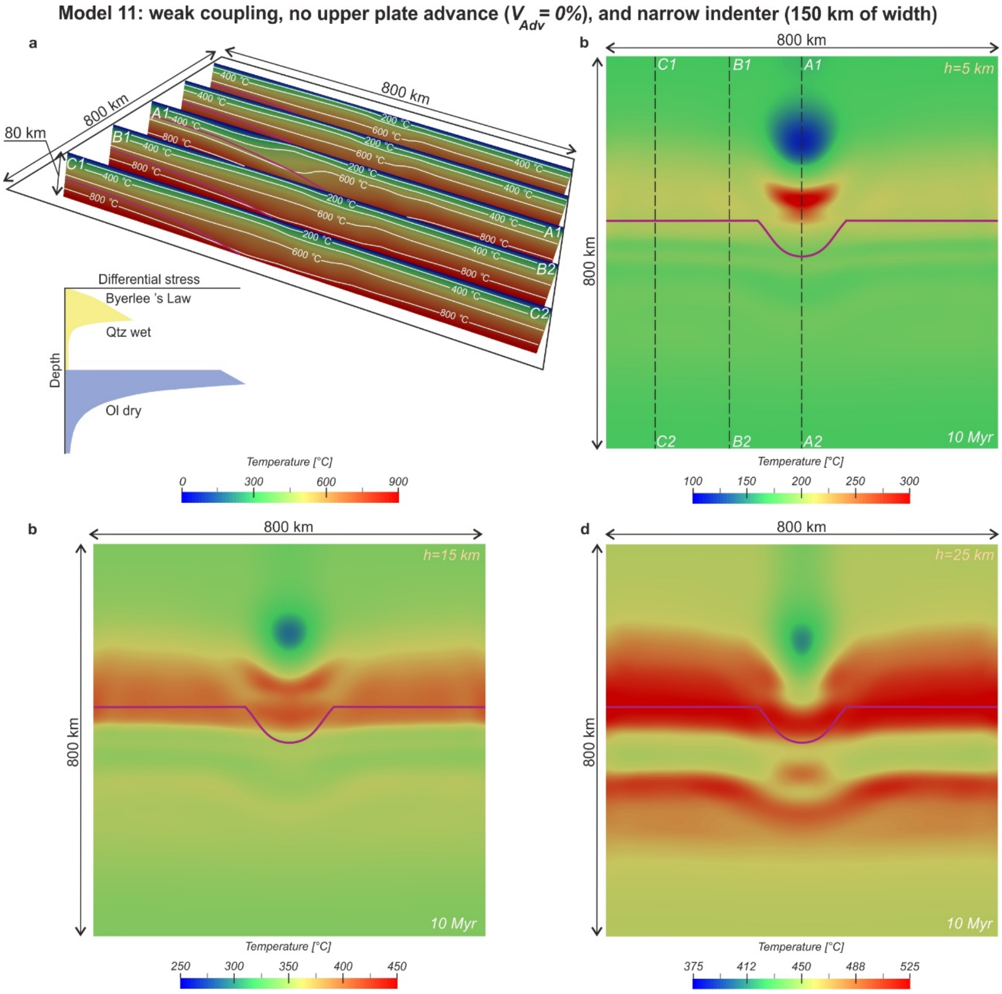
Model 11: weak coupling, no upper plate advance ($V_{Adv} = 0\%$), and narrow indenter (150 km of width)

Figure S10. The temperature distribution for model **11** characterized by weakly coupled rheological structure, no upper plate advance contribution ($V_{Adv} = 0\%$) in the total shortening and narrow indenter width (150 km): a) 3D view, white lines show the temperature isolines; b-d) Plan-views at the 5, 15 and 25 km depth.

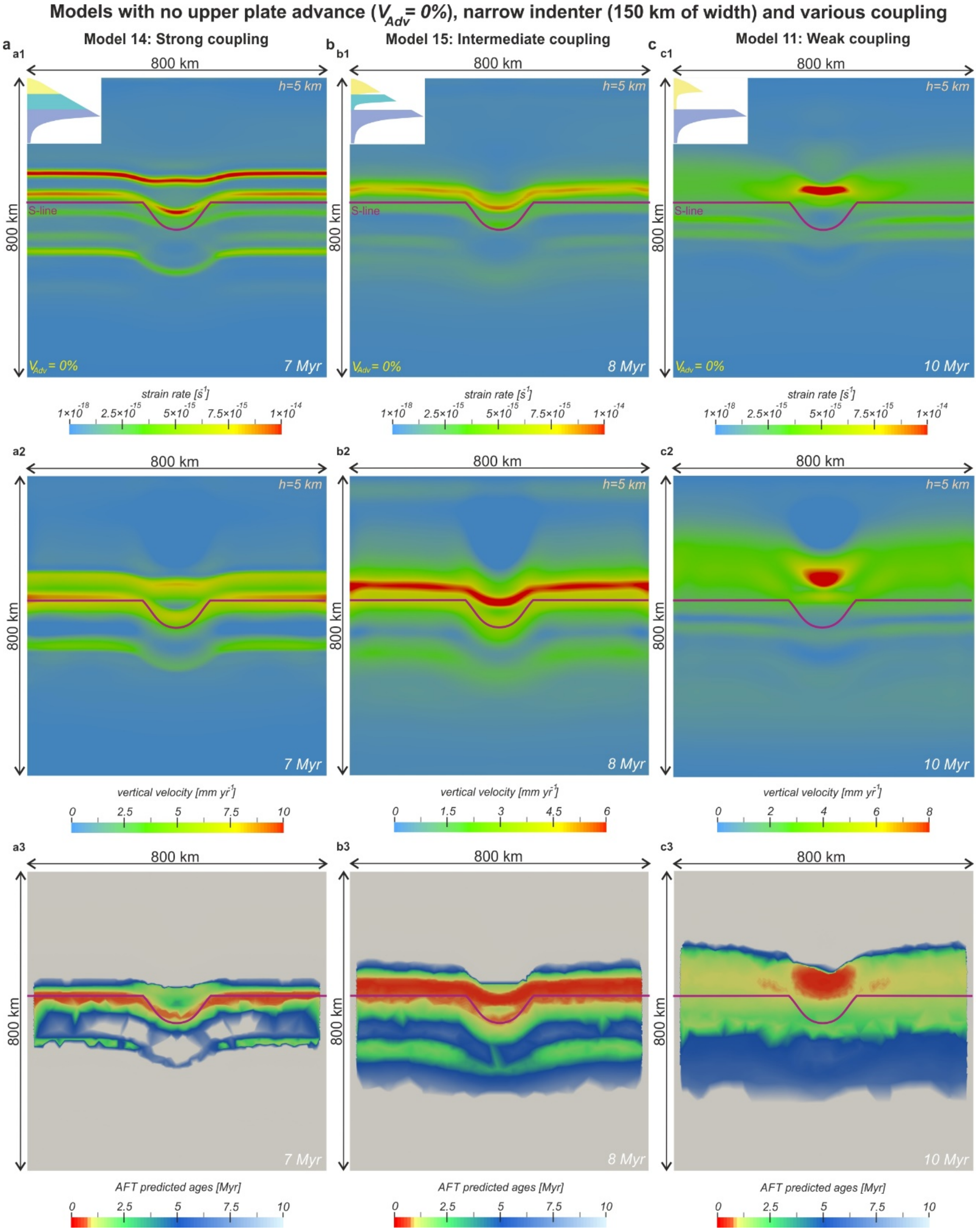

Figure S11. Experiments characterized by no upper plate advance (V_{Adv} = 0%), narrow (150 km-wide) indenter and different rheological structure of the overriding continent: a) strongly coupled model **14**; b) intermediately coupled model **15**; c) weakly coupled model **11**.

Bibliography (excluding Chapters 3 and 4)

Adams, B. A. and T. A. Ehlers (2017). "Deciphering topographic signals of glaciation and rock uplift in an active orogen: a case study from the Olympic Mountains, USA". *Earth Surface Processes and Landforms* 42.11, pp. 1680–1692. DOI: `10.1002/esp.4120`.

Allmendinger, R. W., R. Reilinger, and J. Loveless (2007). "Strain and rotation rate from GPS in Tibet, Anatolia, and the Altiplano". *Tectonics* 26.3. DOI: `10.1029/2006TC002030`.

Angiboust, S., S. Wolf, E. Burov, P. Agard, and P. Yamato (2012). "Effect of fluid circulation on subduction interface tectonic processes: Insights from thermo-mechanical numerical modelling". *Earth and Planetary Science Letters* 357-358, pp. 238–248. DOI: `10.1016/j.epsl.2012.09.012`.

Arkle, J. C., P. A. Armstrong, P. J. Haeussler, M. G. Prior, S. Hartman, K. L. Sendziak, and J. A. Brush (2013). "Focused exhumation in the syntaxis of the western Chugach Mountains and Prince William Sound, Alaska". *Geological Society of America Bulletin* 125.5, pp. 776–793.

Avouac, J. P. and E. B. Burov (1996). "Erosion as a driving mechanism of intracontinental mountain growth". *Journal of Geophysical Research-Solid Earth* 101 (B8), pp. 17747–17769. DOI: `10.1029/96JB01344`.

Bajolet, F., A. Replumaz, and R. Lainé (2013). "Orocline and syntaxes formation during subduction and collision". *Tectonics* 32.5, pp. 1529–1546. DOI: `10.1002/tect.20087`.

Barbarand, J., A. Carter, I. Wood, and T. Hurford (2003). "Compositional and structural control of fission-track annealing in apatite". *Chemical Geology* 198.1, pp. 107–137. DOI: `10.1016/S0009-2541(02)00424-2`.

Bathe, K.-J. (1982). *Finite element procedures.* New Jersey: Prentice-Hall.

Batt, G. E., M. T. Brandon, K. A. Farley, and M. Roden-Tice (2001). "Tectonic synthesis of the Olympic Mountains segment of the Cascadia wedge, using two-dimensional thermal and kinematic modeling of thermochronological ages". *Journal of Geophysical Research: Solid Earth* 106 (B11), pp. 26731–26746. DOI: `10.1029/2001JB000288`.

Beaumont, C., R. A. Jamieson, M. H. Nguyen, and B. Lee (2001). "Himalayan tectonics explained by extrusion of a low-viscosity crustal channel coupled to focused surface denudation". *Nature* 414.6865, pp. 738–742. DOI: `10.1038/414738a`.

Beaumont, C., P. Fullsack, and J. Hamilton (1992). "Erosional control of active compressional orogens". *Thrust tectonics* 99, pp. 1–18.

Bendick, R. and T. A. Ehlers (2014). "Extreme localized exhumation at syntaxes initiated by subduction geometry". *Geophysical Research Letters* 41.16, pp. 5861–5867. DOI: `10.1002/2014GL061026`.

Berger, A. L., J. A. Spotila, J. B. Chapman, T. L. Pavlis, E. Enkelmann, N. A. Ruppert, and J. T. Buscher (2008). "Architecture, kinematics, and exhumation of a convergent orogenic wedge: A thermochronological investigation of tectonic–climatic interactions within the central St. Elias orogen, Alaska". *Earth and Planetary Science Letters* 270.1, pp. 13–24. DOI: `10.1016/j.epsl.2008.02.034`.

Bonnardot, M.-A., R. Hassani, E. Tric, E. Ruellan, and M. Régnier (2008). "Effect of margin curvature on plate deformation in a 3-D numerical model of subduction zones". *Geophysical Journal International* 173.3, pp. 1084–1094. DOI: `10.1111/j.1365-246X.2008.03752.x`.

Brandon, M. T., M. K. Roden-Tice, and J. I. Garver (1998). "Late Cenozoic exhumation of the Cascadia accretionary wedge in the Olympic Mountains, northwest Washington State". *Geological*

Society of America Bulletin 110.8, pp. 985–1009. DOI: `10.1130/0016-7606(1998)110<0985:LCEOTC>2.3.CO;2`.

Braun, J. (2003). "Pecube: a new finite-element code to solve the 3D heat transport equation including the effects of a time-varying, finite amplitude surface topography". *Computers & Geosciences* 29.6, pp. 787–794. DOI: `10.1016/S0098-3004(03)00052-9`.

Braun, J., T. Simon-Labric, K. E. Murray, and P. W. Reiners (2014). "Topographic relief driven by variations in surface rock density". *Nature Geoscience* 7.7, pp. 534–540. DOI: `10.1038/ngeo2171`.

Braun, J., C. Thieulot, P. Fullsack, M. DeKool, C. Beaumont, and R. Huismans (2008). "DOUAR: A new three-dimensional creeping flow numerical model for the solution of geological problems". *Physics of the Earth and Planetary Interiors*. Recent Advances in Computational Geodynamics: Theory, Numerics and Applications 171.1, pp. 76–91. DOI: `10.1016/j.pepi.2008.05.003`.

Braun, J. and S. D. Willett (2013). "A very efficient O(n), implicit and parallel method to solve the stream power equation governing fluvial incision and landscape evolution". *Geomorphology* 180–181, pp. 170–179. DOI: `10.1016/j.geomorph.2012.10.008`.

Burg, J.-P., P. Nievergelt, F. Oberli, D. Seward, P. Davy, J.-C. Maurin, Z. Diao, and M. Meier (1998). "The Namche Barwa syntaxis: evidence for exhumation related to compressional crustal folding". *Journal of Asian Earth Sciences* 16.2, pp. 239–252. DOI: `10.1016/S0743-9547(98)00002-6`.

Burov, E. B. and A. B. Watts (2006). "The long-term strength of continental lithosphere: "jelly sandwich" or "crème brûlée"?" *GSA Today* 16.1, p. 4. DOI: `10.1130/1052-5173(2006)016<4:TLTSOC>2.0.CO;2`.

Burov, E. B. (2011). "Rheology and strength of the lithosphere". *Marine and Petroleum Geology* 28.8, pp. 1402–1443. DOI: `10.1016/j.marpetgeo.2011.05.008`.

Buscher, J. T., A. L. Berger, and J. A. Spotila (2008). "Exhumation in the Chugach-Kenai Mountain Belt Above the Aleutian Subduction Zone, Southern Alaska". In: *Active Tectonics and Seismic Potential of Alaska*. American Geophysical Union (AGU), pp. 151–166. DOI: `10.1029/179GM08`.

Carlson, W. D., R. A. Donelick, and R. A. Ketcham (1999). "Variability of apatite fission-track annealing kinetics: I. Experimental results". *American mineralogist* 84.9, pp. 1213–1223.

Carter, N. L. and M. C. Tsenn (1987). "Flow properties of continental lithosphere". *Tectonophysics* 136.1, pp. 27–63. DOI: `10.1016/0040-1951(87)90333-7`.

Champagnac, J.-D., P. Molnar, C. Sue, and F. Herman (2012). "Tectonics, climate, and mountain topography". *Journal of Geophysical Research: Solid Earth* 117, B02403. DOI: `10.1029/2011JB008348`.

Craw, D., P. O. Koons, D. M. Winslow, C. P. Chamberlain, and P. K. Zeitler (1994). "Boiling fluids in a region of rapid uplift, Nanga Parbat Massif, Pakistan". *Earth and Planetary Science Letters* 128.3, pp. 169–182. DOI: `10.1016/0012-821X(94)90143-0`.

Crowley, J. L., D. J. Waters, M. P. Searle, and S. A. Bowring (2009). "Pleistocene melting and rapid exhumation of the Nanga Parbat massif, Pakistan: Age and P–T conditions of accessory mineral growth in migmatite and leucogranite". *Earth and Planetary Science Letters* 288.3, pp. 408–420. DOI: `10.1016/j.epsl.2009.09.044`.

Crowley, K. D., M. Cameron, and R. L. Schaefer (1991). "Experimental studies of annealing of etched fission tracks in fluorapatite". *Geochimica et Cosmochimica Acta* 55.5, pp. 1449–1465. DOI: `10.1016/0016-7037(91)90320-5`.

Davy, P. and D. Lague (2009). "Fluvial erosion/transport equation of landscape evolution models revisited". *Journal of Geophysical Research: Earth Surface* 114 (F3). DOI: `10.1029/2008JF001146`.

Dodson, M. H. (1973). "Closure temperature in cooling geochronological and petrological systems". *Contributions to Mineralogy and Petrology* 40.3, pp. 259–274. DOI: `10.1007/BF00373790`.

Eberhart-Phillips, D., D. H. Christensen, T. M. Brocher, R. Hansen, N. A. Ruppert, P. J. Haeussler, and G. A. Abers (2006). "Imaging the transition from Aleutian subduction to Yakutat collision in central Alaska, with local earthquakes and active source data". *Journal of Geophysical Research: Solid Earth* 111 (B11). DOI: `10.1029/2005JB004240`.

Ehlers, T. A. and C. J. Poulsen (2009). "Influence of Andean uplift on climate and paleoaltimetry estimates". *Earth and Planetary Science Letters* 281.3, pp. 238–248. DOI: `10.1016/j.epsl.2009.02.026`.

Elliott, J., J. T. Freymueller, and C. F. Larsen (2013). "Active tectonics of the St. Elias orogen, Alaska, observed with GPS measurements". *Journal of Geophysical Research: Solid Earth* 118.10, pp. 5625–5642. DOI: `10.1002/jgrb.50341`.

England, P. and P. Molnar (1990). "Surface uplift, uplift of rocks, and exhumation of rocks". *Geology* 18.12, pp. 1173–1177. DOI: `10.1130/0091-7613(1990)018<1173:SUUORA>2.3.CO;2`.

Enkelmann, E., T. A. Ehlers, P. K. Zeitler, and B. Hallet (2011). "Denudation of the Namche Barwa antiform, eastern Himalaya". *Earth and Planetary Science Letters* 307.3, pp. 323–333. DOI: `10.1016/j.epsl.2011.05.004`.

Enkelmann, E., A. Piestrzeniewicz, S. Falkowski, K. Stübner, and T. A. Ehlers (2017). "Thermochronology in southeast Alaska and southwest Yukon: Implications for North American Plate response to terrane accretion". *Earth and Planetary Science Letters* 457, pp. 348–358. DOI: `10.1016/j.epsl.2016.10.032`.

Enkelmann, E., P. G. Valla, and J.-D. Champagnac (2015). "Low-temperature thermochronology of the Yakutat plate corner, St. Elias Range (Alaska): bridging short-term and long-term deformation". *Quaternary Science Reviews* 113, pp. 23–38. DOI: `10.1016/j.quascirev.2014.10.019`.

Enkelmann, E., P. K. Zeitler, J. I. Garver, T. L. Pavlis, and B. P. Hooks (2010). "The thermochronological record of tectonic and surface process interaction at the Yakutat–North American collision zone in southeast Alaska". *American Journal of Science* 310.4, pp. 231–260. DOI: `10.2475/04.2010.01`.

Falkowski, S., E. Enkelmann, K. Drost, J. A. Pfänder, K. Stübner, and T. A. Ehlers (2016). "Cooling history of the St. Elias syntaxis, southeast Alaska, revealed by geochronology and thermochronology of cobble-sized glacial detritus". *Tectonics* 35.2, pp. 447–468. DOI: `10.1002/2015TC004086`.

Falkowski, S., E. Enkelmann, and T. A. Ehlers (2014). "Constraining the area of rapid and deep-seated exhumation at the St. Elias syntaxis, Southeast Alaska, with detrital zircon fission-track analysis". *Tectonics* 33.5, pp. 597–616. DOI: `10.1002/2013TC003408`.

Farley, K. A. (2000). "Helium diffusion from apatite: General behavior as illustrated by Durango fluorapatite". *Journal of Geophysical Research: Solid Earth* 105 (B2), pp. 2903–2914. DOI: `10.1029/1999JB900348`.

Farley, K. A., D. Shuster, and R. Ketcham (2011). "U and Th zonation in apatite observed by laser ablation ICPMS, and implications for the (U–Th)/He system". *Geochimica et Cosmochimica Acta* 75.16, pp. 4515–4530. DOI: `10.1016/j.gca.2011.05.020`.

Ferguson, K. M., P. A. Armstrong, J. C. Arkle, and P. J. Haeussler (2015). "Focused rock uplift above the subduction décollement at Montague and Hinchinbrook Islands, Prince William Sound, Alaska". *Geosphere* 11.1, pp. 144–159. DOI: `10.1130/GES01036.1`.

Flowers, R. M., R. A. Ketcham, D. L. Shuster, and K. A. Farley (2009). "Apatite (U–Th)/He thermochronometry using a radiation damage accumulation and annealing model". *Geochimica et Cosmochimica Acta* 73.8, pp. 2347–2365. DOI: `10.1016/j.gca.2009.01.015`.

Fuis, G. S., T. E. Moore, G. Plafker, T. M. Brocher, M. A. Fisher, W. D. Mooney, W. J. Nokleberg, R. A. Page, B. C. Beaudoin, N. I. Christensen, A. R. Levander, W. J. Lutter, R. W. Saltus, and N. A. Ruppert (2008). "Trans-Alaska Crustal Transect and continental evolution involving subduction underplating and synchronous foreland thrusting". *Geology* 36.3, pp. 267–270. DOI: `10.1130/G24257A.1`.

Godard, V., R. Cattin, and J. Lavé (2004). "Numerical modeling of mountain building: Interplay between erosion law and crustal rheology". *Geophysical Research Letters* 31.23. DOI: `10.1029/2004GL021006`.

Green, P., Duddy, I. R., Gleadow, A. J. W., Tingate, P.R., and Laslett, G. M. (1986). “Thermal annealing of fission tracks in apatite: 1. A qualitative description”. *Chemical Geology: Isotope Geoscience section* 59, pp. 237–253. DOI: `10.1016/0168-9622(86)90074-6`.

Grotzinger, J., T. H. Jordan, F. Press, and R. Siever (2009). *Understanding Earth.* W. H. Freeman. 671 pp.

Gulick, S. P. S., J. M. Jaeger, A. C. Mix, H. Asahi, H. Bahlburg, C. L. Belanger, G. B. B. Berbel, L. Childress, E. Cowan, L. Drab, M. Forwick, A. Fukumura, S. Ge, S. Gupta, A. Kioka, S. Konno, L. J. LeVay, C. März, K. M. Matsuzaki, E. L. McClymont, C. Moy, J. Müller, A. Nakamura, T. Ojima, F. R. Ribeiro, K. D. Ridgway, O. E. Romero, A. L. Slagle, J. S. Stoner, G. St-Onge, I. Suto, M. D. Walczak, L. L. Worthington, I. Bailey, E. Enkelmann, R. Reece, and J. M. Swartz (2015). “Mid-Pleistocene climate transition drives net mass loss from rapidly uplifting St. Elias Mountains, Alaska”. *Proceedings of the National Academy of Sciences* 112.49, pp. 15042–15047. DOI: `10.1073/pnas.1512549112`.

Gupta, A. (2000). *WSMP: Watson Sparse Matrix Package.* RC 21888 (98472). Yorktown Heights, NY: IBM T.J. Watson Research Center, p. 41.

Haeussler, P. J., P. O’Sullivan, A. L. Berger, and J. A. Spotila (2008). “Neogene exhumation of the Tordrillo Mountains, Alaska, and correlations with Denali (Mount McKinley)”. In: *Geophysical Monograph Series.* Ed. by J. T. Freymueller, P. J. Haeussler, R. L. Wesson, and G. Ekström. Vol. 179. Washington, D. C.: American Geophysical Union, pp. 269–285.

Hayes, G. P., D. J. Wald, and R. L. Johnson (2012). “Slab1.0: A three-dimensional model of global subduction zone geometries”. *Journal of Geophysical Research: Solid Earth* 117 (B1), B01302. DOI: `10.1029/2011JB008524`.

Herman, F., D. Seward, P. G. Valla, A. Carter, B. Kohn, S. D. Willett, and T. A. Ehlers (2013). “Worldwide acceleration of mountain erosion under a cooling climate”. *Nature* 504.7480, pp. 423–426. DOI: `10.1038/nature12877`.

Hirth, G. and D. Kohlstedt (2003). “Rheology of the upper mantle and the mantle wedge: A view from the experimentalists”. In: *Inside the subduction Factory.* Ed. by J. Eiler. Vol. 138. Geophysical Monograph Series. Washington, D. C.: American Geophysical Union, pp. 83–105.

Hodges, K. V., J. M. Hurtado, and K. X. Whipple (2001). “Southward extrusion of Tibetan crust and its effect on Himalayan tectonics”. *Tectonics* 20.6, pp. 799–809. DOI: `10.1029/2001TC001281`.

Howard, A. D., W. E. Dietrich, and M. A. Seidl (1994). “Modeling fluvial erosion on regional to continental scales”. *Journal of Geophysical Research: Solid Earth* 99, pp. 13971–13986. DOI: `10.1029/94JB00744`.

Jackson, J. (2002). “Strength of the continental lithosphere: Time to abandon the jelly sandwich?” *GSA Today* 12.9, p. 4. DOI: `10.1130/1052-5173(2002)012<0004:SOTCLT>2.0.CO;2`.

Jackson, S. E., N. J. Pearson, W. L. Griffin, and E. A. Belousova (2004). “The application of laser ablation-inductively coupled plasma-mass spectrometry to in situ U–Pb zircon geochronology”. *Chemical Geology* 211.1, pp. 47–69. DOI: `10.1016/j.chemgeo.2004.06.017`.

Jadamec, M. A. and M. I. Billen (2012). “The role of rheology and slab shape on rapid mantle flow: Three-dimensional numerical models of the Alaska slab edge”. *Journal of Geophysical Research: Solid Earth* 117 (B2), B02304. DOI: `10.1029/2011JB008563`.

Johnston, S., G. Gehrels, V. Valencia, and J. Ruiz (2009). “Small-volume U–Pb zircon geochronology by laser ablation-multicollector-ICP-MS”. *Chemical Geology* 259.3, pp. 218–229. DOI: `10.1016/j.chemgeo.2008.11.004`.

Ketcham, R. A., A. Carter, R. A. Donelick, J. Barbarand, and A. J. Hurford (2007). “Improved modeling of fission-track annealing in apatite”. *American Mineralogist* 92.5, pp. 799–810. DOI: `10.2138/am.2007.2281`.

Ketcham, R. A., R. A. Donelick, and W. D. Carlson (1999). “Variability of apatite fission-track annealing kinetics: III. Extrapolation to geological time scales”. *American Mineralogist* 84.9, pp. 1235–1255.

Koehler, R. D. (2013). *Quaternary Faults and Folds (QFF)*. DDS 3. Alaska Division of Geological & Geophysical Surveys. DOI: `10.14509/24956`.

Kooi, H. and C. Beaumont (1994). "Escarpment evolution on high-elevation rifted margins: Insights derived from a surface processes model that combines diffusion, advection, and reaction". *Journal of Geophysical Research: Solid Earth* 99 (B6), pp. 12191–12209. DOI: `10.1029/94JB00047`.

Koons, P. O. (1987). "Some thermal and mechanical consequences of rapid uplift: an example from the Southern Alps, New Zealand". *Earth and planetary science letters* 86.2, pp. 307–319.

Koons, P. O., P. K. Zeitler, C. P. Chamberlain, D. Craw, and A. S. Meltzer (2002). "Mechanical links between erosion and metamorphism in Nanga Parbat, Pakistan Himalaya". *American Journal of Science* 302.9, pp. 749–773. DOI: `10.2475/ajs.302.9.749`.

Koons, P. O., B. P. Hooks, T. L. Pavlis, P. Upton, and A. D. Barker (2010). "Three-dimensional mechanics of Yakutat convergence in the southern Alaskan plate corner". *Tectonics* 29.4, TC4008. DOI: `10.1029/2009TC002463`.

Koptev, A., T. A. Ehlers, M. Nettesheim, and D. M. Whipp (2019). "Response of a Rheologically Stratified Lithosphere to Subduction of an Indenter-Shaped Plate: Insights Into Localized Exhumation at Orogen Syntaxes". *Tectonics* 38.6, pp. 1908–1930. DOI: `10.1029/2018TC005455`.

Lague, D., N. Hovius, and P. Davy (2005). "Discharge, discharge variability, and the bedrock channel profile". *Journal of Geophysical Research: Earth Surface* 110, F04006. DOI: `10.1029/2004JF000259`.

Lamb, S. and P. Davis (2003). "Cenozoic climate change as a possible cause for the rise of the Andes". *Nature* 425.6960, pp. 792–797. DOI: `10/bzjjfh`.

Liu, Y. and D. Zhong (1997). "Petrology of high-pressure granulites from the eastern Himalayan syntaxis". *Journal of Metamorphic Geology* 15.4, pp. 451–466. DOI: `10.1111/j.1525-1314.1997.00033.x`.

Mahadevan, L., R. Bendick, and H. Liang (2010). "Why subduction zones are curved". *Tectonics* 29.6, TC6002. DOI: `10.1029/2010TC002720`.

Michel, L., T. A. Ehlers, C. Glotzbach, B. A. Adams, and K. Stübner (2018). "Tectonic and glacial contributions to focused exhumation in the Olympic Mountains, Washington, USA". *Geology* 46.6, pp. 491–494. DOI: `10.1130/G39881.1`.

Mohadjer, S., T. A. Ehlers, M. Nettesheim, M. B. Ott, C. Glotzbach, and R. Drews (2020). "Temporal variations in rockfall and rock-wall retreat rates in a deglaciated valley over the past 11 k.y." *Geology* 48.6, pp. 594–598. DOI: `10.1130/G47092.1`.

Molnar, P. and P. England (1990). "Late Cenozoic uplift of mountain ranges and global climate change: chicken or egg?" *Nature* 346.6279, pp. 29–34. DOI: `10.1038/346029a0`.

Nettesheim, M., T. A. Ehlers, D. M. Whipp, and A. Koptev (2018). "The influence of upper-plate advance and erosion on overriding plate deformation in orogen syntaxes". *Solid Earth* 9.6, pp. 1207–1224. DOI: `10.5194/se-9-1207-2018`.

Pavlis, G. L., M. A. Bauer, J. L. Elliott, P. Koons, T. L. Pavlis, N. Ruppert, K. M. Ward, and L. L. Worthington (2019). "A unified three-dimensional model of the lithospheric structure at the subduction corner in southeast Alaska: Summary results from STEEP". *Geosphere* 15.2, pp. 382–406. DOI: `10.1130/GES01488.1`.

Pichon, X. L. (1968). "Sea-floor spreading and continental drift". *Journal of Geophysical Research (1896-1977)* 73.12, pp. 3661–3697. DOI: `10.1029/JB073i012p03661`.

Pickering, J., W. Matthews, E. Enkelmann, B. Guest, C. Sykes, and B. M. Koblinger (2020). "Laser ablation (U-Th-Sm)/He dating of detrital apatite". *Chemical Geology* 548, p. 119683. DOI: `10.1016/j.chemgeo.2020.119683`.

Plafker, G. and H. C. Berg, eds. (1994). *The geology of Alaska*. The Geology of North America v. G-1. Boulder, Colo: Geological Society of America. 1055 pp.

Plafker, G., W. J. Nokleberg, and J. S. Lull (1989). "Bedrock geology and tectonic evolution of the Wrangellia, Peninsular, and Chugach Terranes along the Trans-Alaska Crustal Transect in the

Chugach Mountains and Southern Copper River Basin, Alaska". *Journal of Geophysical Research: Solid Earth* 94 (B4), pp. 4255–4295. DOI: `10/dm2328`.

Press, W. H., S. A. Teukolsky, B. P. Flannery, and W. T. Vetterling (1992). *Numerical Recipes in FORTRAN 77: The Art of Scientific Computing*. Cambridge University Press. 1016 pp.

Rahn, M. K., M. T. Brandon, G. E. Batt, and J. I. Garver (2004). "A zero-damage model for fission-track annealing in zircon". *American Mineralogist* 89.4, pp. 473–484. DOI: `10.2138/am-2004-0401`.

Ramos, V. A. and A. Folguera (2009). "Andean flat-slab subduction through time". *Geological Society, London, Special Publications* 327.1, pp. 31–54. DOI: `10.1144/SP327.3`.

Reiners, P. W. and M. T. Brandon (2006). "Using thermochronology to understand orogenic erosion". *Annu. Rev. Earth Planet. Sci.* 34, pp. 419–466.

Reiners, P. W. and T. A. Ehlers, eds. (2005). *Low-temperature thermochronology: techniques, interpretations, and applications*. Reviews in mineralogy and geochemistry v. 58. Chantilly, Va: Mineralogical Society of America. 622 pp.

Reiners, P. W., T. A. Ehlers, and P. K. Zeitler (2005). "Past, Present, and Future of Thermochronology". *Reviews in Mineralogy and Geochemistry* 58.1, pp. 1–18. DOI: `10.2138/rmg.2005.58.1`.

Reiners, P. W., K. A. Farley, and H. J. Hickes (2002). "He diffusion and (U–Th)/He thermochronometry of zircon: initial results from Fish Canyon Tuff and Gold Butte". *Tectonophysics*. Low Temperature Thermochronology: From Tectonics to Landscape Evolution 349.1, pp. 297–308. DOI: `10.1016/S0040-1951(02)00058-6`.

Reiners, P. W., T. L. Spell, S. Nicolescu, and K. A. Zanetti (2004). "Zircon (U-Th)/He thermochronometry: He diffusion and comparisons with 40Ar/39Ar dating". *Geochimica et Cosmochimica Acta* 68.8, pp. 1857–1887. DOI: `10.1016/j.gca.2003.10.021`.

Roe, G. H. (2005). "Orographic Precipitation". *Annual Review of Earth and Planetary Sciences* 33.1, pp. 645–671. DOI: `10.1146/annurev.earth.33.092203.122541`.

Ruddiman, W. F. and J. E. Kutzbach (1989). "Forcing of late Cenozoic northern hemisphere climate by plateau uplift in southern Asia and the American west". *Journal of Geophysical Research: Atmospheres* 94 (D15), pp. 18409–18427. DOI: `10.1029/JD094iD15p18409`.

Sandiford, D. and L. Moresi (2019). "Improving subduction interface implementation in dynamic numerical models". *Solid Earth* 10.3, pp. 969–985. DOI: `10.5194/se-10-969-2019`.

Schellart, W. P., J. Freeman, D. R. Stegman, L. Moresi, and D. A. May (2007). "Evolution and diversity of subduction zones controlled by slab width". *Nature* 446.7133, pp. 308–311. DOI: `10.1038/nature05615`.

Schneider, D. A., M. A. Edwards, W. S. F. Kidd, P. K. Zeitler, and C. D. Coath (1999). "Early Miocene anatexis identified in the western syntaxis, Pakistan Himalaya". *Earth and Planetary Science Letters* 167.3, pp. 121–129. DOI: `10.1016/S0012-821X(99)00022-9`.

Starke, J., T. A. Ehlers, and M. Schaller (2017). "Tectonic and Climatic Controls on the Spatial Distribution of Denudation Rates in Northern Chile (18°S to 23°S) Determined From Cosmogenic Nuclides: ^{10} Be Denudation Rates in Northern Chile". *Journal of Geophysical Research: Earth Surface*. DOI: `10.1002/2016JF004153`.

Stewart, R. J. and M. T. Brandon (2004). "Detrital-zircon fission-track ages for the "Hoh Formation": implications for late Cenozoic evolution of the Cascadia subduction wedge". *Geological Society of America Bulletin* 116.1, pp. 60–75.

Stewart, R. J., B. Hallet, P. K. Zeitler, M. A. Malloy, A. Allen Charlotte M., and D. Trippett (2008). "Brahmaputra sediment flux dominated by highly localized rapid erosion from the easternmost Himalaya". *Geology* 36.9, pp. 711–714. DOI: `10.1130/G24890A.1`.

Strunden, J., T. A. Ehlers, D. Brehm, and M. Nettesheim (2015). "Spatial and temporal variations in rockfall determined from TLS measurements in a deglaciated valley, Switzerland". *Journal of Geophysical Research: Earth Surface* 120.7, pp. 1251–1273. DOI: `10.1002/2014JF003274`.

Tagami, T., R. F. Galbraith, R. Yamada, and G. M. Laslett (1998). "Revised Annealing Kinetics of Fission Tracks in Zircon and Geological Implications". In: *Advances in Fission-Track Geochronology: A selection of papers presented at the International Workshop on Fission-Track Dating, Ghent, Belgium, 1996.* Ed. by P. van den Haute and F. de Corte. Solid Earth Sciences Library. Dordrecht: Springer Netherlands, pp. 99–112.

Tagami, T. and P. B. O'Sullivan (2005). "Fundamentals of Fission-Track Thermochronology". *Reviews in Mineralogy and Geochemistry* 58.1, pp. 19–47. DOI: `10.2138/rmg.2005.58.2`.

Tan, E., L. L. Lavier, H. J. A. V. Avendonk, and A. Heuret (2012). "The role of frictional strength on plate coupling at the subduction interface". *Geochemistry, Geophysics, Geosystems* 13.10. DOI: `10.1029/2012GC004214`.

Thieulot, C., P. Fullsack, and J. Braun (2008). "Adaptive octree-based finite element analysis of two- and three-dimensional indentation problems". *Journal of Geophysical Research: Solid Earth* 113 (B12), B12207. DOI: `10.1029/2008JB005591`.

Tucker, G. E. and G. R. Hancock (2010). "Modelling landscape evolution". *Earth Surface Processes and Landforms* 35.1, pp. 28–50. DOI: `10.1002/esp.1952`.

Tucker, G. E., S. Lancaster, N. Gasparini, and R. Bras (2001). "The channel-hillslope integrated landscape development model (CHILD)". In: *Landscape erosion and evolution modeling.* Boston, MA: Springer, pp. 349–388.

Turowski, J. M., D. Lague, and N. Hovius (2009). "Response of bedrock channel width to tectonic forcing: Insights from a numerical model, theoretical considerations, and comparison with field data". *Journal of Geophysical Research: Earth Surface* 114 (F3). DOI: `10.1029/2008JF001133`.

van der Beek, P. (1995). "Tectonic evolution of continental rifts. Inference from numerical modelling and fission track thermochronology". Theses. Vrije Universiteit.

von Blanckenburg, F. (2005). "The control mechanisms of erosion and weathering at basin scale from cosmogenic nuclides in river sediment". *Earth and Planetary Science Letters* 237.3, pp. 462–479. DOI: `10/cmt9bw`.

Whipple, K. X. (2004). "Bedrock Rivers and the Geomorphology of Active Orogens". *Annual Review of Earth and Planetary Sciences* 32.1, pp. 151–185. DOI: `10.1146/annurev.earth.32.101802.120356`.

– (2014). "Can erosion drive tectonics?" *Science* 346.6212, pp. 918–919. DOI: `10.1126/science.aaa0887`.

Willenbring, J. K. and F. von Blanckenburg (2010). "Long-term stability of global erosion rates and weathering during late-Cenozoic cooling". *Nature* 465.7295, pp. 211–214. DOI: `10.1038/nature09044`.

Willett, S. D. (1999). "Orogeny and orography: The effects of erosion on the structure of mountain belts". *Journal of Geophysical Research: Solid Earth* 104 (B12), pp. 28957–28981. DOI: `10.1029/1999JB900248`.

Willett, S. D., C. Beaumont, and P. Fullsack (1993). "Mechanical model for the tectonics of doubly vergent compressional orogens". *Geology* 21.4, pp. 371–374. DOI: `10.1130/0091-7613(1993)021<0371:MMFTTO>2.3.CO;2`.

Willgoose, G. (2005). "Mathematical Modeling of Whole Landscape Evolution". *Annual Review of Earth and Planetary Sciences* 33, pp. 443–459. DOI: `10.1146/annurev.earth.33.092203.122610`.

Willingshofer, E. and D. Sokoutis (2009). "Decoupling along plate boundaries: Key variable controlling the mode of deformation and the geometry of collisional mountain belts". *Geology* 37.1, pp. 39–42. DOI: `10.1130/G25321A.1`.

Wilson, J. T. (1966). "Did the Atlantic Close and then Re-Open?" *Nature* 211.5050, pp. 676–681. DOI: `10.1038/211676a0`.

Wolfe, M. R. and D. F. Stockli (2010). “Zircon (U–Th)/He thermochronometry in the KTB drill hole, Germany, and its implications for bulk He diffusion kinetics in zircon”. *Earth and Planetary Science Letters* 295.1, pp. 69–82. DOI: `10/cd4bqg`.

Worthington, L. L., H. J. A. van Avendonk, S. P. S. Gulick, G. L. Christeson, and T. L. Pavlis (2012). “Crustal structure of the Yakutat terrane and the evolution of subduction and collision in southern Alaska”. *Journal of Geophysical Research: Solid Earth* 117, B01102. DOI: `10.1029/2011JB008493`.

Zeitler, P. K., A. L. Herczeg, I. McDougall, and M. Honda (1987). “U-Th-He dating of apatite: A potential thermochronometer”. *Geochimica et Cosmochimica Acta* 51.10, pp. 2865–2868. DOI: `10.1016/0016-7037(87)90164-5`.

Zeitler, P. K., A. S. Meltzer, P. O. Koons, D. Craw, B. Hallet, C. P. Chamberlain, W. S. F. Kidd, S. K. Park, L. Seeber, and M. Bishop (2001). “Erosion, Himalayan geodynamics, and the geomorphology of metamorphism”. *GSA Today* 11.1, pp. 4–9.

Zienkiewicz, O. C. and Y. K. Cheung (1967). *The finite element method in structural and continuum mechanics: numerical solution of problems in structural and continuum mechanics*. Vol. 1. McGraw-Hill.